Thermo-Mechanical Analysis and Experimental Investigation on Weld Induced Residual Stress, Distortion and its Mitigation for Submerged Arc Welded Butt Joints of P91 Steel Plate

.

A Thesis Submitted in

Partial Fulfillment of the Requirements

for the Degree of

DOCTOR OF PHILOSOPHY

by

SAURAV SUMAN

(Roll No.- 166103031)

DEPARTMENT OF MECHANICAL ENGINEERING

INDIAN INSTITUTE OF TECHNOLOGY GUWAHATI

GUWAHATI- 781039, INDIA

MAY 2021

DEPARTMENT OF MECHANICAL ENGINEERING
INSTITUTE OF TECHNOLOGY GUWAHATI
GUWAHATI- 781039, ASSAM, INDIA

CERTIFICATE

This is to certify that the thesis entitled "**Thermo-Mechanical Analysis and Experimental Investigation on Weld Induced Residual Stress, Distortion and its Mitigation for Submerged Arc Welded Butt Joints of P91 Steel Plate**" is submitted by **Mr. Saurav Suman** to the Indian Institute of Technology Guwahati for the award of the degree of Doctor of Philosophy. It is a record of original research work carried out under my supervision in the Department of Mechanical Engineering, Indian Institute of Technology Guwahati and has not been submitted elsewhere to award any other degree or diploma.

Dr. Pankaj Biswas

Professor

Department of Mechanical Engineering

Indian Institute of Technology Guwahati

Guwahati- 781039, India

Date: May 16, 2021

Declaration

I declare that

a. The present thesis work is original and has been done by me under the guidance of my supervisor.
b. I have adequately cited and referenced the original sources where others' works have been involved.
c. I have followed academic morality principles and honesty and have neither fabricated nor falsified any idea/data in the present thesis.
d. I have confirmed the norms and guidelines given in the ethical code of conduct of the institute.
e. I realized that any defilement of the above would cause disciplinary action by the institute and induce disciplinary action from the sources that have not been appropriately cited.

Date: May 16, 2021

(Saurav Suman)

Dedicated

To

God

&

My Family

ACKNOWLEDGEMENTS

"The essence of great works is gratitude" I would like to express my heartfelt gratitude towards all those who have immensely helped me during this long strenuous journey and continuously supported me to emerge as a proficient researcher and a mature individual. I oblige everyone who imparts their advice, support and assistance to complete my thesis successfully.

First and foremost, I must express my most profound sense of gratitude and respect for my thesis supervisor, **Prof. Pankaj Biswas,** for providing me with the opportunity to work under his supervision. I am also grateful for his valuable advice and guidance on my research, career, and personal life, which will always be priceless. I heartily appreciate his sincere contribution of time, research expertise and in-depth knowledge throughout the thesis work. I thank him for his generous and caring gesture in ups and downs during my PhD pursuit.

I offer sincere thanks to my doctoral committee members, Dr. Swarup Bag, Prof. Sukhomay Pal and Prof. S. K. Majumder, for their insightful advice, comments and encouragement. I also express thanks and appreciation for their challenging questions and evaluation, which encouraged me to widen my research in various perspectives. I am also fortunate and grateful to receive guidance and support from Dr. M. M. Mahapatra (IIT Bhubaneswar) to work with him through collaboration.

My sincere gratefulness to past and current heads of department Prof. S. K. Dwivedy and Prof. S. Senthivelan for their kind permission for enrolment, registration and several essential supports at IIT Guwahati. I am also grateful to all the Mechanical Engineering Department faculty members for giving me a comfortable and friendly environment for pursuing my research.

Further, I would like to extend my expression of gratitude to Mr. Nand Kanan Das, assistant workshop superintendent and all the staff of the workshop, especially Mr. Dilip Chhetri, Mr. Chandan Banikya, Mr. Dhaneswar Khaklary, Mr. Mrinal Sarma, Mr. Bijoy Kumar Choudhary, Mr. Gohain, Mr. Minesh Ch. Medhi and Mr. Ali for extending their help in the fabrication of experimental setups and various other experimental works. I sincerely acknowledge the assistance received from Mr. Saiffuddin Ahmed, Mr. Sanjib Sarma, Mr. Jiten Basumatary, Mr. Pranjol Paul and Dr. Dhruba Jyoti Bordoloi in various experimental proceedings. I also express

my special obligations to Central Instrumental Facility, IIT Guwahati, to provide experimental facilities related to thesis work.

"*A perfect life partner makes life blissful.*" this is to my caring, supporting and thoughtful beloved wife, Suruchi, who always has stood by me through all my travails, my absences, my fits of pique and impatience. From the depth of my heart, thank you for your encouragement and for being the most vital support system throughout my PhD pursuit.

"*No matter how far we come, our parents are always with us*." I will always be grateful to my parents to provide their best of life advice, lessons and support, which made me a person with great value and ethics. I will always be grateful for your kind blessings.

"Friends at work make work easier", I have been fortunate to be surrounded by friends, Avilash Sahoo, Prabhat Kumar, Sushant Bordoloi, Lenin, Sanasam Vipej, Ricky and lab mates, Saibal, Kanchan, Pradeep Pankaj and Lakshami Dhara. Thank you all for your support and encouragement. I also thank my seniors Mr. Biplab Das, Dr. P. V. S. S Sridhar, Dr. Arpan Kr. Mandal, Dr. A. Kardian to inspire and instigate me to achieve my PhD pursuit. I specially thank my senior Avinish Tiwari for extending help in every aspects of research work through, fruitful discussions and key advice. I am also grateful to have few amazing friends, Suman, Deepak, Abhinav, for their time and energy to play Table Tennis, Tennis and other activities, which kept me mentally healthy and physically fit. I would forever be grateful to all my friends. I also extend my gratitude to my childhood friends for their well wishes and cheers.

Last but not least, I am grateful to the Almighty without whom nothing is possible.

May, 2021 **Saurav Suman**

Abstract

P91 steel is the modified form of Cr-Mo low alloy steel with enhanced creep strength at elevated temperatures. It also possesses properties like low thermal expansion coefficient and better thermal conductivity, high resistance to corrosion cracking & oxidation at high temperature. Hence, it emerged as a superior replacement of 300 series low alloy steels to increase the power plant's efficiency. Consequently, P91 steel is preferred to manufacture the components like pipelines, pressure vessels and power plant elements such as boilers, steam generators and breeders in nuclear power plants, subjected to high operating temperature at and above 600 ºC. Fabrication of most of these power unit components involves fusion welding processes such as SMAW, GMAW, GTAW, SAW etc. Thick plates are typically welded through multi-pass welding. However, conventional submerged arc welding (SAW), activated TIG and laser welding are widely known for deep penetration, high current density, high welding speed and metal deposition rate, which yield good quality weld even in a single or less number of weld passes. Fusion welding offers good mechanical properties and joint efficiency with flexibility in design and weight reduction. Nonetheless, the rapid heating and cooling cycles of the welding process lead to welding induced residual stresses and distortion. Residual stresses in weld components provoke failures below the design load whereas, distortions wreak havoc on the dimensional accuracy of the fabricated structures. Moreover, the weld components under high temperature and corrosive working environments encounter catastrophic failure under the load, much below the material's yield strength. Hence, it is vital to comprehend its state of proneness and the level of control it requires.

Therefore, the current study explores submerged arc square butt welding of P91 steel plate to investigate the welding induced residual stresses and distortions. This is further extended to finite element modelling and simulation of the submerged arc welding of P91 steel plate. Subsequently, mitigation methods at different stages of welding are also proposed. The submerged arc welding experiment is performed on 10 mm thick P91 steel plate to make square butt single and double side single pass welded joints. Welding induced distortions are estimated in terms of angular distortion and edge deflection using coordinate measuring machine. Deep hole drilling and contour surface residual stress measurement techniques, are employed to determine the residual stress across the thickness and spatial distribution across the weld, respectively. Single side single pass welding resulted in the formation of compressive residual stress distribution throughout the thickness in the fusion zone. However, double-sided single-

pass welded joint developed the tensile residual stress in the mid thickness region of fusion zone.

Finite Element (FE) analysis is also carried out for SAW square butt single and double side single pass welded joints of P91 steel plate. The uncoupled thermal-structural FE analysis is performed in ANSYS Mechanical APDL solver. Temperature-dependent material properties, phase changes, solid-state phase transformation, heat source model and element death & birth technique are considered for precise modelling of P91 steel weldments. Solid-state phase transformation exhibited a significant role in accurate prediction and validation of distortion and residual stress results. The quasi-static region of weld fusion zone unveiled compressive longitudinal residual stress in square butt single side single pass welded joints. HAZ regions observed tensile residual stress in both single and double side welded joints. Pre-process, in-process, and post-process mitigation heat treatments are proposed to control welding induced residual stresses and distortion. These mitigation heat treatments are FE modelled and simulated. The combined transient side heating and heat sinking developed a crown shape residual stress distribution with crest and trough of tensile and compressive residual stress of lower magnitude compared to as-welded case. On the other hand, pre and post weld heat treatments controlled the residual stresses and distortions significantly. Preheating effectively reduced the edge deflection and angular distortion values by 41.7% and 54.1% respectively. Post weld heat treatment narrowed down the abrupt change in residual stress distribution across the weld and reduced their magnitude.

At last, microstructure, mechanical properties, chemical compositions and phases are ornately inspected to check the impact of submerged arc welding and mitigation heat treatments on P91 steel welds. The studies revealed needle-shaped or acicular untempered martensite structure in the fusion zone of as- welded weld joints, favouring high thermal gradient and fast cooling rate in SAW process. Post weld heat treatment ensured the presence of carbide and nitride forming elements (i.e. Cr, V) which formed the precipitates like $Cr_{23}C_6$, VN, VC and enhance the creep strength of the weld joint. Preheating reduced the hardness values of the FZ by 8.2% and 10.4% for as-welded and post-weld heat-treated welds owing to decrease in austenitic grain size. Post weld heat treatment reconstituted the tempered martensite, i.e. equiaxed fine-grained ferrite with cementite particles, which softened the material and reduced the micro-hardness values in FZ and HAZ of the weld equivalent to the base metal.

Table of contents

Abstract..... ix

Table of contents..... xii

List of Figures..... xvi

List of Tables..... xxiii

Nomenclature..... xxiv

Abbreviations..... xxix

1 INTRODUCTION.....1

1.1 Preface.....1

1.2 Background and motivation.....2

1.3 Creep strength enhanced ferritic steels.....3

1.4 Welding induced residual stresses and distortions.....5

1.5 Scope of the thesis.....8

1.6 Thesis objectives.....9

1.7 Organization of thesis.....9

2 LITERATURE REVIEW.....12

2.1 Introduction.....12

2.2 Studies on P91 steel weldment.....12

2.3 FE modelling of submerged arc welding for residual stresses and distortions.....15

2.4 Phase transformation effect in welding.....16

2.5 Mitigation techniques for welding induced residual stresses and distortions.....18

2.6 Summary.....24

2.7 Research gaps.....25

2.8 Detailed thesis objectives.....26

3 METHODOLOGY 28

3.1 Introduction 28

3.2 Submerged arc welding of P91 steel plate 28

3.2.1 SAW experiment setup 29

3.2.2 Materials selection 30

3.2.3 Fixture and clamps 31

3.2.4 SAW experiment 32

3.2.5 Temperature profile measurement 34

3.3 Measurement of welding induced distortion 34

3.4 Measurement of welding induced residual stresses 36

3.4.1 Deep Hole Drilling (DHD) measurement 36

3.4.2 Contour measurement 38

3.5 Thermo-mechanical elastic plastic FE modelling of SAW butt joints of P91 steel ..44

3.5.1 Modelling and meshing 44

3.5.2 Thermal modelling 45

3.5.3 Formulation of heat transfer model 49

3.5.4 Structural modelling 50

3.5.5 Modelling SSPT phenomenon 51

3.5.6 Materials properties 54

3.6 Mitigation techniques 56

3.6.1 FE modelling of preheating 56

3.6.2 FE modelling of in-process mitigation 57

3.6.3 FE modelling of post weld heat treatment 61

3.7 Mechanical and microstructural characterisation 63

3.7.1 Sample preparation 63

3.7.2 Macro and micrograph study 64

3.7.3 Microhardness Test 65

3.7.4 Universal tensile test & fractography 66
3.7.5 XRD and EDS analysis 66
3.8 Summary 66
4 STUDY OF THERMAL HISTORY, DISTORTION AND RESIDUAL STRESSES IN SAW WELDED BUTT JOINTS OF P91 STEEL 68
4.1 Introduction 68
4.2 Weld preparation 68
4.3 Thermal history 70
4.4 Welding induced residual distortion 71
4.5 Welding induced residual stresses 72
4.5.1 Square butt single side single pass weld joint 73
4.5.2 Square butt double side single pass weld joint 75
4.6 Summary 79
5 THERMO-MECHANICAL ELASTIC-PLASTIC ANALYSIS OF SAW BUTT JOINTS OF P91 STEEL 81
5.1 Introduction 81
5.2 Thermal model fitting and temperature distribution 81
5.3 Welding induced distortion 86
5.4 Welding induced residual stress 91
5.4.1 Effect of SSPT phenomenon in residual stress distribution 91
5.4.2 Residual stresses in square butt single and double-side welded joint models 92
5.5 Summary 95
6 FE ANALYSIS OF PRE, IN AND POST WELD HEAT TREATMENTS PROCESS FOR THEIR MITIGATION EFFECTS ON SAW BUTT JOINTS OF P91 STEEL 98
6.1 Introduction 98
6.2 Effect of preheating 98
6.3 Effect of in-process mitigation heat treatments 103
6.3.1 Thermal results 103

6.3.2 Welding induced distortion 107
6.3.3 Welding induced residual stress 108
6.4 Effect of post-weld heat treatment 113
6.5 Summary 115
7 INFLUENCE OF PREHEATING AND PWHT ON RESIDUAL STRESSES AND DISTORTION OF SAW WELDED BUTT JOINTS OF P91 STEEL 118
7.1 Introduction 118
7.2 Preheating and PWHT experiments 118
7.3 Mitigation effect on square butt single side single pass welded joint 118
7.4 Mitigation effect on square butt double side single pass welded joint 124
7.5 Summary 126
8 MICROSTRUCTURE AND MECHANICAL CHARACTERIZATIONS OF SAW WELDED BUTT JOINTS OF P91 STEEL WITH PREHEATING AND POST WELD HEAT TREATMENT 128
8.1 Introduction 128
8.2 Macro and microstructural characterization 129
8.3 Micro-hardness across the weld 135
8.4 Weld strength and ductility 137
8.5 Fracture surface analysis 139
8.6 XRD and EDS analysis 141
8.7 Summary 143
9 CONCLUSIONS AND FUTURE SCOPE 145
9.1 Conclusions of the present work 145
9.2 Future scope 147

List of Figures

Figure 1.1 Development of residual stress in the welding heat cycle [26] ---------- 6

Figure 1.2 Various forms of welding induced distortions ---------- 8

Figure 2.1 Schematic of volumetric change in P91 steel weldment during solid-state phase transformation [74] ----------17

Figure 2.2 Schematic of (a) transient thermal tensioning or side heating [85], (b) In process trailing heat sink [94], [95], (c) DC-LSND or trailing cooling source technique [96], [97] (c) heat sink model [98] (d) trailing heat sink [99] ----------21

Figure 2.3 Schematic of (a) Mechanical tensioning technique [102] (b) Rolling technique [103] (c) Electromagnetic force tensioning technique [104] ----------22

Figure 3.1 Experiment set up of SAW process ----------29

Figure 3.2 Fixture with adjustable clamps ----------32

Figure 3.3 Poor top and bottom reinforcement owing to (a) irregular root opening, (b) extensive metal deposition, inadequate bottom reinforcement, (c) large root opening and improper metal transfer ----------33

Figure 3.4 Working principle of the backing bar ----------33

Figure 3.5 Dimensions of the backing bar ----------34

Figure 3.6 (a) CMM set up, (b) Control points for measurement, (c) Angular distortion angle (θ) ----------35

Figure 3.7 Schematic of steps involved in DHD technique ----------37

Figure 3.8 Bueckner's superposition principle for residual stress distribution [114], [115] --39

Figure 3.9 Schematic of (a) wire EDM cutting set up, (b) CMM set up for distortion measurement ----------41

Figure 3.10 Flow chart for the Levenberg- Marquardt algorithm for the best curve or surface fitting [119]----------43

Figure 3.11 Drafted and meshed models of square butt single and double-side single pass weld joints----------45

Figure 3.12 Schematic of double ellipsoidal heat source model----------49

Figure 3.13 Structural boundary conditions to prevent rigid body motion of the weld joint model----------51

Figure 3.14 Material properties for base and weld materials [35], [135] ----------54

Figure 3.15 (a) Modified thermal expansion coefficient for the base plate and weld metal (b) YS and hardening modulus for base and weld metal [35], [135]----------55

Figure 3.16 Schematic of transient parallel side heating ----------58

Figure 3.17 Model and meshing of transient side heating model ----------58

Figure 3.18 Schematic of heat sink setup ----------59

Figure 3.19 Schematic of hybrid combined side heating and heat sink mitigation ----------60

Figure 3.20 Hardness & microstructure study sample ----------64

Figure 3.21 (a) Dimension of sub-size of the tensile specimen and (b) tensile test sample ---64

Figure 3.22 (a) Stereomicroscope (Nikon), (b) Optical Microscope (Zeiss) ----------65

Figure 3.23 Vickers micro hardness testing machine (Omni Tech)----------65

Figure 4.1 Square butt (a) single-side single pass weld joint (b) double-side single pass weld joint----------69

Figure 4.2 Cross-sectional view of square butt single and double-side single pass weld joint samples----------69

Figure 4.3 Thermal history of square butt single-side single pass welding----------70

Figure 4.4 Thermal history of square butt double-side single pass welding ----------70

Figure 4.5 Distortion along the mid line across the weld centreline for square butt single- and double-side welded joints ----------71

Figure 4.6 Distortion along the edge of square butt single- and double-side single pass welded joints----------72

Figure 4.7(a) Weld sample after drilling and trepanning, (b) Locations for residual stress measurement ----------73

Figure 4.8 Through thickness longitudinal and transverse residual stresses in (a) Fusion zone and (b) Heat Affected zone of square butt single-sided single pass joint (DHD technique) --74

Figure 4.9 Surface deformation measurement on CMM ----------75

Figure 4.10 Surface plot for average surface distortion of both the cut surfaces after the data conditioning ----------76

Figure 4.11 (a) Best fitting surface deformation plot (Adjusted R^2 value= 0.9105), (b) FE model of one of the halves of weld sample for surface deformation load structural FE analysis -----77

Figure 4.12 Contour plot of longitudinal residual stress distribution on the cut surface of square butt double-side single pass welded joint (contour measurement technique) ----------77

Figure 4.13 Longitudinal residual stress across the thickness in the fusion zone of square butt single and double side single pass welded joints ----------78

Figure 5.1 Contour plot of temperature distribution during (a) heating and (b) cooling cycles of square butt single side single pass welding----------82

Figure 5.2 Contour plots for temperature distribution during heating in (a) top side weld pass, (b) bottom side weld pass and (c) cooling cycles of square butt double-side welding ---------83

Figure 5.3 (a) Thermal profile and (b) temperature contour for square butt single side single-pass welding----------84

Figure 5.4 (a) Thermal profile and (b) temperature contour for square butt double side single pass welding----------85

Figure 5.5 Angular distortion in the square butt single-side single pass welded joint ---------86

Figure 5.6 Edge deflection of square butt single-side single pass welded joint ----------87

Figure 5.7 Vertical distortion contour in square butt single-side single pass welded joint (no SSPT) ----------88

Figure 5.8 Vertical distortion contour in square butt single-side single pass welded joint (only volume change) ----------88

Figure 5.9 Vertical distortion contour in square butt single-side single pass welded joint (full SSPT effects)----------89

Figure 5.10 Vertical distortion contour in square butt double-side single pass welded joint (full SSPT effects)----------89

Figure 5.11 Angular distortion in square butt single and double-side single pass welded joints ----------90

Figure 5.12 Edge deflection in square butt single and double-side single pass welded joints 90

Figure 5.13 Longitudinal residual stress distribution in square butt single-side single pass welded joint models (a) without considering SSPT (b) considering full SSPT effects --------91

Figure 5.14 Residual stress distribution across the weld in square butt single side single pass welded joint models----------92

Figure 5.15 Longitudinal residual stress distribution in (a) FZ taken at 25 mm away from the starting end of the weld bead and (b) HAZ of square butt single-side single pass welded joint ----------93

Figure 5.16 Cross sectional view of longitudinal residual stress contour in the FZ of square butt single side welded joint of the section taken parallel to reference hole perpendicular to weld centreline similar to DHD measurement----------94

Figure 5.17 Longitudinal residual stress along the weld centreline in the FZ of square butt double-side single pass welded joint ----------95

Figure 6.1 Time-temperature profile for preheating followed by single pass single side welding ----------99

Figure 6.2 Contour plot of temperature distribution during square butt single side single pass welding (a) with preheating, (b) without preheating ---------- 100

Figure 6.3 Angular distortion in the transverse direction---------- 100

Figure 6.4 Edge deflection in the welding direction ---------- 101

Figure 6.5 Vertical distortion contour of (a) as-welded (b) preheated square butt single side single pass welded joint models---------- 101

Figure 6.6 Contour plot of longitudinal residual stress distribution for (a) preheated, (b) as-welded square butt single side single pass welded joint models---------- 102

Figure 6.7 Longitudinal residual stress in as-welded and preheated square butt single side single pass welded joint models---------- 103

Figure 6.8 Thermal profile for transient side heating with square butt single side single pass welding of P91 steel plate---------- 104

Figure 6.9 Contour plot of temperature distribution during square butt single side single pass welding of P91 steel plate (a) with side heating, (b) without side heating---------- 104

Figure 6.10 Thermal profile for heat sinking beneath the root gap in square butt single side single pass welded P91 steel plate ---------- 105

Figure 6.11 Contour plot of temperature distribution during submerged arc square butt single side single pass welding (a) with heat sinking, (b) without heat sinking---------- 106

Figure 6.12 Thermal profile for combined side heating and heat sinking in square butt single side single pass welding of P91 steel plate ---------- 106

Figure 6.13 Angular distortion for different cases of in- process mitigation heat treatments in square butt single side single pass welded joint models (without considering SSPT effect) 107

Figure 6.14 Angular distortion for different cases of mitigation heat treatments in square butt single side single pass welded joint models (considering SSPT effect)---------- 108

Figure 6.15 Longitudinal residual stress distribution across the weld of square butt single side single pass weld joint with side heating considering (a) different side heating temperatures without SSPT, (b) different side heating temperatures with SSPT, (c) different heating locations without SSPT and (d) different heating locations with SSPT---------- 109

Figure 6.16 Longitudinal residual stress across the weld in square butt single side single pass welded joint models with heat sinking (a) without SSPT effect, (b) with SSPT effect ------ 111

Figure 6.17 Residual stress distribution for combined side heating and heat sink (a) without considering SSPT, (b) considering SSPT ---------- 112

Figure 6.18 Thermal profile of post-weld heat treatment---------- 113

Figure 6.19 Contour plot of longitudinal residual stress distribution in (a) post-weld heat-treated, (b) as-welded square butt single side single pass welded joint models ---------- 114

Figure 6.20 Stress relaxation at a point between the weld and HAZ region on the top surface of the plate during PWHT (considering creep phenomenon) ---------- 115

Figure 7.1 (a) Angular distortion, (b) edge deflection in square butt single-side single pass welded joints with and without preheating ---------- 119

Figure 7.2 Residual stresses in (a) FZ and (b) HAZ of preheated and as-welded square butt single side single pass welded joints ---------- 120

Figure 7.3 Residual stress in (a) FZ and (b) HAZ of as-welded and post-weld heat-treated square butt single side single pass welded joints ---------- 121

Figure 7.4 Residual stress in (a) FZ and (b) HAZ of combined preheated and post-weld heat-treated weld and as-welded square butt single side single pass welded joints---------- 122

Figure 7.5 Extreme values of longitudinal and transverse residual stress in the square butt single side single pass joints of P91 steel under four different cases ---------- 123

Figure 7.6 (a) Angular distortion, (b) edge deflection in square butt double-side single pass welded joint ---------- 124

Figure 7.7 Contour of measured longitudinal residual stress distribution in (a) as welded, (b) preheated, and (c) post-weld heat-treated square butt double side single pass welded joints125

Figure 8.1Cross-sectional view of the weld samples for four cases ---------- 130

Figure 8.2 Microstructure images of the as-welded case in (a) Base metal (b) weld centreline in FZ (c) Fusion boundary line with FZ and HAZ (d) CGHAZ (e) FGHAZ ---------- 131

Figure 8.3 Microstructure images of the preheated weld (a) Base metal (b) Weld Zone in centreline (c) Fusion boundary line with FZ and HAZ (d) CGHAZ (e) FGHAZ---------- 132

Figure 8.4 Microstructure images of the post-weld heat-treated weld (a) base metal (b) Weld Zone in centreline (c) Fusion boundary line with FZ and HAZ (d) CGHAZ (e) FGHAZ--- 133

Figure 8.5 Microstructure images of preheated and PWHT weld (a) Base metal (b) Weld Zone in centreline (c) Fusion boundary line with FZ and HAZ (d) CGHAZ (e) FGHAZ---------- 135

Figure 8.6 Contour plot of hardness values for (a) as welded, (b) Preheated, (c) PWHT weld (d) Preheated and PWHT square butt double sided single pass welded joint---------- 136

Figure 8.7 Micro-hardness across the weld for four cases ---------- 137

Figure 8.8 (a) Engineering Stress vs engineering Strain curve at room temperature, (b) Test specimens after ductile fracture ---------- 138

Figure 8.9 Necking Area and SEM images of fractured surfaces of the tensile specimens of all different cases, fractured under the tensile test conducted at room temperature. ---------- 140

Figure 8.10 EDS of the metal surface of (a) base Metal, (b) as-welded weld, (c) post-weld heat-treated weld ---------- 142

Figure 8.11 X-ray diffraction intensity plots for (a) Base metal, (b) P91 steel weld after PWHT. ---------- 143

List of Tables

Table 1.1 Typical range of the chemical composition of P91 steel ---------- 4

Table 2.1 P91 steel welds of different thicknesses and welding methods----------14

Table 2.2 In process mitigation techniques for thin plate welds----------24

Table 3.1 Chemical composition of base plate----------30

Table 3.2 Chemical composition of Electrode material ----------31

Table 3.3 Composition of Flux----------31

Table 3.5 Range of process parameters for trial welding experiments ----------32

Table 3.6 Temperature-dependent Enthalpy of P91 steel ----------56

Table 4.1 Welding parameters for single and double side SAW joints----------68

Table 5.1 Constant parameters for the double ellipsoidal heat source model ----------82

Table 8.1 Weld samples with different heat treatment conditions ---------- 128

Table 8.2 Tensile test results for four cases and P91 steel plate---------- 139

Table 8.3 Variation (%) in UTS and YS of the welded joint due to preheating and PWHT processes---------- 139

Nomenclature

Ac_1	Lower critical temperature at pearlite transforms to austenite
Ac_3	Upper critical temperature at ferrite completely transforms to austenite
α	Ferrite phase
α^*	Martensite phase
γ	Austenite phase
δ	Delta- ferrite
Ω	Ohm
$\boldsymbol{\theta}$	Angular distortion angle
h	Vertical distortion value at the edge of the weld plate
l	Width of one of the base plates
K	Kelvin
W	Watt
J	Joule
℃	Degree Celsius
A	Ampere
V	Welding voltage
I	Welding current
ϕ	Direction of distortion measurement in deep hole drilling experiment
$d(\phi)$	Hole diameter at measurement direction ϕ
$\varepsilon_{\phi,y}$	Strain component at depth y in measurement direction ϕ
ε_{yy}	Strain at depth 'y' in an axial direction

σ_{ij}	Stress component in *i* plane and *j* direction
E	Elastic modulus
υ	Poisson's ratio
Z_i	Measured value of surface distortion of data points in contour method
$Z_{x,y}$*	Modified value of surface distortion (*Z*) after slope error correction
m	Slope of initial surface distortion plot in contour method
X, *Y*	Coordinates of each target point from origin in contour method
χ^2	Chi- square
$f(x_i', \hat{\beta})$	Curve fitting function model
σ_i	Standard error for i_{th} observation
x_i'	Row vector for independent variables
$\hat{\beta}$	Parameters vector for i_{th} observation
P	Inverse of the measurement error covariance matrix
λ	Non- negative damping factor
G	Gradient operator in Levenberg- Marquardt (L-M) iteration algorithm
I	Inverse of positive scalar quantity
p	Perturbation to update the parameters
Wt.	Weight
T	Temperature
ΔT	Change in temperature
$\hat{a}$	Constant parameter stands for distortion of the hole (DHD measurement)
$\hat{b}$	Constant parameter stands for eccentricity (DHD measurement)
k	Thermal conductivity

$\boldsymbol{\rho}$	Density
$\boldsymbol{c_p}$	Specific heat at constant pressure
$\boldsymbol{t}$	Time
∇	Gradient operator
h_f	Convective heat transfer coefficient
Q_n	Component of the heat flux vector normal to the weld surface
Q_{conv}	Heat loss from the work surface by convection
Q_{supp}	Heat flux supplied from an external welding source
$\boldsymbol{N}$	Element shape function
$\boldsymbol{T_e}$	Nodal temperature vector
$Q_{f,r}$	Heat generation through double ellipsoidal heat source model,
Q	Total heat input of welding
η	Arc efficiency of welding process
$f_{f,r}$	Proportional coefficient representing heat apportionment in front and back of the heat source
$f_A(T)$	Austenite fraction at T temperature
V_A	Fractional phase volume for austenitic equilibrium
M_s	Start temperature for martensitic transformation during cooling
M_f	Finish temperature for martensitic transformation during cooling
$f_m(T)$	Martensite fraction at T temperature
$\Delta f_m(T)$	Differential change in martensitic fraction
$\Delta\varepsilon_{vol\_martensitic}$	Volumetric strain for martensitic transformation

$\Delta\varepsilon_{vol\_austenitic}$	Volumetric strain for austenitic transformation
$\Delta\varepsilon_{tp}$	Transformation plasticity strain
C_{trp}	Coefficient of transformation plasticity
$\sigma_{YS}\|_A$	Yield strength in austenite phase
$\sigma_{YS}\|_M$	Yield strength in martensite phase
C_s	Heat capacity at solidus temperature
C_L	Heat capacity at liquidus temperature
C^*	Specific heat of transition state
L	Latent heat
T_s	Solidus temperature
T_L	Liquidus temperature
T_o	Ambient temperature
v_p	Velocity of preheating heat source
r	Characteristic radial dimensional parameter that defines the distribution of 95% of heat flux deposited.
x, y, z	Cartesian Coordinates
v_{ht}	Velocity of side heating heat source
Re_L	Reynold's number
Pr	Prandtl's number
L	Length of the plate (forced convection cooling in laminar flow)
v_∞	Approach velocity (forced convection cooling in laminar flow)
μ	Viscosity of water
H_p	Hollomon-Jaffe or Larsen miller parameter

C_{HP}	Larsen miller constant
T_a	Absolute temperature
t_r	Time for creep rupture
$\dot{\varepsilon}_{creep}$	Creep strain rate
$C_{1,2,3}$	Constant parameters to represent creep law
A_c, n_c	Constant parameters for Norton's creep law
Cr	Chromium
Mo	Molybdenum
V	Vanadium
Nb	Niobium
N	Nitrogen
P	Phosphorus
S	Sulphur
Al	Aluminium
C	Carbon
Si	Silicon
Mn	Manganese
Zr	Zirconium
B	Bismuth
Ti	Titanium
Fe	Iron
Ni	Nickel
W	Tungsten
Sn	Tin

Abbreviation

CSEF	Creep Strength Enhanced Ferritic
GTAW	Gas Tungsten Arc Welding
MMAW	Manual Metal Arc Welding
SAW	Submerged Arc Welding
TIG	Tungsten Inert Gas
MIG	Metal Inert Gas
GMAW	Gas Metal Arc Welding
SMAW	Shielded Metal Arc Welding
LBW	Laser Beam Welding
FCAW	Flux Cored Arc Welding
FSW	Friction Stir Welding
A-TIG	Activated- Tungsten Inert Gas
FEM	Finite Element Method
3D	Three Dimensional
FE	Finite Element
BM	Base Metal
FZ	Fusion Zone
HAZ	Heat Affected Zone
FGHAZ	Fine-Grained Heat Affected Zone
CGHAZ	Coarse Grain Heat Affected Zone
ICHAZ	Inter Critical Heat Affected Zone
ASTM	American Society of Testing and Materials
ASME	American Society of Mechanical Engineers

AWS	American Welding Society
ORNL	Oak Ridge National Laboratory
OTBM	Over Tempered Base Metal
NDE	Non-Destructive Evaluation
PWHT	Post Weld Heat Treatment
BCC	Body Centered Cubic
FCC	Face Centered Cubic
BCT	Body Centered Tetragonal
PAG	Prior Austenitic Grains
PAGB	Prior Austenitic Grain Boundary
SSPT	Solid State Phase Transformation
TTT	Time Temperature Transformation
DC-LSND	Dynamically Controlled Low Stress No Distortion
TRM	Trailing Rolling Method
FESEM	Field Emission Scanning Electron Microscopy
XRD	X-Ray Diffraction
EDS	Energy Dispersive X-ray Spectroscopy
DHD	Deep Hole Drilling
IGBT	Insulated Gate Bipolar Transistor
ESAB	Elektriska Svetsningsaktiebolaget
DAQ	Data Acquisition
LVDT	Linear Variable Differential Transformer
DIC	Digital Image Correlation
CMM	Coordinate Measuring Machine
EDM	Electric Discharge Machine

UTS	Ultimate Tensile Strength
YS	Yield Strength
HS	Heat Sink
TSH	Transient Side Heating
VC	Vanadium Carbide
VN	Vanadium Nitride
Cr_7C_3	Chromium carbide
$Mn_{23}C_6$	Manganese Carbide
$Cr_{23}C_6$	Chromium Carbide
Cr_2N	Chromium Nitride
NbN	Niobium Nitride
Fe_7W_6	Iron tungsten
Al_2O_3	Aluminium Oxide
MnO	Manganese oxide
CaF_2	Calcium Fluoride
SiO_2	Silicon oxide
TiO_2	Titanium Oxide
CaO	Calcium Oxide
MgO	Magnesium Oxide

CHAPTER 1

INTRODUCTION

1.1 Preface

Creep-Strength-Enhanced Ferritic steels are one of the most preferred steels in high temperature and corrosive working environments like boilers, pipelines, nuclear power plants, chemical industries etc. Additionally, its body-centred cubic structure ensures superior qualities over austenitic steels, such as lower thermal expansion coefficient and better conductivity [1]. For decades, such steels are being evolved and manufactured for different chemical compositions (9–12% Cr, 1–1.5% Mo) and heat treatments. Welding processes like TIG, MIG, GTAW, MMAW, SAW, EBW and LBW welding are practised to fabricate different welded structures of CSEF steels. A conventional SAW process shows various advantages over other welding processes like high current density, high heat input and high deposition rate resulting in better bead quality. SAW process is a fully automatic welding method with controlled parameters, highly suitable for continuous and long weld length [2]. Arc welding encourages non-uniform rapid heating and cooling, which induces residual stresses and distortion. The magnitude of welding induced distortions and stresses depends on the type of weld material, weld components' geometry, welding process parameters, clamping and other welding conditions [3]–[5]. Weld induced residual stresses can cause premature failure even before the maximum load condition. Residual stresses and distortion affect the overall design strength and final dimensional structure of the weld components and may cause catastrophic failure in elevated temperature and pressure working environments. Sometimes, high tensile residual stresses also induce intergranular stress corrosion and hydrogen embrittlement.

Hence, this thesis involves submerged arc welding of one of the CSEF steels to study welding induced residual stresses and distortions. The DHD and contour residual stress measurement experiments are conducted to measure the residual stress distribution through the thickness and across the weld centreline of the weld joint. A three-dimensional transient elastic-plastic thermal-mechanical analysis is carried out to predict the residual stresses and distortion using the FEM method. Several pre-, in-, and post- process mitigation techniques are also proposed and analysed for their mitigation effects. The heating and cooling cycles involved in welding

and other heat treatments adversely affect the weld joints' microstructure, phase, composition, and mechanical behaviour. Hence, microstructural and mechanical behaviours of SAW joints of P91 steel plate are also discussed for the effect of welding and mitigation heat treatments.

1.2 Background and motivation

The escalation of the thermal power plant's efficiency has always been an endeavour in the energy industries. It has been discovered that if the steam pressures in the power plant exceed 30-35 MPa, the service temperatures range of 570–630 ^{o}C can achieve efficiencies of 45-50% [6]. The typical efficiency of a conventional fossil-fired plant ranges between 25–30% for operating pressures and temperatures at ~17 MPa and 560 ^{o}C. If increased, the operating temperature and pressure of thermal power plants can increase the efficiency and reduce the emission of harmful gases like CO_2, SO_2 etc. [7], [8]. Hence, the components involved in this must withstand high operating temperature and pressure, provide microstructural stability and prevent creep, fatigue failure and hydrogen-induced cracking. It should also inhibit corrosion and oxidation. The properties like low coefficient of thermal expansion, better thermal conductivity, ductility and toughness, high resistance to stress corrosion cracking & oxidation and high creep rupture strength make it superior over austenitic stainless steel [9], [10]. Therefore, CSEF steels are used for pipelines, power unit components being the parts of boiler and steam generators, subjected to high operating temperature. Fabrication of these power unit components involves the fusion welding process. Different welding techniques such as TIG, MIG, GMAW and GTAW are considered to weld such low alloy steels of thick and thin plates [11]-[15]. However, most of these welding techniques involve multi-pass welding for the joining of thick plates. Similarly, welding techniques like EBW, LBW and activated TIG are also considered as single-pass welding. On the other hand, the conventional submerged arc welding (SAW) process exhibits various advantages over another arc welding, such as deep penetration, high current density, high metal deposition rate and fully automated high-speed welding [16]. Hence, the conventional SAW process can be effectively utilised in thick plate welding of P91 steel for single or minimum passes.

The welding process's rapid heating and cooling cycles induce residual stresses throughout the plate's thickness and across the weld centreline. The magnitude and distribution of residual stresses are the key inputs for ensuring the product design, safe and economic operation of components and structures over the service life. It becomes more critical in a high temperature and pressure working environment [17]. However, many factors act together to control and

govern the state of residual stresses, such as welding methods, welding operating parameters, material properties, structural components (shape & size), and external welding conditions (fixture, jigs). Therefore, residual stress development in the weld components is one of the most critical research interests. Additionally, it has been discovered that steels in the group of 9–12% chromium are prone to Type IV cracking or, say, catastrophic failure. Hence, awareness and proper mitigation of the "as welded" residual stresses in P91 steel weldment are highly significant fields of interest. Experimental and numerical or finite element methods are equally applicable in determining residual stresses' distribution with their respective limitations. Therefore, a combined experimental and numerical estimation of residual stresses furnishes a detailed understanding of it. It facilitates deciding the appropriate mitigation practices controlling the magnitude, nature and distribution of residual stresses.

The mitigation stages are widely known as pre-process, in-process and post-process mitigation. All three phases of mitigations have a different level of alleviation on both micro and macro residual stresses. Several methods have already been proposed in previous literature, such as welding sequences, preheating, thermal and mechanical tensioning during welding and post-weld heat treatments. P91 steel welds experience solid-state phase transformation, which leads to exceptional residual stress distribution. Hence, the study of various levels of residual stresses mitigation by an individual and combined ways is essential to reach the optimised level of mitigation effect.

1.3 Creep strength enhanced ferritic steels

Cr-Mo low alloys steels are called CSEF steels with main alloying element 9-12% Cr. CSEF steels have come to existence in the last few decades, as P9, T9, P91, T91, P92 etc. In the mid-1960s, 12% of Cr-Mo-V steels were developed to manufacture power plants components. The operating temperature for such components is around and above 560 ^{o}C. The creep strength of 12% steel is derived from the solid solution strengthening and precipitation strengthening. Most of the 12% Cr steels failed in long-term creep exposure because of precipitation of Z-phase (with alloying elements like Cr, V, Nb, N) [18]. It was recently discovered that the high percentage of Cr content accelerates the Z-phase precipitation [19], [20]. As a result, the Cr percentage was brought down to 9%, which enhanced the creep strength of 12% Cr steels. First of all, the 9% Cr CSEF steel was developed by Oak Ridge National Laboratory. Over the years, improvements were incorporated in CSEF steel by adding strong carbide and nitride forming elements such as V and Nb with a controlled amount of N. Hence, the modified form of P9

steel is designated as Grade 91 (i.e., 9Cr-1Mo-V-Nb) steel. Grade 91 steel is designated P91 for pipe, T91 for the tube, and ASTM A335 for the plate. The optimum alloy design of the P91 steel assures the 100% martensitic microstructure with no δ-ferrite. Similarly, the appropriate chemical compositions of P91 steel controls the microstructure stabilization during creep exposure. The acceptable range of most of the elements in P91 steel is given in Table 1.1.

Table 1.1 Typical range of the chemical composition of P91 steel

Element	Composition range (Wt.%)	Element	Composition range (Wt.%)	Element	Composition range (Wt.%)	Element	Composition range (Wt.%)
C	0.08-0.12	**Mo**	0.8-1	**P**	≤ 0.02	**Al**	≤ 0.02
Si	0.2-0.5	**V**	0.1-0.3	**S**	≤ 0.01	**Ni**	≤ 0.4
Mn	0.3-0.6	**B**	≤ 0.01	**Cr**	8.5-9	**N**	0.03-0.07
Zr	≤ 0.01	**Ti**	≤ 0.01	**Fe**	Rest		

The impact of different elements on the mechanical and physical properties as well as microstructural behaviour of P91 steel are explained as follows-

a. **Cr** is the principal alloy element in P91 steel which works as the ferrite stabilizer. It provides a solid solution strengthening with the addition of iron (Fe). Cr attributed the creep strength to P91 steel by forming the Cr-rich $M_{23}C_6$ type carbides precipitates. $M_{23}C_6$ enhances the creep strength of P91 steel by pinning the movement of sub-grain boundaries and dislocations [21].

b. **Mo** and **W** also enhance the solid solution strengthening and work as ferrite stabilizers in P91 steel. The amount of W and Mo must be limited to avoid the formation of δ -ferrite. W and Mo impede the motion of free dislocations by introducing the local strain within the matrix. The W and Mo enhance the solid solution strengthening in increasing hardness and creep strength value [22].

c. **V** and **Nb** form carbide, nitride and carbo-nitride of type MX (M: V, Nb; X: C, N) or [M (C, N)] in P91 steel. Such MX type precipitates enhance precipitation strengthening and help to impede the dislocation movement. It slows down the recovery rate of dislocation structures [23]. Both V and Nb addition promote carbide precipitates that reduce the carbon content in the matrix and enhance steel corrosion strength [10].

d. **Co, Ni** and **Mn** ensure the 100% austenitic transformation during heating, which results in 100% martensitic transformation during cooling. Mn is a poor austenite stabilizer. However, Ni and Co ensure good toughness. Ni and Mn also form an unwanted M_6 (C, N) phase, which causes a high coarsening rate and destabilizes the $M_{23}C_6$ during the creep exposure [24].

e. **C** and **N** are the carbide and carbo-nitride formers that cause precipitation hardening and enhance creep strength. C and N are highly soluble in austenite compared to ferrite [10].

1.4 Welding induced residual stresses and distortions

Residual stresses in welded joints primarily develop due to differential weld thermal cycle (heating, peak temperature and cooling at any moment during welding) experienced by the weld metal and region closed to fusion boundary, i.e., heat-affected zone. The type and magnitude of the residual stresses vary continuously during different welding stages, i.e., heating and cooling. During heating, the base metal region is heated for melting and leads to thermal expansion. The surrounding base metal at comparatively low temperature restricts the same and develops compressive residual stress under thermal expansion. After attaining a peak value, compressive residual stress gradually decreases owing to softening of metal being heated. Compressive residual stress near the faying surfaces eventually reduces to zero as soon as melting starts, and a reverse trend is observed during the cooling stage of the welding. As metal starts to shrink during cooling, tensile residual stresses develop (only if shrinkage is not allowed either due to metallic continuity or constraint from job clamping). Their magnitude keeps on increasing until room temperature is attained.

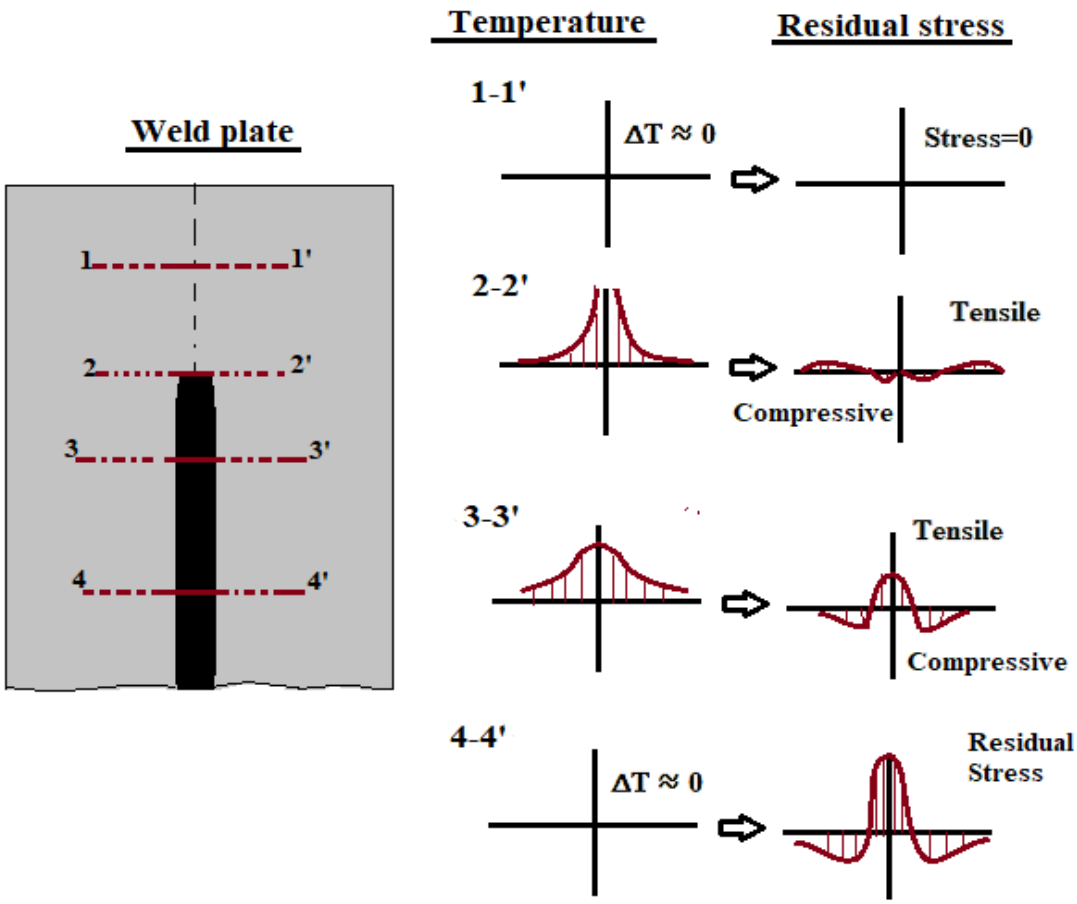

Figure 1.1 Development of residual stress in the welding heat cycle [25]

Figure 1.1 shows the development of residual stresses crosswise to a welded seam in an analogy. This figure considers only shrinking residual stresses. Before applying the welding heat, the seam area is stress-free (Section 1-1'). The welding cycle's highest temperature can be found in (Section 2-2'), i.e., at the weld pool. At this point, there are no residual stresses because molten metal cannot transmit forces at the weld pool. Areas close to the joint expand through welding heat but are supported by areas, which are not so close to the seam. Thus, areas close to the joint show compression stress, areas away from the joint experience tensile stress. In sections 3-3', the already solidified weld metal starts to shrink and is supported by areas close to the seam. As a result, the weld seam shows tensile stresses, and the adjacent areas show compression stresses. In sections 4-4', the tensile residual stress condition is recognised in the weld region at room temperature, as shown in Figure 1.1. However, the phase change and solid-state phase transformation during heating and cooling cycles may also affect weld metal's thermal induced volumetric expansion and contraction. As a result, the final residual stress in fusion and heat-affected weld regions may be of tensile or compressive nature.

In arc welding, plastic thermal strain develops near the weld region because of the weldment and nearby base metal regions. This plastic strain develops permanent distortion of the welded structure, which is termed welding-induced distortion. The mode of welding-induced distortion could show up as in-plane distortion such as stretching and out-of-plane distortion such as bending, rotation or buckling. Hence, depending on the shrinkage pattern and the shape of the welded structure, various distortions such as bending, buckling, and rotation occur. The distortion found in the welded structures is caused by four fundamental dimension changes during the welding process, shown in Figure 1.2.

i. Transverse shrinkage of butt joints: dimensional reduction in a direction perpendicular to the welding line.

ii. Longitudinal shrinkage of butt joints: dimensional reduction in a direction parallel to the welding line. The longitudinal shrinkage amount is smaller than the transverse shrinkage, about 1/1000 of the weld length as reported by several workers.

iii. Angular distortion of butt joints: Angular change due to a non-uniform thermal contraction through the plate's thickness. The non-uniform thermal contraction originates from the uneven heating through the thickness during welding.

iv. Angular distortion of fillet welds: Like the angular distortion of welds in butt joints, the non-uniform thermal contraction through the flanges' thickness creates a moment M about the neutral flange axes.

v. Buckling distortion: buckling distortion is caused by in-plane compressive stresses and is therefore different from the other types of distortions. Buckling may occur in several modes.

vi. Bending distortion: produced by bending stresses induced by the welds' longitudinal shrinkage forces not coinciding with the neutral axis of the weldment.

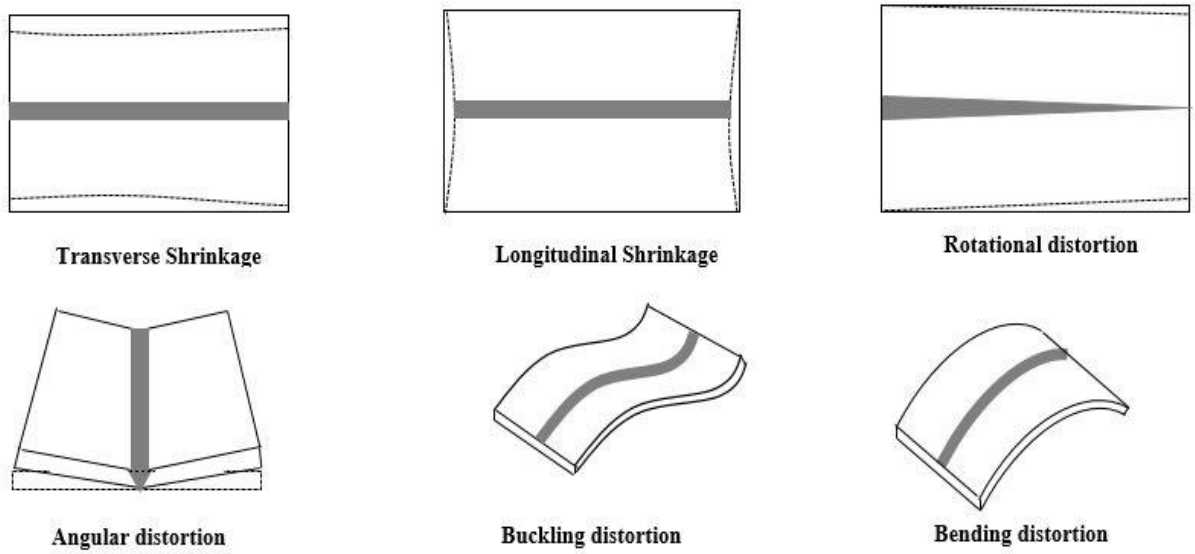

Figure 1.2 Various forms of welding induced distortions

1.5 Scope of the thesis

The thesis aims to inspect the submerged arc welding process on P91 steel weld plate for welding induced mechanical, metallurgical and microstructural changes. A conventional submerged arc welding process is known for its high efficiency, high current density, deep penetration, and automation. Consequently, submerged arc welding can afford good weld bead quality even with a single pass in thick plate welds. Hence, submerged arc welding is performed on a P91 steel 10 mm thick plate with single-pass welding to investigate welding induced residual stress and distortion. The welding induced microstructural evolution and mechanical properties of P91 steel weld are elaborately observed to assess the weld joint's quality. P91 steel is a modified form of Cr- Mo-alloy steel and holds austenitic- martensitic phase transformation in solid-state during thermal cycles of welding. Hence, the study is further extended to stake out this phenomenon in submerged arc welding of P91 steel plates. It leads to finite element modelling and simulation of submerged arc welded P91 steel plate considering temperature-dependent material properties of base and weld metal, phase changes at the solid-state, solid to the liquid state and mushy zone to analyse welding induced residual stresses and distortions.

Welding induced residual stresses and distortion adversely affect the welded components' overall performance, especially in high temperature and pressure working conditions. And it

must be controlled at the welding design stages. Hence, the remedial and corrective steps known as mitigation techniques are also explored in this thesis. Therefore, these mitigation techniques are proposed, FE modelled and simulated for different stages of welding, i.e. before, during and after the submerged arc welding process on the P91 steel plate to assess and compare their mitigation effects. Further, the thesis also includes the mitigation experiment based on the predicted results of the proposed techniques. The thesis also explores the microstructural evolution and mechanical behaviour of P91 steel weld after submerged arc welding and heat treatments related to mitigation experiments.

1.6 Thesis objectives

The objectives of this thesis are as follows:

- Experimental investigations on welding induced distortions and residual stresses in submerged arc square butt-welded joints of P91 steel.
- Thermo- mechanical elastic-plastic finite element modelling and simulation of submerged arc square butt-welded joints of P91 steel by considering temperature-dependent material properties, phase changes, austenitic- martensitic transformation or the solid-state phase transformation effect etc. to analyse welding induced distortions and residual stresses.
- Study different mitigation techniques, i.e. pre-process, in-process and post-process heat treatments on SAW butt joints of P91 steel plate to analyse their mitigation effects on welding induced distortions and residual stresses.
- Study of microstructural evolution and mechanical behaviour of P91 steel welds joints before and after mitigation heat treatments.

1.7 Organization of thesis

The thesis is sub-divided into four major sections. The first section starts with a comprehensive introduction and literature background in chapter 1 and chapter 2. The second section explains the methodologies behind various experiments and finite element modelling methods to achieve the thesis objectives, collectively included in chapter 3. The third section is about results and discussion on welding induced residual stresses and distortions, mitigation of residual stresses and distortions and microstructural and mechanical properties of P91 steel welds, covering chapters 4 to 8. At last, the fourth section includes the conclusions and future scopes of the thesis work, as explained in chapter 9.

Following this introductory **chapter 1**, an inclusive literature survey focused on significant areas related to P91 steel welds and thermo-mechanical modelling of arc welding process is presented in **chapter 2**.

Chapter 3 provides a detailed description of the methodology for experiments and finite element modelling. It explains suitable materials & process parameters for welding experiments and discusses distortion and residual stress measurement techniques. Similarly, the mathematical formulation and boundary conditions in FE modelling are elaborately explained in this chapter.

Chapter 4 presents the results and its correlative discussion on submerged arc welding induced temperature distribution, distortion and residual stresses. It discusses the comparative studies on square butt single and double side single pass submerged arc welded joints of P91 steel plate.

Chapter 5 discusses the FE simulation of submerged arc welding of P91 steel plate to predict welding induced temperature distribution, distortion and residual stresses. The effects of phase changes and solid-state phase transformation on the accuracy of predicted results are separately discussed in this chapter.

Chapter 6 includes FE modelling and simulation of proposed pre, in and post welding mitigation techniques to control distortion and residual stresses in SAW butt joints of P91 steel. The predicted results are analysed and compared for their mitigation results.

Chapter 7 describes the mitigation results of heat treatment experiments to control distortion and residual stresses in SAW butt joints of P91 steel. The mitigation effect is profoundly analysed as individual and combined to compare the results.

Chapter 8 discusses the microstructural evolution and mechanical behaviour of submerged arc welded butt joint of P91 steel to analyse the effect of welding and other mitigation related heat treatment processes.

At last, the overall general conclusions of the thesis are presented in **chapter 9**. The future scopes of the current thesis work are also explained in this chapter.

CHAPTER 2

LITERATURE REVIEW

2.1 Introduction

This chapter provides the literature review on past investigations, which are pertinent to the current thesis work. The literature survey is presented in four sections, excluding the Introduction. The following section 2.2 gives a detailed review of research works on P91 steel and its weldments. The prime focus is on studies of mechanical properties, microstructural behaviour and residual stresses in P91 steel weld joints of different welding processes.

Further, section 2.3 thoroughly reviews finite element modelling and simulation of the submerged arc welding process. The review is confined to mathematical formulation and boundary conditions in thermal and structural FE modelling of welding process considering material properties, process parameters, heat source model etc. It is widely known that P91 steel possesses solid-state phase transformation during the heating-cooling cycles of welding. Hence, a brief review is also presented in section 2.4 on various aspects and strategies on the formulation of solid-state phase transformation in FE modelling. The following section 2.5 discusses various proposed mitigation methods which control and moderate the welding induced residual stresses and distortions. However, this section is more focused on thermal load-based mitigation methods. Hence, the overall literature review is presented in four major sections, as follows-

2.2 Studies on P91 steel weldment

From the last two decades, 9Cr- 1Mo- V steel grabbed the researchers' attention in replacing the 2.25Cr- 1Mo steel and high strength 304 stainless steel for high creep strength, corrosion resistance in a high-temperature work environment up to 625 ^{o}C. Polcik et al. analysed the creep phenomenon in 9 Cr-Mo-V steel at 873 K. They found that the variation in sub-grain size conforms to an exponential change in stress value [26]. Sireesa et al. [27], [28] investigated the effect of three different filler materials: standard 9 Cr- 1 Mo steel, modified 9 Cr- 1 Mo, and nickel-base alloy Inconel 182 on MMAW butt joints of P91 steel. They characterised the microstructures and mechanical properties of those different joints within the fusion zones. Inconel 182 weld showed the highest toughness with lowest tensile properties. Spigarelli and

Quaderini investigated the creep response of P91 steel weld at 600 ^{o}C and found that the fine-grained HAZ region exhibit the highest values of minimum strain rate. They also observed that weld metal had the highest creep strength, while the parent metal exhibited an intermediate level of strength [29]. Tabuchi and Takahashi [30] also discovered that the creep strength of P91 steel weld is lower than the base metal that leads to Type-IV failure in HAZ, especially in high temperatures. Yaghi et al. [31] [32] described two axis-symmetric butt P91 steel pipe welds having 4 or 36 passes with a wall thickness of 7.1 or 40.0 mm, respectively. They introduced a modified data for temperature-dependent material properties of P91 steel. They incorporated it for effective P91 steel weld pipe modelling, leading to comparatively fair prediction results for residual stress distribution. They conducted several FE modelling studies on P91 steel for thick and thin plate multi-pass welding for GTAW, SMAW, MMAW [17], [32]–[35]. They discovered that P91 steel welds develop M- shape residual stress distribution across the weld centreline. The first time, they incorporated the concept of solid-state phase transformation in P91 steel weld for FE modelling, which exhibited its effect on residual stress distribution results [33]. Kumar et al. [36] investigated the residual stress distribution in laser-welded 9mm thick Grade 91 steel plate. They found that the measured longitudinal and transverse residual stress components show a bimodal distribution across the weld with a low tensile or compressive trough at the weld bead centre. Kundu et al. [37] also characterised residual stress distribution in electron beam welded 9 mm thick P91 steel plate and revealed a compressive residual stress distribution in the fusion zone. Zubairuddin et al. [38] investigated the residual stress and distortion in a 3 mm thin GTA welded butt joint of 9Cr-1Mo steel. They also observed an M-shape distribution of residual stress across the weld. In recent years, Pandey et al. have conducted various studies on GTAW, and TIG welded P91 steel plate/ pipes for the effect of weld passes, groove design, heat treatments on mechanical properties, microstructural stability, residual stresses, and creep behaviour [15], [39], [40] [41]. They observed that pipe welding's groove designs (V and narrow grooves) do not affect the welds' hardness and microstructure. They observed that post-weld re-austenitizing based tempering increases the creep rupture life in the applied stress regime by shifting the rupture zone towards the base metal from FGHAZ [42]. They discovered that the narrow groove develops less axial and hoop stresses than conventional groove weld [43]. Maduraimuthu et al. [44] reported on the single pass (i.e., Activated- TIG) and multi-pass (i.e., conventional TIG) welded 6mm and 10 mm thick P91 steel plates for mechanical properties and residual stresses. They revealed that A-TIG welding induces compressive residual stress and favourable mechanical properties

compared to the multi-pass welded joint. The comprehensive studies on P91 steel of various thicknesses, passes, and welding processes are collectively shown in Table 2.1

Table 2.1 P91 steel welds of different thicknesses and welding methods

Authors	Plate thickness	Type of welding	Type of passes	Types of weld
Sireesha et al. [27], [28]	12 mm	MMAW	Multi-pass	V Butt weld
Spigarelli & Quaderini [29]	9.5 mm	GTAW-SMAW	Multi-pass	Circumferential Pipe weld
Yaghi et al. [32]	55 mm	MMAW	Multi-pass	Circumferential Pipe weld
Yaghi et al. [33]	50 mm	GTAW- SMAW	Multi-pass	Circumferential Pipe weld
Kumar et al. [36]	10 mm	LBW	Single-pass	Square butt weld
Hossienzadeh and Bouchard [45]	25 mm	GTAW-SAW	Multi-pass	Circumferential Pipe weld
Kundu et al. [37]	10 mm	EBW	Single-pass	Square butt weld
Zubairuddin et al. [38]	3 mm	GTAW	Single-pass	Square butt weld
Pandey et al. [41]	11 mm	GTAW	Multi-pass	Circumferential Pipe weld
Pandey et al. [45]	18 mm	GTAW-SMAW	Multi-pass	Circumferential Pipe weld
Pandey et al. [46]	5 mm	A-TIG	Single-pass	Square butt Weld
	8 mm	GTAW	Multi-pass	V butt Weld
Madurimuthu et al. [44]	6 mm	A-TIG	Single-pass	Square butt Weld
	10 mm	Conventional TIG	Multi- pass	V butt Weld

Jones et al. introduced Submerged Arc Welding (SAW) process in 1935 [46], considering the advantages of submerged molten weld metal pool during the welding process. The SAW process is widely known for its numerous benefits: high deposition rate, deep weld penetration, high speed, minimal welding fume and least edge preparation required compared to other arc welding processes. Hence, a conventional submerged arc welding process may produce good quality welds of thick plates with single-pass welding [47]. SAW process is suitable for welding carbon steels, low alloy steels, stainless steels, Nickel-based alloys [48]. SAW welds possess high strength and ductility with low hydrogen and nitrogen contents. Submerged arc welding has been used to weld pressure vessels, pipes, shipbuilding, railroad tank cars,

structural engineering, and storage tanks [48]. Many studies on submerged arc welding of Cr-Mo-V group of steels have been conducted through the date. For the first time in 1995, a US patent was filed for submerged arc welding of Cr- Mo-V steel to achieve ideal room temperature and elevated temperature strength, toughness, creep strength, brittleness resistance and crack resistance [49]. However, submerged arc welding was considered for P91 steel welds in 2005 by the researchers in Jiangsu Suyuan Power Equipment Co. Ltd, China. They found that SAW processed P91 steel welds are three times more manufacturing efficient than SMAW [50]. Yu et al. [51] developed and compared the welding wire for submerged arc welding and observed that it meets the high temper and strength at the same AWS and BSEN standards level. Rao et al. [52] performed the complete experimental analysis on the submerged arc welding of 11 mm thick Cr-Mo-V steel plate. The critical input process parameters were welding current, voltage, welding speed, and wire feed. These input parameters were studied on various responses related to weld bead geometry and few mechanical properties. Mohyla and Foldynova [53] conducted submerged arc welding on a P92 steel plate (40 mm thick) to study the effect of post-weld heat treatment on the mechanical properties of the weld. Zhang et al. performed SAW on a P91 steel plate using three different fluxes to assess their effect on microstructural behaviour and mechanical properties [54]. Roy et al. investigated the effect of various compounds in the fluxes and discovered a particular flux composition, which improved overall mechanical properties and microstructure stability [55], [56]. Nevertheless, studies on residual stress and distortion in submerged arc welded P91 steel are rarely found, considering the adverse effects of rapid heating and cooling in welding.

2.3 FE modelling of submerged arc welding for residual stresses and distortions

Welding induced distortions and residual stresses have been of continuous interest among the researchers and fabrication industries to prevent them at the design stage before the actual welding process. Therefore, an effective and precise finite element modelling and welding process simulation is always a substantial research interest. The numerical simulation of arc welding takes place in two main different ways. The first approach involves complex fluid and thermal dynamics. The basic concepts of this approach are conservation of mass, conservation of momentum, latent heat and surface tension boundary conditions which represent the physical phenomena of the molten weld pool and HAZ's thermal behaviour. The second approach considers solid mechanics to model the global thermo-mechanical behaviour of weld structure, which mainly focuses on effectively modelling heat sources. A variety of simplified heat source

models have been proposed in arc welding simulation [57], which accuracy relies on the theoretical and empirical parameters, describing the weld pool size and shape. Submerged arc welding has been simulated for several welding cases considering material properties, welding process parameters, and metallurgical effects. Mahapatra et al. [58], [59] developed a 3D FEM model of single-pass SAW square butt and fillet joints in ANSYS for temperature distribution and angular distortion. They applied the moving surface heat flux as a heat input model and observed fair prediction results. Biswas et al. [60] also applied the moving surface heat flux heat input model for filler deposition to simulate the submerged arc welding of C- Mn steel in the ANSYS FE software package and observed fair prediction results. Wen et al. [61] modelled multi-wire SAW on mild steel pipes of 914 mm diameter and 38 mm thickness using ABAQUS to investigate heat transfer characteristics in FZ and HAZ for 2D & 3D models. They applied a volumetric heat source model for heat input. Ghosh et al. [62] developed an analytical solution to predict transient temperature distribution on submerged arc welded 20 mm thick structural steel plate. HAZ width was found similar to 3D transient thermal conduction and predicted values agreed with the experimental results. Kiran et al. [63] developed a 3D numerical heat transfer, and fluid model for three wires SAW process to analyse the temperature distribution and molten pool behaviour. They used the fluid volume method to track the shape of the free surface. Fanous et al. [64] compared the element death birth technique with his newly developed technique called element movement technique to study the residual stress produced in the welding process. This new technique supported an early thermal interaction between the weld and base metals with less computation time. However, most of the researchers suggested Gaussian's distributed double ellipsoidal volumetric heat source model for efficient modelling of submerged arc welding process [65]–[69]. They observed that this volumetric heat source model provides precise nodal temperature and 3D distribution of residual stresses irrespective of weld materials and process parameters.

The above works show that several studies have been performed in FE modelling of the SAW process for single and multi-pass welding considering different heat source models, base metal and other weld materials. However, literature on FE modelling and simulation of submerged arc welding of P91 steel plate is rarely found.

2.4 Phase transformation effect in welding

FE modelling of welding involves weld parameters, welding methods, restraints, and welding passes. On the other hand, weld metal molten pool phenomena, phase changes, and

microstructure evolution also affect the finite element modelling results. The phase transformation phenomenon is primarily considered in the pressure vessel and piping materials, including austenitic stainless steel, ferritic/ martensitic steel and nickel-based super-alloys. However, austenitic steel welds are well-understood and straightforward to model compared to their ferritic steel counterparts. The reason for this discrepancy stems from the crystal structure found in each material [70]. Austenitic steel possesses a face-centred cubic (FCC) lattice, whereas ferritic steel is predominantly a body-centred cubic (BCC) structure. The iron (Fe) atoms are more distantly in BCC steel relative to the FCC steel structure. Therefore, Pearlite/ Ferrite from BCC (α) structure completely transforms into FCC (γ) structure of austenite and results in volumetric contraction during austenitization or heating up to A_{c1} temperature [71], [72]. Similarly, once the temperature reaches M_s temperature during cooling, martensitic transformation takes place, which transforms austenite, i.e., FCC (γ) to martensite, i.e., BCT (α*) and causes volumetric expansion [71], [72]. P91 steel is one of the ferritic steels. Ac_1 is generally taken at 810-820 °C that reaches up to 920-930 °C (Ac_3) during austenitization [12]. Similarly, M_f and M_s are the temperatures for martensitic transformation taken in the range of 390-375 ^oC and 180 -200 ^oC for P91 steel, respectively. The schematic of volumetric changes during solid-state phase transformation (SSPT) is shown in Figure 2.1.

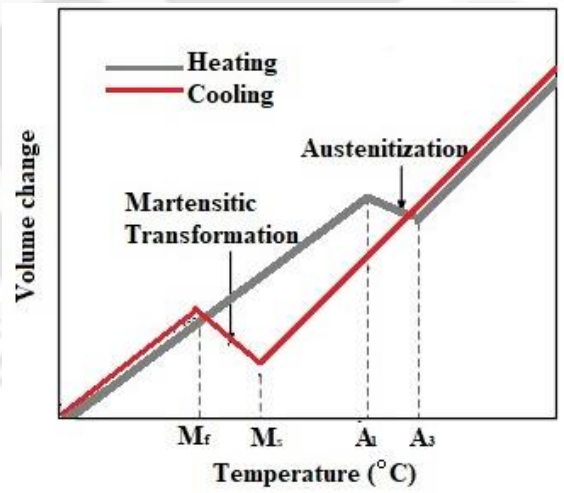

Figure 2.1 Schematic of volumetric change in P91 steel weldment during solid-state phase transformation [73]

Moreover, the microstructural evolution and transformation plasticity effect during phase transformation in solid-state also influence the overall mechanical modelling of heat treatment processes on ferritic steels. Therefore, thermo-mechanical modelling of P91 steel weldment

requires a complex metallurgical model considering all the aspects of phase change and solid-state phase transformation effects.

A number of research articles are reviewed on modelling the phase transformation in the solid-state and solid-liquid state during thermal welding cycles. Taljat et al. [74] studied the effect of volumetric changes on welding induced residual stresses associated with the austenite-to-martensite transformation. They found that volume changes tend to relieve high tensile stresses. They also observed that volume changes on residual stresses are more significant than the effect of higher yield strength caused by the phase transformation. However, the authors did not consider the transformation plasticity contribution. Dai et al. [75] investigated the SA508 steel GTAW joints for the effect of SSPT (bainitic- martensitic transformation) on residual stresses. Both volumetric and transformation plasticity effects were deliberately considered in the FE modelling. They discovered that avoiding SSPT in modelling leads to over prediction of tensile residual stresses. Leblond et al. [76] stated that because there is always a preferred direction on a macroscopic scale in 2D models (plane stress, plane strain or axially symmetric), strains are equal in the three directions and identical to the theoretical value cannot be obtained. Hence, reliable simulations considering metallurgical transformations must involve the full 3D model. W. Piekarska modelled solid-state phase transformation in laser-welded butt joint of S460 steel. Deng and Murakawa investigated the influence of solid-state phase transformation on the evolution of residual stress distributions in butt joints of modified 9Cr–1Mo steel pipes [77]. Yaghi et al. numerically simulated welding and residual stresses in a P91 steel pipe incorporating solid-state phase transformation [32], [73]. They observed an M- shape residual stress distribution across the weld in the transverse direction. Farahani et al. [78] implemented SSPT (austenite- martensite transformation) phenomenon in medium carbon (S45C) steel pipe joints. They mentioned the empirical relations to calculate austenitic and martensitic temperatures. However, they neglected the transformation induced plasticity effects. They also observed that volumetric changes owing to SSPT improve the prediction results for residual stresses and distortions. Hence, the SSPT phenomenon in the FE modelling of the welding process shows a significant effect on simulating and predicting the welding-induced structural results.

2.5 Mitigation techniques for welding induced residual stresses and distortions

Welding distortions adversely affect the dimensional accuracy of the welded structures. On the other hand, residual stresses due to fusion welding are the significant contributors to crack

generation, sudden catastrophic failure, and impairing the structure's fatigue life [25]. Several post welding steps based on thermal and mechanical loads like heat treatments (i.e., austenitizing, tempering, normalising), line heating, peening etc., are established for corrective works on final weld structures [25]. Post welding heat treatment is considered one of the post welding mitigation techniques, which involves heating and cooling in a particular rate and soaking at a fixed temperature for a given time. PWHT was also widely performed to retrieve mechanical properties and microstructure stability of the weld joints [41], [79]–[83]. However, all the post welding steps are corrective techniques, not preventive techniques, which demands additional time, effort and resources [84].

Consequently, pre-process and in-process active distortion and residual stress mitigation techniques are more beneficial in improving product quality by eliminating or reducing the welding induced distortions and residual stresses. Pre and in-process mitigation techniques can also be categorised in two sections based on their thermal and mechanical effects. Thermal load based pre and in- process mitigation techniques are primarily considered here for literature review.

Preheating and inter-pass heating have been established as two thermal load-based pre- process mitigation techniques. Inter-pass heating acts as preheating during multi- pass welding. Researchers like: Armentani et al. [85], Zondi et al. [86], Peric et al. [87], Zhang et al. [88], Lin et al. [89] observed a significant mitigation effect of preheating on welding induced distortion and residual stresses irrespective of types of the welding process, base plate material, welding process parameters etc. Preheating also exhibits a favourable effect like reducing hydrogen inclusion, increasing penetration, and improving ductility, hardness, and tensile strength of weld joint [90], [91]. Singh et al. [92] observed a similar effect on weld tensile properties and hydrogen inclusion in square butt GTAW joint of 6 mm thick P91 steel. Similarly, Zubairuddin et al. [14] observed a significant reduction in welding induced distortion, and residual stress in square butt TIG welded 3mm thick P91 steel plate. However, studies on the effect of preheating in SAW butt joints of P91 steel are rarely found.

The motto of most of the in-process techniques confines to generate a tensioning effect in the longitudinal direction during welding. Deo and Michaleris [84] proposed transient thermal tensioning to reduce buckling distortions, as shown in the schematic in Figure 2.2 (a). It was observed that the buckling distortions could not be mitigated only with the use of mechanical restraints. Using the side heating method, the introduction of tensile stresses in welding reduced

the compressive residual stresses at the plate's free edges to a value below the critical buckling stress. Yang & Dong [93] studied the effect of the in-process rolling and trailing heat sink method on mitigating weld-induced buckling distortions. The pressurized liquid nitrogen was employed as a cooling jet in the trailing heat sink method. The parameters, namely cooling distance, liquid nitrogen flow rate, and cooling jet diameter, were selected for optimal performance. A compressive effect in the through-thickness direction and a corresponding tensile effect in the welding direction were generated using a rolling technique shown in Figure 2.2 (b). A rolling force of 5.5 kN was the minimum force required to eliminate the buckling distortion. Li et al. [94] proposed and conducted an experimental and numerical analysis of a dynamic heat sink (cooling water jet trailing the welding torch on the top surface) for a thin sheet welding using GTAW, as shown in Figure 2.2 (b).

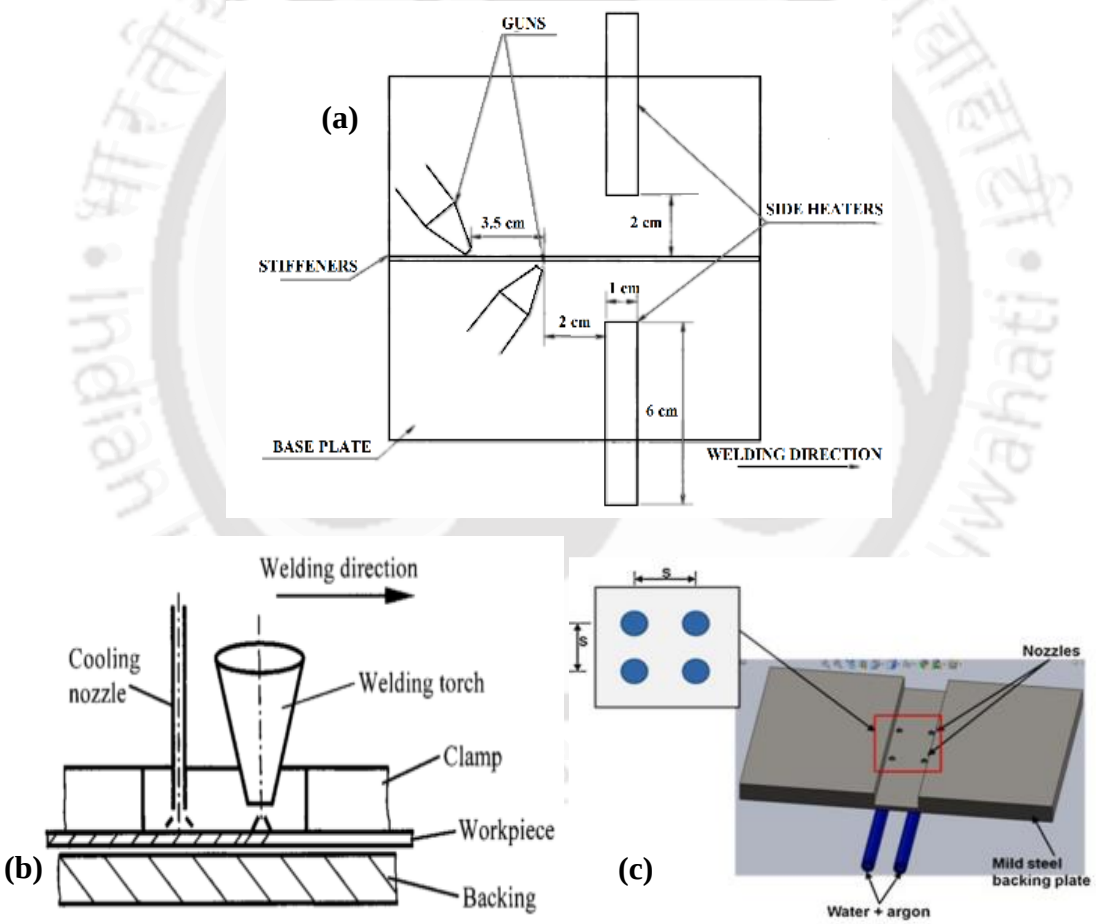

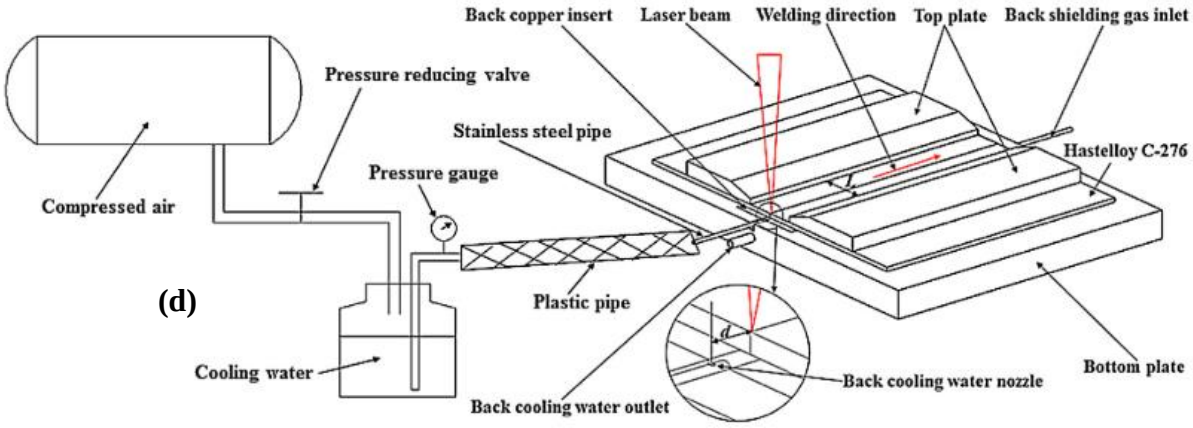

Figure 2.2 Schematic of (a) transient thermal tensioning or side heating [84], (b) In process trailing heat sink [93], [94], (c) DC-LSND or trailing cooling source technique [95], [96] (c) heat sink model [97] (d) trailing heat sink [98]

Guan et al. [95] adopted a dynamically controlled-low stress no distortion (DC-LSND) technique to control weld-induced buckling distortion. In their work, they employed CO_2 snow, produced by compressed liquid CO_2 through nozzles, as a cooling media. It was seen that a trailing cryogenic cooling device drastically reduced the welding distortions. The the DC-LSND technique has substantial impacts on the longitudinal welding distortion and reduced it by 81%. The optimum travel speed of the cooling device was found to be 600 mm/min. They also discovered that microstructure, as produced by the DC-LSND technique, was almost the same as that obtained by the conventional process. Camilleri et al. [96] conducted FE modelling of butt and fillet joints to investigate and compare the effects of the CO_2 cryogenic cooling techniques for reducing out-of-plane distortions. They observed that the Trailing heat sink model is less effective in reducing distortions in fillet weld joints. Bajpei et al. [97] proposed three different heat sink models, employing thick backing plate and cooling fluids, as shown in Figure 2.2 (c). They observed good conformity between experimental and numerical results. They discovered that the heat sink model using a mixture of argon gas and water was the most suitable scheme for mitigation. Guo et al. [98] proposed the same dynamic trailing heat sink source on the bottom surface following the welding torch for a PLW thin sheet (0.5 mm) butt joint. They conducted a rigorous study on cooling intensities and found that intense cooling decreases the longitudinal deflection and reduces the residual stresses. Michaleris and Sun [99] employed both finite element analysis and experimental techniques to study the effect of thermal tensioning on the mitigation of weld-induced buckling distortions. Thermal tensioning was done by simultaneous cooling the bottom of the weld zone by water spraying and heating

the adjacent areas with resistive heating blankets. It was observed that a high-temperature gradient had a detrimental effect on the weld-induced buckling distortions, and too low a value of the same resulted in insufficient tensioning. It was also concluded that the cooling time should be as low as possible to be effective and economical. Li et al. [100] proposed and analysed hybrid transient thermal tensioning and trailing heat sinking on the MIG butt joint of a 3 mm thick Al alloy plate. They employed two TIG heat sources for transient heating and a cooling jet of dry ice particles as trailing cooling source. It is observed that the proposed hybrid mitigation heat treatment reduced the tensile residual stress and distortion by 65% and 58%, respectively.

Further, few mechanical load-based in-process mitigation techniques are also discussed to review their mitigation effects. Price et al. [101] studied the impact of mechanical tensioning, as shown in Figure 2.3 (a), on the out-of-plane distortions in FSW and TIG welding. The plates were subjected to the various magnitudes of tensile stress along the weld line.

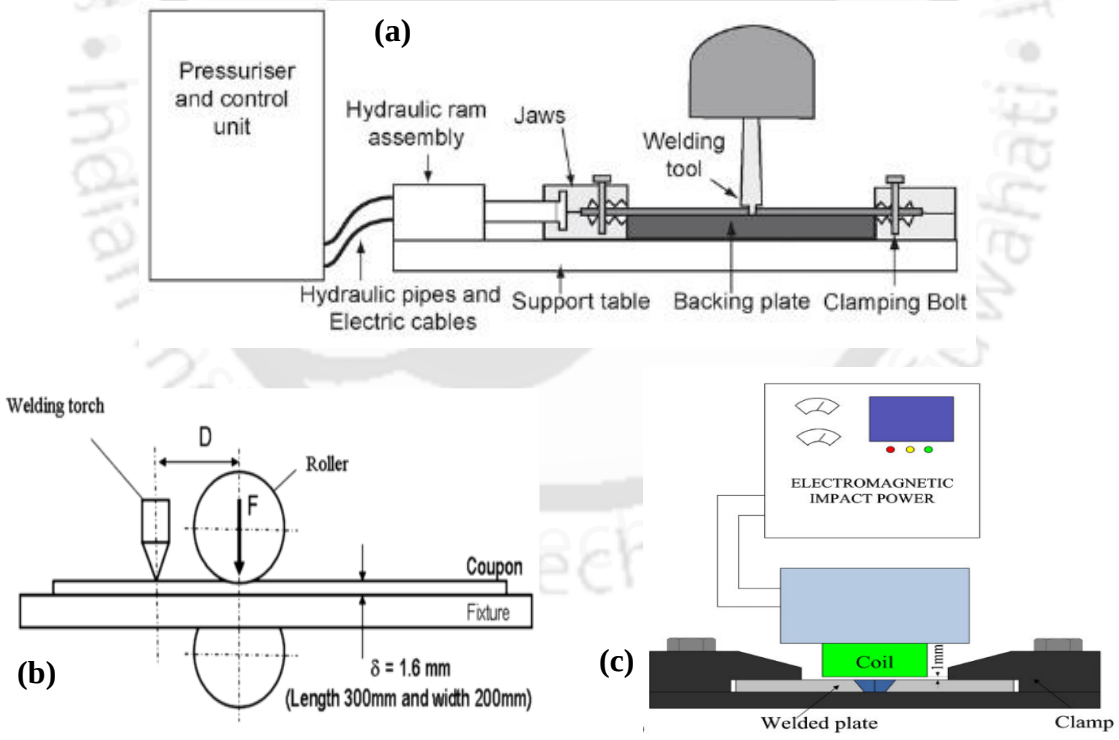

Figure 2.3 Schematic of (a) Mechanical tensioning technique [101] (b) Rolling technique [102] (c) Electromagnetic force tensioning technique [103]

It was reported that tensioning of the order 25–40% of yield eliminated the buckling distortions. It was also noticed that the optimum value of tensioning depends on the welding parameters.

The in-process rolling technique (also termed as *in situ* rolling as shown in Figure 2.3 (b) [102]) has also been suggested as one of the in-process mechanical tensioning methods. Coules et al. [102] compared *in situ* rolling with post-weld rolling on welding induced residual stresses in GMAW butt weld of structure steel. They discovered that *in situ* rolling is ineffective in reducing the longitudinal tensile stress compared to post-weld rolling. In situ rolling's ineffectiveness relates to the magnitude of the thermal contraction strain that occurs in the material at the weld line during cooling. The value is much larger than any residual elastic strain supplied by in situ rolling since the material's yield strain limits the latter. A significant thermal contraction continues for a long time as the material cools. Therefore, any positive strain supplied by *in situ* rolling is irrelevant, since this would be caused by yielding due to thermal contraction during cooling. However, it was found effective for Aluminium alloys and low carbon steels with lower yield strength. Xu et al. [103] proposed non-contact electromagnetic forces for controlling welding buckling distortion and residual stresses in welded thin plates, the schematic of which is shown in Figure 2.3 (c). The electromagnetic force, combined with residual welding stress, contributes to reducing longitudinal compressive plastic strain in the local region near the weld. It also contributes to the formation of the tensile plastic strain. Richards et al. [104] tried to control the generation of residual stress by employing global mechanical tensioning. It was observed that by imposing a mechanical tensioning of 40% of yield value, the magnitude of weld-induced residual stresses tends to a value of zero. Quite a number of mechanical load-based mitigation techniques are discussed here. However, it is observed that the required tensioning effect is much higher and sometimes it reaches beyond the capacity for thick plate welds. Therefore, mechanical methods are effective but least practical for industrial purposes.

All the in-process mitigation techniques are collectively shown in Table 2.2 considering the type of steel, steel plates' thickness, welding methods and mitigation methods. The above observations also show that almost all the in-process mitigation techniques were confined to thin plate (i.e., thickness < 6 mm, can be observed in Table 2.2) weld joints only. On the other hand, it is also observed that thick section welds experience high thermal gradient through the thickness and across the weld line on both top and bottom surfaces of the weld plate. These thermal gradients lead to irregular residual stress contour across the weld centreline in transverse direction and throughout the thickness of the plate. However, researches related to in-process mitigation of residual stresses and weld distortions in thick plate joints are hardly found.

Table 2.2 In process mitigation techniques for thin plate welds

Authors	Mitigation method	Welding type	Baseplate	Thickness
Michaleris and Sun[99]	Thermal tensioning	FCAW	AH 36 steel	4.76 mm
Deo and Michaleris [84]	Transient thermal tensioning	FCAW	AH 36 steel	3.2 mm
Yang and Dong [93]	Transient thermal tensioning	GMAW	Low carbon steel	2.5 mm
Yang and Dong [93]	*In situ* rolling	GMAW	Low carbon steel	2.5 mm
Li et al. [94]	Transient heat sink	GTAW	Titanium ally	2.5 mm
Guan et al. [95]	DC-LSND (Transient heat sink)	GTAW	Stainless steel Aluminium alloy	1.6 mm 1.6 mm
Bajpei et al. [97]	Heat sink (static and transient)	MIG	AA5052-H32 Aluminium alloy	3 mm
Guo et al. [98]	Trailing heat sink	PLW	Hastelloy C-276 alloy	0.5 mm
Price et al. [101]	Mechanical tensioning	FSW TIG	AA2024 (Aluminium alloy)	3.2 mm 6.3 mm
Richard et al. [104]	Mechanical tensioning	FSW FSW	AA2024 (Aluminium alloy)	3 mm 12 mm
Coules et al. [102]	*In situ* rolling	GMAW	S355JR structural steel	6 mm

2.6 Summary

The above literature review provides a wide knowledge about researches in the field of P91 steel welds, submerged arc welding, FE modelling of welding for induced residual stress and distortion and mitigation methods. It is found that welding-related researches on P91 steel are mostly performed on conventional multi-pass GTAW, TIG, SMAW, MMAW processes, though few studies are conducted on the EBW, LBW and A- TIG welding of P91 steel, which considered square butt welding without any edge preparation. These studies suggest that arc welding with high heat input, deep penetration and current density requires less number of weld passes. It is also observed that the required root gap in single pass welding is comparatively less. It is also observed that Gaussian distributed double ellipsoidal heat source model is

adequate to effectively simulate the SAW process. Literatures revealed that implementing phase transformation in FE modelling improves the prediction accuracy of FE results. At last, literatures available on thermal load-based pre, in and post welding mitigation techniques discovered that all the studies are confined to thin plates only.

2.7 Research gaps

Based on the understanding from literature review, the research gaps are as follows:

- Studies on submerged arc welding of P91 steel are very limited.
- Researches on SAW P91 steel welds are mostly focused on the microstructural and mechanical behaviour of the weld joints considering process parameters, weld materials and other similar conditions. However, studies are rarely found on welding induced residual stresses and distortion in SAW P91 steel welds.
- Most experimental studies for weld induced residual stresses in P91 steel welds are performed for multi-pass welding (such as TIG, GTAW, MIG). However, few studies on single pass welding (A-TIG, EBW) are also found. Albeit, such studies are seldom available for SAW welding of P91 steel.
- Thermo-mechanical modelling and simulation of SAW P91 steel welds is barely found, which analyses the welding induced thermal history, distortion and residual stresses.
- Most of the in-process mitigation heat treatments are performed and explored on thin sheet (i.e., thickness < 6 mm) weld joints. However, such studies on thick plate (thickness > 6mm) welds are rarely found.
- Similarly, studies on thermal load-based mitigation of residual stresses and distortions in SAW P91 steel welds are also hardly found in the literatures.

2.8 Detailed thesis objectives

In the view of research gaps mentioned in section 2.7, the current thesis objectives are as follows:

(a) Investigation of welding induced residual stresses and distortions in SAW butt joints of P91 steel:

The submerged arc welding experiments on the P91 steel plate are carried out using proper welding filler material and process parameters. The submerged arc welding induced distortion and residual stress are estimated using appropriate experimental methods.

(b) Thermomechanical elastic-plastic modelling and analysis of SAW butt joints of P91 steel:

Finite element modelling of SAW butt joints of P91 steel is performed and analysed considering temperature-dependent material properties, phase changes, austenitic- martensitic transformation, transformation plasticity, etc., to predict welding induced thermal history, distortions, etc. residual stresses.

(c) Pre-process, in-process, and post-process mitigation heat treatments on SAW butt joints of P91 steel:

Pre, in and post welding mitigation techniques are proposed for SAW butt joints of P91 steel plate. FE modelling and simulation of these techniques are performed to analyse their mitigation effect on welding induced residual stresses and distortions. Based on predicted results, experiments of these mitigation techniques are also carried out.

(d) Microstructural and mechanical characterizations of SAW butt joints of P91 steel:

The microstructural changes in the P91 steel weld are carefully traced to understand the effect of the SAW process and mitigation processes on P91 steel. The tensile properties like YS, UTS, hardness and ductility of P91 steel welds are also assessed for the effect of SAW and mitigation processes.

CHAPTER 3

METHODOLOGY

3.1 Introduction

This chapter provides details about all the experiments, and finite element modelling performed to accomplish the thesis objectives and sequentially explains each stage of methodologies involved in the thesis work. The first section explains the stepwise procedure of the welding experiment, from appropriate materials to successful submerged arc welding of P91 steel. The next section describes the experimental methods to measure welding induced distortions and residual stresses. The next sections describe thermomechanical elastic-plastic modelling of SAW square butt joints of P91 steel. It clarifies all the assumptions, governing equations and boundary conditions for both thermal and structural stages of FE modelling. It also explains the implementation of solid-state phase transformation in FE modelling.

The following section elucidates the concepts and theories of pre-processing, in-process and post-process mitigation techniques on welding induced distortions and residual stresses. It analyses the mathematical formulations and assumptions for FE modelling of these mitigation methods. At last, the section comprises different experimental setups for mechanical testing for microstructural analysis, mechanical strength, XRD analysis, FESEM analysis and EDS analysis to observe the effect of submerged arc welding and mitigation heat treatments on the P91 steel plate.

3.2 Submerged arc welding of P91 steel plate

The conventional submerged arc welding experiment is performed to get good quality square butt single and double side single pass weld joints of P91 steel without any edge preparation. Several factors such as welding experiment set up, weld materials, base plate material, type of flux and fixtures collectively affect the weld's overall quality. However, a set of favourable process parameters is required to achieve an adequate weld bead shape, penetration and top & bottom reinforcement. Hence, these factors and process parameters are explained as follows-

3.2.1 SAW experiment setup

A fully automated submerged arc-welding machine (Make: ADOR FRONTECH) with a capacity of 1250 Amp and 240- 260 V was employed to conduct the welding experiment. The machine was equipped with IGBT inverter technology, mounting tractor head, flux hopper and control box. Before starting the welding experiment, the SAW set-up needs to be assessed to manage the input variables. The welding input variables are voltage, trolley speed (welding speed), wire feed rate, and creep feed. Only one parameter is varied, keeping others constant to calibrate the machine. The input voltage was not regulated as it can be set directly from the transformer. The distance travelled by trolley concerning time determines the welding speed. The amount of wire travel concerning time gave creep speed.

Similarly, the wire feed rate is measured as the length of wire consumed during welding at a given time. A stopwatch and a scale are used for time and length, respectively. The SAW experiment set-up is shown in Figure 3.1 below.

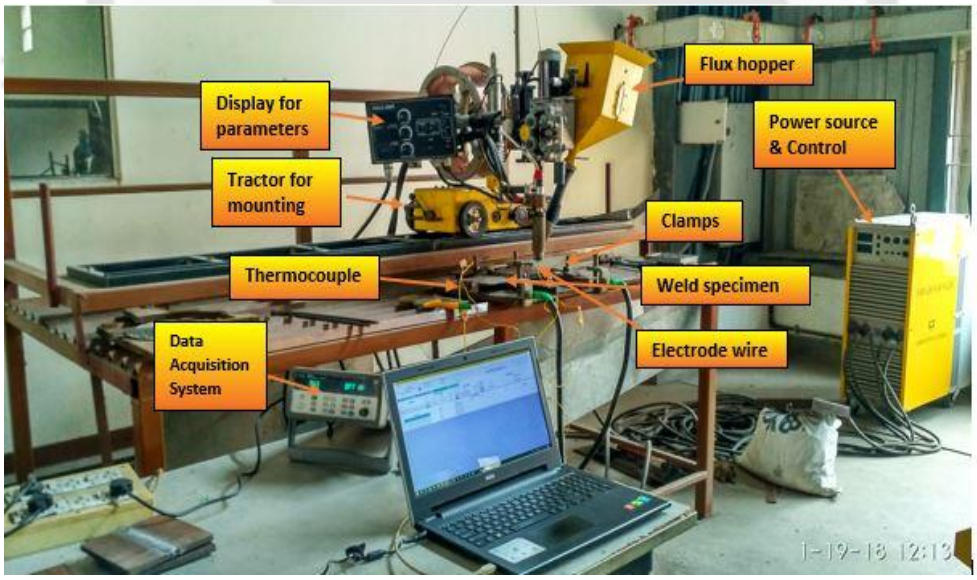

Figure 3.1 Experiment set up of SAW process

3.2.2 Materials selection

The proper combination of base metal, electrode wire, and flux provide a desirable submerged arc welded weld joint quality. Hence, it is essential to select these materials carefully, which is explained as follows-

3.2.2.1 Selection of P91 steel base plate

ASME SA387 or ASTM A355 Gr. 91 Class 2 steel plate of thickness 10 mm is selected from the group of Cr-Mo-V steels. The chemical composition of the material mentioned by the manufacturer is as given in the following Table 3.1. The plate is normalised at temperature 1050 ^{o}C with a 1 min/mm soak time and cooled in still air. It is tempered at a temperature of 780 ^{o}C with a soak time of 30 mins and cooling in still air. The plate is free from radioactive substances and does not exceed the cleaning limit value of 11 Bq/kg. The plate is ultrasonic tested with the Pulse-Echo method.

Table 3.1 Chemical composition of base plate

Element	Composition range (Wt.%)	Composition (Wt.%)	Element	Composition range (Wt.%)	Composition (Wt.%)
C	0.08-0.12	0.1	**Mo**	0.8-1	0.89
Si	0.2-0.5	0.29	**V**	0.1-0.3	0.22
Mn	0.3-0.6	0.46	**B**	≤ 0.01	0.001
P	≤ 0.02	0.016	**N**	0.03-0.07	0.039
S	≤ 0.01	0.001	**Al**	≤ 0.02	0.005
Cr	8.5-9	8.69	**Ni**	≤ 0.4	0.27
Ti	≤ 0.01	0.003	**Zr**	≤ 0.01	0.001

3.2.2.2 Selection of electrode wire

A low-alloyed copper-coated wire, designed for submerged arc welding of a creep-resistant Cr-Mo group of steels [92] of 3.1 mm diameter, is taken suitable for plate's thickness and nozzle diameter. The manufacturer code is OK AUTROD 13.20 (EB-3-21/4Cr1Mo) with electrode classification as AWS A5.23 wire: EB3R [105], [106]. The chemical composition for electrode material as given by the manufacturer is also shown in Table 3.2.

Table 3.2 Chemical composition of Electrode material

Element	C	Si	Mn	P	S	Cr	Mo	V	Cu	N	Al	Ni	Sn
Composition (Wt.%)	0.11	0.16	0.7	0.008	0.002	4.28	0.9	0.01	0.07	0.007	0.01	0.05	0.003

3.2.2.3 Selection of flux

A non-acidic or basic flux is preferred in submerged arc welding since other flux types will burn out carbon and permit elevated oxygen and nitrogen levels, reducing the weld metal's strength and toughness. The ESAB make agglomerated fluoride basic flux suitable for submerged arc welding of Cr-Mo group of steels, and ideal for OK AUTROD 13.20 wire is selected. The manufacturer code of this flux is OK FLUX 10.62 [105], [106]. The grain size of the flux varies from 0.2 mm to 1.6 mm. The flux is preheated before conducting a welding experiment to remove moisture for hydrogen control, which reduces defects. The chemical composition of the flux material is also given in Table 3.3.

Table 3.3 Composition of Flux

Compounds	Al_2O_3+ MnO	CaF_2	SiO_2+ TiO_2	CaO+ MgO
Composition (wt.)	18%	24%	13%	34%

3.2.3 Fixture and clamps

A fixture is fabricated to hold the samples properly during welding. The fixture is equipped with adjustable clamps at four corners of the plate, can be adjusted for different plate thicknesses, shapes and sizes. The fixture is provided with a recess to accommodate flux and hold the molten weld metal for sound bottom reinforcement. The fixture is shown in Figure 3.2. The clamps are removed as soon as the welding process ends.

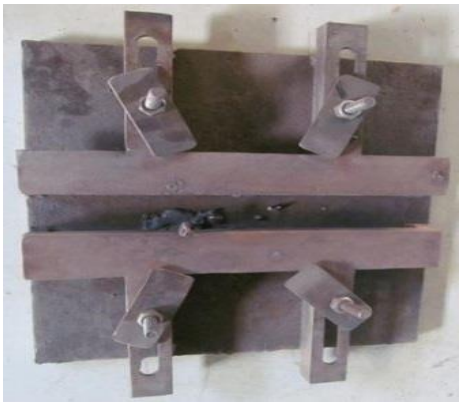

Figure 3.2 Fixture with adjustable clamps

3.2.4 SAW experiment

First of all, some bead on plate experiments are carried out to determine the suitable range of weld process parameters considering the heat input. However, it is observed that bead on plate experiments are insufficient to determine optimum parameters for the thickness more than 5mm. Hence, welding experiments are performed for different root gaps and welding parameters to achieve good weld bead qualities, i.e. top and bottom reinforcements, depth of penetration, weld material deposition and bead shape & size. The range of the welding parameters taken for trial square butt single and double side single pass submerged arc welding of P91 steel are given in Table 3.4.

Table 3.4 Range of process parameters for trial welding experiments

Process parameters	Single side single-pass	Double side single-pass
Current (A)	510-620	460-520
Voltage (V)	22-28	25-28
Welding speed (m/h)	16-24	18-26
Root gap (mm)	2-2.5	2-2.5
Length of stick-out (mm)	25	25

Few trial experiments samples are shown in Figure 3.3. Samples show improper bead length and inadequate reinforcement because of inappropriate root opening, deposition rate and selection of process parameters.

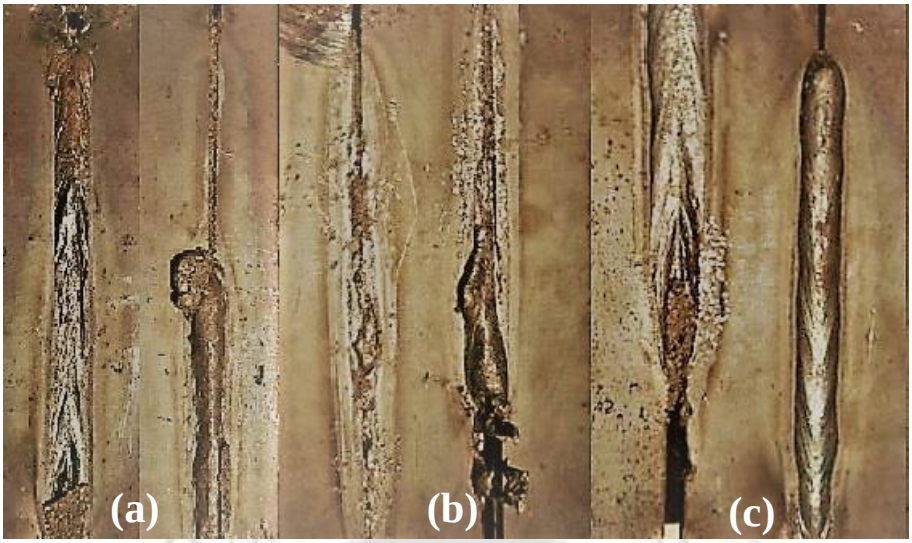

Figure 3.3 Poor top and bottom reinforcement owing to (a) irregular root opening, (b) extensive metal deposition, inadequate bottom reinforcement, (c) large root opening and improper metal transfer

The possible reasons for unstable and improper weld beads are variations in weld power (voltage and current). They need support from the bottom side to hold the molten weld material, which provides it with a proper shape. Therefore, a backing strip or backing bar may be used to get sufficient bottom reinforcement. Hence, a metal/ceramic slab is designed (called a 'Backing bar') and placed beneath the root gap. The backing bar consists of a deep semi-circular groove filled with the same flux in the SAW experiment and forms the required bottom reinforcement. The working principle of the backing bar can also be understood from Figure 3.4. The backing bar used in the present experiments is of Aluminium, which dimension is shown in Figure 3.5. The backing bar is placed in the recess available in the fixture shown in Figure 3.2.

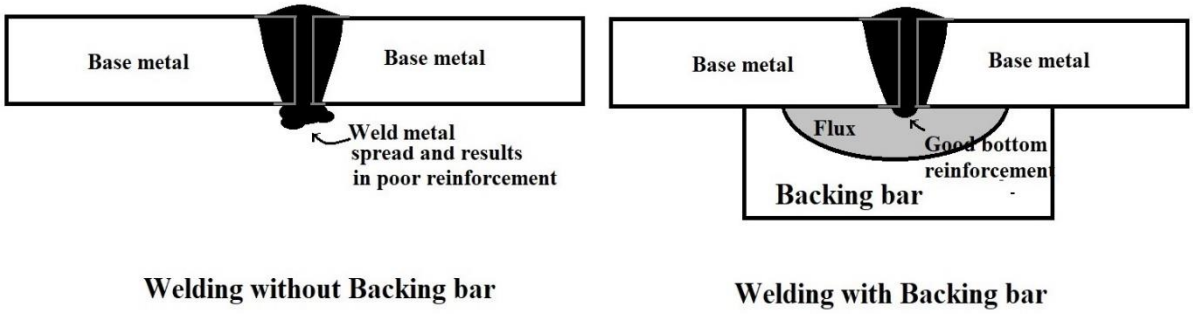

Figure 3.4 Working principle of the backing bar

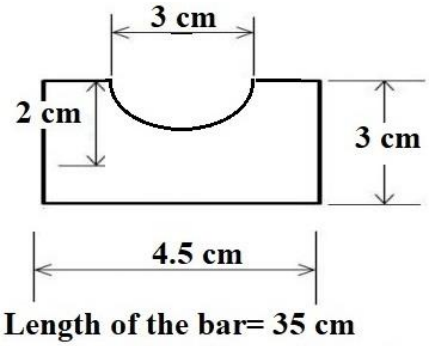

Figure 3.5 Dimensions of the backing bar

3.2.5 Temperature profile measurement

'K' type thermocouples are selected to record the thermal history of a point on the weld joint surface. It is the most common thermocouple used for time-temperature applications. Their measurement range varies from -200 ^{o}C to 1350 ^{o}C. The thermocouple must be calibrated before the actual use for optimal results. The thermocouples are calibrated in the range of 10^{o}C - 90^{o}C and vice-versa in a constant temperature bath to check their heating and cooling rates accuracy.

The calibrated thermocouples are attached to the weld specimen at different locations away from the weld centreline with the help of a spot-welding machine (Make: Dyna weld). The target points are punched to make a small groove, which firmly holds the thermocouple wire for proper connection. The other end of the thermocouple is connected to the multiplexer, which in turn is connected to the data acquisition system (Make: Agilent) for recording the thermal history of the welded sample during the welding experiments. The time interval for capturing the temperature data is kept at 500 milliseconds.

3.3 Measurement of welding induced distortion

The basic principle of measuring welding induced distortion is to compare initial and final (i.e. before welding and after welding in the cooled state) coordinates of the outer surface of any welded structures. The initial shape of the structure may or may not be flat. Therefore, the choice of the reference plane needs careful consideration before the measurement is performed. The measurement of initial or final positions in a given coordinate system may be performed using any instrumentation using physical contact or without physical contact for a point or a field. The measurement may also be conducted in a transient state to track distortion progress throughout the welding. The contact instrument is usually mechanical such as a dial gauge,

coordinate-measuring machine or linear variable-differential transformer (LVDT). The noncontact method is typically optical, such as laser displacement sensors and digital image correlation (DIC). Each dial gauge, LVDT or laser displacement sensor measures the distortion at a point while the DIC is a full-field method. In the present case, angular distortion and edge deflection of the base plate on both sides of the weld bead is measured to analyse welding induced distortions. Hence, this local level small-scale distortion measurement is carried out on a Coordinate measuring machine (CMM) (Make: Carl Zeiss). CMM consists of a spherical stylus, a work bed, control joystick and a control system interfaced with U-soft software. The workpiece under observation is placed on a V Block and positioned on the machine's horizontal bed. The overall CMM set-up is shown in Figure 3.6 (a).

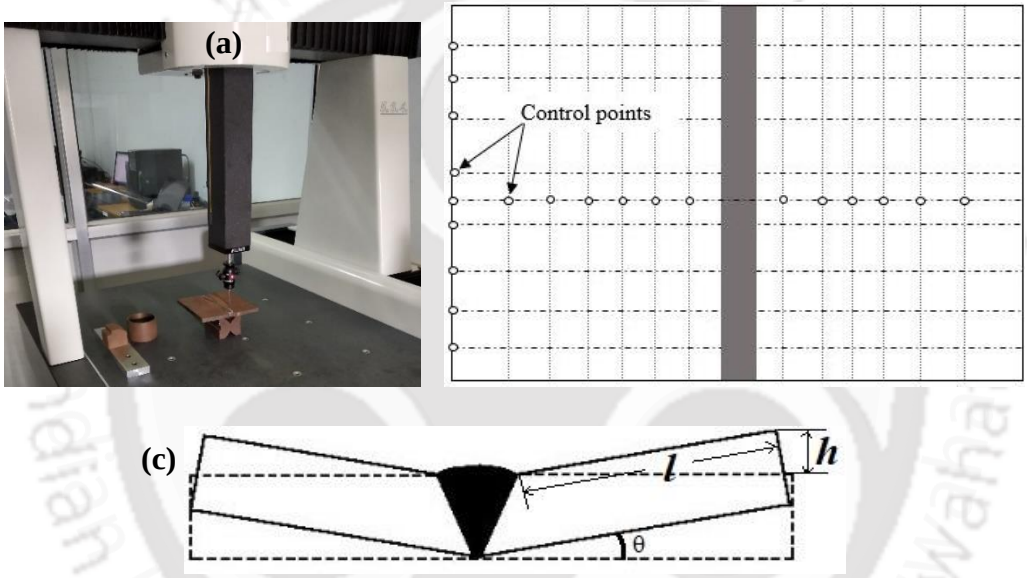

Figure 3.6 (a) CMM set up, (b) Control points for measurement, (c) Angular distortion angle (**θ**)

The control points and straight lines are scribed on the specimen's top face using tri- square and centre punch, respectively, as shown in Figure 3.6 (b). The points shown as a small circle are the control points to measure edge deflection and angular distortion. Angular distortion can also be assessed in terms of angular deformation angle across the weld [i.e. $\theta = sin^{-1}(h/l)$] as shown in Figure 3.6 (c). It represents the slope of one side of the weld concerning the horizontal surface. Since welding induced longitudinal and transverse residual stresses are exceedingly investigated here, the longitudinal and transverse shrinkage are not considered in the current study.

3.4 Measurement of welding induced residual stresses

The destructive residual stress measurement experiments work on the principle of stress relaxation. These are categorized based on the degree of destruction done to the specimen in the strain relaxation process. The residual stress measurement techniques are classified as (i) destructive and (ii) semi-destructive. Deep hole drilling (DHD) and contour techniques are semi-destructive and destructive residual stress measurement techniques. DHD technique can estimate through-thickness and pointwise biaxial residual stress values. Whereas, contour technique provides a spatial residual stress field on the targeted surface [107]. Hence, DHD and contour methods both are applied to measure residual stresses in the present study.

3.4.1 Deep Hole Drilling (DHD) measurement

FZ and HAZ of a weld joint are the most susceptible sections for welding induced residual stresses. On the other hand, residual stresses may vary throughout the thickness of the plate, especially in the thick weld sections. Therefore, the DHD technique is employed to determine residual stresses in FZ and HAZ of the welded joint throughout its thickness [17], [108], [109]. The DHD technique works on the principle of stress/strain relaxation phenomenon. The change in dimensions or strain determines the corresponding residual stress values. Hence, the pointwise bi-axial equivalent stress components are obtained throughout the thickness based on constitutive relations.

3.4.1.1 Experimental procedure

The DHD experiment is accomplished in four stages. The schematic diagram is shown in Figure 3.7.

(a) Hole drilling- At first, the top and bottom crowns of the weld bead of the weld specimen are removed in the area of interest. Two bushes of soft material are glued on both sides of the plate surface on the targeted locations, which works as a reference for the hole diameter. At last, a 3 mm diameter hole is drilled in targeted regions of FZ and HAZ.

(b) Deformation measurement: The hole diameters are measured for the respective deformation at different depths and orientations (0^o, 45^o & 90^o) throughout the plate thickness with the help of an air probe. The deformation measurement is performed after drilling and trepanning processes to trace the change in diameters at different depths and

orientations. The strain corresponding to diametral changes evaluates the in-plane bi-axial residual stress.

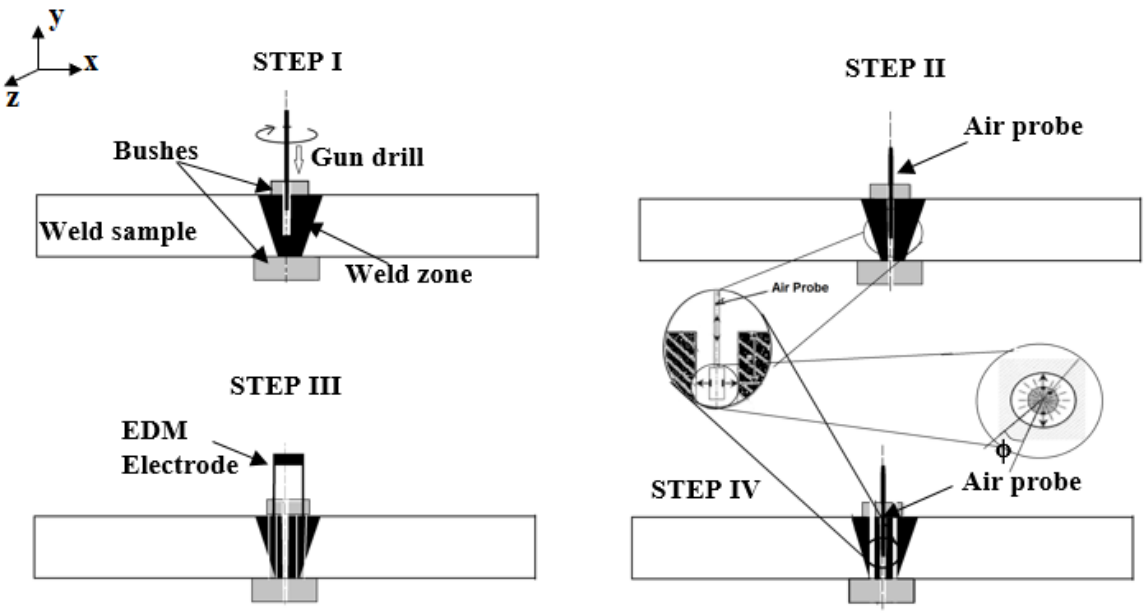

Figure 3.7 Schematic of steps involved in DHD technique

(c) Trepanning: The trepanning process is performed on a die-sinking electrical discharge machine to remove a cylindrical volume concentric with a hole. The outer and inner diameters of the cylindrical volume are 16 mm & 12 mm, taking the drilled hole as its axis. It releases the residual stresses in the cylindrical volume, which the corresponding deformation is measured in the inner surface of the hole.

The residual stresses are assumed to remain completely relaxed in an elastic manner throughout the trepanned. The change in diameter after trepanning is given by Eq.(3.1).

$$\Delta d\phi = d'(\phi) - d(\phi) \tag{3.1}$$

Hence, the corresponding strain is obtained as in Eq.(3.2). Finally, the biaxial stress components can be obtained based on the constitutive relations as given by Eq.(3.3) [110].

$$\varepsilon_{\phi}(\phi, y) = \frac{\Delta d(\phi)}{d(\phi)} \tag{3.2}$$

$$\varepsilon_{\phi,y}(\phi,y) = -\frac{1}{E}\left[\sigma_{xx} f(\phi,y) + \sigma_{zz} g(\phi,y) + \tau_{xz} h(\phi,y) - \upsilon\sigma_{yy}\right]$$

$$\varepsilon_{yy}(\phi,y) = \frac{1}{E}\left[-\sigma_{yy} - \upsilon(\sigma_{xx} + \sigma_{zz})\right] \quad (3.3)$$

The Young's modulus (E) is obtained for both base and weld metals by conducting a tensile test. The values of $f(\phi,y)$, $g(\phi,y)$ and $h(\phi,y)$ are given by-

$$f(\phi,y) = \hat{a}(1+b\cos 2\phi),\ g(\phi,y) = \hat{a}(1-\hat{b}\cos 2\phi)\ \&\ h(\phi,y) = 4\hat{a}\hat{b}\sin 2\phi$$

The value of '$\hat{a}$' is taken as 1 as uniform expansion is assumed for the hole. Similarly, the value of '$\hat{b}$' can be taken as 1 for the plate thickness = 10 mm [110]. The stress-strain constitutive relation (Eq.(3.3)) in matrix form is given by Eq.(3.4) [111].

$$\bar{\varepsilon} = -[M].\bar{\sigma} \quad (3.4)$$

where $\bar{\varepsilon} = \left[\varepsilon_{\phi_1,y_1}, \varepsilon_{\phi_2,y_2}, \varepsilon_{\phi_3,y_3}, \ldots\ldots\ldots \varepsilon_{\phi_n y_n}, \varepsilon_{yy}\right]^T$, $\bar{\sigma} = \left[\sigma_{xx}, \sigma_{yy}, \tau_{xy}, \sigma_{zz}\right]$

$$\&\ [M] = \begin{bmatrix} f(\phi_1,y_1) & g(\phi_1,y_1) & h(\phi_1,y_1) & -\upsilon \\ f(\phi_2,y_2) & g(\phi_2,y_2) & h(\phi_2,y_2) & -\upsilon \\ .. & .. & .. & .. \\ f(\phi_n,y_n) & g(\phi_n,y_n) & h(\phi_n,y_n) & -\upsilon \\ -\upsilon & -\upsilon & 0 & 1 \end{bmatrix}$$

Finally, the stress vectors are obtained as Eq.(3.5) given below-

$$\bar{\sigma} = -[M]^*.\bar{\varepsilon} \quad (3.5)$$

where $[M]^*$ (inverse pseudo matrix) $= ([M]^T [M])^{-1} [M]^T$

3.4.2 Contour measurement

The contour method effectively maps complex and spatially varying residual stress fields that are difficult and slow to map using conventional pointwise measurement techniques [112]. Contour measurements are typically performed on metallic parts, which can be cut using a wire EDM. It does not show any specific restriction on the specimen's size and shape, as the FE model can be performed for the given specimen and displacement boundary condition.

Figure 3.8 illustrates a variation of Bueckner's superposition principle [113], [114], which states that a component under internal stresses if cut into two parts, release the trapped stresses through the cut surface in terms of surface deformation. Once the deformation is pushed back, it develops an internal stress distribution in the cut parts equivalent to residual stress distribution on the cut surface.

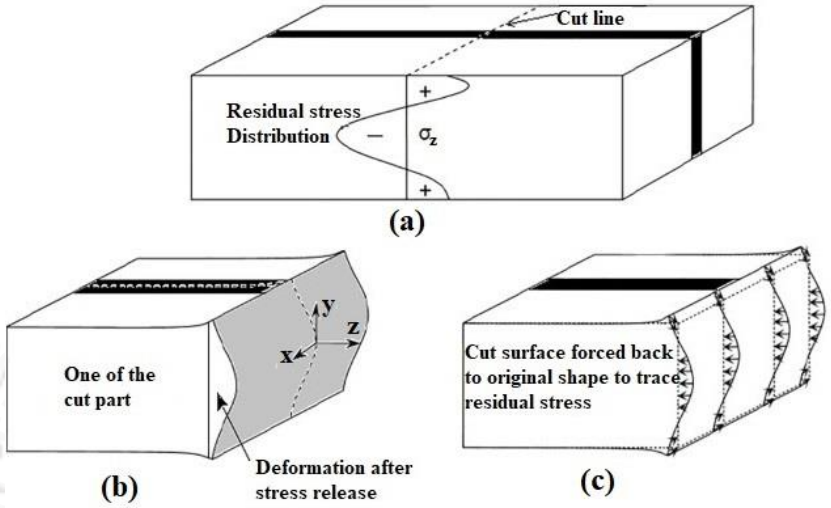

Figure 3.8 Bueckner's superposition principle for residual stress distribution [113], [114]

Figure 3.8 (a) presents fundamental components of the internal residual stress distribution. The component is cut into two parts along the plane at $x = 0$. Figure 3.8 (b) shows one-half of the parts in the post-cut state with relaxed stresses. The surface contour is measured to calculate surface deformation. A stress-free body of the same material and similar shape and size is taken for analysis. One of the faces similar to the cut part's deformed surface is taken to push back the distortion results (which is applied in the negative direction). Hence, the displacement load results in residual stress on the surface, as shown in Figure 3.8 (c).

3.4.2.1 Experiment procedures

The contour measurement involves four significant steps, which includes cutting, surface deformation measurement, deformation data analysis and finite element modelling. These steps are elaborately explained as follows-

(a) Cutting of weld specimen

Wire Electric Discharge Machining (Wire EDM) is widely known for its delicate machining process. It generates negligible plastic distortion, i.e. does not induce any residual stress [112]. The cutting is performed by an electrically charged wire which spark erosion removes the

materials without any physical contact. The spark region is submerged in deionized water throughout the cutting, diminishing its thermal effects. It also provides a precision of cutting position in micrometre. Hence, wire EDM is preferred for cutting in the contour technique. The schematic of the cutting process is shown in Figure 3.9 (a). The cutting speed, cutting feed and other wire EDM cutting parameters are the key factors for a smooth cut surface with minimum surface roughness.

(b) Surface deformation measurement

The surfaces after cutting operation need to be measured for surface deformation data. In general, the peak-to-valley magnitude of the surface contours is found to be in the order of 10 µm to 100 µm [112]. A coordinate measuring machine can trace the surface heights of this level of precision. Hence, it can be used for accurate measurement. The cut surfaces are exposed to the probe for physical contact, which will provide the exact coordinates of target points. The schematic of the CMM set-up is shown in Figure 3.9 (b). The positioning of the workpiece on the CMM bed also affects the distortion data reading for the exposed surface. Hence, the raw deformation data must be rectified before the FE structural analysis.

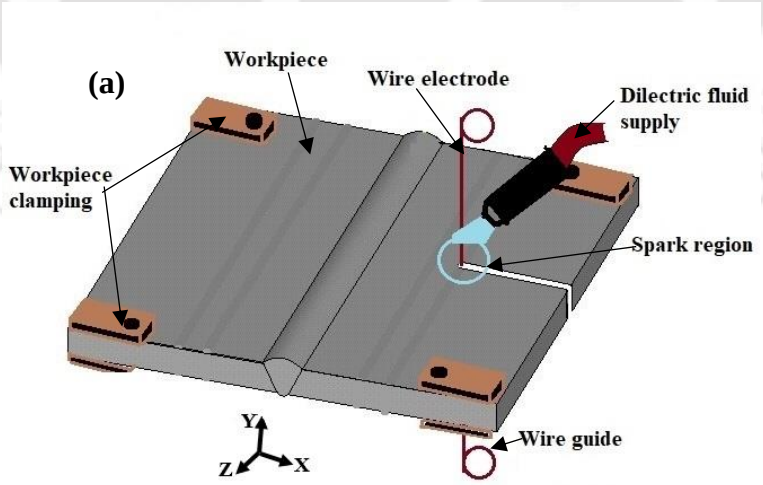

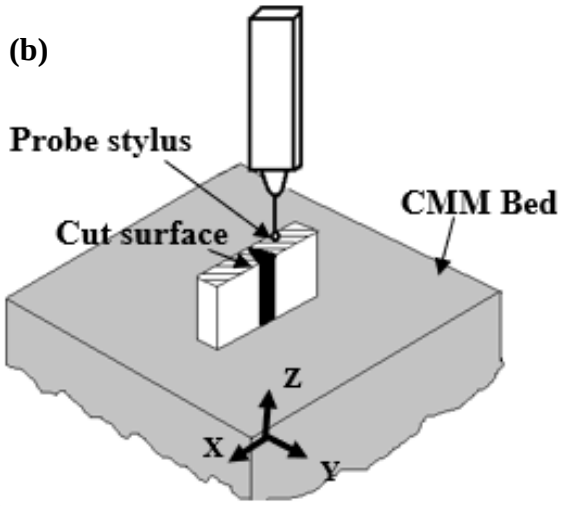

Figure 3.9 Schematic of (a) wire EDM cutting set up, (b) CMM set up for distortion measurement

(c) Surface deformation data conditioning

The non-uniformity in the cutting process and misalignment in the sample positioning on the CMM bed cause erroneous surface deformation data of the cut surface. Therefore, the following corrective steps are taken-

i) Slope correction along x and y direction to align the target surface to a horizontal surface.

ii) Removal of surface roughness and noise error.

i) The pointwise surface deformation values are obtained as Z coordinate of CMM readings. The slope correction of the cut surface is done by assuming all the extreme edges of the cut surface along the X & Y directions at the same level. Accordingly, the Z coordinate values for each data point are modified for the constant slope value. Eqs. (3.6) & (3.7) give the final and modified Z coordinates of each observation point.

$$Z_x^* = Z_i - m \times X \tag{3.6}$$

$$Z_y^* = Z_i - m \times Y \tag{3.7}$$

Both the cut surfaces' average Z coordinate values are considered to avoid cutting process-induced errors [115]. The averaging of contours of both the cut samples also remove shear stresses due to cutting [115]. At last, the average point values must be smoothed for a surface continuous at least up to its first derivative to be applied in finite element modelling [116]. Hence, the surface fitting extracts a form of smooth surface deformation. It was typically

accomplished by fitting the data to a predefined 2D polynomial function using a fitting toolbox in commercially available graphing and data analysis software (**ORIGINPRO 9.1**). Nonlinear fitting aims to estimate the parameter values which best describe the data. The whole process can be described in three crucial steps as follows-.

a) Generate an initial function curve from the initial values.
b) Iterate to adjust parameter values to make data points closer to the curve.
c) Stop when minimum distance reaches the stopping criteria to get the best fit

Levenberg- Marquardt (L-M) iteration algorithm is opted for surface fitting in view of the explicit nature of distortion data. It is a standard nonlinear least square algorithm, which works on the principle of multiple regression. This algorithm involves choosing the parameters that would minimize the theoretical surface deviations from the data points. This method is also called χ^2 chi-square minimization, which expression is given by Eq.(3.8) [117].

$$\chi^2 = \sum_{i=1}^{n} \left[\frac{Z_i - f(x_i', \hat{\beta})}{\sigma_i} \right]^2 = (Z_i - f(x_i', \hat{\beta}))^T . P . (Y_i - f(x_i', \hat{\beta})) \tag{3.8}$$

Levenberg- Marquardt algorithm combines the Gauss-Newton method and the steepest descent method. It starts with calculating $\chi^2(b)$ for the given initial values 'b_i'. It introduces an algorithmic parameter λ (a non-negative damping factor) whose values decide the iteration updates to smooth out the graph [118]. The parameters adaptively vary between the gradient descent update and the Gauss-Newton update. Eq. (3.9) provides the expression for the L-M algorithm, where the value λ decides the parameter updates, i.e. smaller value of λ results in the Gaussian- Newton update while a larger value of λ results in the Gradient descent update. The two separate terms in the left-hand side of Eq. (3.9) represent the Gaussian- Newton and Gradient descent algorithms.

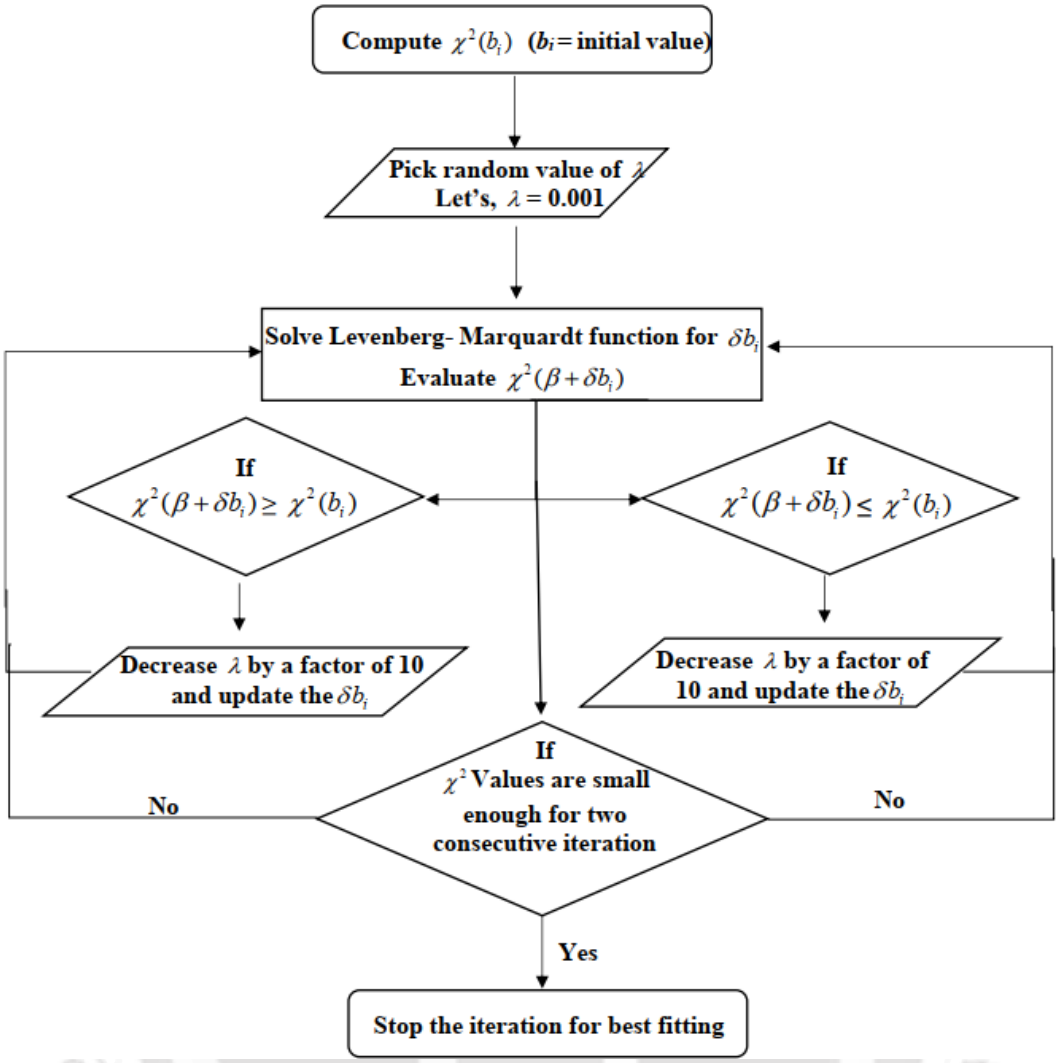

Figure 3.10 Flow chart for the Levenberg- Marquardt algorithm for the best curve or surface fitting [118]

G stands for gradient operator $\frac{\partial f(x_i, \hat{\beta})}{\partial \hat{\beta}}$, and '*I*' represent the inverse of a positive scalar quantity which determines the length of the step in the steepest descent direction, and *p* stands for perturbation to update the parameters [118]

$$[G^T PG + \lambda I]p = G^T P(Z_i - f(x_i, \hat{\beta})) \tag{3.9}$$

The iteration conditions can also be understood from the flow chart [119], as shown in Figure 3.10.

(d) FE analysis (Static structural modelling)

The one half of the cut weld specimen is modelled in an FE software package, '**ANSYS**'. The cut surface's exact shape was traced on graph paper from the cut part. A fine uniform meshing is performed near the weld bead region and through the thickness of the plate. Whereas comparatively coarser meshing is preferred along the length and width of the plate. A solid 3D hexagonal brick element (**SOLID 185**) is chosen for structural analysis. The distortion values are applied as the nodal displacement load on each node of the targeted surface. The distortion values are taken in the opposite direction of the measured values. The corresponding static structural analysis results generate stress values similar to the welding induced residual stress distribution. Zero displacement loads are applied to the nodes at the corners to prevent rigid body motion.

3.5 Thermo-mechanical elastic-plastic FE modelling of SAW butt joints of P91 steel

Thermo-mechanical elastic-plastic finite element modelling of the welding process is a well-established numerical method to analyse welding induced thermal history, distortion and residual stresses. Hence, the submerged arc welding process is modelled and simulated here in two major stages of uncoupled thermal and structural loads using Ansys Parametric Design Language (**APDL**) in **ANSYS** Mechanical FE solver. On the other hand, P91 steel is ferritic-martensitic steel and possesses solid-state phase transformation, which is also prudently considered in FE modelling. Hence, the whole procedures are sequentially explained in the following sub-sections.

3.5.1 Modelling and meshing

The SAW square butt joints are modelled considering the exact weld bead shape and size, including top and bottom caps similar to the welded plate. An eight-node three-dimensional solid element with only one degree of freedom, i.e., **SOLID 70** is selected for thermal FE modelling. Similarly, an eight nodes 3D solid element with three degrees of freedom, **SOLID 185,** is applied for structural FE analysis. The mesh sensitivity analysis is performed to optimize the number of nodes, elements size, the spacing ratio etc., considering the convergence criterion for most minor computational data and time for accurate FE results. Once the convergence value reaches the order of (10^{-4})**,** the meshing is assumed optimized. An utter fine meshing is done in the welding region and its nearby high-temperature gradient regions. The element size becomes coarser for the regions away from the weld bead region, which reduces the overall computational data and time. The square butt single and double side

single pass joint models with their appropriate meshing are shown in Figure 3.11. In the meshing attributes, the base and weld metals are assigned their respective material properties differentiated with colours in Figure 3.11. The single and double-side square butt joint models consist of 41264 nodes & 32450 brick elements, and 59343 nodes & 50100 brick elements. The elements within the welding region represent the weld metal added during the welding. The element birth-death technique capably replicates a weld metal molten pool in the root gap throughout the welding process. First of all, all the elements present in the weld region are killed, i.e. all the assigned properties to those elements become zero.

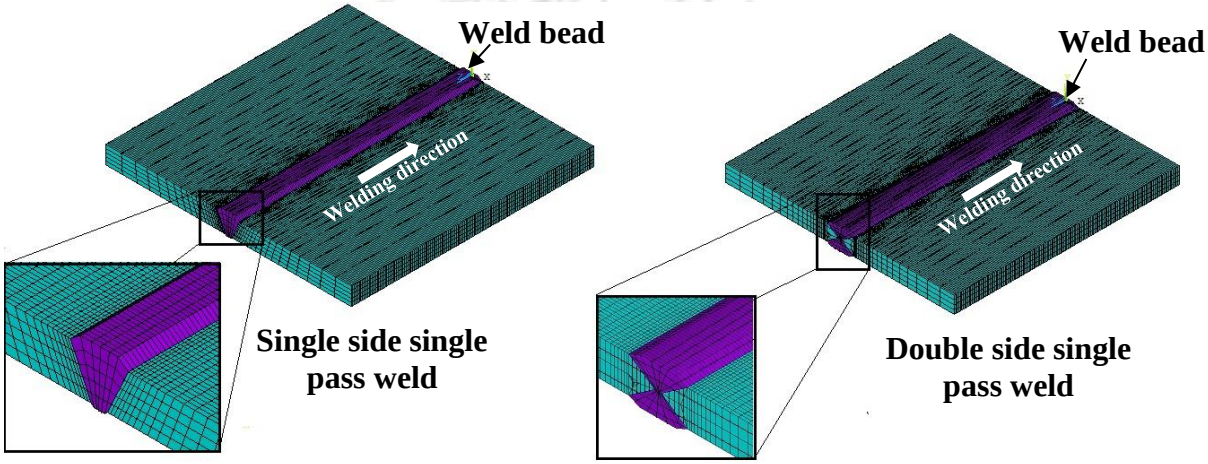

Figure 3.11 Drafted and meshed models of square butt single and double-side single pass weld joints

The application of a moving heat source within the weld region reactivates the deactivated or killed elements. It retrieves all the relevant elements' properties at associated temperature, which symbolizes the inclusion of a molten weld pool similar to the actual welding process.

3.5.2 Thermal modelling

It is strained to accommodate the actual welding condition as far as possible to develop the thermal model. The assumptions for the thermal model are as follows-

a) All the thermal properties are considered as the function of temperature.
b) No forced convection is considered.
c) Phase changes are also considered.
d) Linear Newtonian convection cooling is considered on all the surfaces except the weld zone.
e) Radiation loss being small, the same is neglected.

f) Arc efficiency is incorporated to account for other losses.

3.5.2.1 Formulation of finite element heat transfer model in arc welding

The governing differential equation of heat conduction for homogeneous and isotropic material is given by the Eq. (3.10) in the rectangular coordinate system (x, y, z) as below:

$$\frac{\partial}{\partial x}\left[k\frac{\partial T}{\partial x}\right]+\frac{\partial}{\partial y}\left[k\frac{\partial T}{\partial y}\right]+\frac{\partial}{\partial x}\left[k\frac{\partial T}{\partial x}\right]=\rho c_p\frac{\partial T}{\partial t} \tag{3.10}$$

Eq. (3.10) can also be written as follows:

$$\rho c_p\frac{\partial T}{\partial t}=-\{L\}^T\{q\} \tag{3.11}$$

$$\{L\}^T\{T\}=\vec{\nabla}T \text{ and } \{L\}^T\{q\}=\vec{\nabla}.q$$

According to Fourier's law, the heat flux vector in terms of the thermal gradient is given by Eq. (3.12).

$$\{q\}=-[D]\{L\}T \tag{3.12}$$

where

$[D]=\begin{bmatrix}k & 0 & 0\\ 0 & k & 0\\ 0 & 0 & k\end{bmatrix}$ (Conductive matrix) and $\{L\}^T=\begin{Bmatrix}\partial/\partial x\\ \partial/\partial y\\ \partial/\partial z\end{Bmatrix}$ (Vector operator).

So, Eq. (3.12) can be written as the Eq. (3.13):

$$\rho c_p\frac{\partial T}{\partial t}=-\{L\}^T([D]T\{L\}) \tag{3.13}$$

3.5.2.2 Boundary conditions for thermal analysis

The thermal analysis involves following boundary conditions to model thermal changes during the welding process.

I. Initial Condition

A specified temperature that covers the entire elements of the specimen at room temperature (T_0) before the welding starts is given by Eq. (3.14).

$$T = T_0 \text{ at } t = 0 \tag{3.14}$$

II. Boundary Condition

To develop the second and third boundary conditions, we consider the energy balance at the work surface as:

Heat supply = Heat loss

a) A specific heat flow in the weld bead region

$$Q_n = -Q_{\text{supp}} \text{ Or, } -Q_n = -k\frac{\partial T}{\partial n}$$
$$\text{or, } Q_n = -k\vec{\nabla}T\vec{n} = -k\left(l_x \partial T/\partial x + l_y \partial T/\partial y + l_z \partial T/\partial z\right) \tag{3.15}$$

b) Heat loss due to convection from the surface except for the weld bead region (Newton's law of cooling)

$$Q_{conv} = h_f(T - T_0) \tag{3.16}$$

Therefore, considering the energy balance finally the equation will be as

$$Q_n = -Q_{conv} \text{ Or, } -k\frac{\partial T}{\partial n} = h_f(T - T_0) \tag{3.17}$$

where $\vec{\nabla}T = \left(\vec{i}\,\partial T/\partial x + \vec{j}\,\partial T/\partial y + \vec{k}\,\partial T/\partial z\right)$ = Temperature gradient vector, $\vec{n} = \vec{i}\,l_x + \vec{j}\,l_y + \vec{k}\,l_z$ = Unit outward normal vector.

It is essential to take care that heat flux Q_{supp} and convection loss Q_{conv} should not occur on the exact boundary surface, i.e. if heat loss by convection exists, heat gain Q_{supp} cannot or vice versa.

Finally, the integral form of the heat flow equation can be obtained by combining the differential equation of the heat flow and the boundary conditions. A virtual change in the temperature is assumed as *T*. Taking the virtual change in the temperature in both the volume integral of the conduction differential equation and the respective surface integrals for the different boundary conditions yield the integral form equation as below:

$$\int_{vol}\left(\rho c\delta T\left(\frac{\partial T}{\partial t}\right)+\{L\}^{T}(\delta T)([D]\{L\}T)\right)d(vol)$$
$$=\int_{s_1}\delta TQ_{\sup}d(s_1)+\int_{s_2}\delta T(T_0-T)d(s_1) \tag{3.18}$$

3.5.2.3 Finite element formulation in matrix form

The temperature T is the function of time as well as the coordinate system so, Eq. (3.19) gives the matrix of T as:

$$T=\{N\}^{T}\{T_e\} \tag{3.19}$$

where $T= T(x, y, z, t)$ and $N= N(x, y, z, t)$

Thus, the time derivative of the Eq. (3.19) is as below:

$$\overset{*}{T}=\frac{\partial T}{\partial t}=\{N\}^{T}\left\{\overset{*}{T_e}(t)\right\} \tag{3.20}$$

Here, δT has the same form as T and so δT can further be written as in the Eq. (3.21)

$$\delta T=\{\delta T_e\}^{|T}\{N\} \tag{3.21}$$

The combination of $\{L\}\,T$ can be given as $\{L\}\,T$-$[B]\,T_e$ where

$$[B]=\{L\}\{N\}^{T} \tag{3.22}$$

Hence, the Eq. (3.19), along with the combination of Eqs. (3.18)-(3.22) yields as

$$\int_{vol}\rho c\{\delta T_e\}^{T}\{N\}\{N\}^{T}.d(vol)+\int_{vol}\{\delta T_e\}^{T}[B]^{T}[D][B]\left\{\overset{*}{T_e}\right\}.d(vol)$$
$$=\int_{S_1}\{\delta T_e\}^{T}\{N\}q_{\sup}dS_1+\int_{S_2}\{\delta T_e\}^{T}\{N\}h_f\left(T_0-\{N\}^{T}\{T_e\}\right)dS_2 \tag{3.23}$$

The density remains constant, and specific heat c varies over the element. Temperatures in terms of $\{T_e\}$ $\{\delta T_e\}$ and $\left\{\overset{*}{T_e}\right\}$ vary as the nodal values. Now, since all quantities seem to be pre-multiplied $\{\delta T_e\}$, so it can be declined. Thus, Eq. (3.23) finally marked down in the form of Eq. (3.24) as follows:

$$\rho \int_{vol} c\{N\}\{N\}^T .d(vol)\left\{\overset{*}{T_e}\right\} + \int_{vol} [B]^T [D][B].d(vol)\left\{\overset{*}{T_e}\right\} = \int_{S_1} \{N\} q_{sup} dS_1 + \int_{S_2} T_0 \{N\} h_f dS_2 - \int_{S_2} h_f \{N\}\{N\}^T \{T_e\} dS_2 \quad (3.24)$$

Hence, the integral form is written in matrix form as follows,

$$\left[C_e^t\right]\left\{\overset{*}{T_e}\right\} + \left(\left[K_e^{tb}\right] + \left[K_e^{tc}\right]\{T_e\}\right)\{T_e\} = \left\{Q_e^f\right\} + \left\{Q_e^c\right\} \quad (3.25)$$

where $\left[C_e^t\right] = \int_{vol} c\{N\}\{N\}^T .d(vol)$ = Element specific heat matrix, $\left[K_e^{tb}\right] = \int_{vol} [B]^T [D][B].d(vol)$ = Element conductive matrix, $\left[K_e^{tc}\right] = \int_{S_1} \{N\} q_{sup} dS_1$ = Element convective matrix, $Q_e^f = \int_{S_2} h_f \{N\}\{N\}^T dS_2$ = Element heat flow, $Q_e^c = \int_{S_2} T_0 \{N\} h_f dS_2$ = Element heat flow vector.

3.5.3 Formulation of heat transfer model

For an arc welding process, heat deposition may be characterized as Gaussian distribution of heat flux [120], [121]. Moreover, previous researches on FE modelling of the SAW process endorse the double ellipsoidal heat source model as one of the best suitable heat source models [120], [122], [123]. Hence, assuming the heat from the welding arc applied at any given instant of time, as a Gaussian distributed double ellipsoidal volumetric heat source model as shown in Figure 3.12, then, the rate of heat generation is given by the Eq. (3.26):

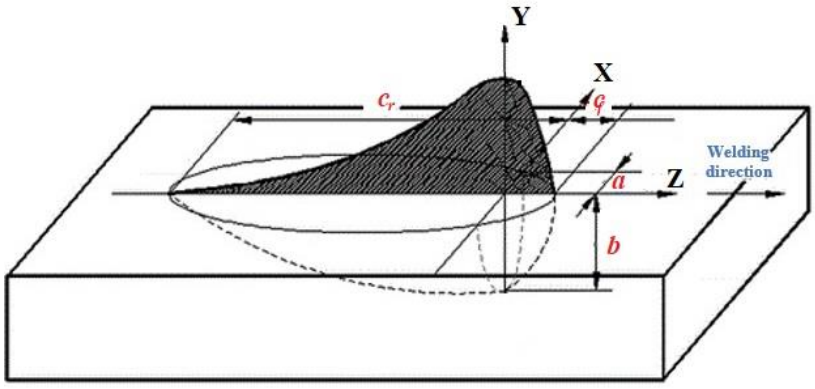

Figure 3.12 Schematic of the double ellipsoidal heat source model

$$Q_{f,r}(x,y,z,t) = \frac{6\sqrt{3} f_{f,r} Q\eta}{abc_{f,r}\prod^{3/2}} \exp\left[-3\left\{\left(\frac{x}{a}\right)^2 + \left(\frac{y}{b}\right)^2 + \left(\frac{z+v(\tau-t)}{c_{f,r}}\right)^2\right\}\right] \quad (3.26)$$

$$Q = VI$$

The value $f_{f,r}$ can be calculated from the following relations.

$$f_f = \frac{2c_r}{c_r + c_f} \quad (3.27)$$

$$f_r = \frac{2c_f}{c_r + c_f} \quad (3.28)$$

The value of constant parameters (*a*, *b*, c_f and c_r) can directly be measured for the considered weld joint sample [124].

3.5.4 Structural modelling

The thermal analysis is carried out first to find out the nodal temperature values as a function of time. Therefore, the structural or elastic-plastic analysis is performed to predict welding induced distortion and residual stresses. It can be done by applying the nodal temperature loads for the time steps and sub-steps similar to thermal analysis.

In this analysis, the quasi-static equation of force equilibrium has been applied, given by Eq. (3.29).

$$\nabla\sigma + F = 0 \quad (3.29)$$

And, the stress-strain relationship or constitutive relationship is defined as follows

$$\{\sigma\} = [D]\{\varepsilon_e\} \quad (3.30)$$

Moreover, the elastic strain is obtained by excluding plastic strain, thermal strain and strain induced by phase changes and solid-state phase transformation in P91 steel as given by the Eq. (3.31) as follows:

$$\varepsilon_e = \varepsilon - \varepsilon_{pl} - \varepsilon_{th} - (\varepsilon_{vol} + \varepsilon_{phase} + \varepsilon_{trp}) \quad (3.31)$$

Therefore, the stress-strain relationship is now given by Eq. (3.32) as follow:

$$\{\sigma\} = [D]\left(\{\varepsilon\} - \{\varepsilon_{pl}\} - \{\varepsilon_{th}\} - \{\varepsilon_{vol}\} - \{\varepsilon_{phase}\} - \{\varepsilon_{trp}\}\right) \quad (3.32)$$

The six degrees of freedom of the weld joint model are constrained to prevent the plate's rigid body motion. Zero displacement loads are applied on the nodes at the corner of the weld joint model, as shown in Figure 3.13.

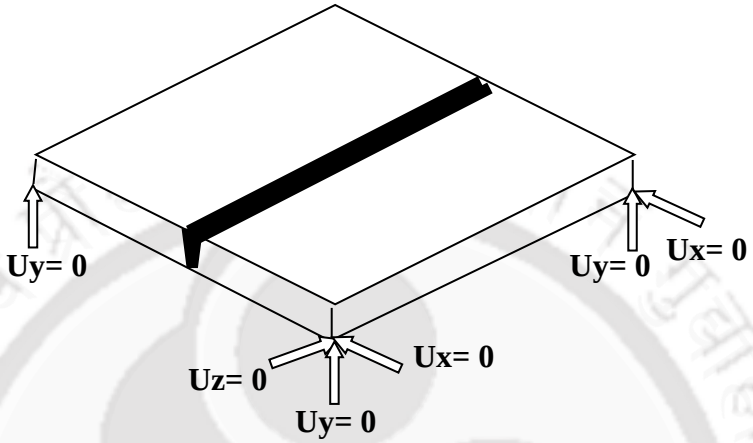

Figure 3.13 Structural boundary conditions to prevent rigid body motion of the weld joint model

The effect of solid-state phase transformation is incorporated in the structural modelling stage. It considers mechanical effect in terms of thermal expansion coefficient change and yield strength value within the temperature range of austenitic- martensitic transformation. The solid-state phase transformation and its effect are elaborately explained in the following subsection, i.e. 3.5.5.

3.5.5 Modelling SSPT phenomenon

The metallurgical changes associated with solid-state phase transformation during welding heating and cooling cycles are analysed using various phase transformation laws. When the nodal temperature reaches appropriate temperatures of austenitization during heating, Pearlite/Ferrite from BCC (α) structure completely transforms into austenite, i.e. FCC (γ) structure, which results in volumetric contraction. The rate of austenitic transformation depends upon nucleation rate and growth speed of the edge length of pearlite colonies and their true interlamellar spacing [125]. Johnson Mehl Avrami Kolmogorov theory provides the temperature-dependent austenite fraction [18], which is given by Eq. (3.33).

$$f_A(T) = \left[1 - \exp\left(-\frac{\pi}{3} I G^3 t^4\right)\right] V_A(T) \tag{3.33}$$

It quantitatively designates the ferrite-austenite transformation during heating. Similarly, once the nodal temperature reaches the martensitic transformation temperature range during cooling, austenite (FCC structure) transforms into martensite (BCT structure, α*), promoting volumetric expansion. The martensite fraction at real-time temperature (T) is defined by Koistenen-Marburger law [77] expressed as Eq. (3.34).

$$f_m(T) = \left[1 - \exp\left(-0.011(M_s - T)\right)\right] \tag{3.34}$$

The change in the martensitic fraction during cooling from M_s (375 °C) to M_f (200 °C) in differential form is given by Eq. (3.35).

$$\Delta f_m(T) = \left[-0.011 \exp\left(-0.011(M_s - T)\right)\right] \Delta T \quad (M_f \le T \le M_s) \tag{3.35}$$

The corresponding total volumetric strain for P91 steel weld is obtained as 3.75×10^{-3} [32]. Hence, the corresponding volumetric strain for the instantaneous martensitic fraction is given in Eq. (3.36), within the temperature range ($M_f \le T \le M_s$).

$$\Delta\varepsilon_{vol\_martensitic} = 3.75\times10^{-3} \Delta f_m \qquad (M_f \le T \le M_s) \tag{3.36}$$

The corresponding volumetric strain for complete austenitic transformation for P91 steel weld is obtained as -2.228×10^{-3} [31], [126], [127]. A linear volumetric strain variation due to austenitic transformation is considered in the FE modelling for volumetric contraction [128]. The expression for volumetric strain during austenitic transformation is the linear relationship with the temperature range given by Eq. (3.37).

$$\Delta\varepsilon_{vol\_austenitic} = \frac{-2.288\times10^{-3} \Delta T}{A_{c3} - A_{c1}} \qquad (A_{c3} \le T \le A_{c1}) \tag{3.37}$$

These volumetric changes owing to the SSPT phenomenon are considered by including additional components of the volumetric strain in total strain calculation. Hence, the strain associated with martensitic and austenitic transformation owing to both volumetric change and thermal load is given by Eq. (3.38) and Eq. (3.39), respectively.

$$\Delta\varepsilon + \Delta\varepsilon_{vol\_martensitic} = \left(\alpha.\Delta T\right) + -4.825\times10^{-5} \exp[0.011(T - 375)]\Delta T \tag{3.38}$$

$$\Delta\varepsilon + \Delta\varepsilon_{vol\_austenitic} = \alpha.\Delta T - 2.288\times10^{-5}.\Delta T \quad (3.39)$$

From Eqs. (3.38) & (3.39), the effect of volumetric changes in terms of volumetric strains is instigated by modifying the thermal expansion coefficient values in the transformation temperature range of base and weld metals. The mechanical properties in the austenitic transformation temperature range are mostly weaker. Hence, martensitic transformation is more significant than austenitic transformation for residual stresses results.

Thermal stresses in welding and other heat treatments entail permanent distortion or plastic distortion during solid-state phase transformation, termed as transformation-induced plasticity [129], [130]. The effect of transformation plasticity is generally modelled for two contributions: Greenwod- Johnson model considers plastic contribution [131], and the Magee model considers the shear component of martensitic variants during transformation. Magee effect has negligible influence on residual stress modelling [131]. Hence, Inoue, Leblond and Fischer derive an expression from calculating transformation plasticity induced plastic strain component [132], which is given by Eq.(3.40) below:

$$\Delta\varepsilon_{tp} = 3C_{trp}\left(1-f_M\right)\Delta f_M\sigma \quad (3.40)$$

The value C_{trp} is calculated experimentally and is of the order of 10^{-5} MPa [132]. Few researchers recommended that yield strength reduces by 30 MPa in the martensitic temperature range to consider the transformation induced plasticity in FE modelling of P 91 steel weld [77], [133].

Phase transformations also correlate with the microstructural changes during the thermal cycles. The yield strength of the material in its different microstructural phases replicates the mechanical strength of that phase [73], [77]. Hence, microstructural phase changes due to solid-state martensitic-austenitic transformation in P91 steel also influence the yield strength of the material. Eq. (3.41) determine the variation in yield strength value for microstructural changes during austenite- martensite transformation as follows[130]:

$$\sigma_{YS} = f_A(T).\sigma_{YS}\big|_A + f_M(T).\sigma_{YS}\big|_M \quad \text{(MPa)} \quad (3.41)$$

The yield strength values for both the base plate and weld material during the austenitic phase change are set to the base plate's values to implement its effect in FE modelling. Similarly, the weld material's yield strength is taken for both weld material and the base plate during the martensitic transformation [13], [32].

3.5.6 Materials properties

The material properties are taken varying with temperature and are shown in Figure 3.14.

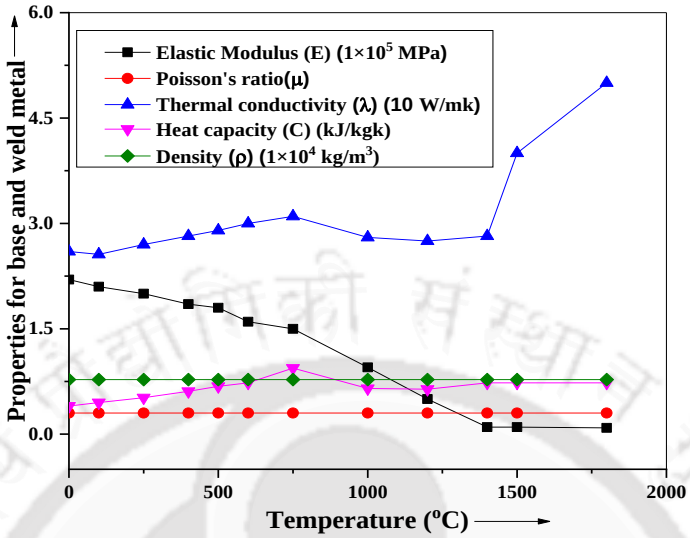

Figure 3.14 Material properties for base and weld materials [34], [134]

Based on the relations mentioned in Eqs. (3.38)-(3.39), the thermal expansion coefficients dramatically changed within the martensitic-austenitic temperature range and are shown in Figure 3.15 (a). The plot for temperature-dependent yield strength and hardening modulus values for both base and weld metal is also shown in Figure 3.15 (b).

Enthalpy of both base and weld material is substantial to consider phase change during austenitic- martensitic transformation and solid to mushy zone, mushy zone to liquid phase transformations. The corresponding enthalpy values are calculated at their respective temperature ranges based on the dissipated latent heat energy.

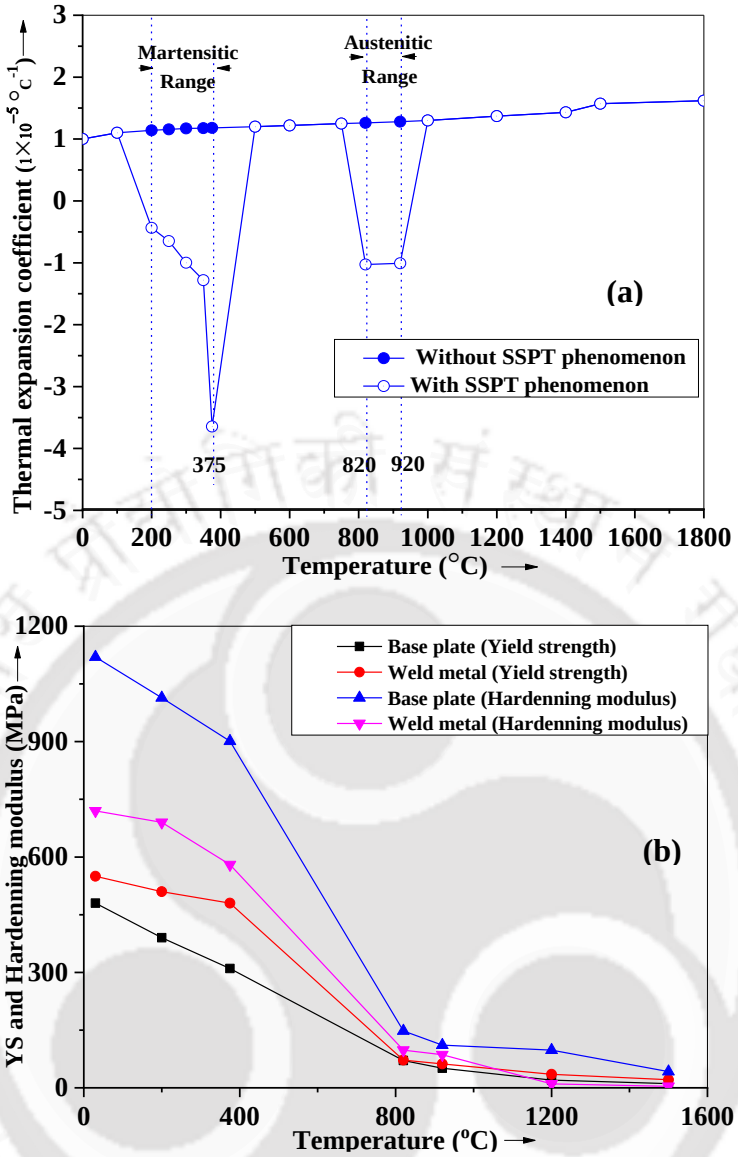

Figure 3.15 (a) Modified thermal expansion coefficient for the base plate and weld metal (b) YS and hardening modulus for base and weld metal [34], [134]

Enthalpy values are calculated for four stages of phase changes w.r.to their temperature ranges. Eq.(3.42) shows the expression for calculating enthalpy value at temperatures below solidus temperature [135].

$$H = \rho.C^*.\left[T - T_o\right], \text{(Below solidus temperature)} \tag{3.42}$$

where $C^* = C_{avg} + L/(T_L - T_s), C_{avg} = C_s + C_L/2$

Once the temperature crosses the solidus temperature, the same expression with different heat capacity and temperature range is given by Eq. (3.43) [135].

$$H_L = H_s + \rho.C^*.\left[T_s - T_o\right], \text{ (At solidus temperature)} \quad (3.43)$$

Eq.(3.44) gives the expression which includes the enthalpy value at solidus temperature and the enthalpy value obtained for the temperature difference of solidus liquidus temperatures in the temperature range between solidus to liquidus, i.e. in the transition state. The solidus and liquidus temperatures for P91 steel are 1500 ^{o}C and 1420 ^{o}C, respectively [32]. And, the latent heat value for P91 steel is obtained as 260 kJ/kg [32]. Eqs. (3.45)- (3.46) give the expressions for enthalpy at the liquidus state temperature [135].

$$H_{TR} = H_s + \rho.C.\left[T_s - T_o\right], \text{ Enthalpy solidus-liquidus temperature} \quad (3.44)$$

$$H_L = H_s + \rho.C^*.\left[T_L - T_s\right], \text{ Enthalpy at the liquidus temperature} \quad (3.45)$$

$$H_\infty = H_L + \rho.C_L.\left[T - T_L\right], \text{ Enthalpy over liquidus temperature} \quad (3.46)$$

The enthalpy values are calculated at different temperatures in their respective phase change conditions, given in Table 3.5 below.

Table 3.5 Temperature-dependent Enthalpy of P91 steel

Temperature (^{o}C)	**100**	**250**	**375**	**500**	**820**	**920**	**1200**	**1420**	**1500**
Enthalpy (MJ/m^3)	574	1436	2154	2873	4711	5286	6895	8054	8514

3.6 Mitigation techniques

The heating and cooling cycles in the welding process are controlled and modified to manage the temperature distribution and thermal gradient across the weld region and plate thickness. The thermal cycles can be altered at three different stages, i.e., before, during and after the welding process. Heat treatments based pre, in and post welding mitigation techniques are elaborately discussed in section 2.5. Hence, these pre, in and post welding heat treatments are FE modelled and analysed for SAW butt joints of P91 steel, which are explained as follows-

3.6.1 FE modelling of preheating

The planning and preparation of the weld joint plates, selection of consumables, mounting of weld specimen onto the jigs and selection of weld parameters should be considered to ensure the intended quality of weld joint. These conditions have already been considered here and explained in section 3.2. Similarly, preheating, prudent selection of weld passes and sequences

are also crucial in reducing the welding distortions and residual stresses [85]. As the present study involves square butt single side and double side single pass welding, preheating must show a significant role as a pre-process mitigation.

Preheating is defined as raising the base plate's temperature to a specific desired temperature termed as preheating temperature from the room temperature. Preheating is mainly carried out in the region besides the root gap. Preheating reduces shrinkage stresses in the weld, prevents excessive hardening, and slows down cooling [136]. Preheating temperature depends on factors like welding heat (Q), the chemical composition in base metal (CET), hydrogen diffusion (HD) and plate thickness (t), which is expressed as Eq. (3.47) [137]. Preheating temperature for P91 steel welds lies between 200-300 ºC [10], [138].

$$T_p = 697 \times CET + 160 \times \tanh\left(t/35\right) + 62 \times HD^{0.35} + \left(53 \times CET - 32\right) \times Q - 328 \tag{3.47}$$

A disk shape surface heat flux model has been imposed on both sides of the weld zone to FE model the preheating process. The expression for the surface heat flux elliptical model is given in Eq. (3.48).

$$Q_r = \frac{Q}{\pi r^2}\left(e^{-2\left[\frac{x^2+(z-v_p t)^2}{r^2}\right]}\right) \tag{3.48}$$

3.6.2 FE modelling of in-process mitigation

As disused in previous section 2.5, most of the in-process mitigation thermal load based techniques work on the principle of developing a tensioning effect during the welding [139]. Hence, various thermal load based in-process mitigation methods are discussed here to analyse its mitigation effect on SAW butt joints of P91 steel.

3.6.2.1 Transient parallel side heating

According to Well's model of residual stress induction, the reduction in thermal gradient decreases the equilibrium temperature of the thermal/stress cycle [140]. It can be achieved by heating both sides of the root gap in a specific region at a particular temperature to maintain the required thermal gradient.

Transient parallel side heating process is performed using a heating torch (TIG/MIG, oxyacetylene torch). The deciding factors for the mitigation effect of transient side heating are

the heating locations away from the weld region, speed of heating torch, and intensity of heating. In the present case, the speed of the heating torch is kept the same as welding speed, and the heating temperature and torch locations are varied for the comparative study. Hence, an FE simulation of this transient side heating is carried out to examine the effect of changing the heating locations and intensities. The schematic of the transient thermal tensioning or side heating is shown in Figure 3.16.

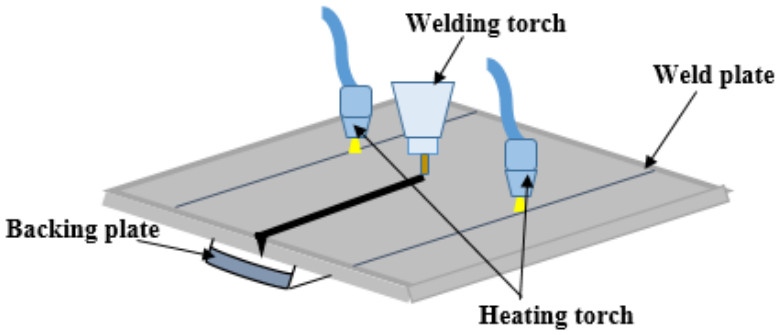

Figure 3.16 Schematic of transient parallel side heating

The weld joint, similar to the SAW butt joint of the P91 steel specimen, is modelled with actual weld bead shape and size. The model resembles a genuine weld bead, and heat is applied with the volumetric heat source double ellipsoidal bead shape model. A 10 mm wide region is selected as a side heating region on both sides of the weld line. Fine meshing or comparative more refined elements are taken in the weld fusion zone and side heating zone. The overall model and meshing are shown in Figure 3.17.

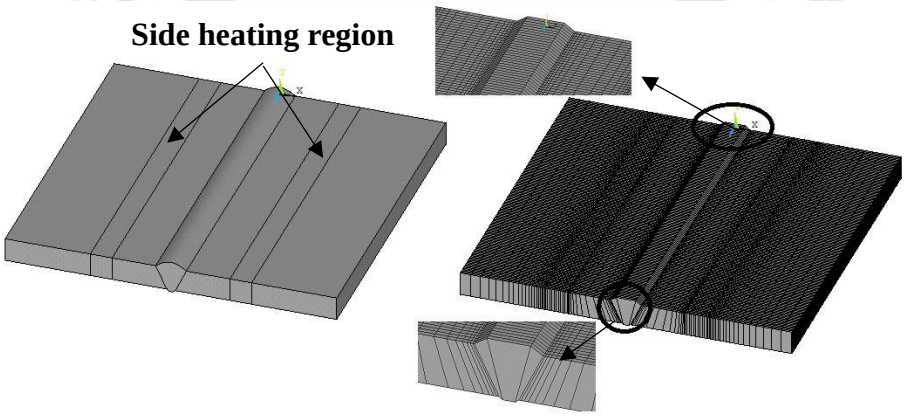

Figure 3.17 Model and meshing of transient side heating model

SSPT is also considered to examine its effect separately. The welding parameters are taken the same as the welding experiment, so that effect of mitigation can be arbitrated.

A disc shape surface heat flux model has been adopted to model the transient side heating process, which applies the heat on the targeted surface area moving at the speed of the welding torch. The expression for surface heat flux is given as in Eq. (3.49).

$$Q_r = \frac{Q}{\pi r^2}\left(e^{-2[\frac{x^2+(z-v_{ht}t)^2}{r^2}]} \right) \tag{3.49}$$

3.6.2.2 Heat sinking

A cooling source beneath the root gap and its vicinity used for intense cooling effect is a heat sink. It cools the metal rapidly from high temperatures and thereby produces a tensile action in the weld. The proposed heat sink can be applied by using the cooling media of running water through a macro-sized water channel touching the bottom region in the vicinity of the root gap of the weld plate. The schematic diagram shown in the Figure 3.18 presents the heat sink arrangement. It consists of a water inlet pipe supplying water to the channel kept below the weld plate. This arrangement provides a high value of heat transfer coefficient representing an intense cooling effect.

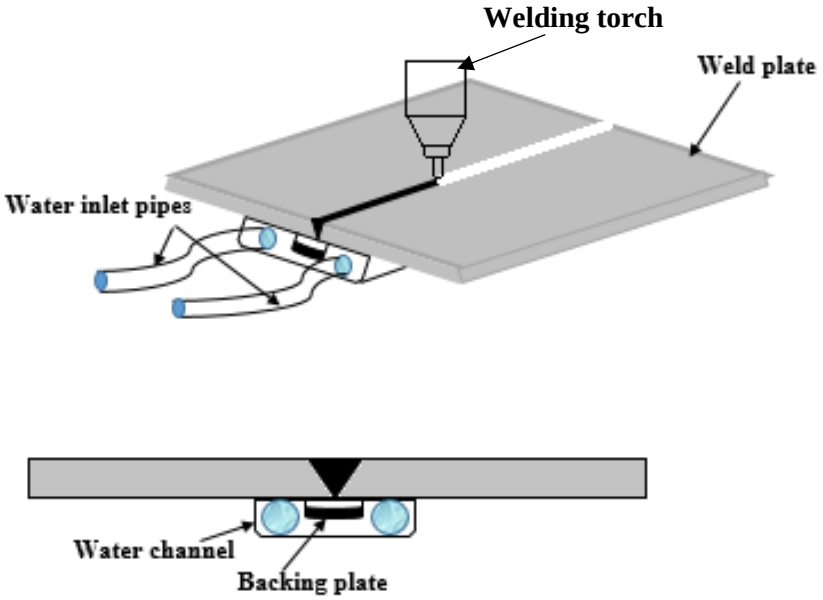

Figure 3.18 Schematic of heat sink setup

The intense cooling effect of the heat sink is simulated as the heat transfer between the specimen and the cooling media (water flow parallel to plate length considering laminar flow) described by forced convection cooling [141] given by Eq. (3.50). Eq. (3.50) determines the average heat transfer coefficient, which is applied as the convective boundary condition on the targeted surface throughout the length of the weld specimen.

$$h = (0.664 \times \mathrm{Re}_L^{1/2} \times \mathrm{Pr}^{1/3}) \times k / L \tag{3.50}$$

$$\mathrm{Re}_L = \frac{L v_\infty \rho}{\mu} \;\&\; \mathrm{Pr} = \frac{\mu C_p}{k}$$

In the present case, the convective heat transfer coefficient values are arbitrarily chosen for the comparative study for their cooling effect in mitigation.

3.6.2.3 Combined transient side heating and heat sink

Many literatures are found on the mitigation effect of either side heating or heat sink processes as thermal tensioning techniques. However, few pieces of research have conducted the thermal tensioning mitigation technique with combined side heating and heat sink methods [100], [142]. Though, all the studies have been performed on thin sheet weld joints.

The combined hybrid side heating and heat sink mitigation processes consist of heating sources on both sides of the weld line and a cooling source just beneath the root gap and both of its sides for submerged arc butt welding of thick plate. The schematic of the experiment set-up is shown in Figure 3.19.

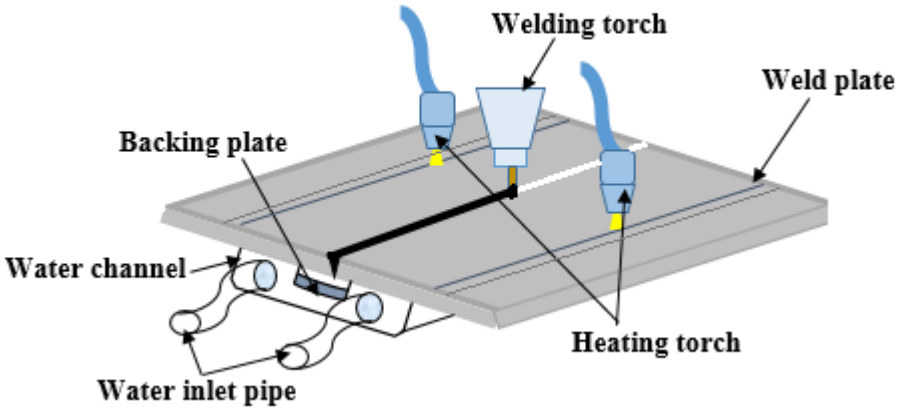

Figure 3.19 Schematic of hybrid combined side heating and heat sink mitigation

The FE modelling of these three combined processes, i.e., welding, side heating and heat sink cooling is performed, based on the formulations explained in the earlier sections 3.6.2.1 and 3.6.2.2.

3.6.3 FE modelling of post-weld heat treatment

As far as CSEF steel welds are concerned, post welding heat treatments (tempering, normalising etc.) are highly recommended [10], [90] to recover microstructural stability and mechanical properties of the weld joint. On the other hand, PWHT also causes stress relaxation in welded joints. The heating rate, soaking temperature and time, and cooling rate are the deciding factors for the effect of PWHT on the welded specimens. AWS recommended the minimum PWHT temperature of 730 ^{o}C for one hour [27], [143]. Similarly, the ASME Code for boiler and pressure vessel also recommended a similar temperature range of 730-760 ^{o}C for one hour to improve the hardness, UTS, YS and toughness values and proper stress relief. Hollomon-Jaffe parameter $\boldsymbol{H_P}$ is introduced to estimate the correct range of heating temperature and heating & cooling rates for the heat treatment on weld specimens [144]. The $\boldsymbol{H_p}$ **(**Hollomon-Jaffe parameter or Larson-Miller parameter**)** is given by Eq. (3.51) [27].

$$H_p = T_a(C_{HP} + Logt_r) \tag{3.51}$$

A higher C_{HP} = 30 is employed for such low alloyed steel, i.e. P91 steel [145]. The suggested minimum required temperature of PWHT is 760 ^{o}C for a holding time of 2 h to improve the microstructure and mechanical properties of the P91 steel weld. Hence, the same heat treatment parameters are considered for stress relaxation to understand its mitigation effect. The heating is carried out at 100-150 ^{o}C/min until the temperature is below 760 ^{o}C. Then, the sample is soaked at 760 ^{o}C for 2 h (recommended to improve microstructure stability and mechanical properties) for annealing. Finally, the cooling process occurs at the rate of 150 oC/min, followed by cooling in the air until room temperature to recover the weld zone's martensitic structure [146].

3.6.3.1 Creep phenomenon in FE modelling of PWHT

Stress relaxation during PWHT involves primary and secondary stages of the creep phenomenon. Hence, the creep phenomenon must be considered in modelling PWHT. The creep effect is modelled using an implicit creep equation that provides the creep environment

with temperature-dependent constants data. The heating cycle and soaking time & temperature may play essential roles in defining their stress relaxation effects during PWHT. Several creep laws or implicit equations are available to consider the three stages of the creep phenomenon.

Nevertheless, creep occurs in its primary and secondary phases for stress relaxation cases during PWHT. In the secondary stage, the creep induced strain almost remains constant for corresponding stress distribution in the given time duration. One of the best suitable creep laws to consider such stress relaxation effect is Norton's creep law. Its most generalized form is given by Eq. (3.52) [147].

$$\bar{\varepsilon}_{creep} = C_1 \sigma^{C_2} e^{-C_3/T} \tag{3.52}$$

The value A_c and n_c can be obtained by conducting a stress relaxation test on the base or weld metal. The stress relaxation test was carried out on the welding wire, and the values obtained for A_c and n_c were considered the same for both weld and base metals. The stress relaxation test starts at an estimated strain rate of 5×10^{-5}, and the specimen was kept at the same strain for the holding time of 2 h at the constant temperature of 760 °C. The test brings about the stress vs time graph, revealing the change in stress (maximum to minimum) throughout the holding time at a fixed temperature. The initial maximum stress for loading was much below the stress-strain curve's proportionality limit for the same wire's uniaxial tensile test at elevated temperature. The initial stress was taken below the proportionality limit. It is explained through Norton's Bailey creep behaviour which expresses the change in stress w.r.to time during stress relaxation and given by the equation below Eq. (3.53) [147].

$$\frac{d\sigma}{dt} = -mEA_c^{\frac{1}{m}} \sigma^{\frac{n_c}{m}} \left[\frac{\sigma_0 - \sigma}{E} \right]^{\frac{m-1}{m}} \tag{3.53}$$

Therefore, for the uniaxial stress relaxation test or a consistent creep strain rate case, the elastic modulus is assumed constant with $m = 1$. So, Eq. (3.53) gives the expression for Norton's creep law similar to Eq. (3.52) as given by Eq. (3.54) [147].

$$\frac{d\sigma}{dt} = -EA_c \sigma^{n_c} \tag{3.54}$$

Therefore, the proportionality limit has been considered the maximum initial stress for the stress relaxation test for a constant elastic modulus. Each experiment was conducted below the constant elastic modulus value for the tensile specimen. A high temperature (760 °C) tensile

test is conducted with a proportionality limit (or, say, the stress-strain curve becomes nonlinear) at the value of 112 MPa. As a result, two stress relaxation tests were performed at the two initial stress values of 90 MPa and 98.3 MPa. The stress vs time plots provides the rate of change with time, which values are put in Eq. (3.54) and E = 128 GPa (for welding wire). Hence, the values of A_c and n_c are calculated as 2.312×10^{-17} and 8, respectively.

3.7 Mechanical and microstructural characterisation

Investigations of microstructure and mechanical properties of weld joints are also significant to understand the microstructural evolution and mechanical behaviour of SAW butt joints of P91 steel after welding and mitigation related heat treatments.

The weld bead shape and size are visually inspected through macrography. Microstructural characterisation provides an explicit detail about different zones across the weld bead, i.e. FZ, CGHAZ, FGHAZ, ICHAZ & base metal.

Similarly, mechanical characterisation of the weld joint includes assessing the weld's mechanical strength or tensile properties (i.e., YS, UTS, ductility, etc.) and microhardness of various zones across the weld. EDS, XRD and Fractographic analyses are also performed on these welded joints to characterise chemical composition, phase and fracture surface, respectively.

3.7.1 Sample preparation

The samples are cut across the weld bead for microstructural, hardness and tensile strength studies using wire EDM. The same samples are used for macro and microstructure analysis. The cut sample of the double-sided weld is shown in Figure 3.20. The tensile sample is prepared with **ASTM E8-04** standard for sub size of the flat specimen. The gauge length is taken as 60 mm. The overall dimension of the tensile sample is shown in Figure 3.21.

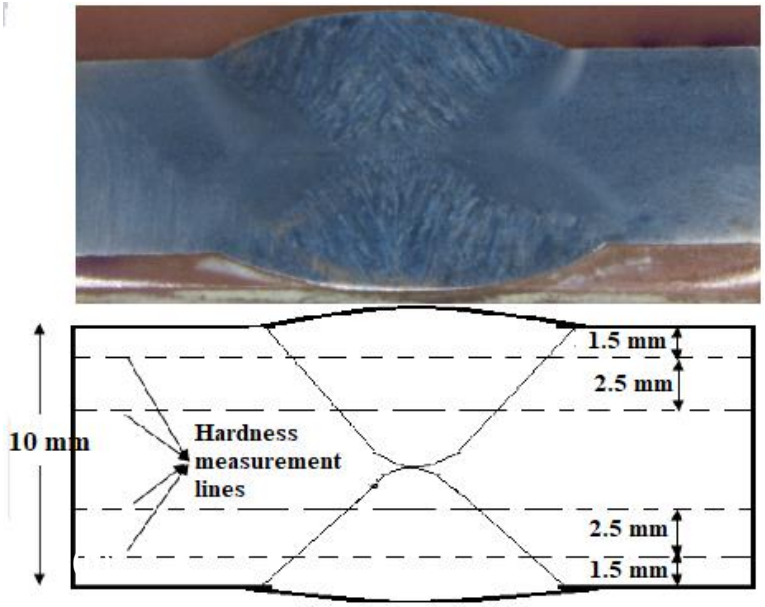

Figure 3.20 Hardness & microstructure study sample

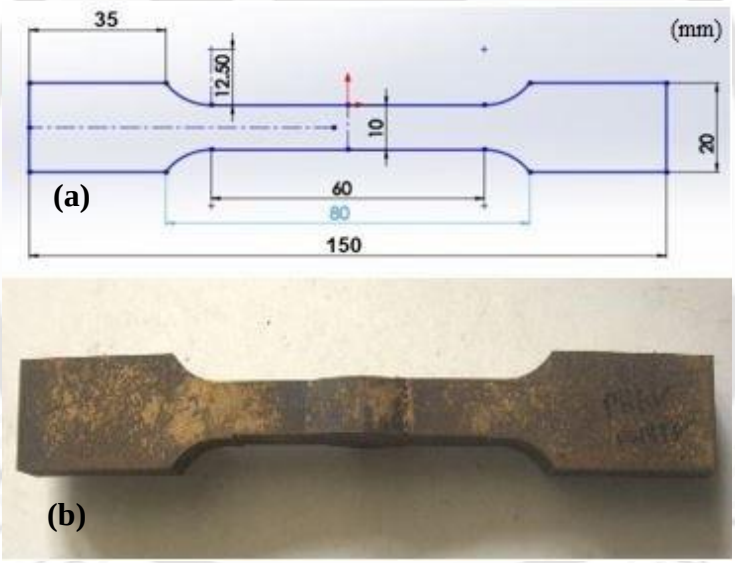

Figure 3.21 (a) Dimension of sub-size of the tensile specimen and (b) tensile test sample

3.7.2 Macro and micrograph study

The cross-sectional images are captured using a stereomicroscope (Make: Nikon) as shown in Figure 3.22 (a), to examine the overall quality (bead shape, depth of penetration etc.) of the weld bead. Microstructure characterization is performed on an optical microscope (Make: Carl Zeiss) as shown in Figure 3.22 (b) in different zones i.e. Base Metal Zone, FZ and HAZ across the weldment. A specimen requires special preparation to reveal the microstructure. Hence, first of all, samples are polished with emery paper with grades varying from coarse to fine size.

Finally, the exposed surface is etched in the solution of 100 ml Ethanol mixed with 2-3 g Picric acid and 4-5 ml Hydrochloric acid also known as Villella's reagent [17].

(a) **(b)**

Figure 3.22 (a) Stereomicroscope (Nikon), (b) Optical Microscope (Zeiss)

3.7.3 Microhardness Test

The microhardness measurement is performed on a Vickers microhardness tester (Make: Omni Tech), as shown in Figure 3.23. The dwelling load of 2 kg is gradually applied for 10s of dwelling time. Two lines are marked through the top and bottom sides of the weld bead for hardness measurement. Moreover, the other two lines are drawn to pass the middle regions of the weld bead. The hardness measurement is also performed on 300 random points within the HAZ and fusion zone to obtain a contour diagram of hardness distribution across the weld.

Figure 3.23 Vickers microhardness testing machine (Omni Tech)

3.7.4 Universal tensile test & fractography

UTS, YS and ductility of the welds are characterised by performing a tensile test on a universal hydraulic servo-controlled universal tensile testing machine (Make: Instron). The tensile test was conducted at a strain rate of 0.1mm/sec at room temperature. The test is also conducted for the electrode wire and base metal to assess and compare the strength of weld joints. FESEM analysis is also conducted for fractography of the small sample taken from the fractured tensile samples to investigate the fracture surface's nature.

3.7.5 XRD and EDS analysis

The intensity of different phase angles is recorded through an X-ray diffractometer (Make: Rigaku) to determine phase changes. Similarly, The chemical composition is quantitatively characterised with the help of energy-dispersive (X-ray) spectroscopy before and after the PWHT to compare it with the composition in base metal.

3.8 Summary

This chapter provided a thorough description of the methodologies applied to achieve the stated thesis objectives. First, a clear explanation is given on materials (Baseplate, electrode, flux) selection, welding parameters and other critical factors in conducting the submerged arc welding experiment on P91 steel. Further, it describes appropriate experimental methods to determine welding induced temperature, distortion and residual stresses.

Finite element modelling of SAW butt joints of P91 steel is broadly explicated in different subsections. Thermal and structural modelling stages are separately discussed for boundary conditions, governing equations and finite element formulations.

Further, the mathematic formulation and boundary conditions are also elaborately explained for FE modelling and simulation of different pre, in, and post-process mitigation heat treatments for SAW butt joints of P91 steel. At last, the experiment setups for microstructural and mechanical characterisation of the welded joints are introduced.

CHAPTER 4

STUDY OF THERMAL HISTORY, DISTORTION AND RESIDUAL STRESSES IN SAW WELDED BUTT JOINTS OF P91 STEEL

4.1 Introduction

This chapter provides a detailed experimental estimation of welding induced thermal history, distortions and residual stresses in SAW welded square butt joints of P91 steel. The chapter includes five sections, excluding the Introduction. Section 4.2 explains the overall quality of SAW welded square butt single and double side single pass joints of P91 steel.

Further, the following sections provide a comparative analysis of thermal history, distortion and residual stresses in both SAW welded square butt single and double side single pass joints.

4.2 Weld preparation

Based on the trial experiments considering weld bead width, depth of penetration and top & bottom reinforcement, a set of welding process parameters are obtained for both SAW welded square butt single and double side single pass joints, given in Table 4.1.

Table 4.1 Welding parameters for single and double side SAW joints

Parameters	Wire feed rate (mm/min)	Welding Voltage (V)	Travel Speed (mm/s)	Welding Current (A)	Electrode stick out (mm)
Single side	200	23	5.14	560	25
Double side (Top)	200	22.5	5.1	470	25
Double side (Bottom)	200	24	5	460	25

Figure 4.1 (a) and (b) present the top and bottom sides of single pass single and double side square butt joint specimens. A sound and narrow bead profile for bottom side weld bead are observed in square butt single side single pass welding. Similarly, adequate top and bottom reinforcements are achieved for both the weld joint cases. Figure 4.2 shows the cross-sectional view of both the weld joints to observe bead shape, size, and depth of penetration. The maximum HAZ width of ~7.7 mm is observed near the mid thickness of the square butt single-side single pass weld,

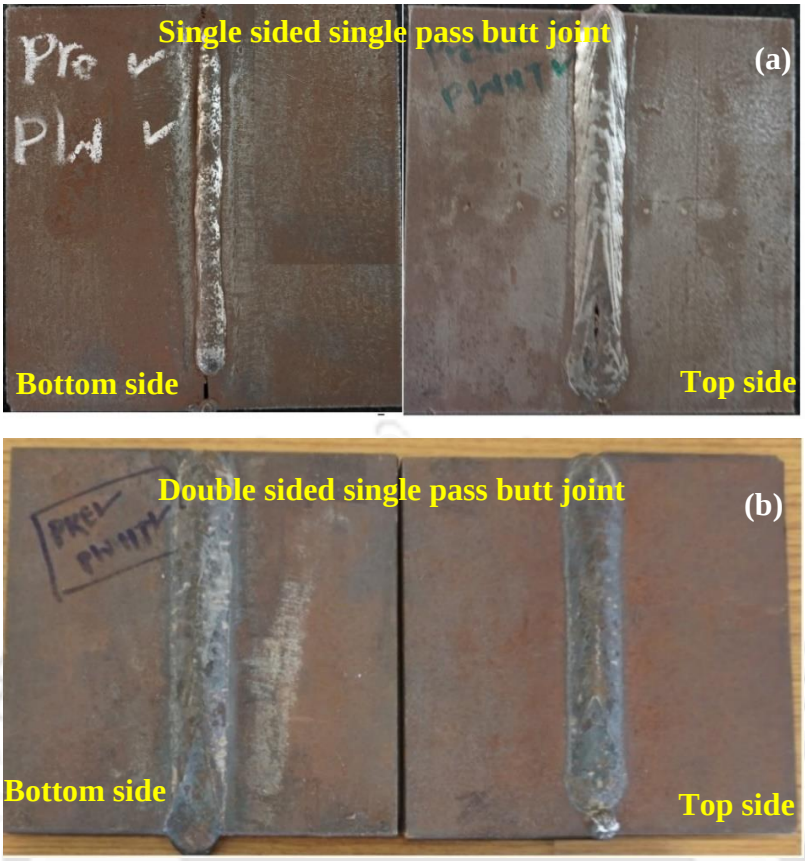

Figure 4.1 Square butt (a) single-side single pass weld joint (b) double-side single pass weld joint

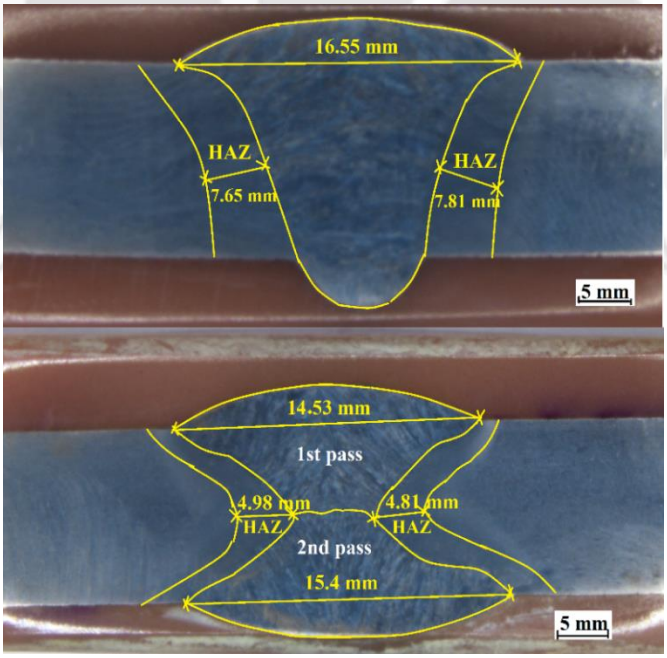

Figure 4.2 Cross-sectional view of square butt single and double-side single pass weld joint samples

It is reduced to 4.9 mm for square butt double side single-pass welding owing to less heat input in each weld pass. A solid penetration depth is observed, especially in square butt single side single pass welding without any edge preparation.

4.3 Thermal history

The thermal histories recorded through the DAQ system for different points away from the weld bead on the top surface of the plate of both square butt single and double side single pass welded joints shown in Figures 4.3 and 4.4, respectively.

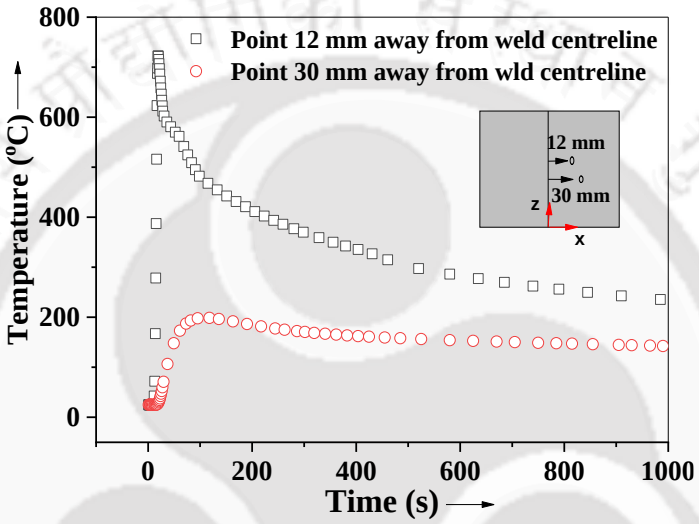

Figure 4.3 Thermal history of square butt single-side single pass welding

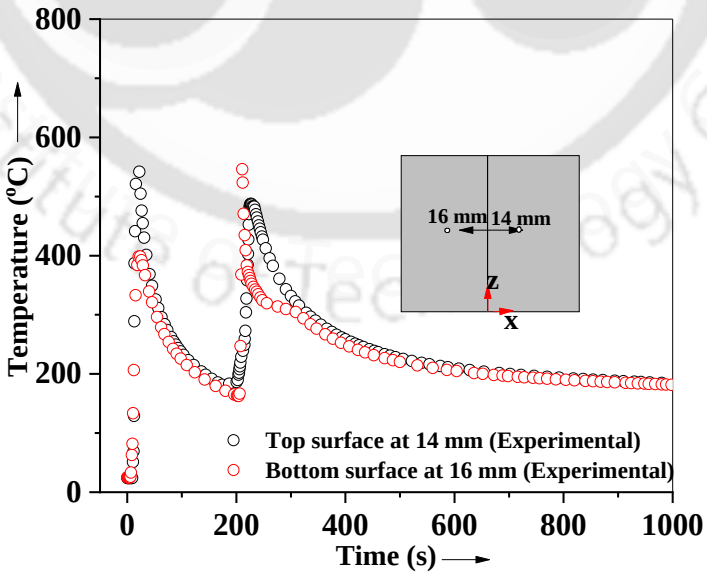

Figure 4.4 Thermal history of square butt double-side single pass welding

The thermal profile for the square butt single side single pass welding shows the peak temperature of around 723 ^{o}C at a point 12 mm away from the weld centreline on the top surface. Whereas, for double-side single pass welding, the measured peak temperature of 557 ^{o}C is observed for the 1st weld pass at a point 14 mm away from the weld centreline. Similarly, the peak temperature of 570 ^{o}C is observed for the 2nd weld pass by the thermocouple attached at a point 16 mm away from the weld centreline on the bottom surface. The temperature vs time graphs of both the cases display a rapid heating and cooling cycle of welding. The bottom side weld pass exhibits the sudden rise in temperature from the top side weld pass's cooling stage in double side welding.

These abrupt heating and cooling cycles are the sole causes of microstructural instability and change in mechanical properties of arc welded joints. Similarly, the resultant thermal expansion and contraction associated with these thermal cycles also instigated welding-induced residual stresses and distortions. Therefore, the study and analysis of welding induced distortion and residual stresses beforehand is important.

4.4 Welding induced residual distortion

The vertical distortion is measured for each marked point on the top surface of the weld plate as explained in section 3.3, which are plotted in terms of angular distortion and edge deflection as shown in Figure 4.5 and Figure 4.6 below.

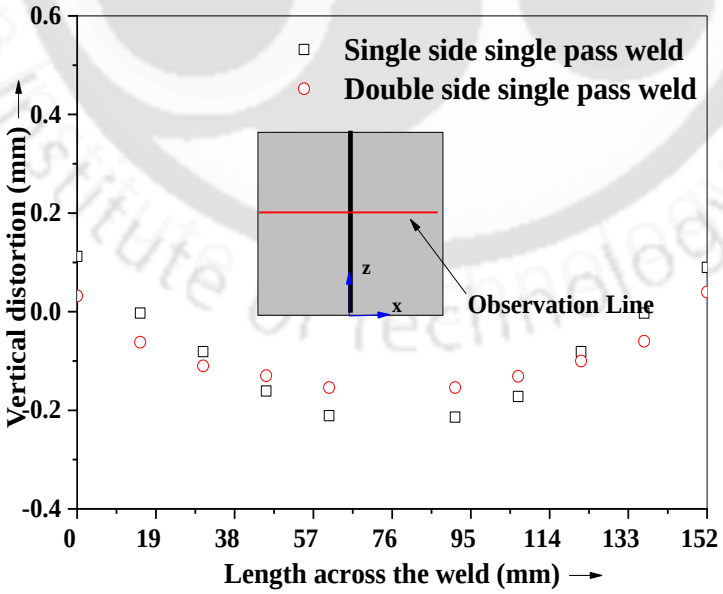

Figure 4.5 Distortion along the midline across the weld centreline for square butt single- and double-side welded joints

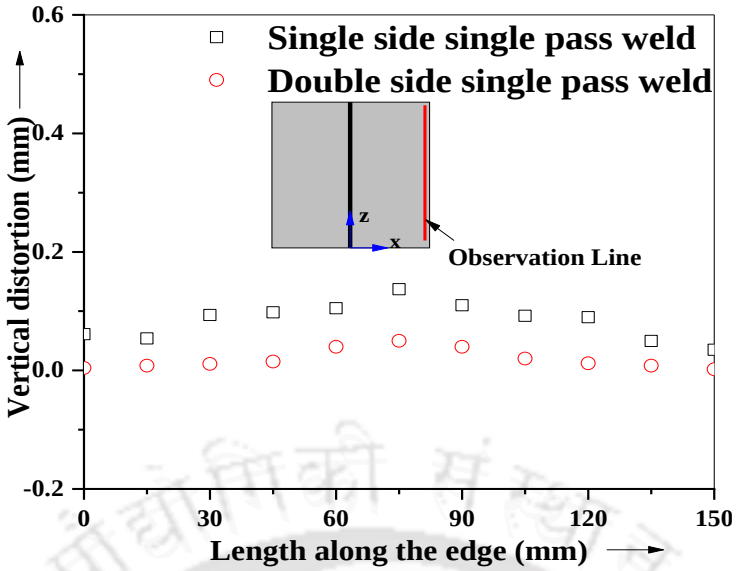

Figure 4.6 Distortion along the edge of square butt single- and double-side single pass welded joints

In both cases, it is observed that double side welding reduces the overall distortion. The maximum angular distortion value for square butt single-side single pass joint is observed around ~0.12 mm at the midpoint on the top surface of the base plate edge. Similarly, the angular distortion in terms of angular distortion angle (α) is calculated as (~0.23^{o}). As far as the double-side single pass welded butt joint is concerned, the maximum angular distortion value of ~0.04 mm is observed at the midpoint on the top surface of the base plate edge, which is reduced by around 70%. Similarly, double side single pass welding also reduced the angular distortion angle to around ~0.14 ^{o,} i.e., by 39%.

The distortion along the welding direction is estimated as edge deflection. Figure 4.6 shows that the distortion value at one of the ends of the plate edge also reduced from ~0.07 mm (for square butt single side single pass weld) to almost zero, i.e., around ~0.004 mm (for square butt double side single pass weld). The deflection pattern also changed for the flatter edge of the square butt double side single pass welded joint, as shown in Figure 4.6.

4.5 Welding induced residual stresses

DHD and contour techniques are performed for residual stress measurement in square butt single side, and double side single pass welded joints. The P91 steel welds show unique residual stress distribution in both the welding cases as discussed following-

4.5.1 Square butt single side single pass weld joint

The DHD technique measured biaxial residual stress values in FZ and HAZ after removing the top and bottom weld crowns/ caps. The experiment is carried out as explained in the methodology section 3.4.1. Figure 4.7 (a) presents the as-welded sample after the drilling and trepanning processes. It shows that DHD is performed at two locations (in the quasi-static region and 25 mm away from the start position) in FZ along the weld centreline. At the same time, only one location is chosen for HAZ. Figure 4.7 (b) shows the axes of the drilled holes in FZ and HAZ.

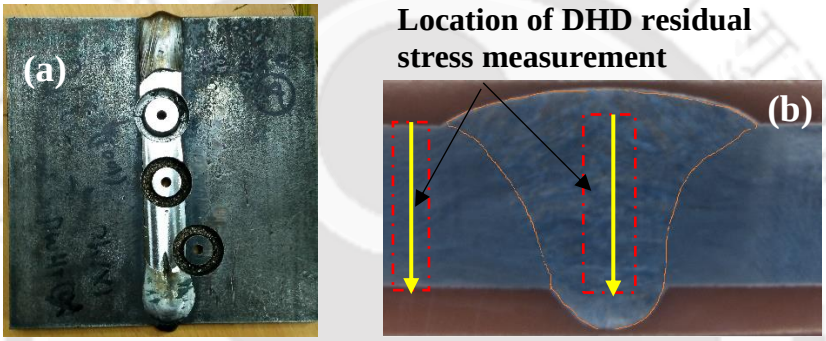

Figure 4.7(a) Weld sample after drilling and trepanning, (b) Locations for residual stress measurement

Figure 4.8 (a) presents the measured longitudinal and transverse residual stress values in the FZ for the measurement region in the FZ, 25 mm away from the start position. The x-axis in Figure 4.8 (a) shows the total thickness of the FZ region, including top and bottom weld bead crowns. It is observed that both longitudinal and transverse stress values are compressive in the fusion zone throughout its thickness. The maximum value of (-118 MPa) is observed at 4 mm thickness from the top. The compressive residual stress decreased sharply to -3.5 MPa towards the bottom side at 11 mm thickness. The maximum value of compressive transverse residual stress is observed as -40 MPa. This compressive stress was also reduced to -20 MPa towards the bottom side. However, transverse residual stress almost remains constant throughout the thickness in the FZ.

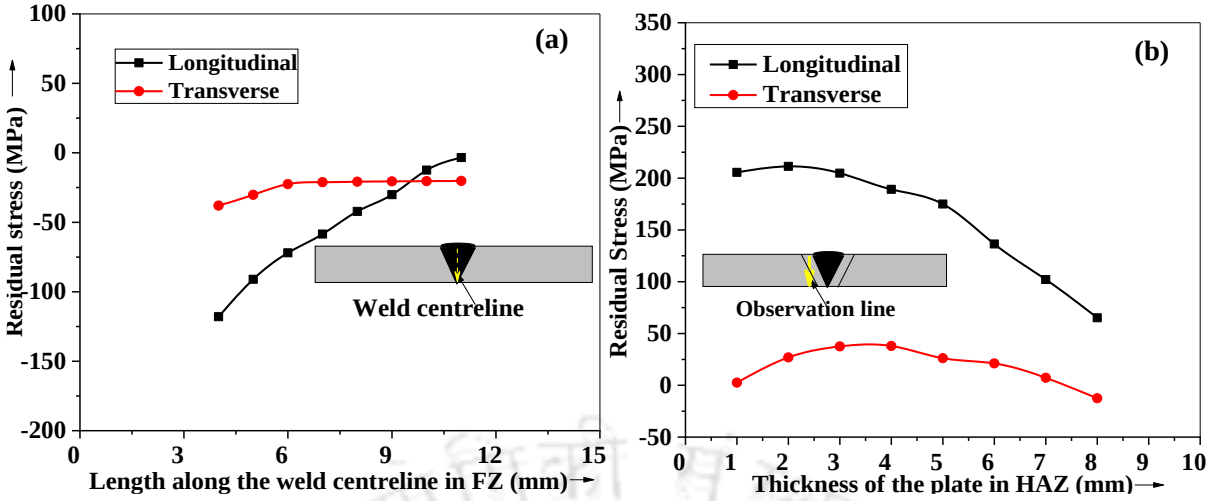

Figure 4.8 Through thickness longitudinal and transverse residual stresses in (a) Fusion zone and (b) Heat Affected zone of square butt single-sided single pass joint (DHD technique)

Similarly, Figure 4.8 (b) presents the DHD measured longitudinal and transverse residual stresses in HAZ. It is observed that in HAZ, both longitudinal and transverse residual stresses are tensile. The longitudinal residual stress value at 1 mm thickness from the top side of the weld joint is 202 MPa (i.e. maximum). The value gradually decreased to 65 MPa at 8 mm thickness. However, it has been discovered that the transverse residual stress values are comparatively much lower than longitudinal stress. The transverse stress values gradually decrease from 1 MPa (at 1 mm thickness) to -12.5 MPa (compressive) towards the bottom surface.

In general, volumetric shrinkage in the weld develops tensile residual stress during the cooling process. However, martensitic transformation in Gr. 91 steel weld stirs up the microscopic volumetric expansion during the cooling cycle. At the same time, a comparatively faster cooling rate induces martensitic transformation, which increases the volumetric expansion effect. In addition, since square butt single-side single-pass welding involves less weld material than V or X butt multi-pass welding, it experiences less volumetric shrinkage effect (i.e., less tensile residual stress) [44]. As a result, compressive residual stress is induced in a single-sided single pass welded joint. A similar compressive residual stress pattern throughout the thickness of FZ is observed for laser-welded square butt single-pass joint of 10 mm thick Gr. 91 steel [36].

4.5.2 Square butt double side single pass weld joint

Contour measurement is performed on square butt double-side single pass welded joint to measure spatial residual stress distribution on the cut surface across the weld centreline. The whole experiment involves four significant steps, as explained in methodology section 3.4.2.

First, both the surface deformations are precisely measured for targeted points (Total number of targeted points= 900) on the cut surface. The surface deformation at a point represents the vertical position (z- coordinate) of that point. Whereas x and y coordinates of the cut surface define the location of targeted points. The surface deformation measurement on CMM is shown in Figure 4.9.

Figure 4.9 Surface deformation measurement on CMM

The precision of deformation data is subjected to various factors like; cutting precision, surface roughness, positioning of sample on CMM bed and probe surface, etc. Hence, both contours of the cut surfaces are averaged at each point (x, y) to remove the effect of shear stresses and imperfection in cutting.

However, despite proper levelling and alignment of the sample on the CMM platform, the surface plot obtained for the exposed surface remains distorted. Consequently, the third most important step, ‘data conditioning’, takes place. The surface plot's orientation and smoothness are rectified, as explained in methodology section 3.4.2.1. The surface plot of average surface deformation values after the data conditioning is shown in Figure 4.10 below.

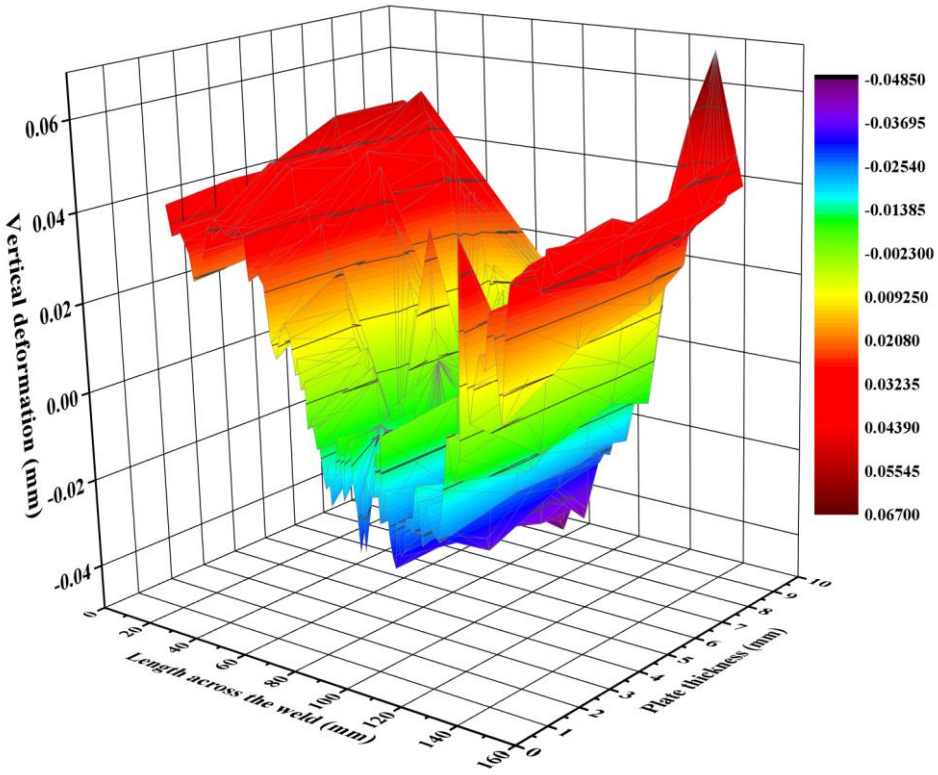

Figure 4.10 Surface plot for average surface distortion of both the cut surfaces after the data conditioning

Smoothening of the surface plot is accomplished through the nonlinear surface fitting, using the Levenberg- Marquardt (L-M) algorithm [117], as explained in methodology section 3.4.2. Hence, the best-fitted surface for the measured surface deformation plot is obtained, as shown in Figure 4.11 (a). At last, static structural FE analysis is performed with nodal displacement load matching the surface deformation plot. The deformation values are applied as displacement load in the negative direction to the corresponding nodes on the surface equivalent to the cut surface to obtain the analogous stress distribution same as welding induced residual stresses. The six degrees of freedom are constrained as initial boundary conditions to prevent rigid body motion of the plate. The cut section's FE model with appropriate meshing and constraints is also shown in Figure 4.11 (b).

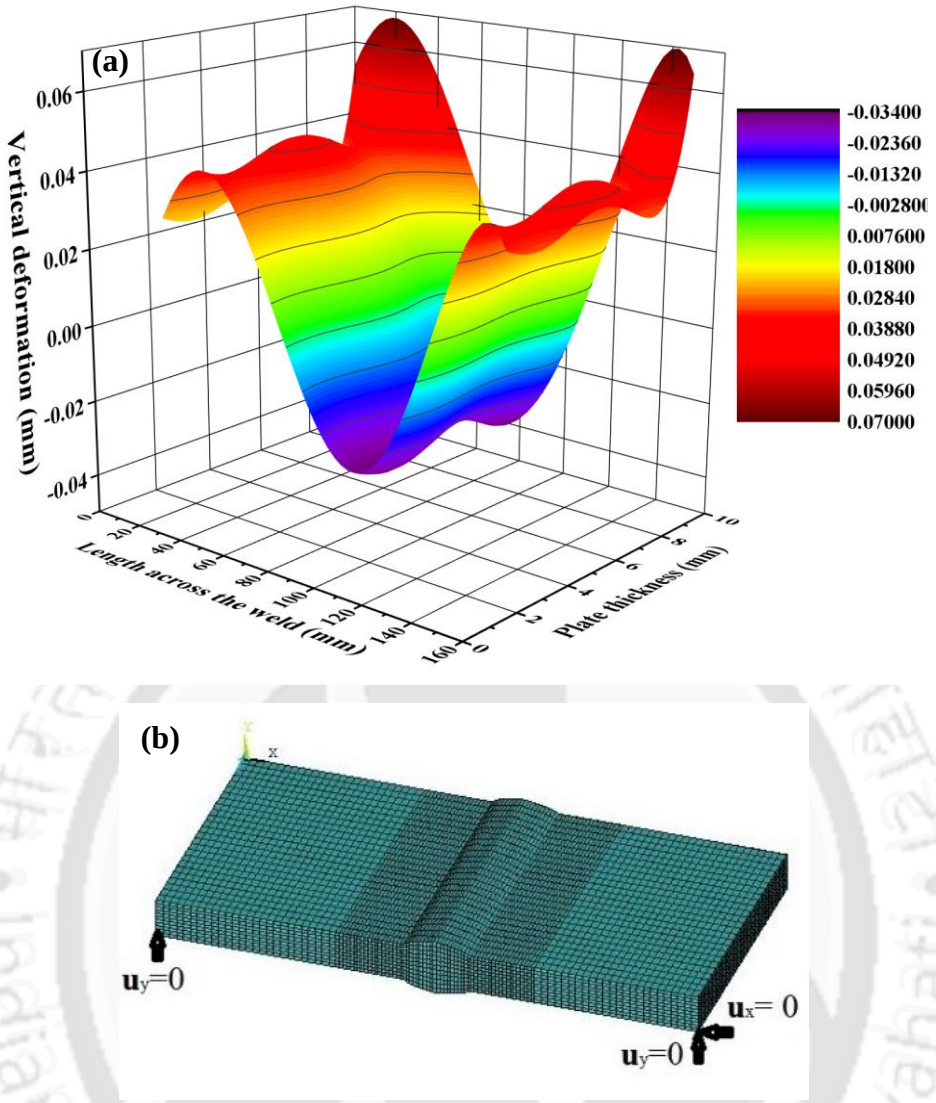

Figure 4.11 (a) Best fitting surface deformation plot (Adjusted R^2 value= 0.9105), (b) FE model of one of the halves of weld sample for surface deformation load structural FE analysis

Hence, the contour plot of longitudinal residual stress distribution on the cut surface of the double-side single pass welded joint is shown in Figure 4.12.

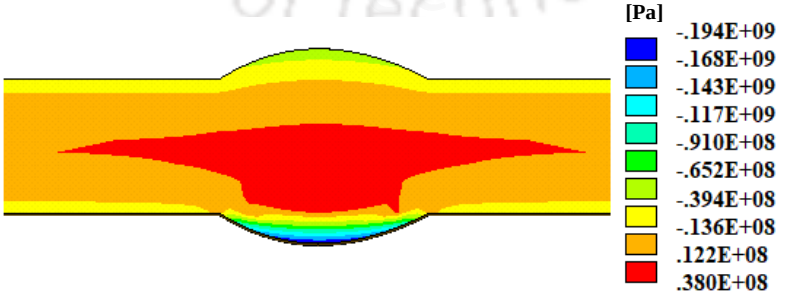

Figure 4.12 Contour plot of longitudinal residual stress distribution on the cut surface of square butt double-side single pass welded joint (contour measurement technique)

The tensile residual stress distribution is observed in the mid-region of the weld plate. However, compressive stresses are observed in the top and bottom sides of the fusion zone. The possible reason for compressive residual stress is fast cooling through exposed areas of top and bottom regions compared to mid-region. The slow cooling rate affects the martensite transformation of the P91 steel weld during cooling. It leads to less volumetric expansion and originates tensile residual stress in a double-side butt weld's mid thickness region. The maximum compressive residual stress in the double-sided weld's contour plot is observed as -194 MPa. On the other hand, the peak value of tensile residual stress is observed as 38 MPa.

Figure 4.13 presents longitudinal residual stress values in the FZ of both square butt single- and double-side single pass welded joints. It presents a comparative explanation of residual stress distribution in the FZ of both the weld joints. For the square butt single side single pass weld joint, the observation points are within 4 mm (top) to 11 mm (bottom) thickness in the FZ, signifying the removal of the top and bottom weld bead crowns DHD measurement. However, the whole thickness, including weld bead crowns, is considered for square butt double-side single pass weld joint.

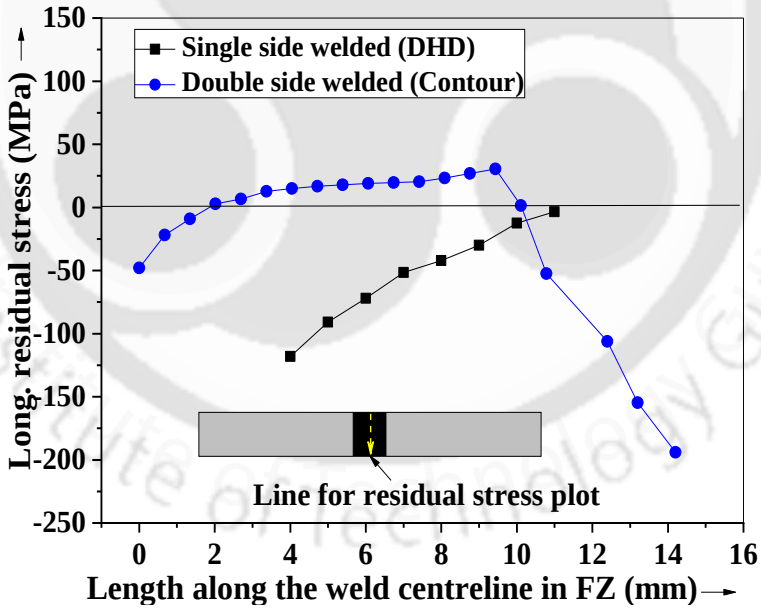

Figure 4.13 Longitudinal residual stress across the thickness in the fusion zone of square butt single and double side single pass welded joints

Compressive residual stress is observed in the FZ of square butt single-sided single pass weld, decreasing from top to bottom. However, the square butt double-sided single pass weld shows tensile residual stress in the mid-thick region, as shown in Figure 4.13. The residual stresses

on top and bottom points are observed as –58.9 MPa and -193.1 MPa, respectively. It is also observed that the tensile residual stress reaches its peak in the lower half of the plate thickness at 9 mm from the top surface with a value of 32.4 MPa. The top and bottom weld bead crown regions of square butt single side single pass joint may also show compressive residual stress, which is assessed from FE results explained in the next chapter.

4.6 Summary

In this chapter, the thermal history, welding induced distortion and residual stresses are studied for both square butt single and double side single pass welded joints of P91 steel plate. The conclusion of the above studies are as follows-

- Compressive residual stress is observed in the fusion zone of square butt single side single pass welded joint throughout its thickness.
- Hence, it is revealed that submerged arc single side single pass welding of P91 steel endorses its unique austenitic- martensitic solid-state phase transformation during heating and cooling cycles.
- However, square butt double-side single pass submerged arc welding induced tensile residual stress in the mid thickness region of FZ, with compressive residual stresses in the top and bottom weld bead outer surfaces.
- As far as welding induced distortion is concerned, double side single pass welding induces less distortion than single-side single pass welding.
- Similar residual stress distribution has been observed for other arc welding processed P91 steel [25], [31]–[33] [36].

CHAPTER 5

THERMO-MECHANICAL ELASTIC-PLASTIC ANALYSIS OF SAW BUTT JOINTS OF P91 STEEL

5.1 Introduction

Thermomechanical elastic-plastic FE modelling and simulation of the welding process is a well-established numerical method to predict and analyse welding induced distortions and residual stresses. Therefore, this chapter describes FE modelling of submerged arc welding of P91 steel plate for square butt single and double side welded joints. The precise thermal modelling of the welding process results in accurate prediction of welding induced distortion and residual stresses. Hence, the second section explains the thermal model fitting of predicted nodal temperature results. It is observed that considering element birth & death technique, double ellipsoidal heat source model and temperature-dependent material properties lead to the high accuracy of predicted thermal results.

Further, the following sections describe the prediction of welding induced distortion and residual stress results, which consider implementing solid-state phase transformation at various stages of FE modelling. The successful modelling of solid-state phase transformation phenomenon is perceived in predicted results of welding induced distortions, and residual stresses in square butt single side single pass SAW joint. Residual stress distribution across the weld bead is explored and analysed for both square butts single and double side welded joints. Predicted distortion and residual stress results are also fairly matched with measured results.

5.2 Thermal model fitting and temperature distribution

The double ellipsoidal heat source model is considered for both single and double side welding. The constant parameters in the double ellipsoidal heat source model are physically measured for both square butt single and double side welded joint samples, listed in Table 5.1. The contour plots of temperature distribution during heating and cooling cycles of single side single pass welding are shown in Figures 5.1. The peak temperature and Gaussian distribution of temperature contour are also noticeable in the contour plots.

Table 5.1 Constant parameters for the double ellipsoidal heat source model

Parameters	a	b	c_{front}	c_{rear}	f_{front}	f_{rear}
Single sided	8	10	10	28	1.47	0.53
Double sided (top side)	7.2	5.5	8	26	1.53	0.47
Double sided (bottom side)	7.3	5.5	8	25.5	1.52	0.48

The element birth and death technique effectively replicated the addition of molten weld metal during welding, as observed in Figure 5.1 (a). The contour plot also replicates the heat distribution on heating during the welding. While Figure 5.1 (b) presents the temperature contour during the cooling cycle. The peak temperature of 1893 ^{o}C is observed in FZ of single side single pass welding.

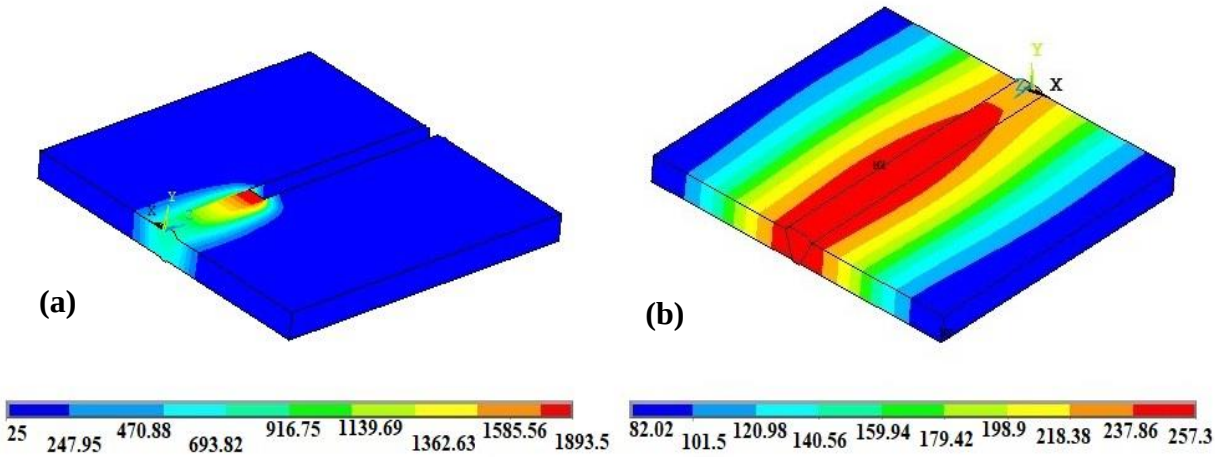

Figure 5.1 Contour plot of temperature distribution during (a) heating and (b) cooling cycles of square butt single side single pass welding

Similarly, Figure 5.2 (a) & (b) exhibit the inclusion of molten weld metal during top and bottom weld passes of double-side single pass welding. Figure 5.2 (c) shows the cooling cycle once the welding is performed. The peak temperature of 1784 ^{o}C is observed for the top side first weld pass, while the bottom side weld pass shows a peak temperature of 1860 ^{o}C. The peak temperature of the top side weld pass is slightly lower than the single side single pass weld because of less weld material per pass. However, heat from the earlier weld pass increased the peak temperature in the second weld pass.

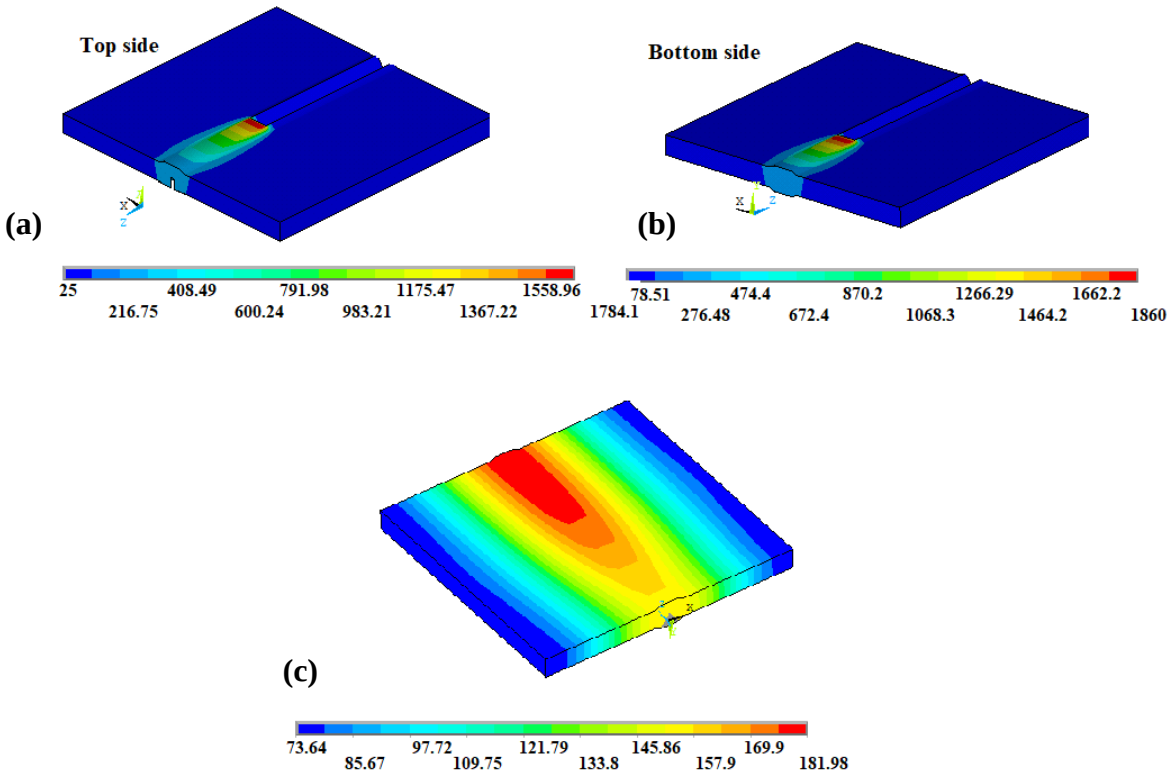

Figure 5.2 Contour plots for temperature distribution during heating in (a) top side weld pass, (b) bottom side weld pass and (c) cooling cycles of square butt double-side welding

The high thermal gradient between the weld zone and the base metal zone is the most responsible factor for inducing distortion and residual stresses in the welded structure.

The time-temperature curve and temperature contour across the weld of square butt single side single pass weld joint are shown in Figure 5.3. The thermal profile shows a predicted peak temperature of around 745 ^{o}C at a point 12 mm away from the weld centreline on the top surface of the weld plate.

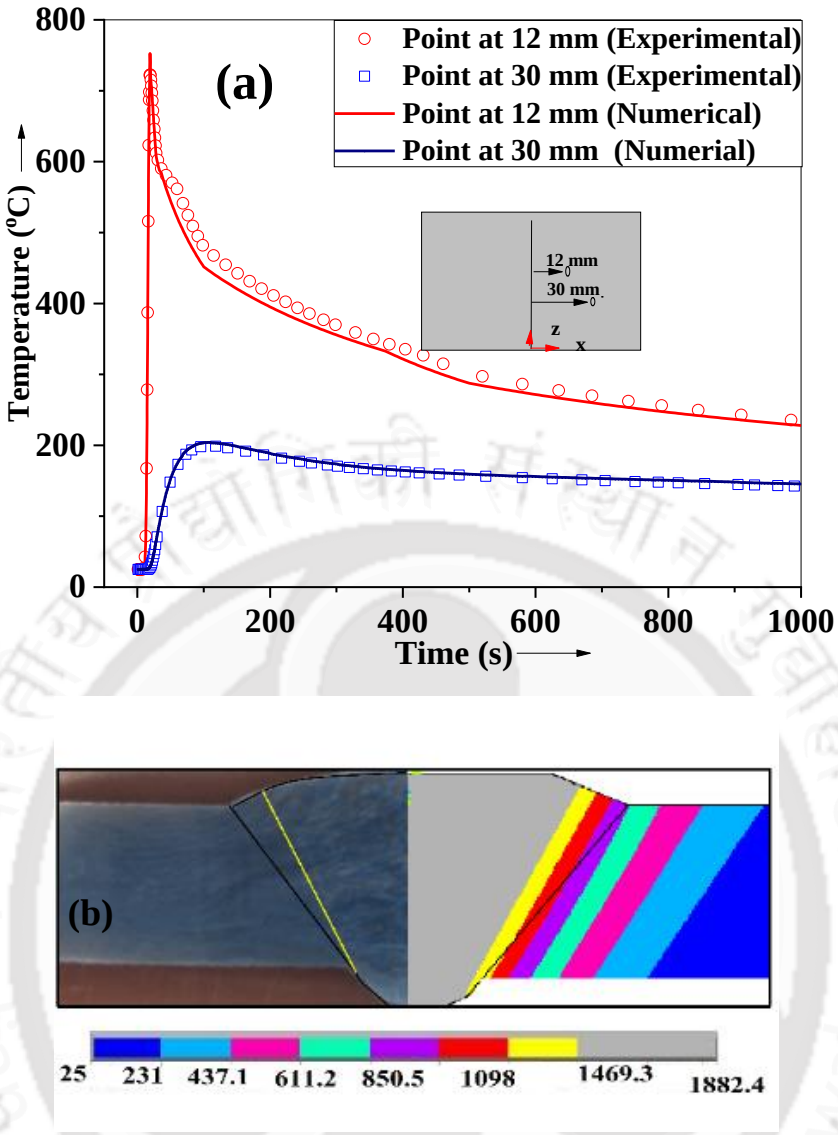

Figure 5.3 (a) Thermal profile and (b) temperature contour for square butt single side single-pass welding

This peak temperature slightly deviates by almost 3% from the measured value of 723 °C at the same point for submerged arc square butt single side single pass welded joint. Hence, the double ellipsoidal heat source model is an appropriate choice for modelling the submerged arc welding process.

Similarly, the macrograph of the square butt single side single pass welded joint adequately replicates the predicted temperature contours and precisely matching the bead shape, as shown in Figure 5.3 (b). The region below the temperature Ac_1, i.e., lower transformation temperature, represents the heat-affected zone. The rest of the region represents base metal.

Figure 5.4 presents the temperature curve and temperature contour across the weld for square butt double side single pass welding. The predicted peak temperature of 571 ^{o}C is observed at a point 14 mm away from the weld centreline for the first weld pass compared to the measured peak temperature of 557 ^{o}C on the top surface of the weld plate. Similarly, the second pass peak temperature is observed at 610 ^{o}C for the point 16 mm away from the weld centreline on the bottom surface of the plate. Hence, the predicted thermal profiles precisely replicate the measured temperature-time plot for the single and double side submerged arc welding processes.

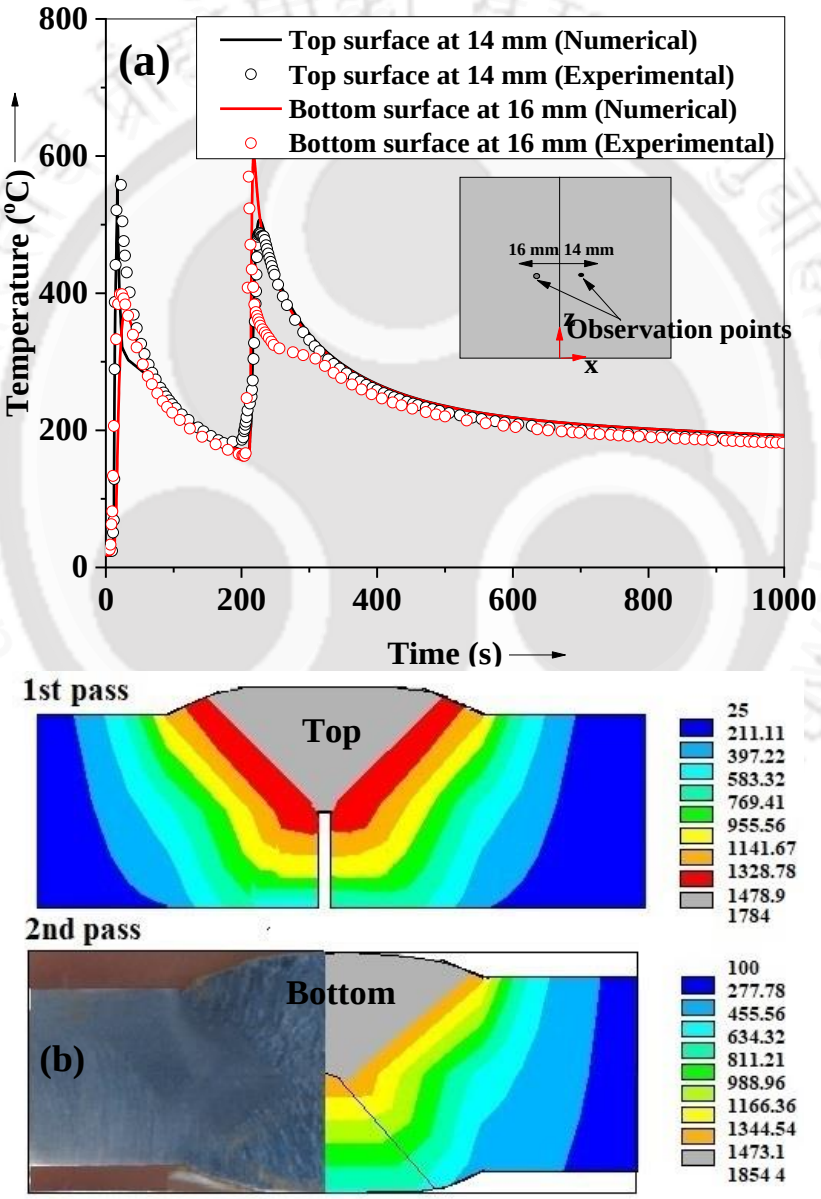

Figure 5.4 (a) Thermal profile and (b) temperature contour for square butt double side single pass welding

Figure 5.4 (b) also shows the macrograph of the top, and bottom side welds of the square butt double side single pass welded joint, which adequately replicates the predicted temperature contours and exactly matches the actual bead shape. Since the predicted temperature results are fairly comparable to the experimental results, it can efficaciously be applied as nodal temperature load in the structural analysis.

5.3 Welding induced distortion

The welding induced distortion in square butt single-side single pass weld joint is considered here to analyse the effect of solid-state phase transformation in submerged arc welding of P91 steel. The distortion patterns of angular distortion and edge deflection are shown in Figure 5.5 and Figure 5.6 below.

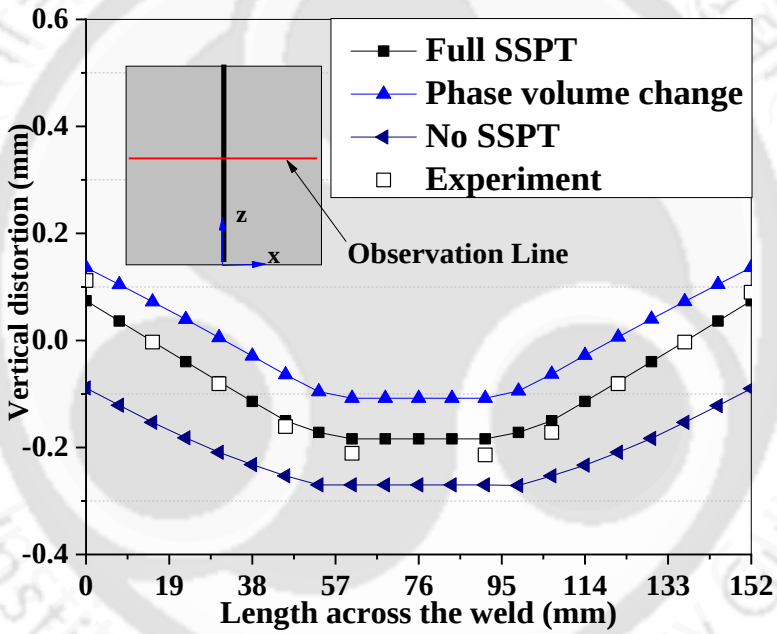

Figure 5.5 Angular distortion in the square butt single-side single pass welded joint

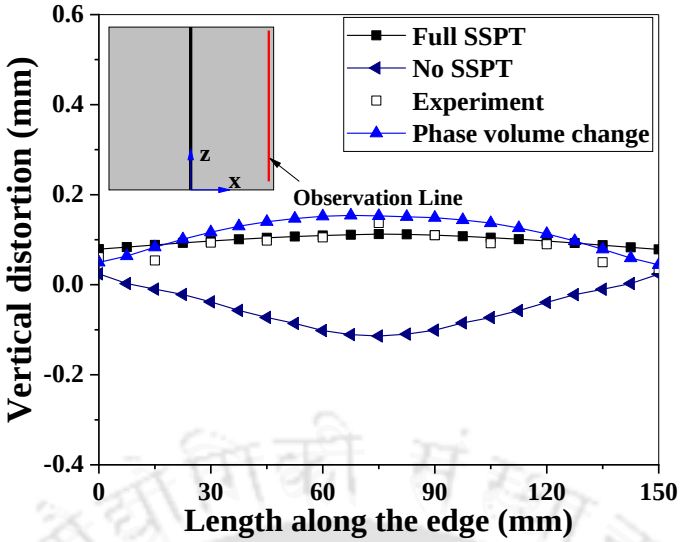

Figure 5.6 Edge deflection of square butt single-side single pass welded joint

Three conditions are considered to analyse the effect of SSPT phenomenon in P91 steel welds named as (i) no SSPT effect, (ii) only volumetric changes during SSPT and (iii) all SSPT effects (i.e., volumetric changes, transformation plasticity and microstructural changes effects). Figure 5.5 and Figure 5.6 show that the predicted distortion results significantly deviate from the experimental results for no SSPT effect. The edge deflection is observed to be concave, which is opposite to experimental results, as observed in Figure 5.6. Consequently, the vertical distortion value at the mid edge point also decreased by a large margin, as observed in Figure 5.5 and Figure 5.6. The predicted distortion value of -0.07 mm at the mid edge point deviates from 0.12 mm distortion value measured for single side single pass square butt joint of P91 steel.

However, implementing volumetric changes due to SSPT shapes up the distortion results to match the actual edge deflection pattern of actual weld joint sample, as observed in Figure 5.6. However, it over predicted the angular distortion and edge deflection results, as observed in Figure 5.5 and Figure 5.6.

Finally, the microstructural change-induced yield strength and transformation induced plasticity effect during SSPT are also included in FE modelling. These collectively improved the accuracy of distortion results. The predicted vertical distortion value at the mid edge of the welded plate reaches the value of ~ 0.1 mm, much closer to the measured value of 0.12 mm, i.e., by a difference of 1.7%. Similarly, the predicted vertical distortion values at one of the ends of the edge is observed as 0.08 mm, close to the measured value of 0.07 mm. Hence, the

predicted results are close enough to measured distortion values at the mid and endpoints of the weld plate's edge. However, the predicted results matched the experimental measured distortion across the plate edge and the weld centreline.

The contour diagram of all three modelling cases, i.e., without SSPT, volume changes due to SSPT and full SSPT effects are shown in Figure 5.7, Figure 5.8 and Figure 5.9, respectively.

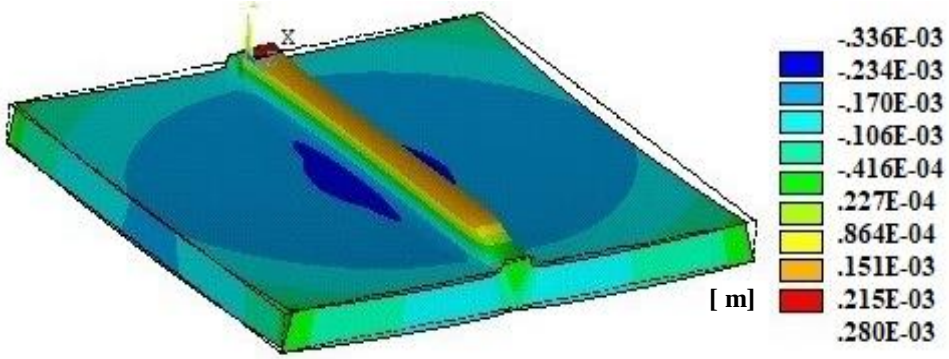

Figure 5.7 Vertical distortion contour in square butt single-side single pass welded joint (no SSPT)

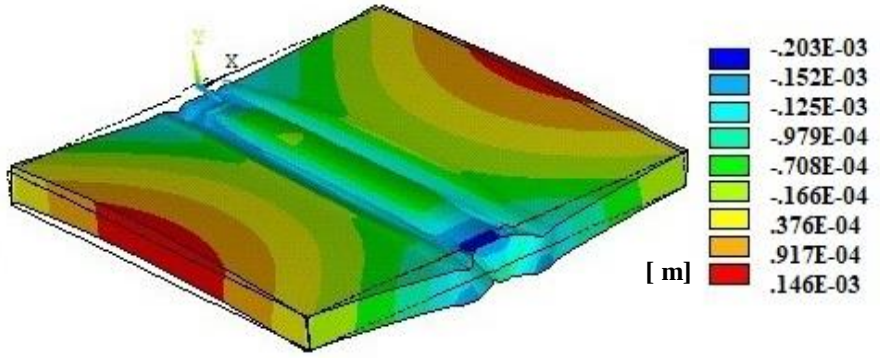

Figure 5.8 Vertical distortion contour in square butt single-side single pass welded joint (only volume change)

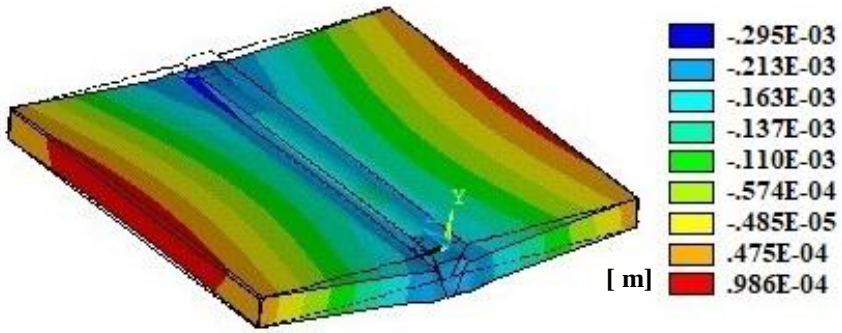

Figure 5.9 Vertical distortion contour in square butt single-side single pass welded joint (full SSPT effects)

The concaveness of the plate edge is noticeable in Figure 5.7 for the modelling case without considering the SSPT phenomenon. Whereas the SSPT induced volumetric changes to show a significant change in the distortion pattern, as shown in Figure 5.8. Hence, it is observed that considering SSPT enhances the prediction accuracy by providing more relevant results.

Therefore, FE modelling of square butt double-side single pass weld joint is performed considering full SSPT effects. The contour diagram of vertical distortion in the square butt double-sided single pass weld joint is also shown in Figure 5.10 below.

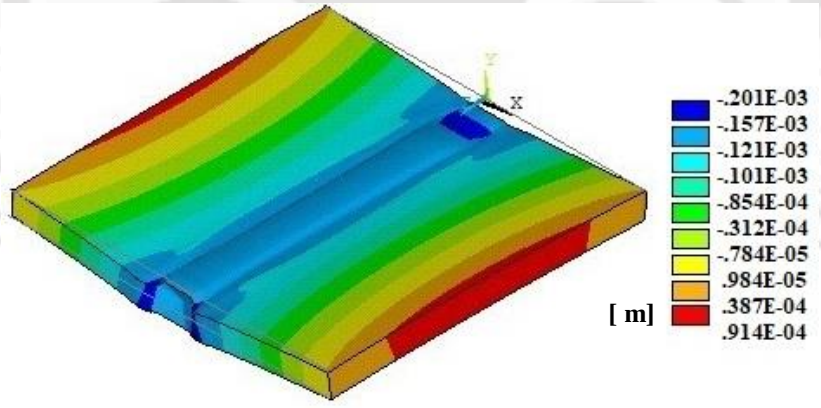

Figure 5.10 Vertical distortion contour in square butt double-side single pass welded joint (full SSPT effects)

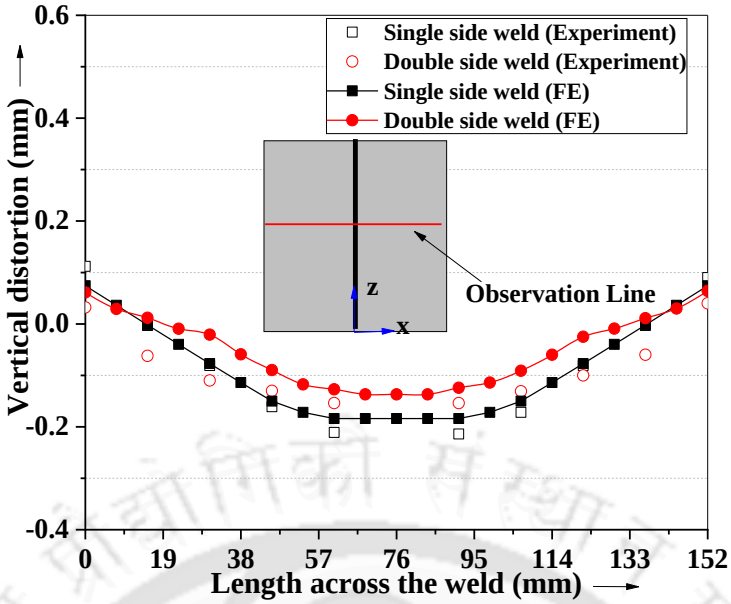

Figure 5.11 Angular distortion in square butt single and double-side single pass welded joints

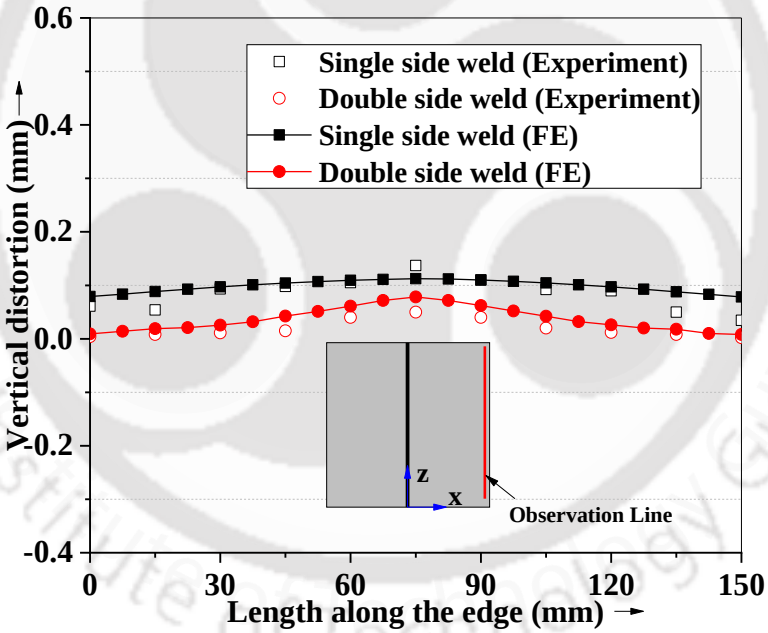

Figure 5.12 Edge deflection in square butt single and double-side single pass welded joints

The predicted distortion pattern also reasonably matches the experimentally measured results in the square butt double side single pass welded joint. Double side single pass welding reduced the welding induced distortion values, which are also observed in Figure 5.11 and Figure 5.12.

5.4 Welding induced residual stress

As DHD measurement was performed in FZ and HAZ of square butt single-sided single pass welded joint, the predicted residual stresses within the measurement region (i.e., 3 mm hole diameter) must be considered for comparison. Moreover, the DHD technique measures the residual stress values developed after the stress relaxation in the trepanned core region of 12 mm diameter, as explained in methodology section 3.4.1. Hence, the nodal residual stress values of all the nodes within the trepanned core region are selected to calculate the average value of residual stress at each thickness. Finally, it represents the predicted residual stress value comparable with the experimentally measured residual stress values.

Square butt single side single pass weld joint model is considered here to analyse the effect of solid-state phase transformation in FE modelling as discussed below-

5.4.1 Effect of SSPT phenomenon in residual stress distribution

The contour plots for longitudinal residual stress distribution in single-side single pass square butt joint are shown in Figure 5.13 for the weld joint model with and without considering SSPT effects.

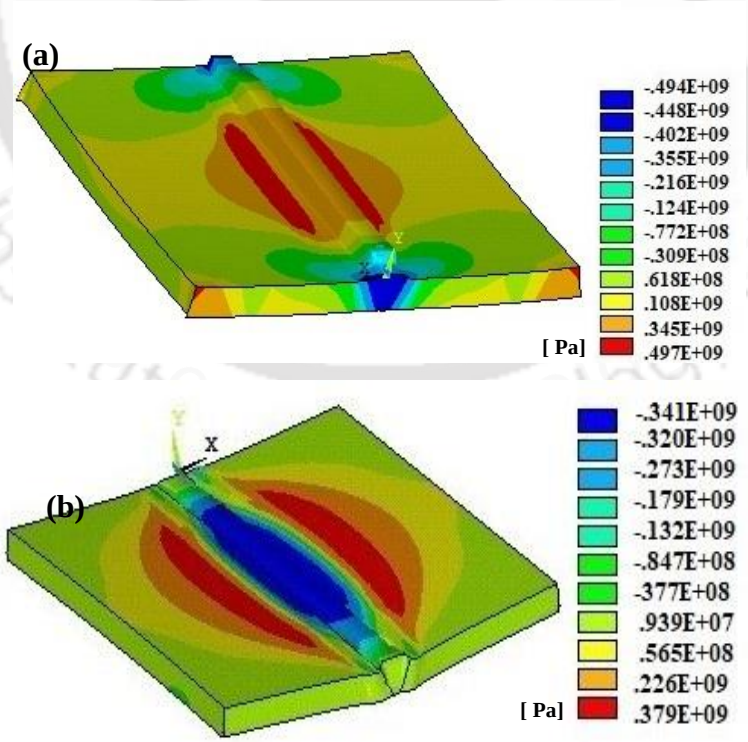

Figure 5.13 Longitudinal residual stress distribution in square butt single-side single pass welded joint models (a) without considering SSPT (b) considering full SSPT effects

Figure 5.13 (a) shows that without the SSPT phenomenon, the quasi-static region of the weld joint model expectedly developed tensile residual stress. Though, the HAZ region unexpectedly shows tensile peak value. The steel (like austenitic steel) with no solid state phase transformation phenomenon also exhibits similar residual stress distribution [150], [151]. In contrast, the contour plot in Figure 5.13 (b) shows that the whole quasi- static weld region developed compressive residual stress in the P91 steel weld. However, the start and end regions show tensile residual stress. Consequently, the HAZ region shows tensile residual stress distribution. Figure 5.14 presents the residual stress distribution across the weld centreline to understand and differentiate the SSPT effect.

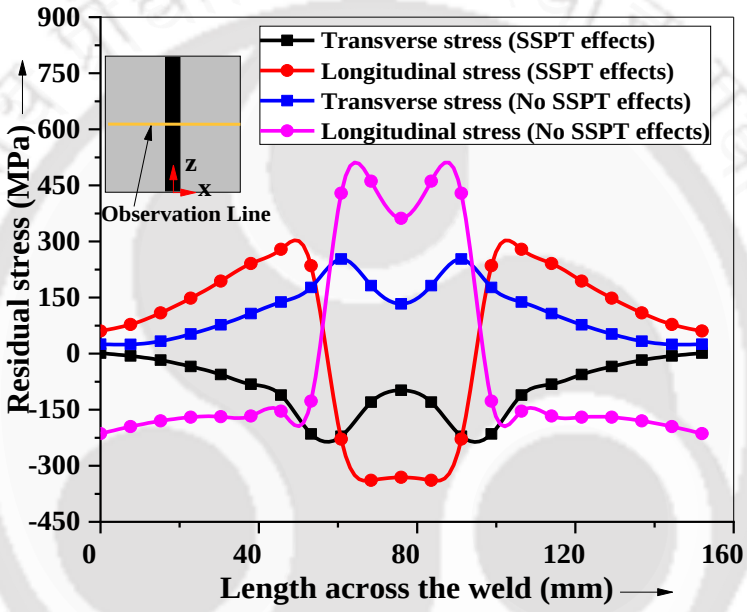

Figure 5.14 Residual stress distribution across the weld in square butt single side single pass welded joint models

P91 steel weld shows compressive residual stress in the weld region and tensile stress in the nearby region between weld and base metal. Maduraimuthu et al. [44] also observed a similar residual stress distribution (i.e. compressive peak of about -275 MPa in the FZ region) across the weld on the top surface for square butt single pass activated TIG welding of P91 steel plate.

5.4.2 Residual stresses in square butt single and double-side welded joint models

Figure 5.15 presents the longitudinal residual stress along the weld centreline in the FZ and along an observation line in HAZ of square butt single-side welded joint similar to DHD measurement. The predicted results in the plot are the average value of longitudinal residual stress within the trepanned core region (i.e. 12 mm diametral region of the trepanned core

around the reference hole). Figure 5.15 shows that the predicted results are quite comparable and reasonably matches the measured results. However, the weld bead top crown region shows compressive peak values while bottom bead crown shows lower tensile or compressive residual stress. The possible reasons for lower tensile or lower compressive residual stress in bottom bead crown may be less volumetric expansion under martensitic transformation and dominance of the volumetric shrinkage effect during cooling. The predicted results vary with a slight difference in the maximum value of compressive residual stress at thickness 4 mm (from the weld bead top surface) is observed as -169.1 MPa. The corresponding measured value is -118 MPa.

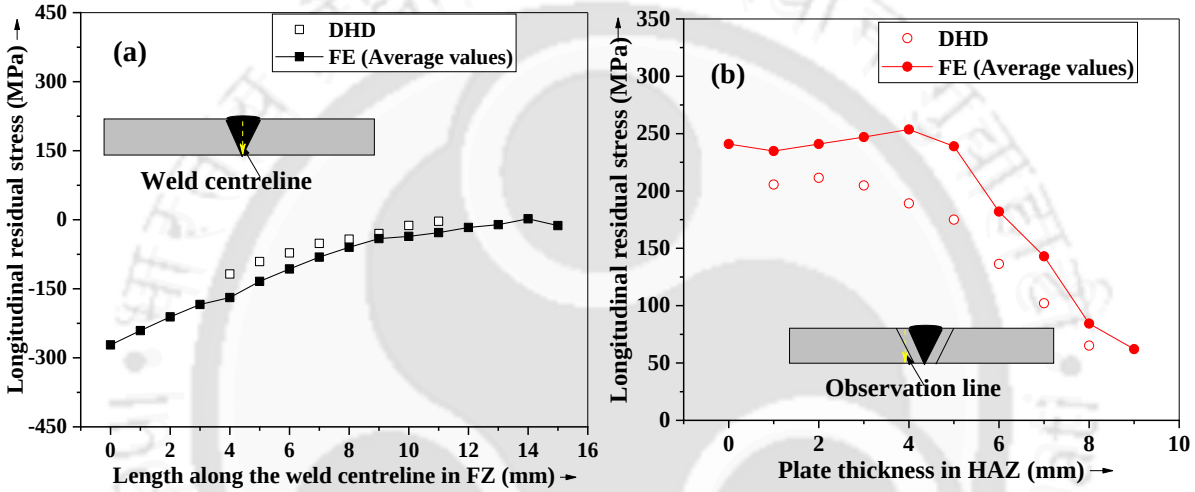

Figure 5.15 Longitudinal residual stress distribution in (a) FZ taken at 25 mm away from the starting end of the weld bead and (b) HAZ of square butt single-side single pass welded joint

However, the predicted results are reasonably matching the measured results for the bottom side points. The weld bead top and bottom crowns region show higher peaks of compressive residual stresses. The comparatively faster cooling rate in top and bottom bead regions induces the martensitic transformation while cooling, resulting in volumetric expansion and compressive residual stress. The stress distribution in HAZ also matches the residual stress distribution pattern similar to the measured results. However, the point values show some significant deviation within the thickness range of 3-5 mm. The minimum prediction error for longitudinal residual stress in FZ of square butt single side single pass weld joint is 9.5% at the 9 mm thickness.

Figure 5.16 shows the cross-sectional view of the longitudinal residual stress contour in the FZ. The section is taken within the DHD measurement region in FZ (explained in section 4.5.1)

after removing weld bead top and bottom crowns, i.e., within the plate thickness range from 1 mm to 9 mm. It also reveals compressive residual stress throughout the thickness in the FZ of single-pass single side SAW welded butt joint, which is similar to low tensile or compressive residual stress distribution in single side single-pass laser-welded 10 mm thick P91 steel plate as observed by Kumar et al. [36].

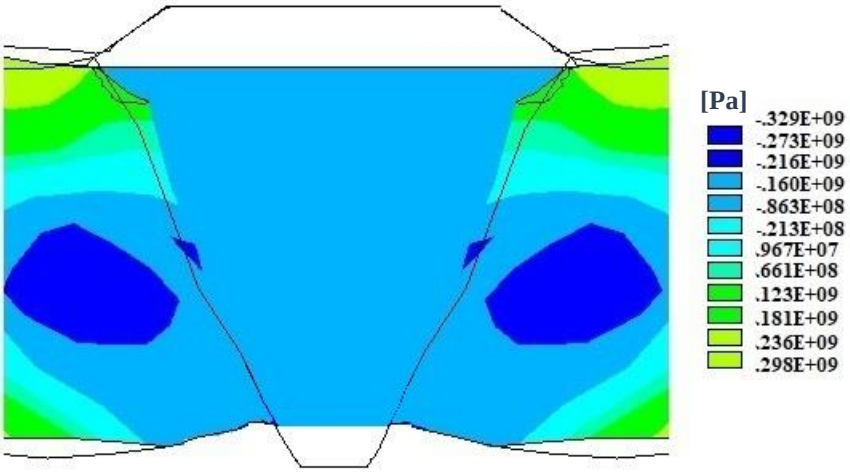

Figure 5.16 Cross-sectional view of longitudinal residual stress contour in the FZ of square butt single-side welded joint of the section taken parallel to reference hole perpendicular to weld centreline similar to DHD measurement

The residual stress values in the FZ region are close enough to the measured results. Though, it does not match precisely because it is not equivalent to the average value of nodal residual stress values. Figure 5.17 shows the predicted and measured longitudinal residual stress in the FZ of the square butt double-side single pass welded joint.

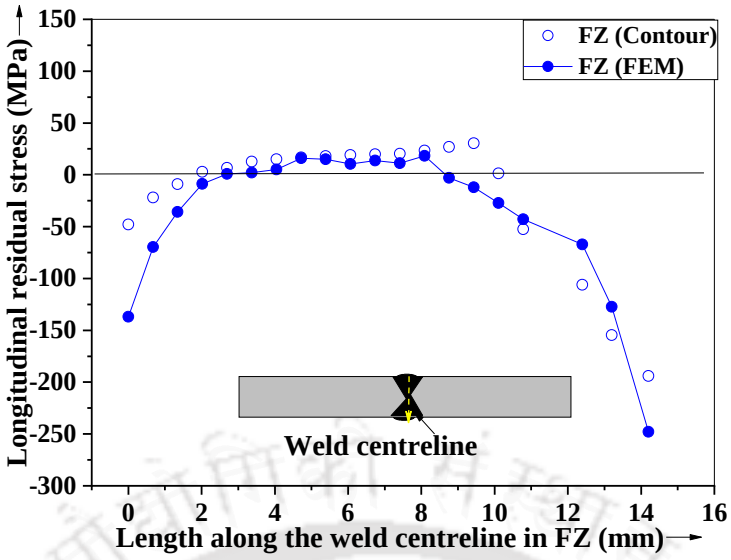

Figure 5.17 Longitudinal residual stress along the weld centreline in the FZ of square butt double-side single pass welded joint

It reveals tensile residual stress in the mid thickness region of the weld fusion zone, similar to measured results. However, the lower half of the mid thickness range between 5- 11 mm of the square butt double-side single pass welded joint model shows compressive residual stress of lower magnitude, which slightly deviates from the experimental results. Both top and bottom regions observe compressive residual stress with maximum predicted values of -122 MPa and -214.2 MPa, respectively. However, the measured residual stress values for the same points in the top and bottom regions are -58.9 MPa and -193.1 MPa. However, the residual stress values within the thickness region 2- 9 mm, fairly matched the experimental results. The minimum prediction error for longitudinal residual stress in FZ of square butt double side single pass weld joint is 4.2% at the thickness of 4.7 mm. Hence, the overall distribution of predicted longitudinal residual stress along the weld centreline in FZ of square butt double side welded joint replicates the measured spatial distribution of longitudinal residual stress in the fusion region on the cut surface.

5.5 Summary

This chapter discussed the finite element modelling of submerged arc square butt single and double side single pass welded joints of P91 steel. In finite element modelling, the focus is given to heat source modelling, element birth and death technique, temperature dependency of material properties and unique properties of austenite- martensite solid-state phase transformation in P91 steel. The following observations are made from the above studies:

- The volumetric changes under the SSPT phenomenon show a significant contribution in precise FE modelling of solid-state phase transformation in P91 steel welds.
- It is also revealed that microstructural changes and transformation plasticity induced changes during SSPT have an essential role in the overall accuracy of predicted results.
- However, the volumetric changes owing to the SSPT phenomenon under predict the residual stress distribution for higher compressive peak in FZ of the single side single pass weld.
- The predicted thermal results fairly matched with the experimental results. However, without considering the SSPT phenomenon, the finite element model over predicts the residual stress (tensile stress in weld bead region) results and under predicts the distortion results.
- The quasi-static weld bead region in square butt single side single pass submerged arc welded joint exhibited compressive longitudinal and transverse residual stress distribution.

CHAPTER 6

FE ANALYSIS OF PRE, IN AND POST-WELD HEAT TREATMENTS PROCESS FOR THEIR MITIGATION EFFECTS ON SAW BUTT JOINTS OF P91 STEEL

6.1 Introduction

The welding induced residual stresses and distortions must be mitigated to prevent catastrophic failure and improve the fatigue life of the weld joint. Hence, this chapter discusses mitigation techniques to control welding induced residual stresses and distortions in submerged arc welded joints of P91 steel. It includes a comparative study of different mitigation steps at different welding stages, i.e. before, during, and after.

Thermo-mechanical elastic-plastic finite element modelling is widely known to simulate different heat treatment processes [152] effectively. Therefore, this chapter performs FE analysis of pre, in and post welding mitigation heat treatments on square butt single side single pass welded joint to observe and compare their mitigation effects. The phase transformation effect of P91 steel is successfully applied in the FE modelling of all the mitigation processes. Hence, the mitigation effects of each heat treatment are explained in further sections. Section 6.2 explains pre-welding mitigation, which comprises preheating of base metal region near the root gap at a fix temperature range. Similarly, sections 6.3-6.5 explain in- process mitigation heat treatments (i.e., side heating, heat sinking, hybrid combined side heating and heat sinking), which regulate the temperature gradient, heating and cooling intensity and rate of heating & cooling during the welding process. At last, section 6.7 presents the mitigation effect of post-weld heat treatment on P91 steel welds. The post-weld heat treatment process is efficiently modelled for specific heating rate, heating temperature, holding time, cooling rate etc. to assess their degree of mitigation on welding induced residual stresses.

6.2 Effect of preheating

The process parameters similar to the experiment mentioned are taken for the square butt single side single pass weld joint model for both the cases with and without preheating. The predicted thermal profiles are plotted for two nodal points during the preheating process, one at the plate's edge near the root gap (Region 1) and another in the preheating region (Region 2) on the plate's

top surface. The time-temperature profiles for the welding process with and without preheating are shown in Figure 6.1. The thermal profile in the preheating region shows that the initial temperature in the region increased by 200- 250 oC, which decreases the thermal gradient in the transverse direction of the weld region. It is observed that the peak temperatures of welding increased to 1904 ^{o}C (Region 1) and 521 ^{o}C (Region 2) after preheating, compared to peak temperatures of 1823 ^{o}C (Region 1) and 361 ^{o}C (Region 2) for welding without preheating. Preheating raises the localised temperature near the welding region, which reduces the difference between the surrounding temperature and the peak temperature of welding. Figure 6.2 presents the temperature contour plots of the square butt joint model for the welding process with and without preheating. It presents a descent in the thermal gradient across the weld region after preheating. Hence, it affects the magnitude of thermal expansion or contraction for the same thermal expansion coefficient value.

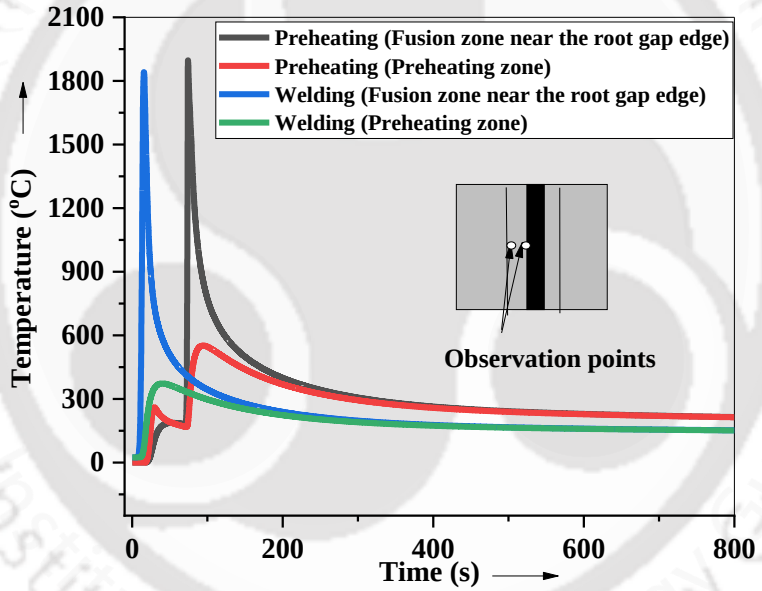

Figure 6.1 Time-temperature profile for preheating followed by single pass single side welding

It is also observed that preheating slowed down the cooling rate of the welding process. The slow cooling rate influences the martensitic transformation, which affects the volumetric contraction or says welding induced distortion and residual stresses.

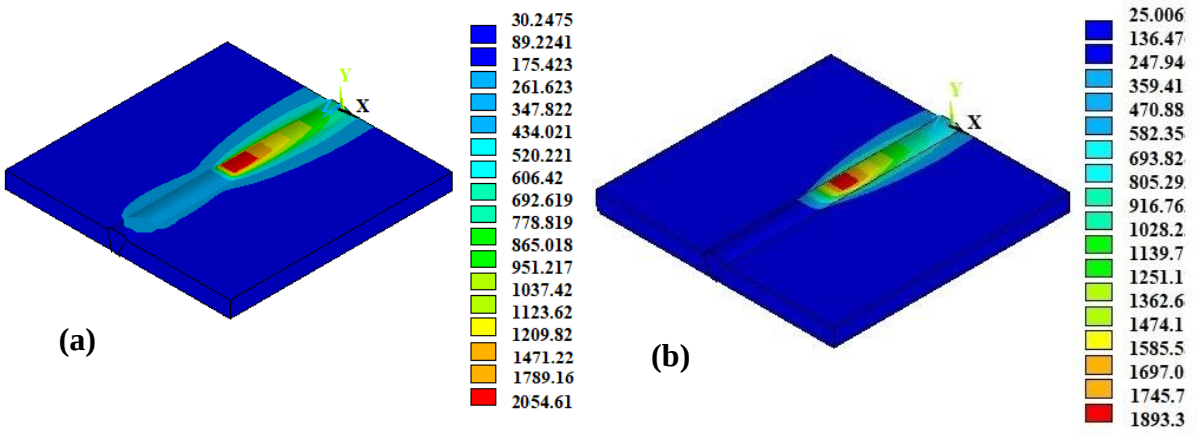

Figure 6.2 Contour plot of temperature distribution during square butt single side single pass welding (a) with preheating, (b) without preheating

The angular distortion and edge deflection in preheated square butt single-side single pass welded joint is shown in Figure 6.3 and Figure 6.4, respectively. The effect of implementing solid-state phase transformation is also observed in Figure 6.3 and Figure 6.4.

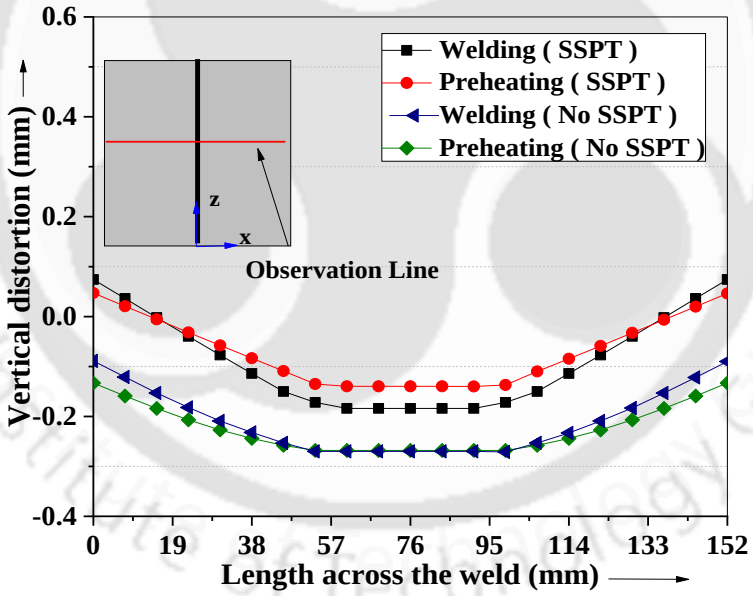

Figure 6.3 Angular distortion in the transverse direction

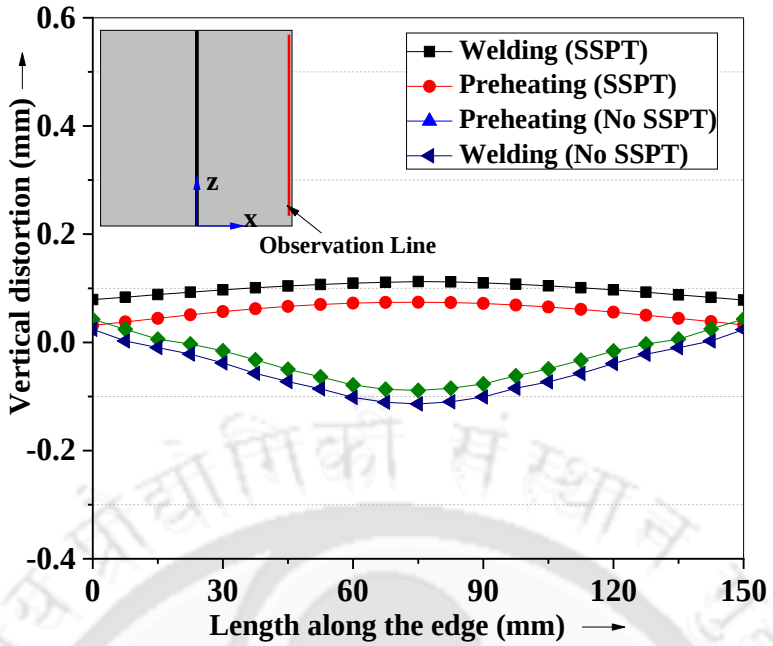

Figure 6.4 Edge deflection in the welding direction

Preheating reduces the vertical distortion value from 0.12 mm (measured) to 0.07 mm at the mid edge point on the top surface of the plate, i.e., by 44%. Simultaneously, the edge deflection value at both ends of the plate edge reduced from 0.07 mm (measured) to 0.024 mm (predicted), i.e., by 60%. However, the edge deflection pattern at the edge remained the same. The angular deformation angle was also reduced from 0.23º (measured) to 0.143º for preheated single-side welded butt joint model.

The preheating effect is also quite noticeable from the vertical distortion contour plots, as shown in Figure 6.5.

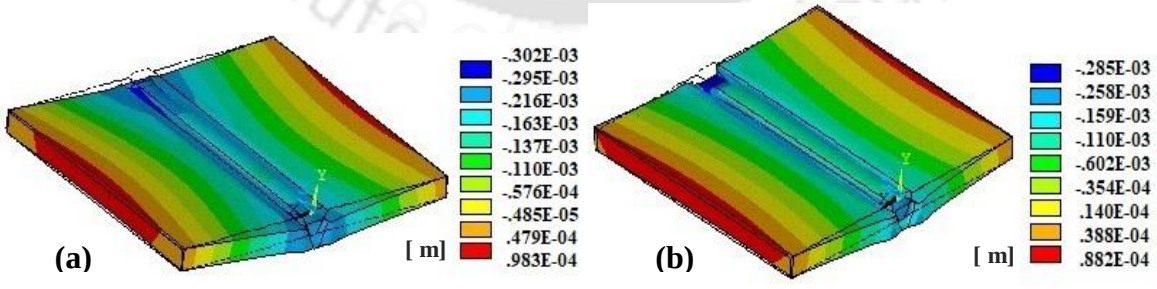

Figure 6.5 Vertical distortion contour of **(**a) as-welded (b) preheated square butt single side single pass welded joint models

Figure 6.5 also shows that the distortion pattern is the same for both as-welded and preheated square butt single side single pass weld joint model with a difference in distortion value. Therefore, preheating is a promising mitigation method in reducing welding-induced distortions.

The contour plots of longitudinal residual stress distribution in as-welded and preheated square butt single side single pass weld joint models are shown in Figure 6.6. It is observed that preheating reduces the residual stress values in the weld and its localised region. It also decreases the magnitude of tensile residual stress in the region between the base metal and weld bead, which can also be observed in the contour diagram as shown in Figure 6.6.

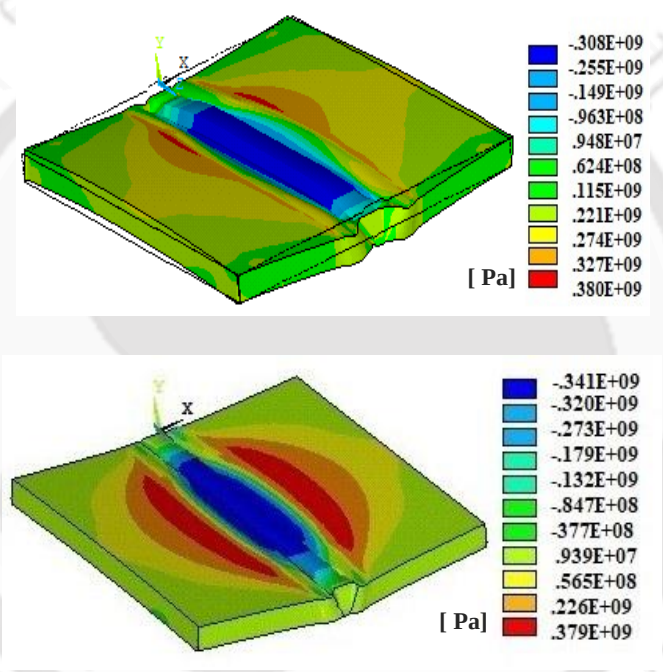

Figure 6.6 Contour plot of longitudinal residual stress distribution for (a) preheated, (b) as-welded square butt single side single pass welded joint models

Figure 6.7 presents the longitudinal residual stress values on the top surface across the welds' weld centreline. The magnitude of compressive residual stress decreases in the weld region because of the increase in overall temperature and decrease in cooling rate. Similarly, the magnitude of tensile residual stress decreases in the HAZ region. Hence, the preheating expectedly shows a modest mitigation effect on residual stress distribution as observed in published works [14].

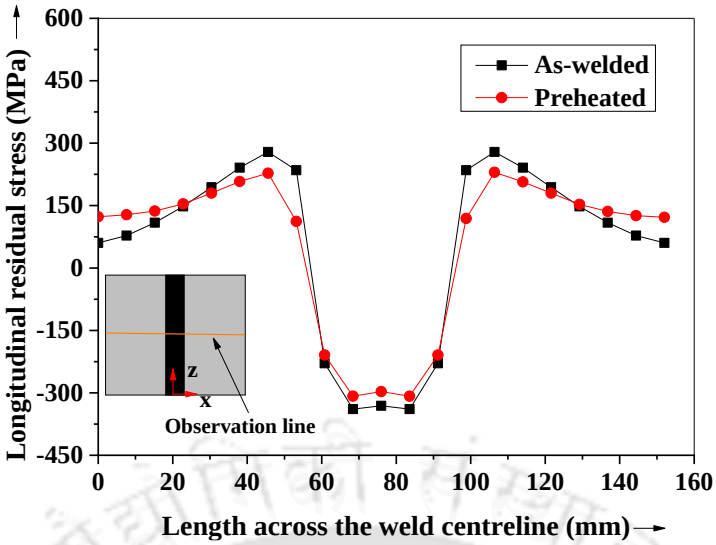

Figure 6.7 Longitudinal residual stress in as-welded and preheated square butt single side single pass welded joint models

6.3 Effect of in-process mitigation heat treatments

The in-process mitigation heat treatments involve transient side heating, heat sinking and combined side heating & heat sinking, as explained in the methodology section. These mitigation heat treatments are modelled and analysed along with submerged arc welding of square butt single-side single-pass P91 steel plate. The modelling is performed with and without solid-state phase transformation phenomenon to understand and compare its effect. The process parameters for the square butt single side single pass welding model are taken similar to the experiment performed given in and kept the same for all the in-process mitigation (i.e., side heating, heat sinking and combined side heating & heat sinking) cases.

6.3.1 Thermal results

The thermal profile and temperature contour of all the three in-process mitigation heat treatment conditions are discussed in the subsequent sub-sections, which are as follows:

6.3.1.1 Transient side heating

The side heating temperatures must be below the lower transformation temperature of P91 steel, i.e. Ac_1. Hence, the three side heating temperatures are taken for the current study as 350 ^{o}C, 500 ^{o}C and 650 ^{o}C. Figure 6.8 shows the thermal profile of transient side heating for the two observation points on a top surface of the plate in the fusion zone and side heating zone.

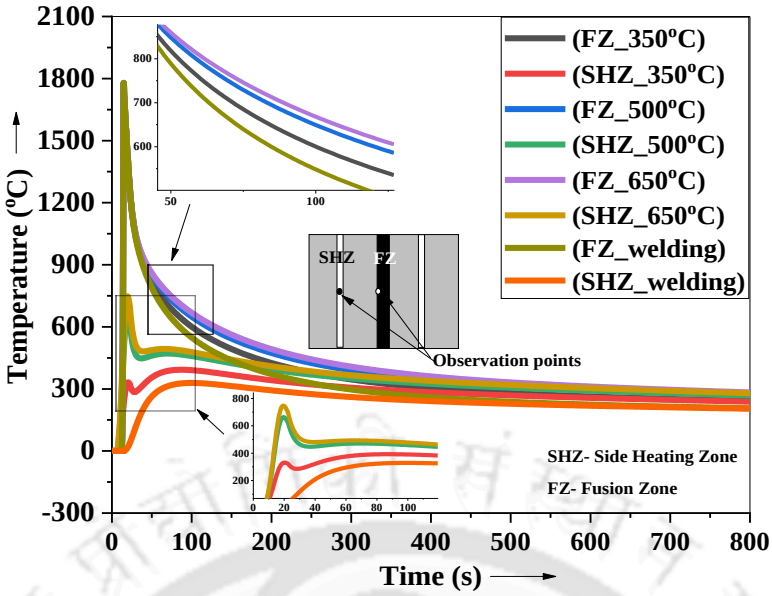

Figure 6.8 Thermal profile for transient side heating with square butt single side single pass welding of P91 steel plate

The enlarged view of thermal profiles of cooling stage reveals that the temperature graph is elevated with side heating, which signifies that side heating decreases the cooling rate. The side heating region's thermal profile reveals that side heating causes an apparent sudden rise in the localized temperature, which subsides the thermal gradient across the weld region in the transverse direction. Figure 6.8 also reveals that both thermal gradient and cooling rate decrease with an increase in heating intensity. Figure 6.9 show the temperature contour across the weld on the top surface of the weld plate during welding with and without side heating processes.

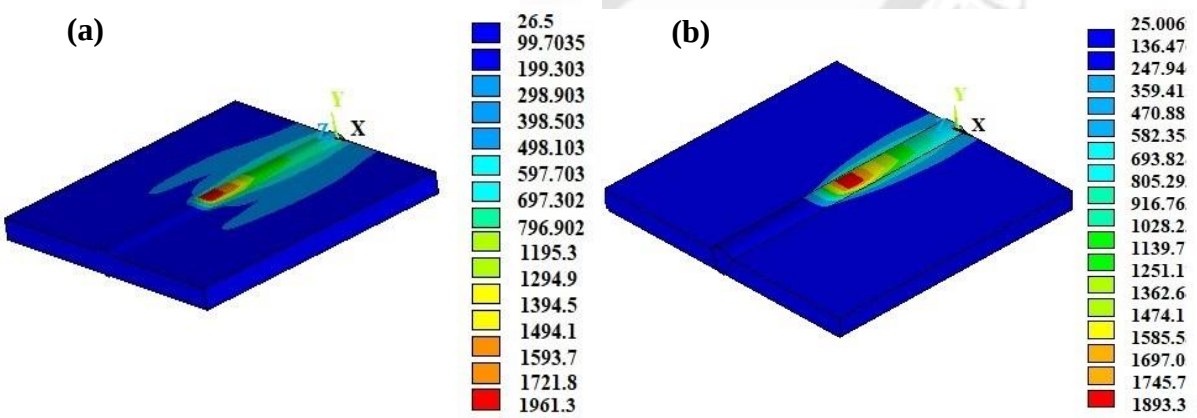

Figure 6.9 Contour plot of temperature distribution during square butt single side single pass welding of P91 steel plate (a) with side heating, (b) without side heating

The change in thermal gradient in the transverse direction of weld bead and change in peak temperatures in the regions are pretty noticeable. The peak temperature of welding also increased by a slight difference from 1893 ^{o}C to 1961 ^{o}C.

6.3.1.2 Heat sinking

The effect of heat sinking is assessed for different convective heat transfer coefficient values. Figure 6.10 presents the thermal profile for in-process heat sinking for different convective heat transfer coefficient values.

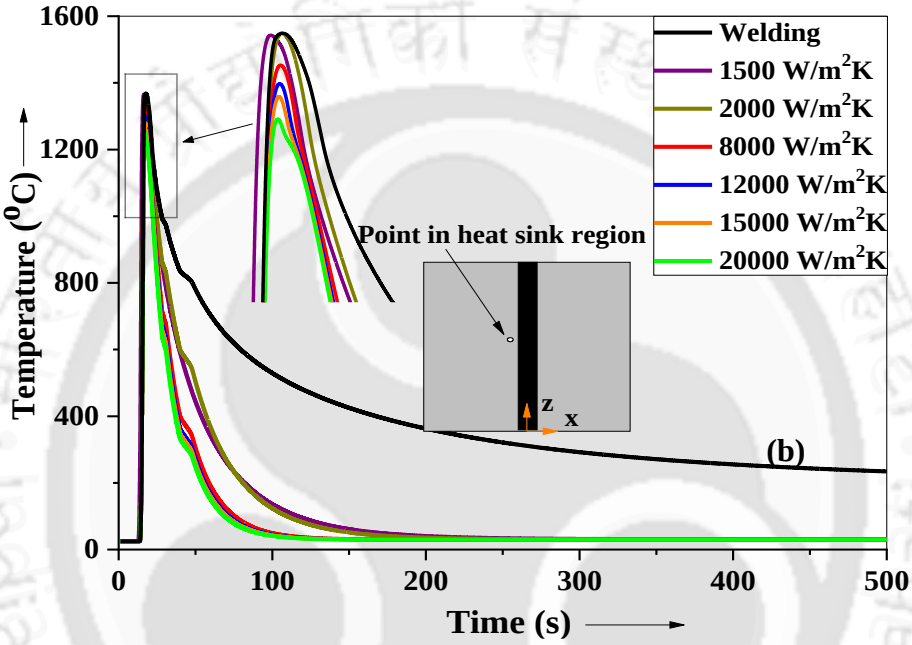

Figure 6.10 Thermal profile for heat sinking beneath the root gap in square butt single side single pass welded P91 steel plate

Intense heat sinking causes a sudden drop in the cooling cycle thermal profile, which increases the cooling rate. It also causes a sudden drop in the thermal gradient within the weld region. The weld region's peak temperature dropped by some extent for higher values of convective heat transfer coefficient. The thermal profile became narrower for heat sinking cases, which indicates faster cooling. It also indicates that the weld plate stays at a high temperature for a short duration.

Figure 6.11 present the temperature contour on the plate's top surface for welding with and without heat sinking. It reveals a contraction in the front and rear part of the heating cycle's temperature contour, which shows the cooling effect of heat sinking. Heat sinking diminished

the peak temperature from 1893 ^{o}C to 1658 ^{o}C for heat sink cases with convective heat transfer coefficient value (h= 20000 W/m^{2}k).

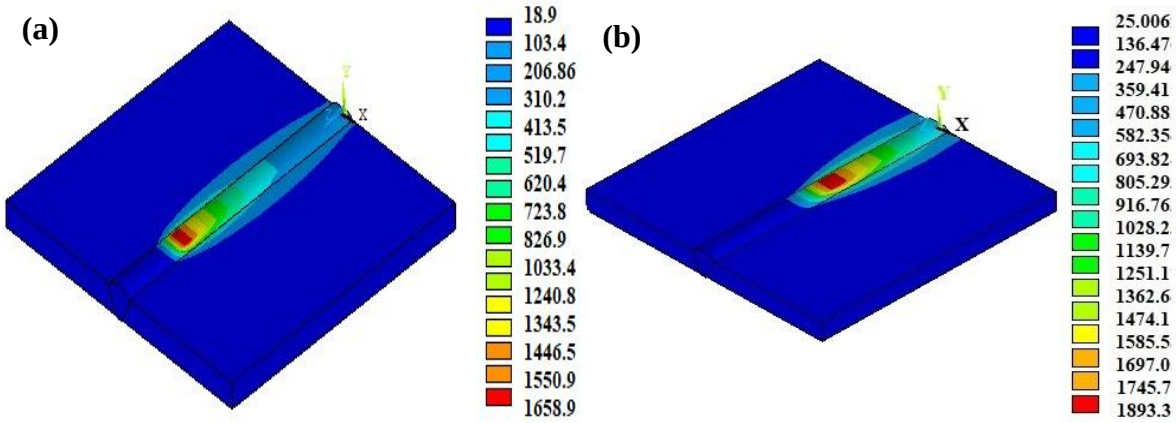

Figure 6.11 Contour plot of temperature distribution during submerged arc square butt single side single pass welding (a) with heat sinking, (b) without heat sinking

6.3.1.3 Combined transient side heating and heat sinking

Figure 6.12 presents the thermal profile of four different cases: welding without in-process mitigation; welding with side heating (region at 30 mm from weld centreline); welding with the heat sink (h = 20000 W/m^{2}K), and welding with combined side heating and heat sink.

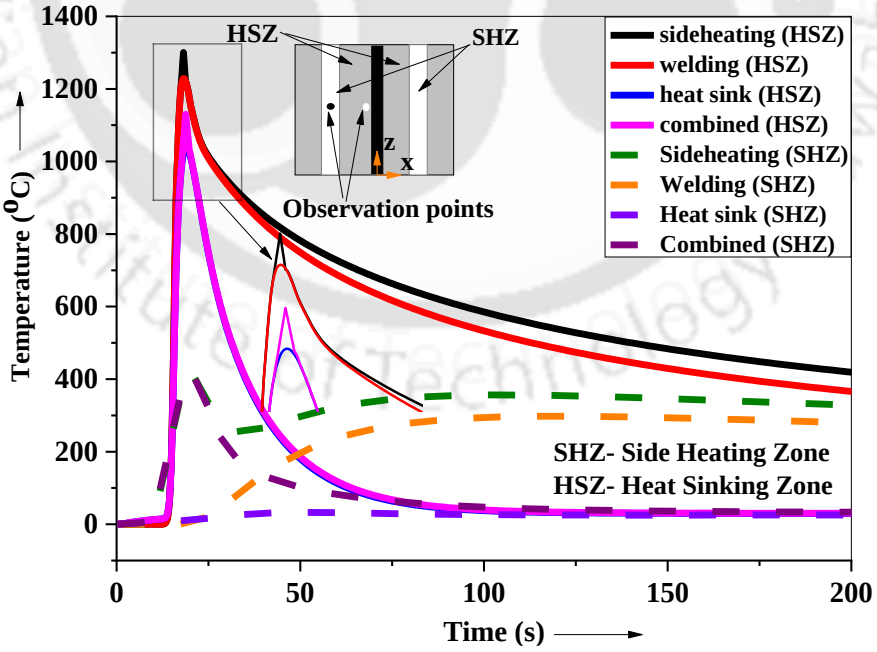

Figure 6.12 Thermal profile for combined side heating and heat sinking in square butt single side single pass welding of P91 steel plate

Two observation points are selected in the heat sink region near the FZ and side heating region to trace the change in temperature w.r.t time. The enlarged view of peak temperature reveals that the peak temperature slightly increased from 1250 ^{o}C to 1297 ^{o}C after side heating, and the cooling rate decreased. On the other hand, the heat sink causes a decrease in the peak temperature from 1250 ^{o}C to 1134 ^{o}C for the same point and the cooling rate increases. The heat sink effect prevails the side heating effect for cooling rate in combined side heating and heat sinking heat treatments. In contrast, side heating dominates the heat sinking effect to diminish the thermal gradient between the side and weld regions.

6.3.2 Welding induced distortion

Figure 6.13 presents the FE predicted angular distortion pattern for as-welded and different mitigation heat treatments cases without considering the SSPT phenomenon. It is observed that transient side heating effectively reduces the vertical distortion value, which is noticeable in Figure 6.13. However, the angular distortion pattern remains unchanged. On the other hand, heat sinking increased the angular distortion angle from 0.12^{o} to 0.26^{o}. The combined transient side heating and heat sink are also ineffective in controlling welding induced angular distortion value and pattern.

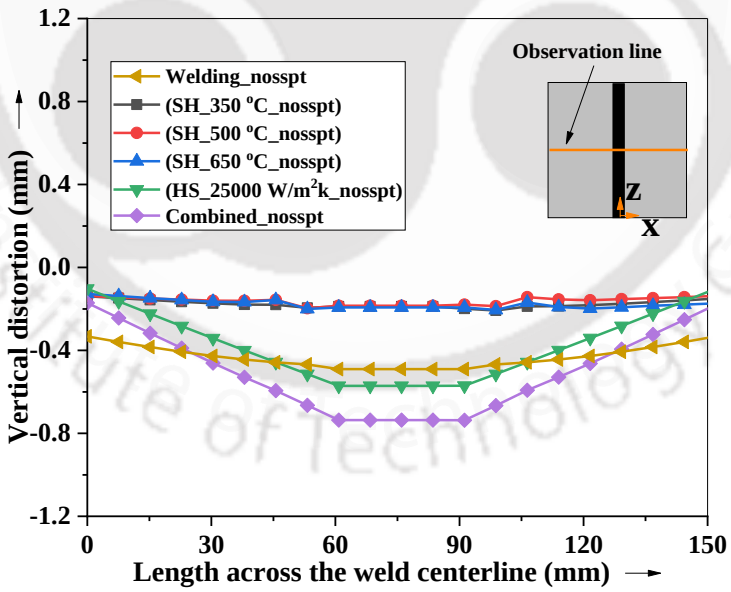

Figure 6.13 Angular distortion for different cases of in-process mitigation heat treatments in square butt single side single pass welded joint models (without considering SSPT effect)

Figure 6.14 presents the angular distortion pattern for as-welded and all the mitigation cases, considering the SSPT phenomenon.

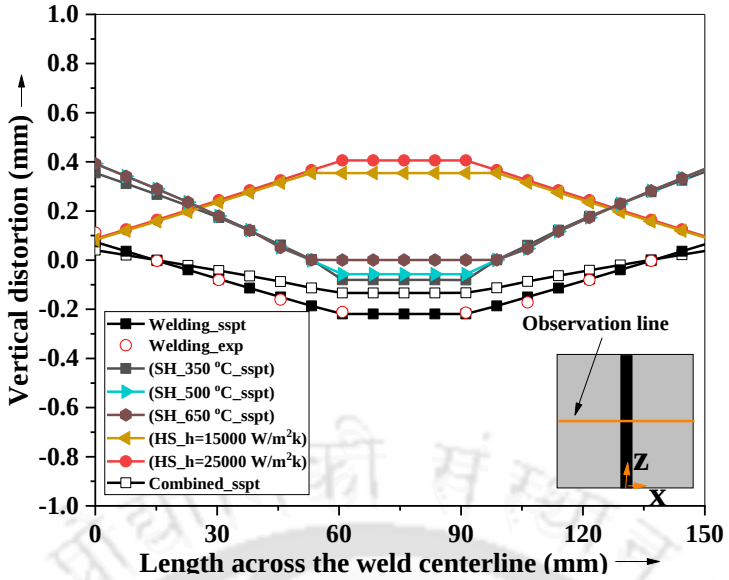

Figure 6.14 Angular distortion for different cases of mitigation heat treatments in square butt single side single pass welded joint models (considering SSPT effect)

Both side heating and heat sinking are found less effective in reducing the distortion values. In transient side heating, the region near the heating area experiences thermal expansion under direct heating effect and brings more distortion near the plate's edge [153]–[155], as observed from Figure 6.14. In heat sinking, the concave pattern of angular distortion changed to a convex pattern owing to localised volumetric contraction under intense cooling[156]. Nonetheless, the combined transient side heating and heat sinking showed a modest mitigation effect by decreasing the vertical distortion value by almost 50% in the weld bead region, decreasing the angular deformation angle from 0.23 ^{o} (measured) 0.133 ^{o}. It also reduced the distortion value at the mid-point of the plate's edge from 0.12 mm (measured) to 0.04 mm, as shown in Figure 6.14.

6.3.3 Welding induced residual stress

The residual stress distribution is compared for each in-process mitigation heat treatment with an as-welded condition. The longitudinal residual stress across the weld region on a top surface of the weld plate is considered for comparison as follows-

6.3.3.1 Transient side heating

In side heating, the localized secondary heating source produces compressive stress during welding ($-\sigma_z$). The magnitude of developed compressive stress is proportional to the temperature gradient ($\partial T/\partial x$). Subsequently, the compressive stress would induce the thermal

tensioning stress ($+\sigma_{tension}$) in the weld bead region [155], [157]. It unveils that an increase in the heating temperature at a distance '*x*' from the weld zone produces sharp thermal gradients in the heating region, which produces a thermal tensioning effect.

Figure 6.15 show the longitudinal residual stress distribution on the weld plate's top surface across the weld centreline for square butt single side single pass welding of P91 steel plate with side heating. It considers heating intensity and heating torch location as two deciding factors for side heating's mitigation effect.

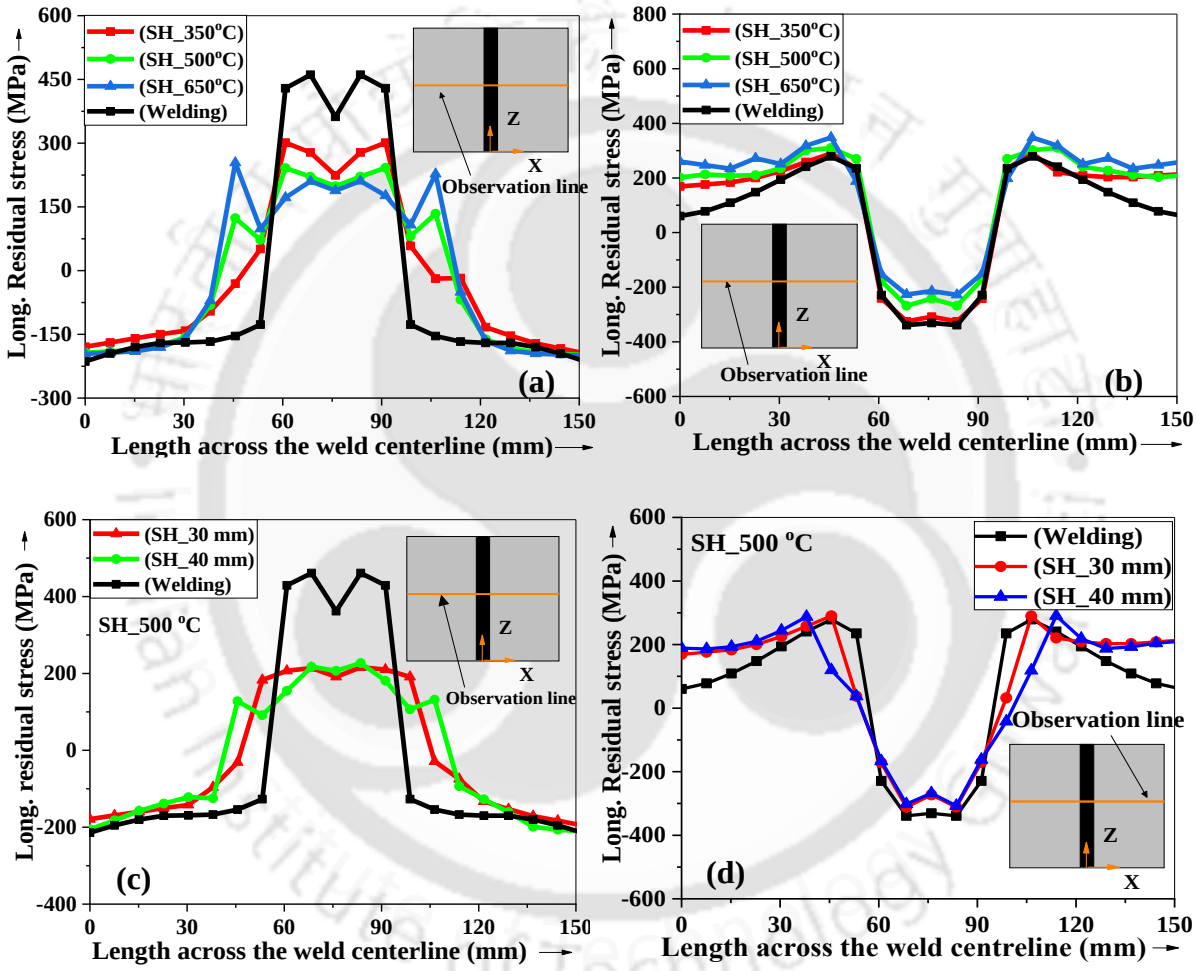

Figure 6.15 Longitudinal residual stress distribution across the weld of square butt single side single pass weld joint with side heating considering (a) different side heating temperatures without SSPT, (b) different side heating temperatures with SSPT, (c) different heating locations without SSPT and (d) different heating locations with SSPT

Figure 6.15 (a) shows the longitudinal residual stress distribution for three SH temperatures, 30 mm away from the weld bead, without considering the SSPT phenomenon. The tensile residual stress value at the weld centreline dropped from 362 MPa (as-welded) to 264 MPa

(SH_350 ^{o}C), i.e., by 38%. The heating area displays changes like compressive stress (welded) to tensile (SH_350 ^{o}C). A similar result is observed for higher heating temperatures, i.e., higher tensile residual stress is developed for higher heating temperatures. However, the weld region's residual stress values did not vary much for higher heating temperatures of 500 ^{o}C and 650 ^{o}C.

Figure 6.15 (b) presents the longitudinal residual stress distribution considering the SSPT effect. As side heating slows down the cooling rate, it affects the martensitic transformation, contributing to less volumetric contraction and reduces the weld region's compressive residual stress value. As the SH temperatures are below the transformation temperature, the P91 steel plate experiences the usual volumetric expansion in the heating region during side heating. As a result, it induces compressive plastic strain during welding. Hence, it developed tensile residual stress in side heating areas.

Figure 6.15 (c) and (d) show the longitudinal residual stress distribution for different heating torch locations away from the weld bead with and without considering the SSPT phenomenon. It is observed that heating torch location affects the tensile longitudinal residual stress value in side heating areas. The more we increase the heating torch's distance from the weld bead, the less it affects the thermal gradient near the weld region. Hence, the change in the heating location does not significantly affect longitudinal residual stress distribution in the weld region. However, the heating regions experience tensile peaks for both with and without SSPT phenomenon cases.

6.3.3.2 Heat sinking

The localized secondary cooling source in heat sinking produces a quenching effect in the weld and nearby regions. It induced compressive stress ($-\sigma_{compressive}$) in the vicinity of the weld bead region [97], [158]. Figure 6.16 (a) and (b) show the longitudinal residual stress across the weld centreline on the weld plate's top surface for P91 steel with and without SSPT, respectively.

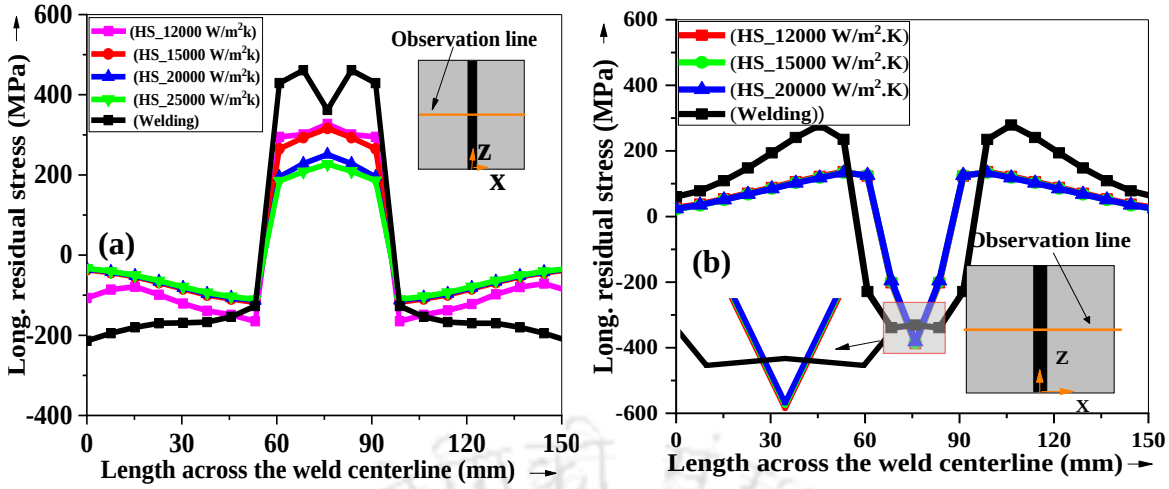

Figure 6.16 Longitudinal residual stress across the weld in square butt single side single pass welded joint models with heat sinking (a) without SSPT effect, (b) with SSPT effect

For a higher convective heat transfer coefficient (h= 20000 W/m^{2}k), the tensile residual stress on the fusion zone centreline reduced from 362 MPa to 227 MPa, i.e. by 37.3%. The plate's edge region shows a massive compressive residual stress value change from -200 MPa to -23 MPa. The possible reason for this alteration is that parent base metal balances the state of residual stress across the weld centreline in the transverse direction against the change in the residual stress in the weld region [97].

However, on considering the SSPT effect, Figure 6.16 (b) shows that compressive longitudinal residual stress distribution shrinks within the weld bead region due to contraction in the thermal profile (observed in Figure 6.10). The rapid cooling or quenching effect of heat sinking reduces longitudinal residual stress values throughout the weld centreline. The maximum tensile longitudinal residual stress value in the HAZ region dropped from 235 MPa to 133 MPa, i.e. by 43.4%. Similarly, the longitudinal residual stress in and near the weld centreline expectedly diminished to a much lower compressive value of -388 MPa (h= 20000 W/m^{2}k) from -339 MPa (as-welded), i.e., by 12.1%.

6.3.3.3 Combined side heating and heat sinking

Both transient side heating and static heat sinking effectively mitigate the welding induced distortions and residual stresses in P91 steel welds with and without the SSPT phenomenon. However, side heating and heat sinking exhibited a different kinds of mitigation results. Therefore, the study is further extended to assess the effect of combining transient side heating

and static heat sinking processes. Figure 6.17 (a) and (b) show the longitudinal residual stress across the weld for combined TSH and HS during welding.

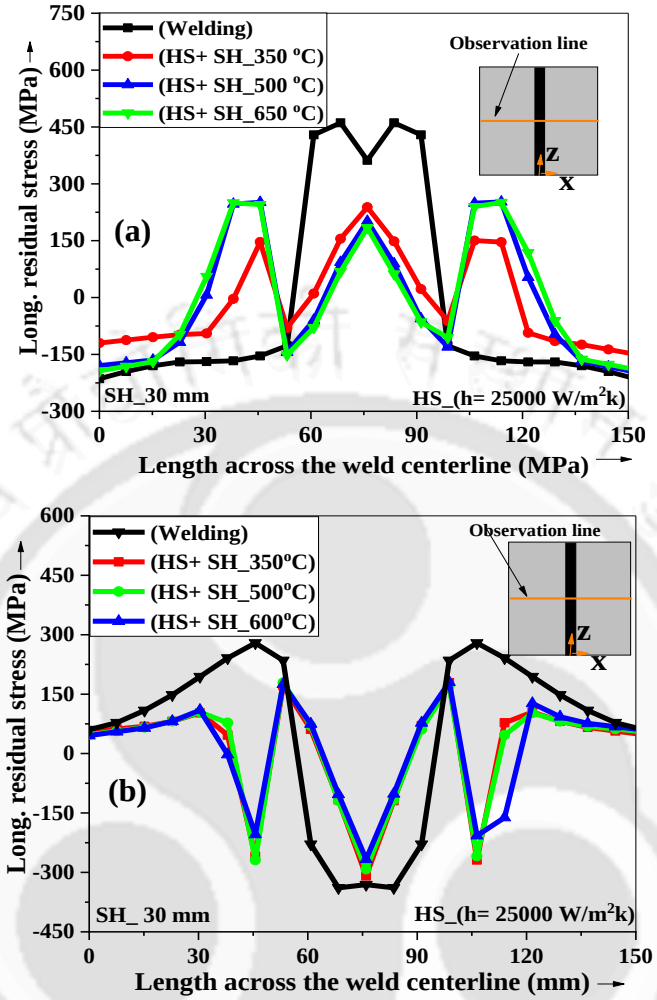

Figure 6.17 Residual stress distribution for combined side heating and heat sink (a) without considering SSPT, (b) considering SSPT

The combined mitigation heat treatment develops a crown shape longitudinal residual stress distribution across the weld in the transverse direction. The residual stress is expectedly reduced in the weld bead region more efficiently than TSH and HS processes for no SSPT phenomenon case, as shown in Figure 6.17 (a). The longitudinal residual stress value on weld centreline diminished from 362 MPa (as- welded) to 184.1 MPa (combined TSH_600 ºC+ HS_h= 25000 W/m^{2}k) i.e., by 49.1%. The heating regions also developed tensile peaks of higher values (> 200 MPa) under transient side heating effects. However, the region between side heating and heat sinking areas shows compressive residual stress and cause an abrupt change in residual stress distribution across the weld in the transverse direction.

On considering the SSPT phenomenon, it is observed that residual stress value on weld centreline decreased in magnitude but remained compressive. The reason behind this alteration is that transient side heating weakens the overall cooling effect of heat sinking. Therefore, the compressive residual stress value decreased for the weld centreline by increasing the side heating temperature. The crown shape distribution of residual stress across the weld centreline develops a sharp gradient of residual stress value with multiple compressive and tensile residual stress peaks.

6.4 Effect of post-weld heat treatment

Figure 6.18 presents the thermal profile of the PWHT process predicted through FE modelling of the process. It represents the three stages of post-weld heat treatment. It can be observed that the specific heating rate, soaking time & temperature, and cooling rate in the heat treatment are competently simulated, same as explained in the methodology section. The soaking temperature is kept at 760 ^{o}C for 2 h of holding time.

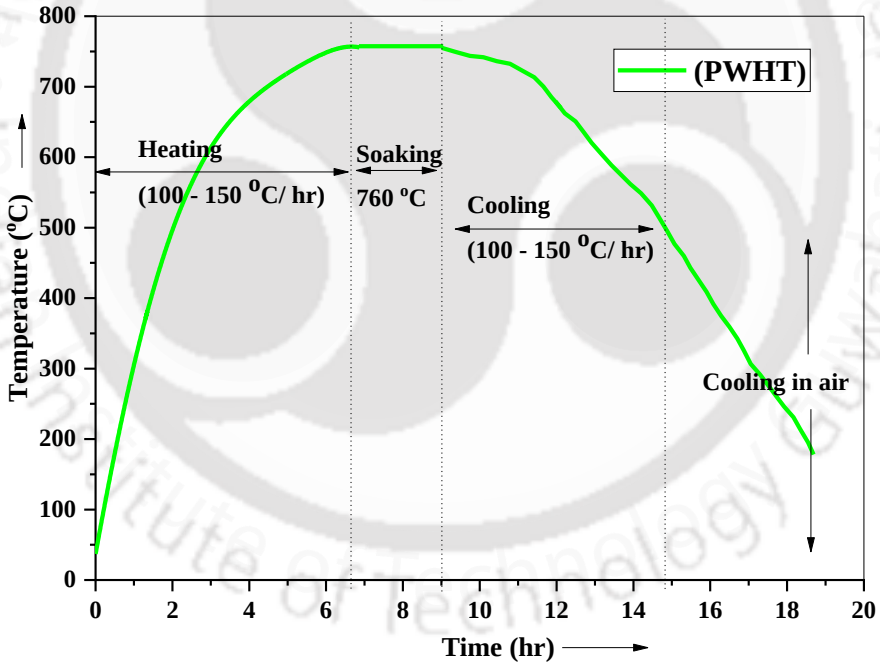

Figure 6.18 Thermal profile of post-weld heat treatment

Figure 6.19 present the contour plots of longitudinal residual stress distribution in post-weld heat-treated and as-welded P91 steel weld joints considering SSPT phenomenon. From the contour plot, it is observed that post-weld heat treatment eliminated the tensile residual stress peak in the region between the weld bead and base metal. PWHT also diminished the compressive residual stress values in weld bead region almost by 85-90%.

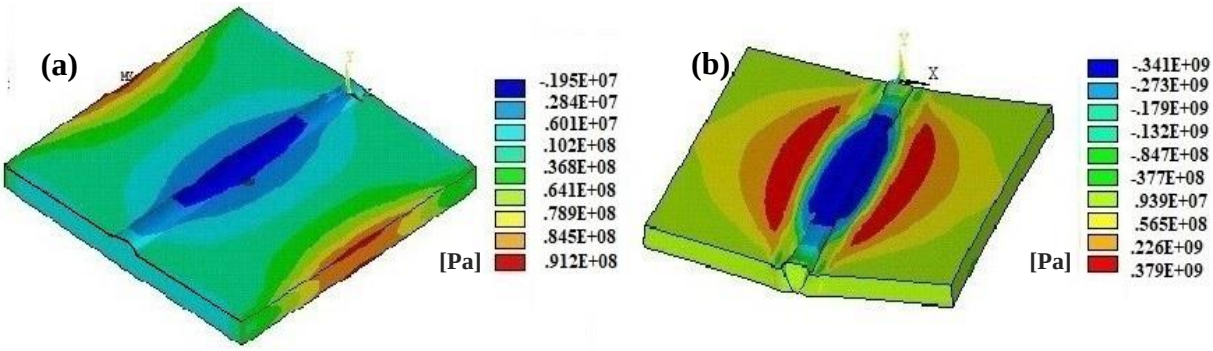

Figure 6.19 Contour plot of longitudinal residual stress distribution in (a) post-weld heat-treated, (b) as-welded square butt single side single pass welded joint models

The PWHT induces a drastic change in residual stress distribution. Plastic deformation during the heating stage of heat treatment holds a significant contribution towards reduction in residual stresses owing to a gradual drop in YS & elastic modulus [159]. It also observed that the creep phenomenon shows a significant stress relaxation effect in FE modelling of PWHT [159]. Hence, Norton's creep model is adopted for FE modelling of PWHT.

The stress relaxation pattern during PWHT cycles for a point within the weld bead and base metal region is shown in Figure 6.20. It noticeably exhibits the influence of heating, soaking and cooling rate or time during heat treatment. Figure 6.20 reveals that stress relaxation mainly occurs in the primary stage of creep phenomena, where plastic strain or creep strain develops during heating. These creep strain develops under the influence of trapped residual stresses and lowers YS and elastic modulus. Thus, plastic distortion in terms of creep strain release the residual stresses. Similarly, further stress relaxation occurs during the soaking time at constant creep strain. Known as secondary stage of phenomena [34].

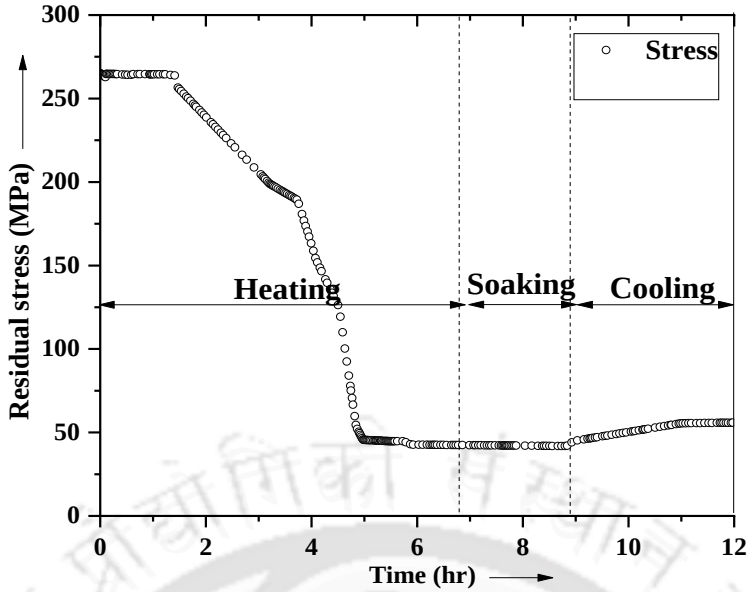

Figure 6.20 Stress relaxation at a point between the weld and HAZ region on the top surface of the plate during PWHT (considering creep phenomenon)

Though, the secondary stage of creep shows insignificant contribution towards stress relaxation. It signifies that soaking time has no significant role in stress reduction during heat treatment. Dong et al. also observed a similar stress relaxation pattern in the P91 steel girth weld during PWHT [159].

6.5 Summary

A detailed study is performed by FE modelling pre-welding, during welding, and post-heat treatments to compare their mitigation effects. The mitigation models for the three stages of welding exhibited a modest mitigation effect. The overall outcomes of this chapter are as follows:

- Preheating is found promising in mitigating welding-induced distortion and residual stresses in SAW welded P91 steel.
- Transient side heating causes minor changes in residual stress distribution in the weld bead region besides the heating intensity and side heating locations.
- Heat sinking adeptly extenuates the tensile residual stress in HAZ in SAW welded P91 steel.
- The combined side heating and heat sinking processes developed a crown shape longitudinal residual stress distribution across the weld centreline.

- Finally, post-weld heat treatment also shows a significant stress relaxation effect on SAW welded P91 steel.

On the contrary, post-weld heat treatment is obligatory for P91 steel welds to recover their overall mechanical behaviour and microstructural stability [40], [41], [160]. Similarly, preheating is known for its preventive responses on hydrogen embrittlement and inclusion [91]. It was also discovered that square butt single and double side single pass submerged arc welded P91 steel possess compressive residual stress in the weld bead region. Hence, despite good mitigation outcomes of in-process mitigation heat treatment, it is less practical and productive on SAW welded P91 steel than preheating and PWHT.

CHAPTER 7

INFLUENCE OF PREHEATING AND PWHT ON RESIDUAL STRESSES AND DISTORTION OF SAW WELDED BUTT JOINTS OF P91 STEEL

7.1 Introduction

Based on the findings of previous chapters, it is realized that preheating and PWHT promise mitigation techniques to control weld induced distortion and residual stresses. Hence, this chapter deals with pre and post welding heat treatment effects on submerged arc single side and double side square butt-welded joints of P91 steel plates. Preheating and post-weld heat treatment experiments are carried out to compare their effects. Post weld heat treatment is carried out in an automatic furnace with a controlled heating rate, temperature, and cooling rate. This chapter is focused on experimental validation of numerically predicted results for their mitigation effects.

7.2 Preheating and PWHT experiments

The oxy-acetylene flame is used as a heat source to perform preheating over the area of 20 mm on both sides of the welding zone [14]. The preheating temperature is monitored using infrared thermal imaging and monitored through thermocouple attachment.

The PWHT is accomplished on weld joint samples within 48 hours of the welding experiment in an automatic furnace provided with control units for time and temperature. The furnace consists of 4 heating rods, collectively controlled to acquire specific heating and cooling rates. The heating rate, soaking time, temperature, and cooling rate are kept the same as discussed in section 6.4 and shown in Figure 6.18.

7.3 Mitigation effect on square butt single side single pass welded joint

Preheating reduced the edge deflection and angular distortion, as shown in Figure 7.1. Preheating efficaciously minimized the vertical distortion value at the mid edge's point on the top surface from ~ 0.12 mm (as welded) to ~ 0.07 mm (preheated), i.e., by 41.6%. While, the vertical distortion value at the end point of the edge on the top surface reduced from ~ 0.07 mm

(as welded) to ~ 0.03 mm (preheated), i.e., by 57%. Angular distortion angle also reduced from ~ 0.23° to ~ 0.143° (i.e., 37.8%) for the preheated single-side welded butt joint. The mitigation effects of preheating are observed in Figure 7.1.

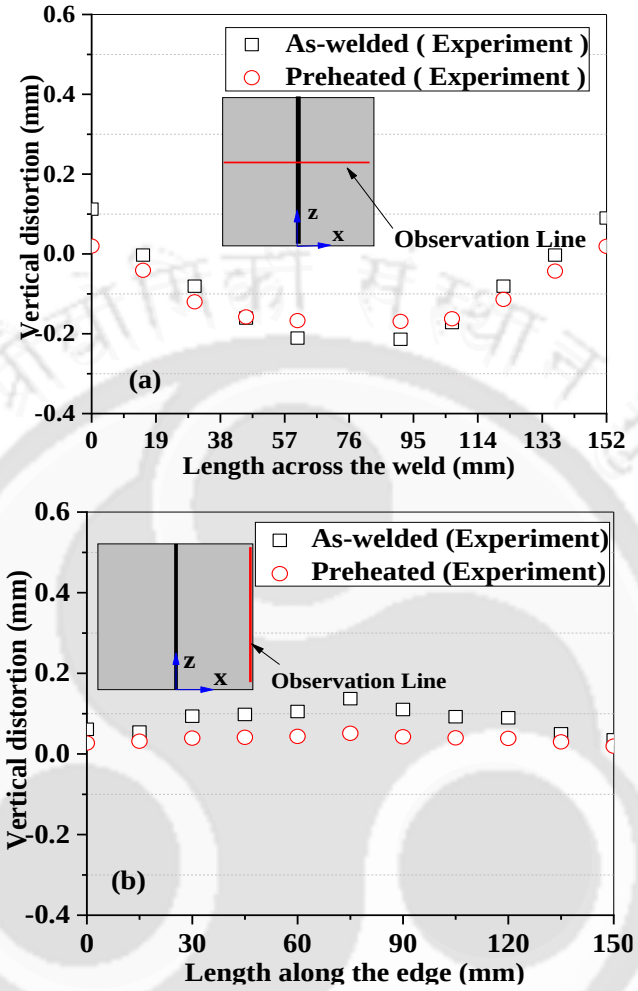

Figure 7.1 (a) Angular distortion, (b) edge deflection in square butt single-side single pass welded joints with and without preheating

The residual stress is measured through the thickness of the welded plate in the HAZ and FZ by performing the DHD technique. Residual stress distributions in the HAZ and FZ throughout the plate's thickness (neglecting weld bead top and bottom crowns) for the preheated and as-welded joints are shown in Figure 7.2.

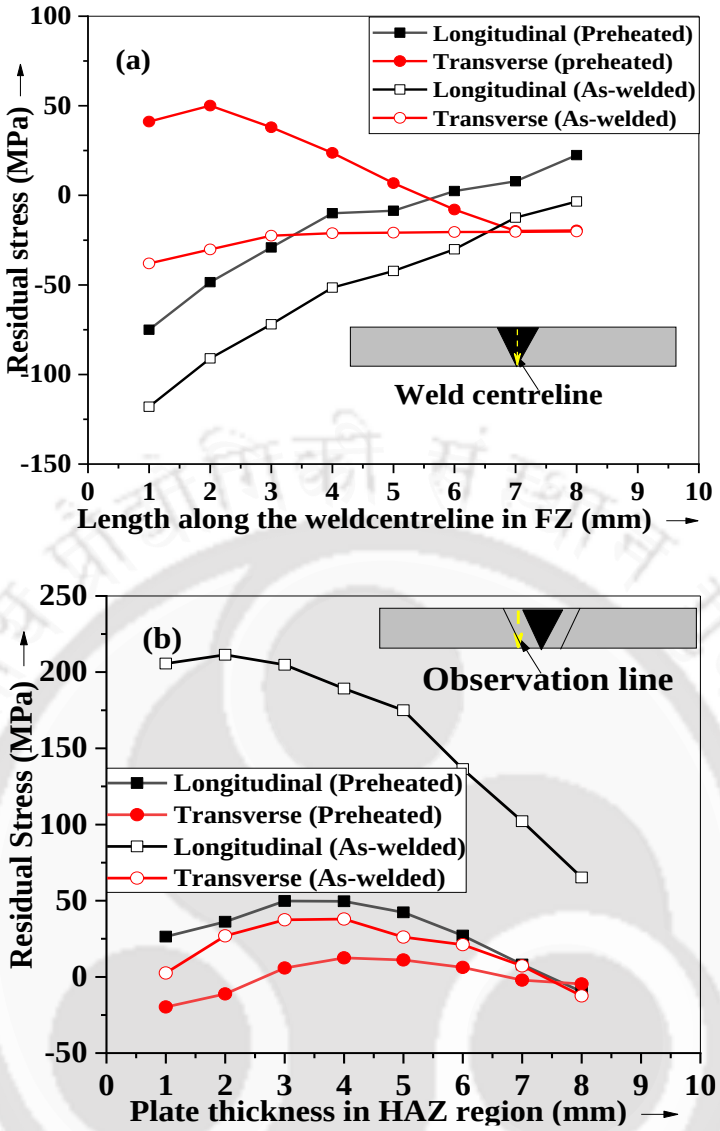

Figure 7.2 Residual stresses in (a) FZ and (b) HAZ of preheated and as-welded square butt single side single pass welded joints

In FZ, longitudinal residual stress shows the same pattern throughout the thickness for both as-welded and preheated weld joints. However, the residual stress values decreased to -75 MPa from -118 MPa at 1 mm of thickness, i.e., 36%. The longitudinal residual stress transformed to tensile stress of 22.5 MPa (preheated) from compressive stress of -4.2 MPa (as-welded) in the bottom region of the welded plate. The transverse residual stress values in the FZ dramatically changed from top to bottom of the plate thickness after preheating. The top side shows the highest variation or transformation of compressive residual stress values from -38.1 MPa to a tensile residual stress of 41.2 MPa. In HAZ, the maximum value of longitudinal stress effectively reduced to just 26 MPa (preheated) from 200 MPa (as welded weld) at 1 mm thickness of the plate, i.e. by 87%. After preheating, transverse residual stress within the HAZ

varies similar to as-welded case throughout the plate thickness with lower values. However, the transverse residual stress value remains the same for the bottom side region of HAZ and FZ, as shown in Figures (a) and (b).

The same comparative study is carried out to analyse the effect of PWHT on residual stress distribution. The residual stress distribution (neglecting weld bead top and bottom crowns) in HAZ and FZ of post-weld heat-treated and as-welded cases are shown in Figure 7.3 (a) and (b) below.

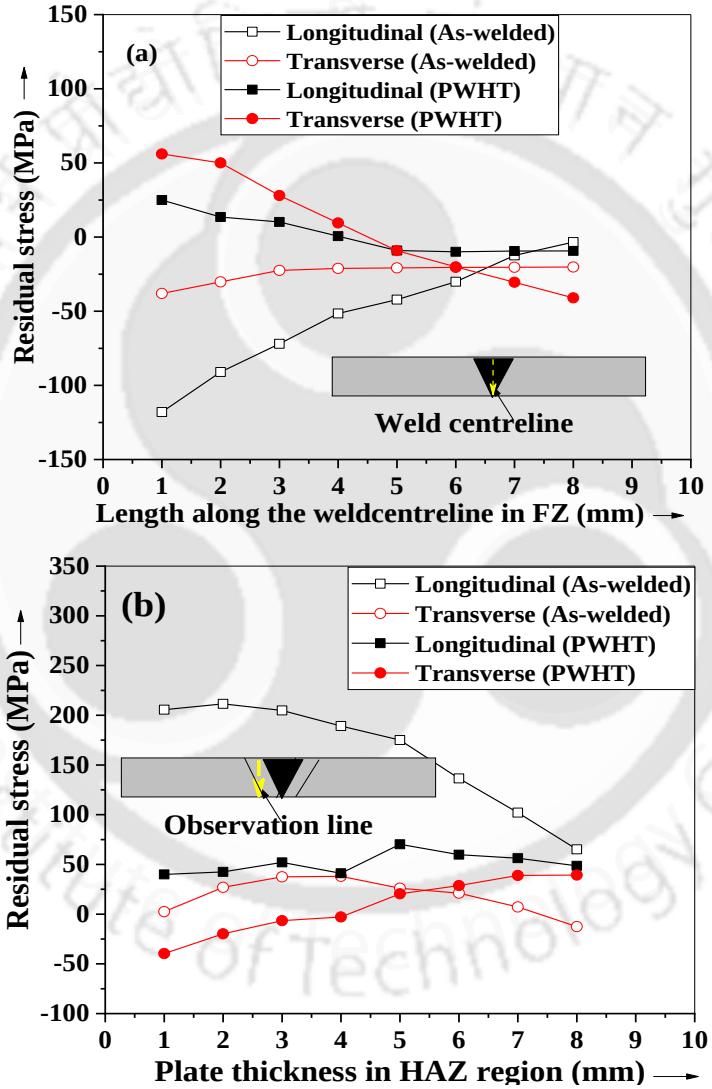

Figure 7.3 Residual stress in (a) FZ and (b) HAZ of as-welded and post-weld heat-treated square butt single side single pass welded joints

On performing PWHT, both longitudinal and transverse residual stresses values are reduced in both FZ and HAZ. The FZ's longitudinal residual stress at 1 mm thickness transformed from compressive stress of -118 MPa (as-welded) to tensile residual stress of 26 MPa (PWHT).

Similarly, transverse residual stress also transformed from compressive residual stress of –50 MPa to tensile residual stress of around 50 MPa at 1 mm thickness. HAZ also experiences a similar mitigation effect for longitudinal residual stress, which reduced from 202 MPa to around 49.1 MPa, i.e., by almost 76%. Transverse residual stress was also reduced in FZ and HAZ and developed a linear distribution throughout the thickness.

Finally, both preheating and PWHT processes are applied to assess the combined effect of both processes. The residual stress distributions for this case are shown in Figure 7.4 (a) and (b) for both transverse and longitudinal residual stress in HAZ and FZ.

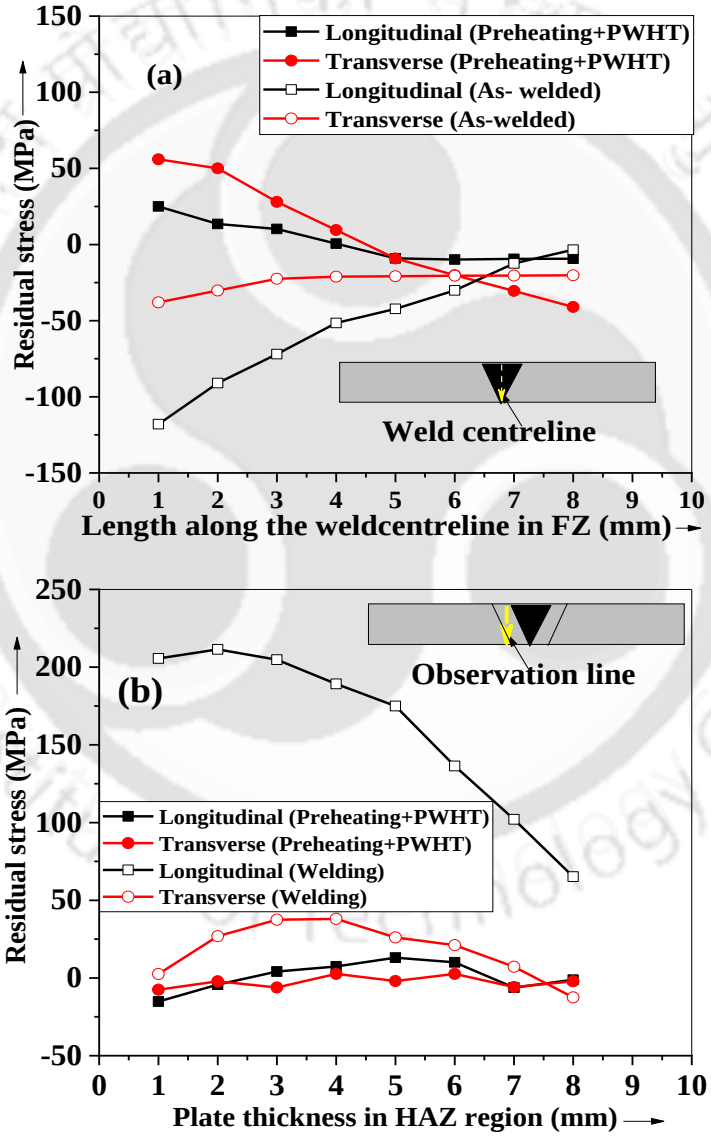

Figure 7.4 Residual stress in (a) FZ and (b) HAZ of combined preheated and post-weld heat-treated weld and as-welded square butt single side single pass welded joints

It is observed that the combined preheating and PWHT processes efficiently mitigates the welding induced residual stress distribution in both longitudinal and transverse directions for both HAZ and FZ.

Figure 7.4 (a) shows the longitudinal and transverse stress distribution in the weld fusion zone. Here, it is observed that combined preheating and PWHT efficaciously mitigates the stress distribution. The longitudinal stress value at 1 mm thickness is observed as 15 MPa, transformed from compressive to tensile value from as-welded condition. Similarly, the transverse stress value at 1 mm thickness is observed as -16 MPa, compared to the corresponding value (-40 MPa) of as-welded welds. It is also observed that for both the regions, i.e. HAZ and FZ, the variation in residual stress distribution is not as sharp as for as-welded conditions followed by preheating and PWHT. The longitudinal stress value in HAZ at 1 mm thickness transformed from tensile stress to compressive stress (i.e.-15 MPa), as shown in Figure 7.4 (b). The longitudinal stress values remain tensile in the mid thickness region but with a much lower value of 5-12 MPa than the as-welded case. The transverse stress distribution is observed to be compressive throughout the thickness. The mid thickness region shows the significantly small tensile residual stress in the transverse direction.

To clearly understand the effect of preheating, PWHT and combined pre and post-weld heat treatments on residual stress distribution, a bar diagram of the extreme value of longitudinal and transverse residual stresses are presented here, as shown in Figure 7.5.

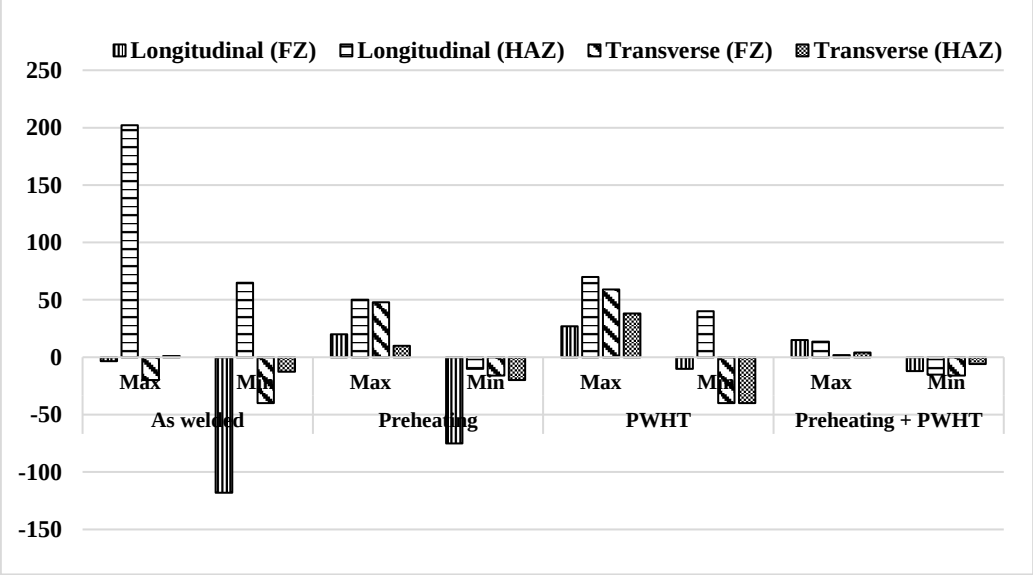

Figure 7.5 Extreme values of longitudinal and transverse residual stress in the square butt single side single pass joints of P91 steel under four different cases

Both longitudinal and transverse maximum residual stress values (tensile or compressive) are observed in the as-welded sample. As expected, the minimum residual stress values (tensile or compressive) are observed for the combined preheated & PWHT weld sample. It signifies that preheating combined with post-weld heat treatment on submerged arc square butt single side single pass joint of P91 steel shows maximum and better mitigation effect than PWHT without preheating.

7.4 Mitigation effect on square butt double side single pass welded joint

In square butt double side single pass submerged arc welding of the P91 steel plate, preheating is carried out by maintaining a temperature range of 250- 300 ^{o}C near the root gap before each pass. Hence, preheating is performed similarly to single side single pass joint for first-pass. At the same time, the same temperature is maintained as inter pass heating for the second weld pass.

Post weld heat treatment of double-side single pass welded joint is performed for same process parameters similar to single-side single pass welded joint. Preheating in double side welding is found less effective in controlling welding induced distortion. Angular distortion angle decreases from 0.14^{o} to 0.1^{o}. Similarly, the distortion value at the mid edge of the plate diminishes from 0.04 mm to 0.013 mm. Hence, preheating shows a minor mitigation effect on welding induced distortion in double side welded joints as observed in Figure 7.6.

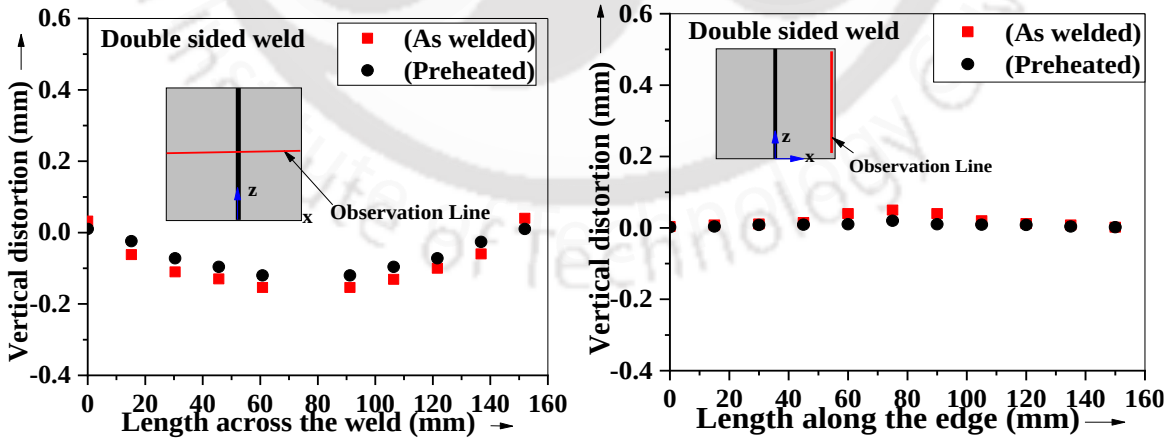

Figure 7.6 (a) Angular distortion, (b) edge deflection in square butt double-side single pass welded joint

The longitudinal residual stress distribution in double side butt welded joints are assessed with contour surface residual stress measurement technique for all the mitigation cases as discussed in the methodology section. The contour plots of longitudinal residual stress distribution on the cut surfaces of all the three cases at the midline across the welding direction are shown in Figure 7.7 for as-welded, preheated, and post-weld heat-treated welds.

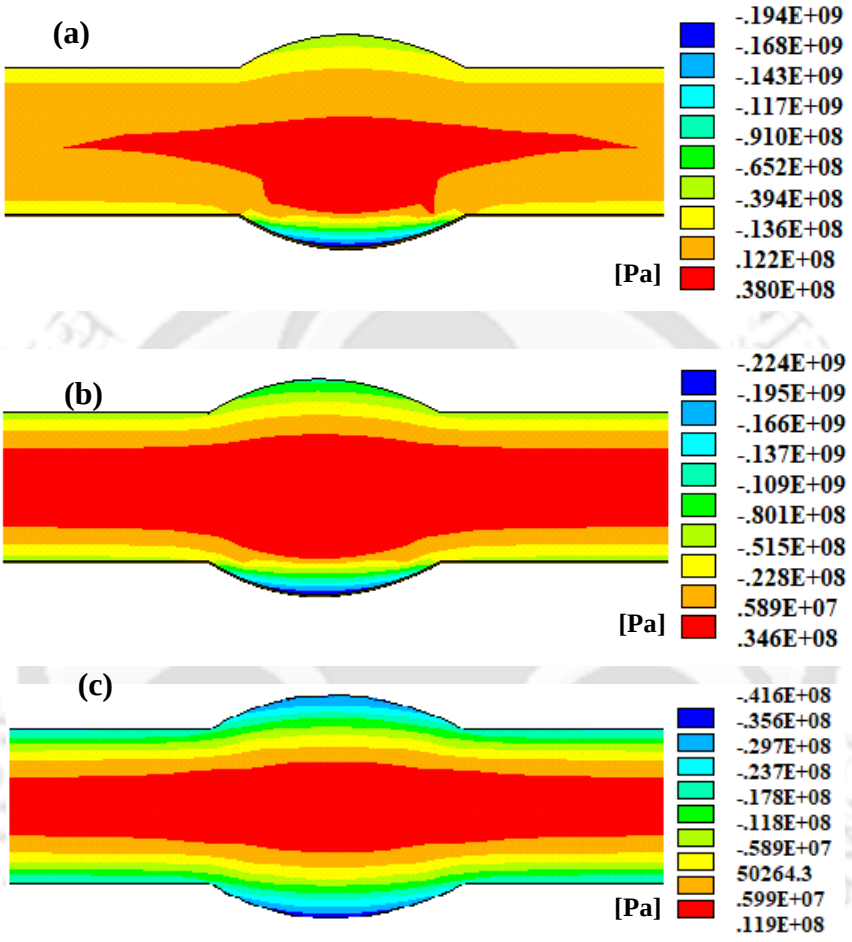

Figure 7.7 Contour of measured longitudinal residual stress distribution in (a) as welded, (b) preheated, and (c) post-weld heat-treated square butt double side single pass welded joints

It is observed that preheating, which is known for reducing thermal gradient, and cooling rate, expectedly reduce the longitudinal residual stress in mid thickness region. Whereas the bottom weld bead crown region exhibits slight increase in compressive residual stress. However, it shows similar kind of dispersal of residual stress same as as-welded case, i.e. compressive residual stress values abruptly vary from bottom surface towards mid region. In HAZ region, preheating slightly decreases the longitudinal residual stress at the top and bottom regions, as

observed in Figure 7.7 (b). On the other hand, post-weld heat treatment successfully diminishes the overall residual stress (both compressive and tensile) values in both weld bead crown and mid regions, as observed in Figure 7.7 (c). Post weld heat treatment mitigated the peak compressive residual stresses, especially in the bottom bead region from -194 MPa (as-welded) to -41 MPa (PWHT). Similarly, PWHT scaled-down the tensile peak values in the mid thickness region from 38 MPa (as-welded) to 11 MPa (PWHT). Consequently, PWHT develops a lower magnitude of compressive and tensile residual stresses throughout the thickness in the FZ and HAZ.

7.5 Summary

This chapter explains preheating and post-weld heat treatment effects on residual stress and distortion of submerged arc square butt single and double-side single pass welded P91 steel plates. Based on the studies, following observations are made:

- It is discovered that in a square butt single side welded joint, preheating reduces the compressive residual stress in FZ. However, it does not show a significant mitigation effect for residual stress distribution in square butt double side welded joint.
- Preheating capably mitigated the welding induced distortion in square butt single-sided welded joint and shows fair mitigation effect in square butt double side welded joint.
- As discussed in section 6.6, the post-weld heat treatment experiment exhibits an excellent stress relaxation in both SAW square butt single and double side single pass weld joints.
- Preheating combined with PWHT shows a better mitigation effect in reducing residual stresses in the SAW square butt joint of P91 steel.

Hence, pre and post-weld heat treatments are pretty effective and productive in controlling weld induced residual stresses and distortion and resumption of mechanical properties and microstructural stability of P91 steel welds.

CHAPTER 8

MICROSTRUCTURE AND MECHANICAL CHARACTERIZATIONS OF SAW WELDED BUTT JOINTS OF P91 STEEL WITH PREHEATING AND POST-WELD HEAT TREATMENT

8.1 Introduction

Previous chapters studied the SAW-induced temperature distribution, distortion, and residual stresses on the P91 steel plate. An efficient nonlinear elastic-plastic thermal-structural FE model was also developed to understand the thermal and structural behaviours of submerged arc square butt-welded joints of P91 steel. In continuation, different mitigation techniques were also proposed, and its FE simulation was also performed. Based on the predicted results, it was observed that all three pre, in and post welding mitigation processes are effective in mitigating welding induced distortions and residual stresses. On the other hand, the importance of PWHT in retaining the mechanical properties and microstructural stability of P91 steel weld is also suggested in published literatures [10], [40], [92], [146]. Similarly, preheating is also known for decreasing hydrogen inclusion and embrittlement. Therefore, the preheating and PWHT experiments were conducted on SAW butt joints of P91 steel and analysed to assess and compare the FE results considering their mitigation effects.

Hence, in this chapter, microstructural and mechanical characterization of SAW butt joints of P91 steel is performed to analyse the effect of submerged arc welding, preheating and PWHT on P91 steel weld. The present studies are performed on submerged arc square butt double side single pass welded joint. The chapter is divided into six sections, excluding the introduction. Four different weld samples are selected based on the applied heat treatments, which are (a) as welded, (b) preheated, (c) post-weld heat-treated, (d) preheated, and post-weld heat-treated weld samples as given in Table 8.1. Section 8.2 describes every aspect of the thermal cycle's effects on the microstructural characteristic of welded joints.

Table 8.1 Weld samples with different heat treatment conditions

Processes performed	Sample '1'	Sample '2'	Sample' 3'	Sample '4'
Preheating	✕	✓	✓	✕
PWHT	✕	✓	✕	✓

Similarly, the micro-hardness of different zones across the weld is discussed in section 8.3. Sections 8.4 and 8.5 describe the tensile properties of the welded joint for different heat treatment processes. At last, the chemical compositions and phases are assessed for their quantitative analysis in the welded joints.

8.2 Macro and microstructural characterization

The macrographs of properly etched samples of all four cases are captured by a stereomicroscope in Figure 8.1. It is observed that the depth of penetration in a single pass for double side single pass submerged arc welding is obtained about 50% of the plate thickness. However, on preheating, the depth of penetration increases to 60-70% of the plate thickness for the same set of process parameters. The fusion boundary and HAZ boundary are also presented in Figure 8.1. It also shows the hardness lines along which microhardness values are measured.

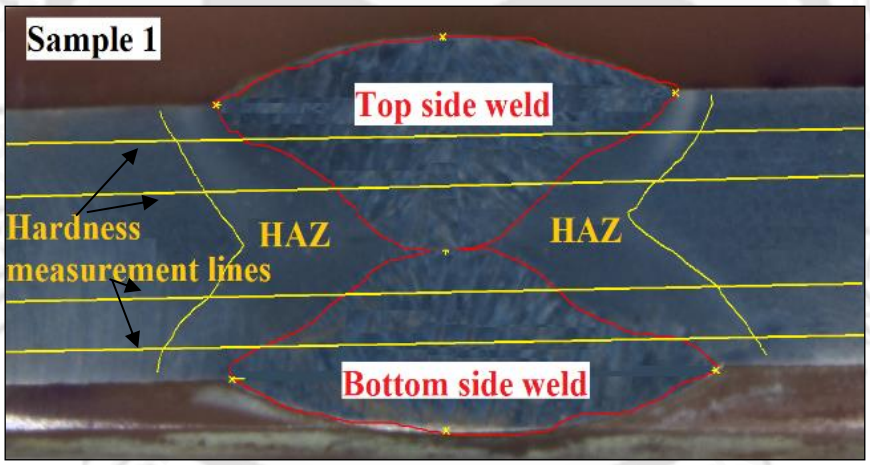

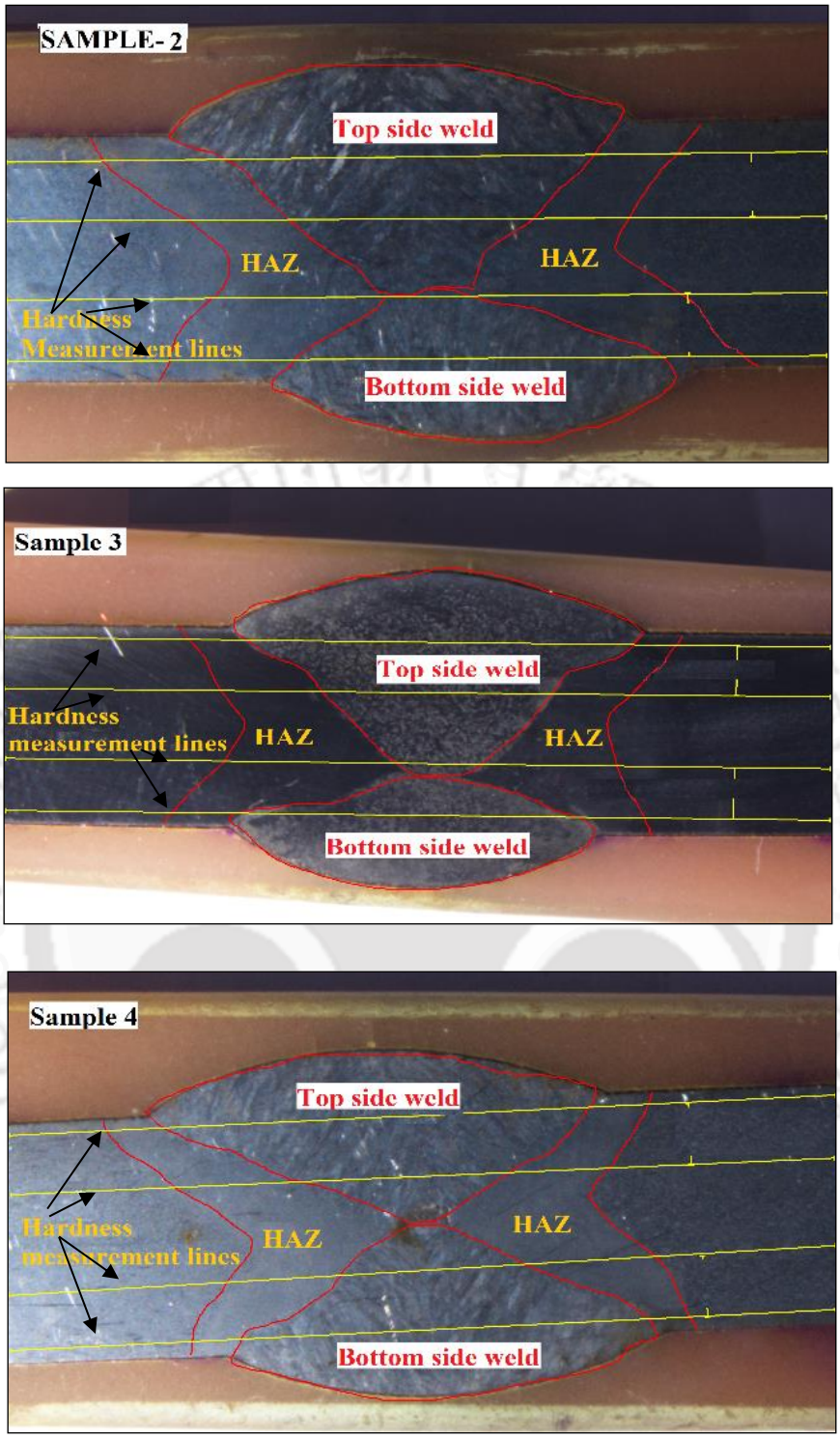

Figure 8.1 Cross-sectional view of the weld samples for four cases

The microstructure is observed for all four cases in different weld zones, i.e. FZ, CGHAZ, FGHAZ and ICHAZ. Figure 8.2 reveal the microstructure of different regions across the weld of the as-welded weld. The base metal shows Ferrite (white spots) and Pearlite (black spots) grain structures favouring the lowest temperature gradient in the base plate region.

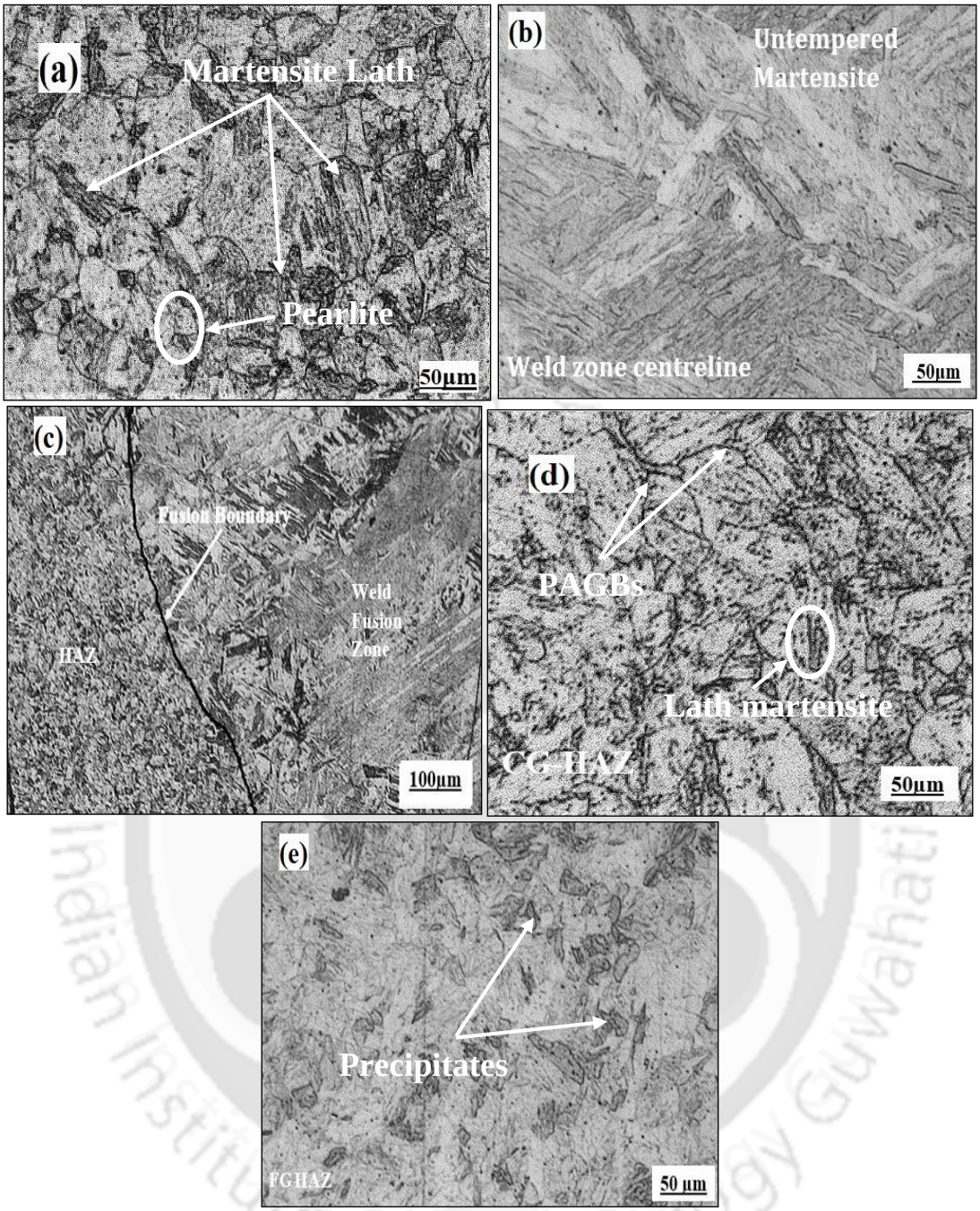

Figure 8.2 Microstructure images of the as-welded case in (a) Base metal (b) weld centreline in FZ (c) Fusion boundary line with FZ and HAZ (d) CGHAZ (e) FGHAZ

Figure 8.2 (b) shows the needle-shaped or acicular untempered martensite structure in the fusion zone. The high thermal gradient in the weld region increases the cooling rate, which transforms the weld metal into a martensite structure during cooling. Figure 8.2 (c) shows the fusion boundary line between FZ and HAZ. The CGHAZ is observed within ~2.5 mm of width, adjacent to the fusion boundary. Figure 8.2 (d) comprises coarse austenitic grain boundaries due to modest thermal gradients in the region. The untempered martensite lath is observed

within the PAGBs indicated by arrows. For moderate peak temperature (above transformation temperature (Ac_3), precipitates get dissolved to form carbide and nitride matrix, resulting in lath martensite in CGHAZ. The FG-HAZ is also shown in Figure 8.2 (e) in the width of ~ 1.5 mm. The peak temperature in FG-HAZ remains below the transformation temperature (Ac_3), and so, the present precipitates could not dissolve completely, which is easily observed in Figure 8.2 (e) [161]. Hence, the whole HAZ is observed in the width of ~5- 7 mm.

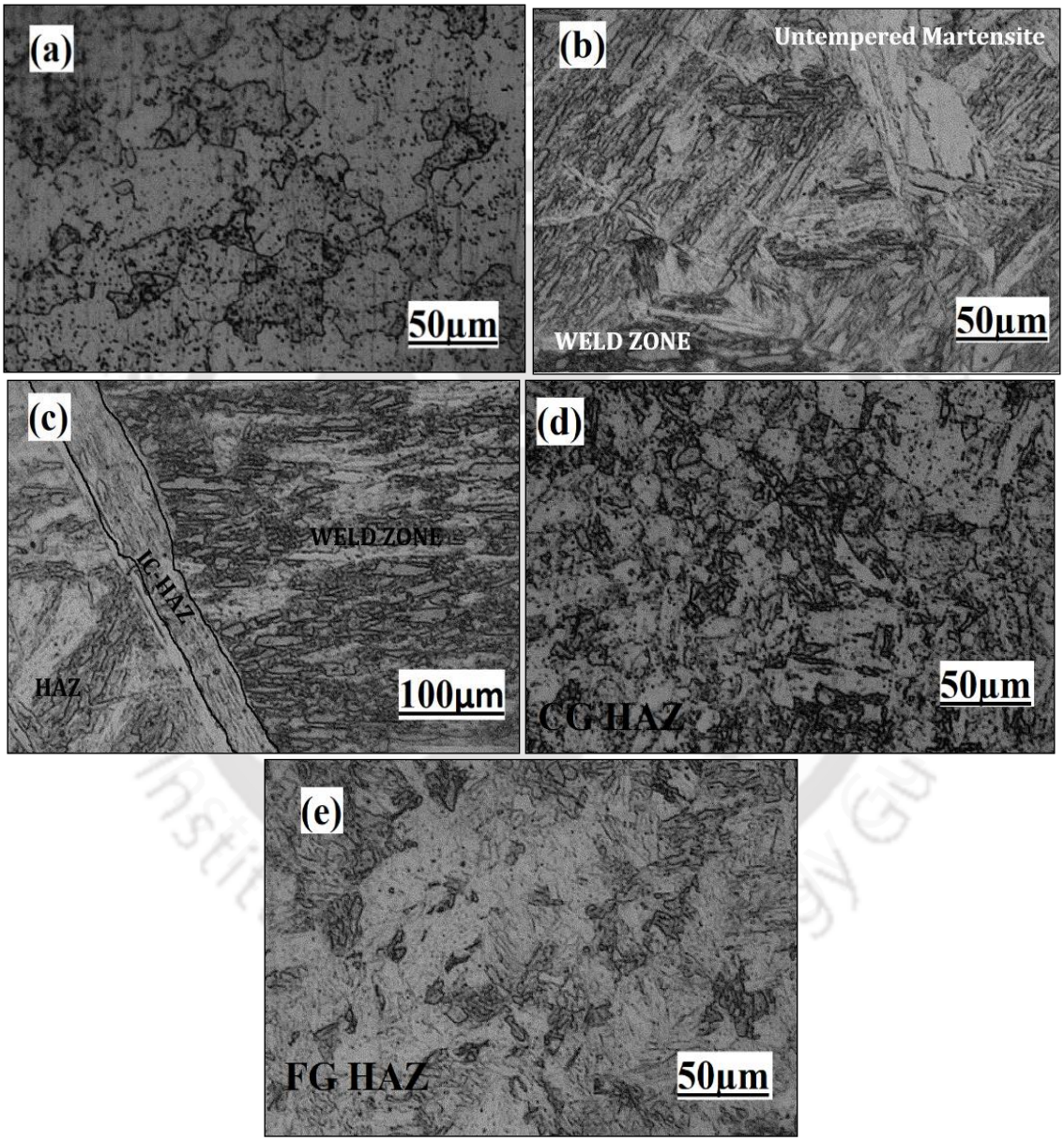

Figure 8.3 Microstructure images of the preheated weld (a) Base metal (b) Weld Zone in centreline (c) Fusion boundary line with FZ and HAZ (d) CGHAZ (e) FGHAZ

Figure 8.3 present the microstructural images of preheated weld sample. Figure 8.3 (a) shows uniform microstructure, i.e. ferrite and pearlite grains in the base metal region. In the fusion

zone, untempered martensite (needle-shaped) grains are observed similar to the as-welded case, as shown in Figure 8.3 (b). Nonetheless, as the preheating process decreases the thermal gradient from the fusion zone towards HAZ, it diminishes columnar structure formation during solidification. In CG-HAZ, the austenitic grain size is smaller than the as-welded sample due to the high heating rate of preheating near the root gap [18]. The microstructures of different zones in the post-weld heat-treated weld are shown in Figure 8.4.

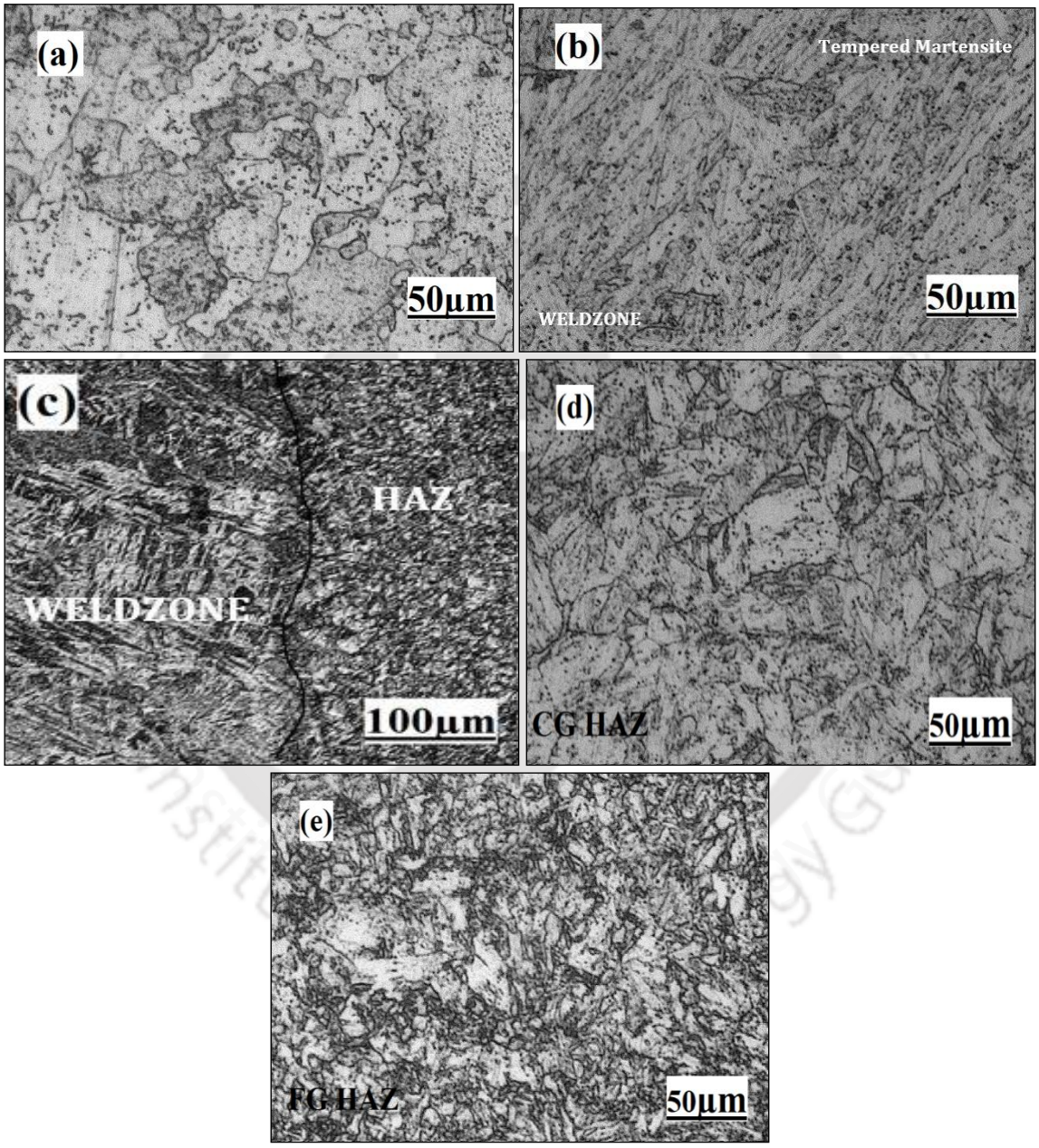

Figure 8.4 Microstructure images of the post-weld heat-treated weld (a) base metal (b) Weld Zone in centreline (c) Fusion boundary line with FZ and HAZ (d) CGHAZ (e) FGHAZ

Coarsening of carbide precipitates is observed after PWHT. In PWHT, the tempering process converted the needle shaped martensitic structure to a fine grained ferritic matrix embedded

with cementite particles, which are observed as black spots in the microstructural image given in Figure 8.4 (b). Both coarse and fine grained-HAZ show the tempered martensite along with coarse and fine austenitic grains, respectively. Coarsening of carbide precipitates are observed after PWHT, as observed in Figure 8.4 (d). Figure 8.5 presents the micrographs of the preheated and post-weld heat-treated weld for various zones across the weld. As PWHT is applied on the preheated welded joint, the effect of preheating is not noticeable from the microstructural images. In FZ, the tempered martensite consists of both ferrite and pearlite grains matrix along with cementite particles.

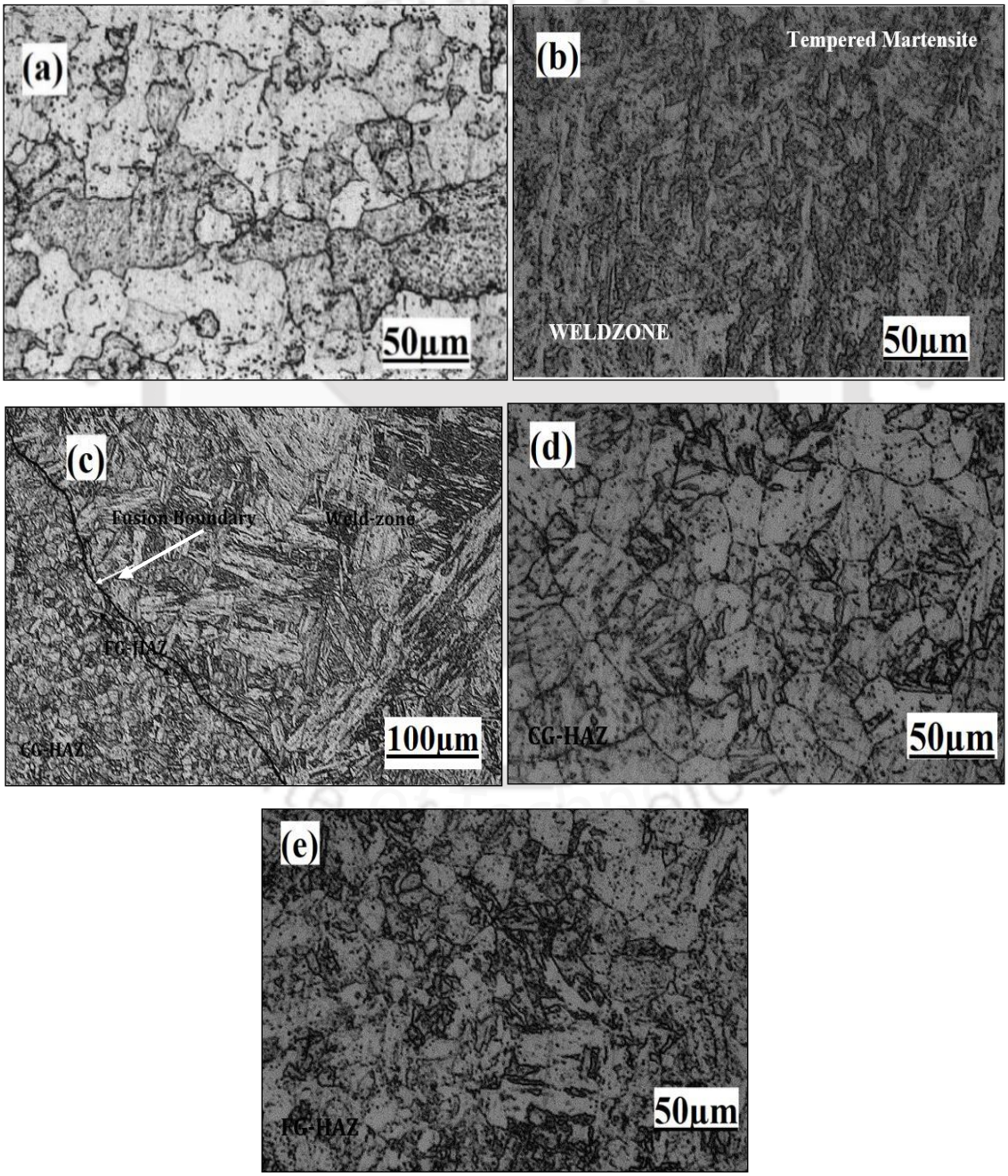

Figure 8.5 Microstructure images of preheated and PWHT weld (a) Base metal (b) Weld Zone in centreline (c) Fusion boundary line with FZ and HAZ (d) CGHAZ (e) FGHAZ

8.3 Micro-hardness across the weld

The contour plots of microhardness values of the four cases are shown in Figure 8.6 (a), (b), (c) & (d). The contour plot shows that the hardness values vary for different zones of weldment and base metal. FZ's hardness distribution is comparatively higher for the as-welded case, with the maximum hardness value of 438 HV. On performing PWHT, the hardness value reduced substantially due to the complete tempering of martensite, which results in the softening of the material. In both PWHT and combined PWHT & preheated welds, the average hardness values in the FZ reduced to 178 HV and 165 HV, respectively.

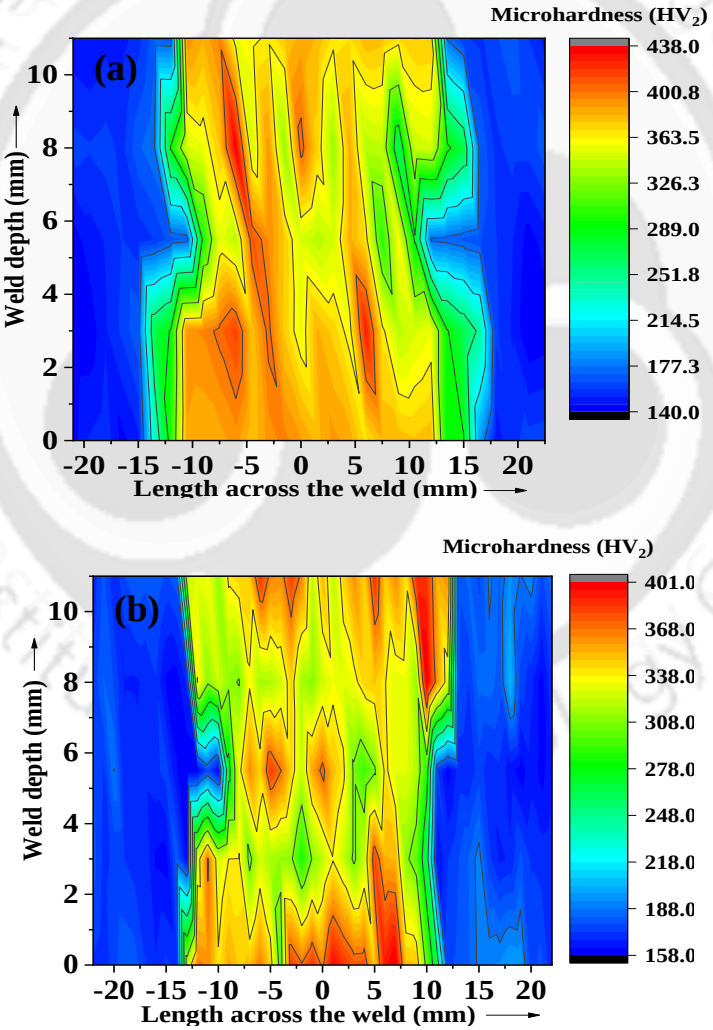

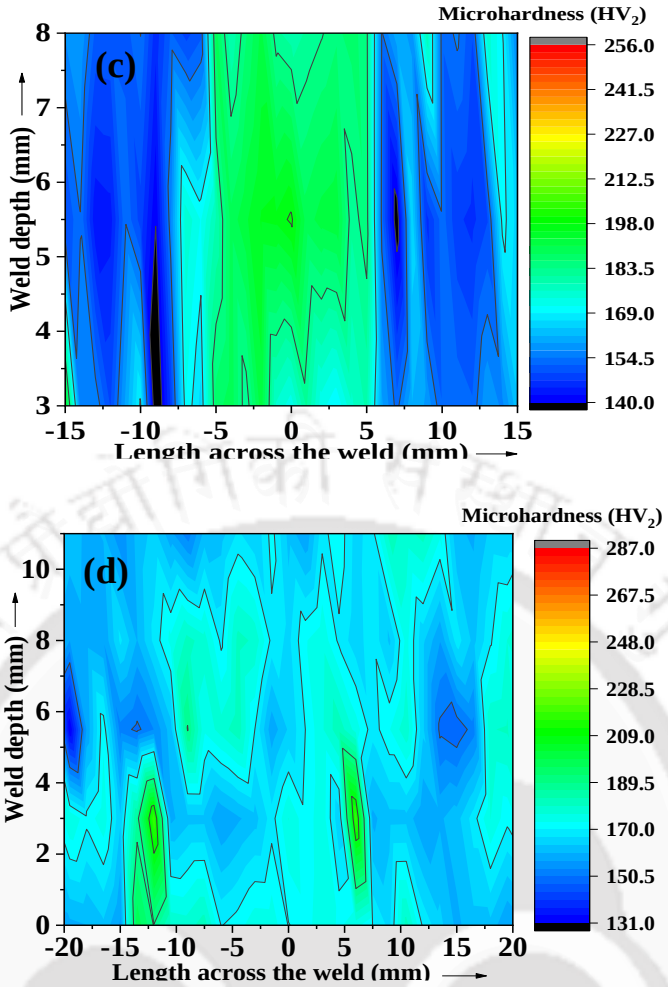

Figure 8.6 Contour plot of hardness values for (a) as welded, (b) Preheated, (c) PWHT weld (d) Preheated and PWHT square butt double-sided single pass welded joint

It is observed that preheating alone reduces the hardness value from 437.2 HV (as-welded) to 401 HV (preheated), i.e. by 8.2%. Similarly, the combined preheating & PWHT reduced the hardness value from 437.2 HV (as-welded) to 174 HV (after combined preheating and PWHT), i.e. by 60.2%. Figure 8.7 (a) shows the linear distribution of microhardness values across the weld bead for all four cases.

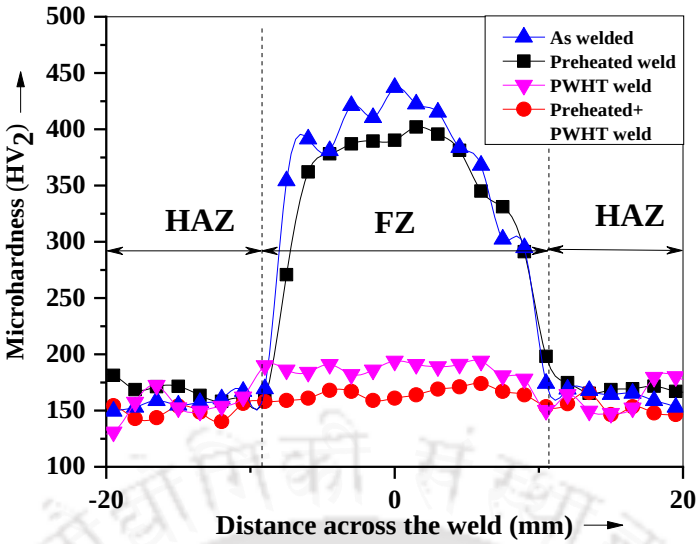

Figure 8.7 Micro-hardness across the weld for four cases

It is noticeable that for as-welded and preheated welds, the hardness values suddenly dropped at the boundary of FZ and HAZ, which designates the presence of inter-critical HAZ. This sudden fall in hardness value makes the Gr. 91 welds prone to cracking and failure. The different peaks of microhardness in the fusion zone of as-welded conditions are also vanished after preheating, which reduced the austenitic grain size in HAZ. Similarly, these grains develop a less columnar structure in the FZ. These collectively decrease the overall hardness values in both HAZ and FZ for uniform distribution across the FZ.

8.4 Weld strength and ductility

The tensile specimens are prepared along with the weld bead to evaluate the actual weld strength. It examines the quality of the weld bead for any welding defects. Two tensile samples were prepared for each welding case. The average values of the two for each case are reported as the final results. The engineering stress vs strain plots are shown in Figure 8.8 (a), collectively obtained for each tensile test conducted at room temperature. After conducting the test, the fractured tensile samples are displayed in Figure 8.8 (b), which exhibits the fracture region in the base plate far away from the weld region for all the cases. The nature of the fracture was ductile for each case which differs with the degree of ductility.

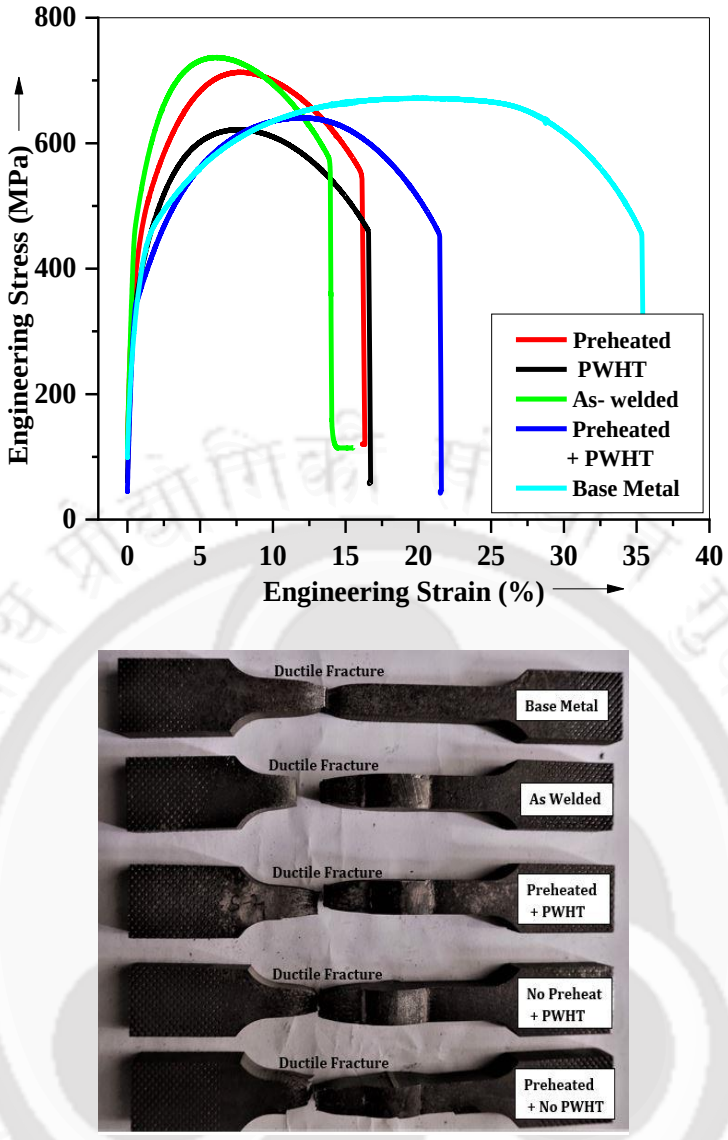

Figure 8.8 (a) Engineering Stress vs engineering Strain curve at room temperature, (b) Test specimens after ductile fracture

Table 8.2 represents the UTS, YS, and % elongation values for all five tensile test cases and includes breaking point strength values. As- welded case shows the highest UTS and YS with the lowest ductility value. The preheating and PWHT processes reduced the UTS and YS values of the welded joints. However, both processes improve the ductility of the welded joints. The percentage variations of UTS, YS and ductility, are also presented in Table 8.3.

Table 8.2 Tensile test results for four cases and P91 steel plate

Sl. No.	Sample	Ultimate Tensile Strength (MPa)	0.2% offset Yield Strength (MPa)	% Elongation	Fracture location
1.	As welded	740	513	14.6	Base plate
2.	Preheat + PWHT	618	389	22.2	Base plate
3.	Preheat	721	488	16.2	Base plate
4.	PWHT	627	396	18.6	Base plate
5.	Base Metal	651	437	35.6	Base plate

It is observed from Table 8.2 and Table 8.3 that preheating and PWHT improved the ductility significantly as compared with the as-welded sample. A similar reduction is observed after PWHT for P91 steel welds in previous literature [42], [163].

Table 8.3 Variation (%) in UTS and YS of the welded joint due to preheating and PWHT processes

Sl. No.	Processes	Ultimate Tensile Strength (% Decrement)	Yield Strength (% Decrement)
1.	Preheating	2.6	4.9
2.	PWHT	15.2	22.8
3.	Preheating + PWHT	16.5	24.2

Due to PWHT, the martensite gets tempered, reducing the hardness value resulting in lower UTS and more weld ductility. It also causes softening of the welds. Hence, PWHT caused a fall in the UTS value of the as-welded and preheated welds from 740 MPa (as-welded weld) and 721 MPa (preheated weld) to 627 MPa (PWHT on as-welded weld) and 618 MPa (PWHT on preheated weld), respectively.

8.5 Fracture surface analysis

The necking areas of the tensile fracture specimen shown in Figure 8.9 present the cup and cone shape in the fractured portion. Such cup and cone shapes are generated from a combination of the shear failure planes at 45^{o} with the axis of the specimen at each peripheral crack surface towards the central axis. Therefore, such an appearance assures ductile failure. The presence of dimples, voids etc., in FESEM images of fracture surfaces characterize the

ductile failure. On comparing the number of voids and dimples, it is observed that post-weld heat-treated welds are more ductile than the as-welded and preheated welds.

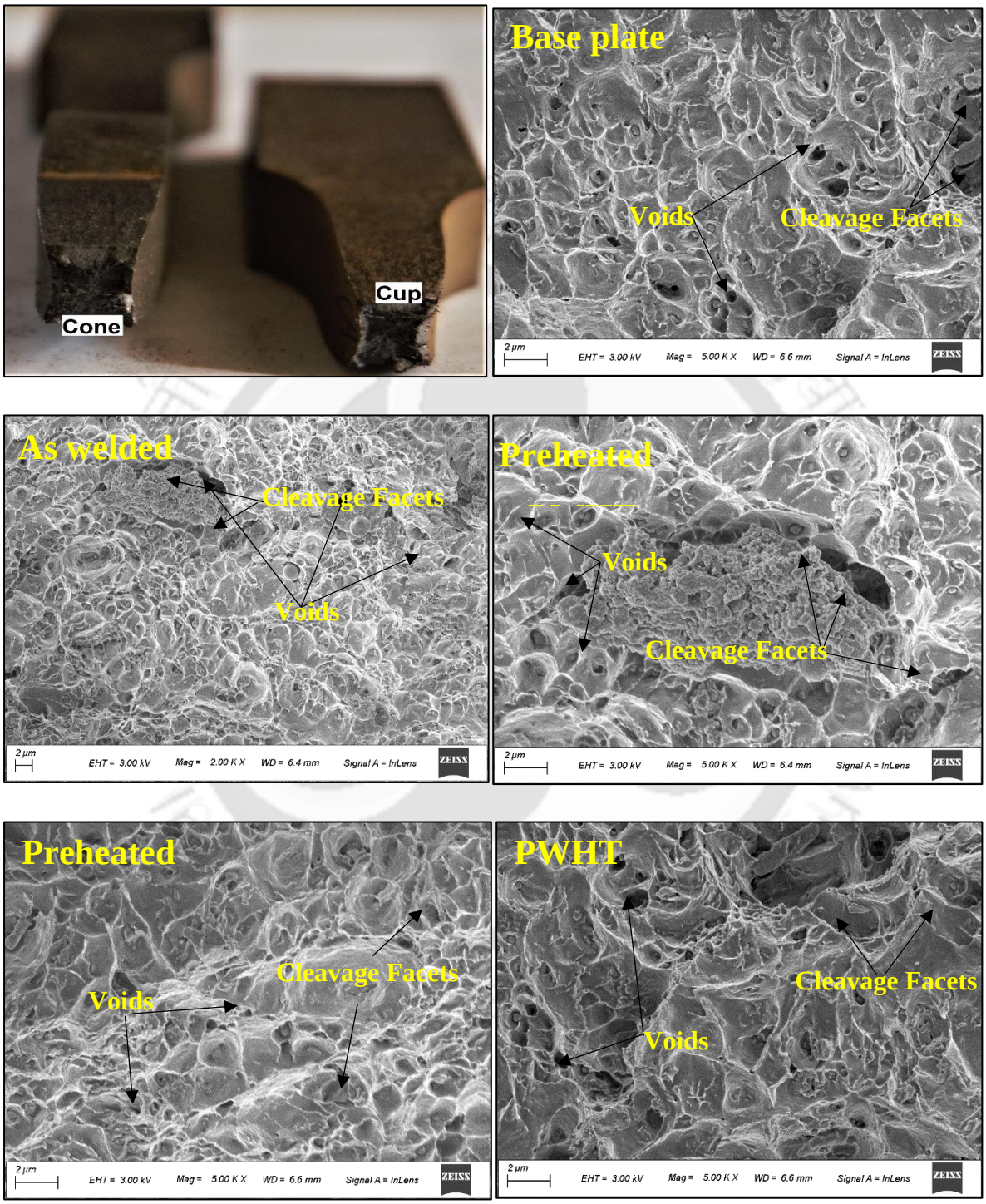

Figure 8.9 Necking Area and SEM images of fractured surfaces of the tensile specimens of all different cases fractured under the tensile test conducted at room temperature.

It signifies that preheating and PWHT improve the ductility of the weld joints individually as well as combined. On preheating, the cooling rate gets slowed down, which increases the fraction of the ferrite phase with coarsened dendrite structure, which induces better ductility of the weld. It also decreases the austenitic grains size, which decreases the hardness, YS and UTS. Similarly, in the post-weld heat-treated weld, converting an acicular martensite structure to a fine-grained ferrite structure softens the matrix and reduces the resistance against plastic distortion. It results in a reduction in hardness and improvement in ductility. The coarsening of cementite particles and equiaxed ferrite grains reduces the dislocation density in the post-weld heat-treated welds, diminishing the magnitudes of YS and UTS.

8.6 XRD and EDS analysis

Pre and post-weld heat treatments also influence the elemental compositions on the crack surfaces for different welding cases. Energy dispersive (x-ray) spectroscopy of the crack regions' top surface is also performed. The X-ray peaks of different elements present on the targeted surfaces are shown in Figure 8.10, which directly provides the weight percentage (Wt.%) of those elements.

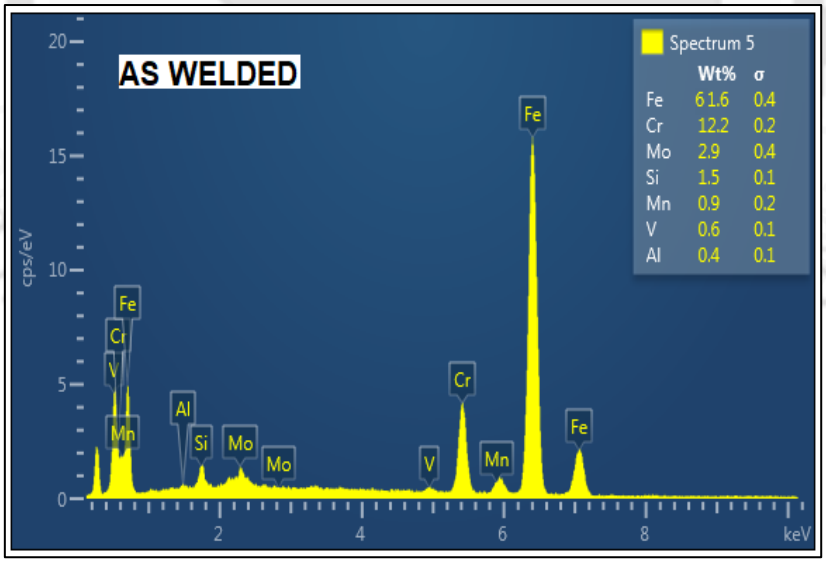

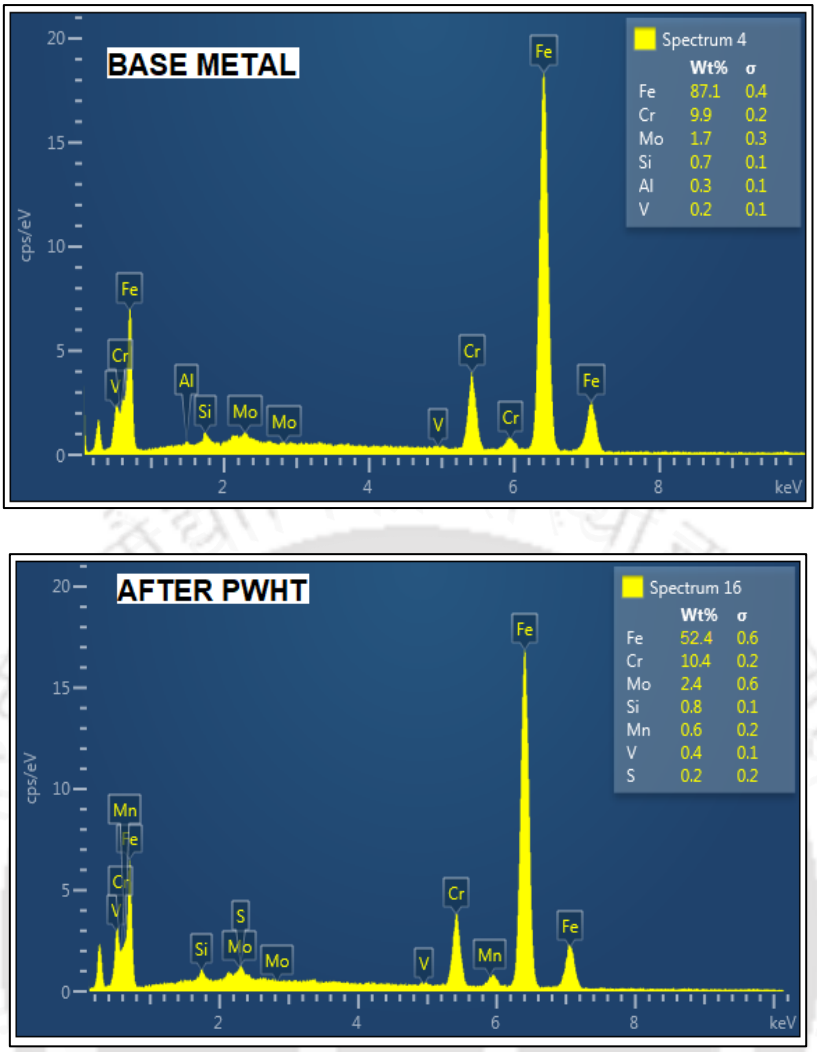

Figure 8.10 EDS of the metal surface of (a) base Metal, (b) as-welded weld, (c) post-weld heat-treated weld

The primary elements present in all the cases are Fe, Cr, Mo, Mn, V, C, Si, Al etc. The abundance of Mn and Mo in the as-welded weld signifies the higher weld strength than preheated and post-weld heat-treated welds [21]. Similarly, Carbide and Nitride forming elements, i.e. Cr and V, develop precipitates like $Cr_{23}C_6$, VN, and VC, which improve the weld's creep strength after PWHT. The existence of such precipitates can also be verified with X-ray diffraction results comparing base material and post-weld heat-treated material, as shown in Figure 8.11. The different phases indicate different precipitates like VC, Cr_7C_3, $Mn_{23}C_6$, and $Cr_{23}C_6$, Cr_2N, NbN, Fe_7W_6 etc. The presence of similar phases was reported by other researchers as well [22, 23].

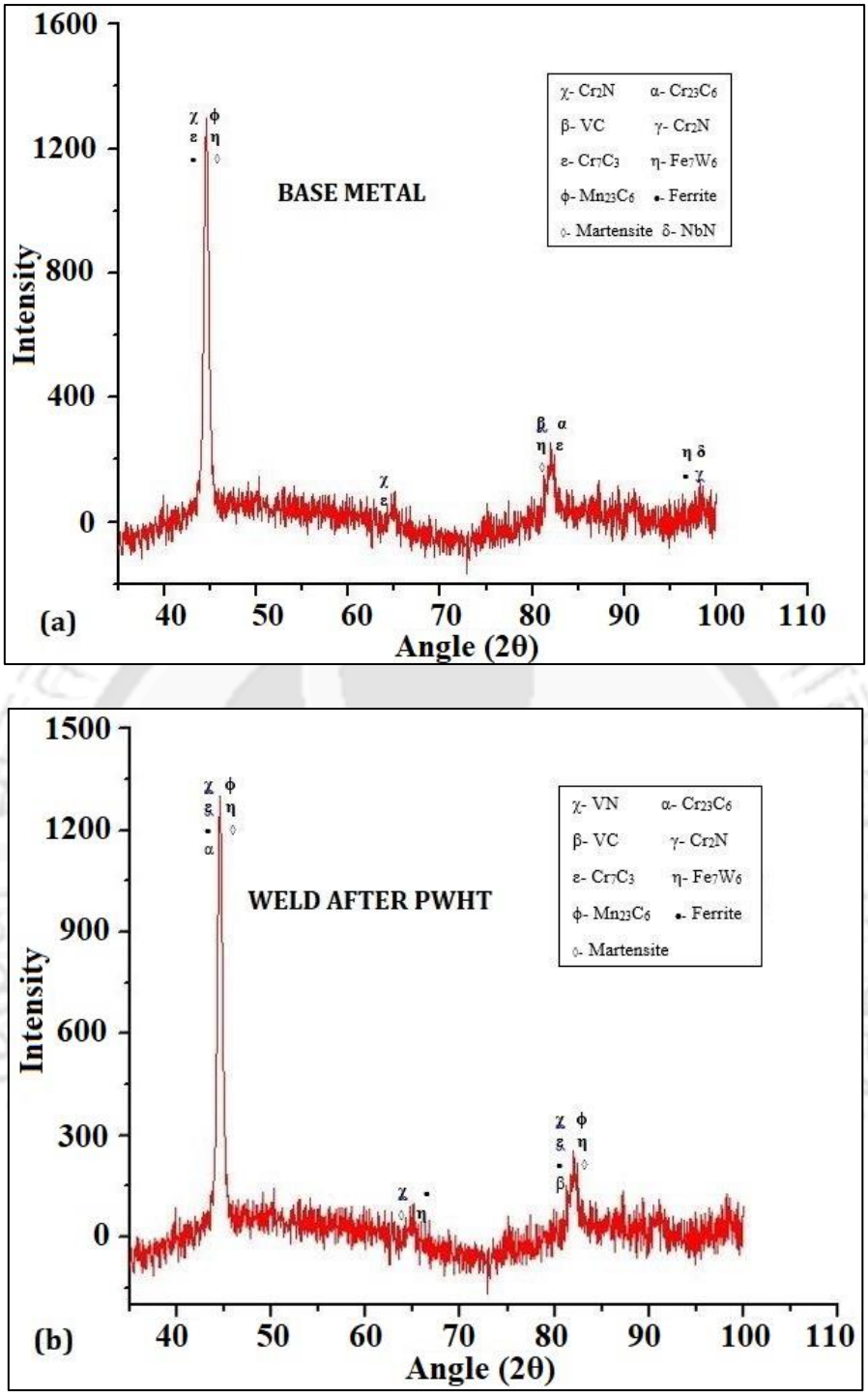

Figure 8.11 X-ray diffraction intensity plots for (a) Base metal, (b) P91 steel weld after PWHT.

8.7 Summary

The effects of preheating and PWHT processes on square butt submerged arc double-side welded joint of P91 steel is presented in this chapter. The study includes characterisations of

microstructure and mechanical properties of the weldments due to preheating and PWHT. Based on the above study, the following conclusions are made.

- The preheating process increases the depth of penetration and improves the bead shape quality.
- Preheating decreased the hardness of the welded joint by 8.2% from the as-welded joint.
- Preheating also reduced the UTS and YS by 2.6% and 4.87%, respectively, compared to the as-welded condition.
- The as-welded sample exhibits the highest UTS and YS, which differ by 13.7% and 21.8% from the base metal.
- The UTS and YS of preheated & post weld heat treated welds are lower than the base metal by 5% and 11%, respectively.
- Post weld heat treated welds witnessed different carbide and nitride precipitates (i.e. $Cr_{23}C_6$, $Mn_{23}C_6$, VC, VN, etc.), which established the desired creep strength in the weldments comparable to the base metal.

CHAPTER 9

CONCLUSIONS AND FUTURE SCOPE

9.1 Conclusions of the present work

P91 steel is one of the most suitable steels for high temperature applications. The steel demonstrates outstanding mechanical and physical properties, especially in a high temperature (> 600 ^{o}C) environment. On the other hand, submerged arc welding is widely known for its automation and high productivity. A conventional submerged arc welding can also provide a decent depth of penetration in single pass welding of a thick plate. Hence, this thesis presents a comprehensive study on submerged arc welding of P91 steel plates.

The submerged arc welding induced temperature distribution, distortion and residual stresses were evaluated by conducting suitable experiments on a 10 mm thick plate. Finite element modelling is one of the well-established methods to simulate and replicate the arc welding process. Therefore, submerged arc welding of the P91 steel plate was also investigated based on the FE simulation results. The thermal history, distortion and residual stresses were elaborately discussed in Chapters 4 and 5. The welding induced distortion and residual stresses are critical post welding issues. It entails additional attention to prevent or condense it. Hence, mitigation techniques were also discussed at various stages before, during and after the welding process. Several mitigation methods are suggested and compared for submerged arc welded P91 steel. Chapters 6 and 7 put across the mitigation techniques to control welding induced distortion and residual stresses. Finite element modelling and simulation were carried out for all pre-, in-, and post-process mitigation processes. The simulation results disclose that in-process mitigation is expectedly effective in reducing the magnitude of residual stress in thick plate welding. Nonetheless, it was not so productive in mitigating residual stress in P91 steel welds, as the initial state of welding induced residual stress is already compressive.

Similarly, pre and post welding mitigation processes were also simulated for appropriate process parameters. These processes were impressive in diminishing and controlling the welding-induced distortion and residual stresses in the P91 steel weld. However, considering other advantages of preheating and post weld heat treatment on mechanical properties of arc

welded joints, experiments were performed on SAW welded joints to examine and assure its mitigation effects.

At last, a detailed study on mechanical and microstructural characterization was also carried on different welding specimens of different mitigation processes. The studies revealed that un-tempered martensite in the FZ of the P91 steel weld resulted in higher hardness and tensile strength with lower ductility. However, preheating and post-weld heat treatment and mitigation effects improved the overall qualities of the weld in terms of better ductility, higher strength and microstructural stability etc.

In accordance with several studies performed on single- and double-sided submerged arc welding of P91 steel for residual stress and distortion, the salient inclusive conclusions are as following:

- The high thermal gradient and high heat intensity induce compressive residual stress in the FZ of SAW welded square butt single side single pass joint of P91 steel.
- SAW welded square butt double side single pass joint shows tensile residual stress distribution in the mid thickness region of FZ owing to slower cooling rate in the region. In contrast, top and bottom regions attain compressive residual stress.
- Hence, conventional single or double side single pass SAW process can be preferred to weld P91 steel thick plate, if compressive residual stress is desired in FZ.
- Solid state phase transformation phenomenon turned out to be one of the key factors for precise finite element modelling of SAW butt joints of P91 steel.
- The numerically predicted residual stresses and distortion results matched fairly well with the experimental results for submerged arc square butt single and double side single pass weld joints.
- Preheating effectively reduces the angular distortion and edge deflection values for both SAW square butt single and double-side single pass joints.
- Preheating exceptionally controls the longitudinal residual stress, which transforms the nature of stress from compressive to tensile in square butt single side single pass welded joint.
- In-process heat treatment mitigation techniques are reasonably competent in reducing the welding induced distortion and residual stresses in thick plate welds.

- The combined side heating and heat sinking developed a crown shape residual stress distribution across the weld centreline with various crests and troughs of compressive and tensile residual stresses, respectively.
- PWHT efficiently mitigated the residual stresses in both FZ and HAZ of both square butt single and double side single pass joints of P91 steel.
- It is observed that soaking time at fix temperature during PWHT does not affect the stress relaxation results and so can be reduced if stress relaxation is the only purpose for PWHT.
- PWHT combined with preheating stimulated a more stable and favourable (least possible tensile or compressive) residual stress distribution across the thickness as well as across the weld centreline.

9.2 Future scope

The current study was focused on thermal history, welding induced distortion and residual stresses in submerged arc welded P91 steel plate. Pre and post weld heat treatment processes were examined for their mitigation effect on submerged arc welded P91 steel. In-process mitigation method was also proposed for thick plate welds (considering the SSPT effects). The study can be extended for following future scope-

- Creep, crack growth and fatigue behaviour can also be explored for submerged arc welded P91 steel joints.
- The submerged arc welding can be conducted on pipes and pressure vessels of P91 steel to explore the residual stress distribution and its mitigations.
- The proposed in-process mitigation can be utilised to design the actual hybrid experimental set up to control the residual stress and distortion in thick ferritic and austenitic plate weld structure.

References

[1] K. Coleman and W. Newell, P91 and Beyond, *Weld. Journal-New York-*, pp. 29–33, 2007.

[2] L. Lindgren, Numerical modelling of welding, *Comput. Methods Appl. Mech. Eng.*, vol. 195, pp. 6710–6736, 2006, doi: 10.1016/j.cma.2005.08.018.

[3] M. Seyyedian Choobi, M. Haghpanahi, and M. Sedighi, Investigation of the effect of clamping on residual stresses and distortions in butt-welded plates, *Sci. Iran.*, vol. 17, no. 5 B, pp. 387–394, 2010.

[4] N. Ma, H. Huang, and H. Murakawa, Effect of jig constraint position and pitch on welding deformation, *J. Mater. Process. Technol.*, vol. 221, pp. 154–162, 2015, doi: 10.1016/j.jmatprotec.2015.02.022.

[5] M. S. Choobi, Investigating the effect of geometrical parameters on distortions in butt-welded plates, *J. strain Anal.*, vol. 48, no. 4, pp. 258–268, 2013, doi: 10.1177/0309324713480766.

[6] S. Paddea, J. A. Francis, A. M. Paradowska, P. J. Bouchard, and I. A. Shibli, Residual stress distributions in a P91 steel-pipe girth weld before and after post weld heat treatment, *Mater. Sci. Eng. A*, vol. 534, pp. 663–672, 2012, doi: 10.1016/j.msea.2011.12.024.

[7] M. Yoshizawa and M. Igarashi, Long-term creep deformation characteristics of advanced ferritic steels for USC power plants, *Int. J. Press. Vessel. Pip.*, vol. 84, no. 1–2, pp. 37–43, 2007, doi: 10.1016/j.ijpvp.2006.09.005.

[8] J. Hald, Microstructure and long-term creep properties of 9-12% Cr steels, *Int. J. Press. Vessel. Pip.*, vol. 85, no. 1–2, pp. 30–37, 2008, doi: 10.1016/j.ijpvp.2007.06.010.

[9] C. Coussement, A. Dhooge, M. de Witte, R. Dobbelaere, and E. van der Donckt, High temperature properties of improved 9% Cr steel weldments, *Int. J. Press. Vessel. Pip.*, vol. 45, no. 2, pp. 163–178, 1991, doi: 10.1016/0308-0161(91)90090-O.

[10] C. Pandey, M. Mohan, P. Kumar, and N. Saini, Some studies on P91 steel and their weldments, *J. Alloys Compd.*, vol. 743, pp. 332–364, 2018, doi:

10.1016/j.jallcom.2018.01.120.

[11] C. Pandey, M. M. Mahapatra, P. Kumar, and N. Saini, Dissimilar joining of CFEF steels using autogenous tungsten-inert gas welding and gas tungsten arc welding and their effect on δ-ferrite evolution and mechanical properties, *J. Manuf. Process.*, vol. 31, pp. 247–259, 2018, doi: 10.1016/j.jmapro.2017.11.020.

[12] W. Sun, A. H. Yaghi, T. H. Hyde, and A. A. Becker, Numerical simulation ofP91 pipe welding including the effects ofsolid-state phase transformation, *Proc. Inst. Mech. Eng. Part L Mater. Des. Appl.*, vol. 92, no. 5, pp. 80–87, 2013, doi: 10.1016/j.acme.2015.05.006.

[13] A. H. Yaghi, T. H. Hyde, A. A. Becker, J. A. Williams, and W. Sun, Residual stress simulation in welded sections of P91 pipes, *J. Mater. Process. Technol.*, vol. 167, no. 2–3, pp. 480–487, 2005, doi: 10.1016/j.jmatprotec.2005.05.036.

[14] M. Zubairuddin, S. K. Albert, M. Vasudevan, S. Mahadevan, V. Chaudhri, and V. K. Suri, Thermomechanical Analysis of Preheat Effect on Grade P91 Steel During GTA Welding, *Mater. Manuf. Process.*, vol. 31, no. 3, pp. 366–371, 2016, doi: 10.1080/10426914.2015.1025964.

[15] C. Pandey, A. Giri, and M. M. Mahapatra, Evolution of phases in P91 steel in various heat treatment conditions and their effect on microstructure stability and mechanical properties, *Mater. Sci. Eng. A*, vol. 664, pp. 58–74, 2016, doi: 10.1016/j.msea.2016.03.132.

[16] R. M. Nugent, R. J. Dybas, J. F. Hunt, and D. W. Meyet, SUBMERGED ARC WELDING, in *Welding Handbook*, 2009, pp. 192–232.

[17] A. H. Yaghi, T. H. Hyde, A. A. Sun, and W. Becker, A Comparison Between Measured and Modeled Residual Stresses in a Circumferentially Butt-Welded P91 Steel Pipe, *J. Press. Vessel Technol.*, vol. 132, no. 1, pp. 1–10, 2010, doi: 10.1115/1.4000347.

[18] L. Cipolla, H. K. Danielsen, D. Venditti, P. E. Di Nunzio, J. Hald, and M. A. J. Somers, Conversion of MX nitrides to Z-phase in a martensitic 12% Cr steel, *Acta Mater.*, vol. 58, no. 2, pp. 669–679, 2010, doi: 10.1016/j.actamat.2009.09.045.

[19] H. K. Danielsen and J. Hald, A thermodynamic model of the Z-phase Cr(V, Nb)N, *Calphad Comput. Coupling Phase Diagrams Thermochem.*, vol. 31, no. 4, pp. 505–514,

2007, doi: 10.1016/j.calphad.2007.04.001.

[20] A. Golpayegani, H. O. Andrén, H. Danielsen, and J. Hald, A study on Z-phase nucleation in martensitic chromium steels, *Mater. Sci. Eng. A*, vol. 489, no. 1–2, pp. 310–318, 2008, doi: 10.1016/j.msea.2007.12.022.

[21] Y.Wang, K. H. Mayer, A. Scholz, K. Durst, and W. Blum, Development of new 11%Cr heat resistant ferritic steels with enhanced creep resistance for steam power plants with operating steam temperatures up to 650 °C, *Mater. Sci. Eng. A*, vol. 510–511, no. C, pp. 180–184, 2009, doi: 10.1016/j.msea.2008.04.116.

[22] K. Sawada, K. Maruyama, Y. Hasegawa, and T. Muraki, Creep Life Assessment of High Chromium Ferritic Steels by Recovery of Martensitic Lath Structure., *Key Eng. Mater.*, vol. 171, no. 174, pp. 109–114, 1999, doi: https://doi.org/10.4028/www.scientific.net/kem.

[23] H. Cerjak, P. Hofer, and B. Schaffernak, Influence of microstructural aspects on the service behaviour of advanced power plant steels, *ISIJ Int.*, vol. 39, no. 9, pp. 874–888, 1999, doi: 10.2355/isijinternational.39.874.

[24] K. Maruyama, K. Sawada, and J. I. Koike, Strengthening mechanisms of creep resistant tempered martensitic steel, *ISIJ Int.*, vol. 41, no. 6, pp. 641–653, 2001, doi: 10.2355/isijinternational.41.641.

[25] N. R. Mandal, Welding residual stress and distortion, in *Ship Construction and Welding*, Springer singapore, 2017, pp. 235–261. doi: https://doi.org/10.1007/978-981-10-2955-4_17.

[26] P. Polcik, T. Sailer, W. Blum, S. Straub, J. Buršík, and a. Orlová, On the microstructural development of the tempered martensitic Cr-steel P 91 during long-term creep—a comparison of data, *Mater. Sci. Eng. A*, vol. 260, no. 1–2, pp. 252–259, 1999, doi: 10.1016/S0921-5093(98)00887-9.

[27] M. Sireesha, S. Sundaresan, and S. Albert, Microstructure and mechanical properties of weld fusion zones in modified 9Cr-1Mo steel, *J. Mater. Eng. Perform.*, vol. 10, no. 3, pp. 320–330, 2001, doi: 10.1361/105994901770345033.

[28] M. Sireesha, S. K. Albert, and S. Sundaresan, Importance of filler material chemistry for optimising weld metal mechanical properties in modified 9Cr – 1Mo steel, *Sci. Technol.*

Weld. Join., vol. 6, no. 4, pp. 247–254, 2001, doi: 10.1179/136217101101538848.

[29] S. Spigarelli and E. Quadrini, Analysis of the creep behaviour of modified P91 (9Cr–1Mo–NbV) welds, *Mater. Des.*, vol. 23, no. 6, pp. 547–552, 2002, doi: 10.1016/S0261-3069(02)00026-2.

[30] M. Tabuchi and Y. Takahashi, Evaluation of Creep Strength Reduction Factors for Welded Joints of Modified 9Cr-1Mo Steel, *J. Press. Vessel Technol.*, vol. 134, no. 3, p. 031401, 2012, doi: 10.1115/1.4006131.

[31] A. H. Yaghi, T. H. Hyde, A. A. Becker, J. A. Williams, and W. Sun, Residual stress simulation in welded sections of P91 pipes, *J. Mater. Process. Technol.*, vol. 167, no. 2–3, pp. 480–487, 2005, doi: 10.1016/j.jmatprotec.2005.05.036.

[32] A. H. Yaghi, T. H. Hyde, A. A. Becker, and W. Sun, Finite element simulation of welding and residual stresses in a P91 steel pipe incorporating solid-state phase transformation and post-weld heat treatment, *J. Strain Anal. Eng. Des.*, vol. 43, no. 5, pp. 275–293, 2008, doi: 10.1243/03093247JSA372.

[33] A. H. Yaghi, T. H. Hyde, A. A. Becker, and W. Sun, Numerical simulation of P91 pipe welding including the effects of solid-state phase transformation on residual stresses, *Proc. Inst. Mech. Eng. Part L J. Mater. Des. Appl.*, vol. 221, no. 4, pp. 213–224, 2007, doi: 10.1243/14644207JMDA152.

[34] A. H. Yaghi, T. H. Hyde, A. A. Becker, and W. Sun, Finite element simulation of welded P91 steel pipe undergoing post-weld heat treatment, *Sci. Technol. Weld. Join.*, vol. 16, no. 3, pp. 232–238, 2011, doi: 10.1179/1362171810Y.0000000018.

[35] A. H. Yaghi, T. H. Hyde, A. A. Becker, and W. Sun, Thermo-mechanical modelling of P91 steel weld microstructure and residual stresses in power plant pipework, *1st Int. Conf. Sustain. Power Gener. Supply, SUPERGEN '09*, no. September, 2009, doi: 10.1109/SUPERGEN.2009.5348007.

[36] S. Kumar, A. Kundu, A. Venkata K. A. Evans, C. E. Truman, and G. K. Dey, Residual stresses in laser welded ASTM A387 Grade 91 steel plates, *Mater. Sci. Eng. A*, vol. 575, pp. 160–168, 2013, doi: 10.1016/j.msea.2013.03.046.

[37] A. Kundu, P. J. Bouchard, S. Kumar, G. K. Dey, and C. E. Truman, Residual stresses in P91 steel electron beam welds, *Sci. Technol. Weld. Join.*, vol. 18, no. 1, pp. 70–75, 2013,

doi: 10.1179/1362171812Y.0000000076.

[38] M. Zubairuddin, S. K. .Albert, S.Mahadevan, M.Vasudevan, V. Chaudhari, and V. K. Suri, Experimental and finite element analysis of residual stress and distortion in GTA welding of modified 9Cr-1Mo steel, *J. Mech. Sci. Technol.*, vol. 28, no. 12, pp. 5095–5105, 2014, doi: 10.1007/s12206-014-1132-0.

[39] C. Pandey, A. Giri, and M. M. Mahapatra, Effect of normalizing temperature on microstructural stability and mechanical properties of creep strength enhanced ferritic P91 steel, *Mater. Sci. Eng. A*, vol. 657, pp. 173–184, 2016, doi: 10.1016/j.msea.2016.01.066.

[40] C. Pandey, S. Sirohi, M. M. Mahapatra, P. Kumar, and K. K. Bansal, Role of Heat Treatment on Grain Refinement and Microhardness of 9Cr–1Mo–V–Nb Steel, *Metallogr. Microstruct. Anal.*, vol. 8, no. 4, pp. 472–478, 2019, doi: 10.1007/s13632-019-00555-y.

[41] C. Pandey and M. M. Mahapatra, Effect of Groove Design and Post-Weld Heat Treatment on Microstructure and Mechanical Properties of P91, *J. Mater. Eng. Perform.*, vol. 25, no. 7, pp. 2761–2775, 2016, doi: 10.1007/s11665-016-2127-z.

[42] C. Pandey, M. M. Mahapatra, P. Kumar, S. Kumar, and S. Sirohi, Effect of post weld heat treatments on microstructure evolution and type IV cracking behavior of the P91 steel welds joint, *J. Mater. Process. Technol.*, vol. 266, no. October 2018, pp. 140–154, 2019, doi: 10.1016/j.jmatprotec.2018.10.024.

[43] C. Pandey, M. M. Mahapatra, and P. Kumar, A comparative study of transverse shrinkage stresses and residual stresses in P91 welded pipe including plasticity error, *Arch. Civ. Mech. Eng.*, vol. 18, no. 3, pp. 1000–1011, 2018, doi: 10.1016/j.acme.2018.02.007.

[44] V. Maduraimuthu, M. Vasudevan, V. Muthupandi, A. K. Bhaduri, and T. Jayakumar, Effect of activated flux on the microstructure, mechanical properties, and residual stresses of modified 9Cr-1Mo steel weld joints, *Metall. Mater. Trans. B Process Metall. Mater. Process. Sci.*, vol. 43, no. 1, pp. 123–132, 2012, doi: 10.1007/s11663-011-9568-4.

[45] F. Hosseinzadeh and P. J. Bouchard, Mapping Multiple Components of the Residual

Stress Tensor in a Large P91 Steel Pipe Girth Weld Using a Single Contour Cut, *Exp. Mech.*, vol. 53, no. 2, pp. 171–181, 2013, doi: 10.1007/s11340-012-9627-z.

[46] L. T. Jones, H. E. Keanedy, A. M. Roternathd, and C. Berkeley, Electric Welding, US 2043960, 1936 doi: 10.1145/178951.178972.

[47] K. Weman, Submerged Arc Welding. Welding Processes Handbook, in *Welding Processes Handbook*, Second., 2012, pp. 105–117. doi: 10.1533/9780857095183.105.

[48] R. M. Nugent, R. J. Dybas, J. F. Hunt, and D. W. Meyet, SUBMERGED ARC WELDING, in *Welding Handbook*, 2009, pp. 192–232.

[49] S. N. A. Gotoh; and Takeshi Nakagawa, Submerged arc welding method for high strength Cr - Mo steel, 5430269, 1995

[50] Y. Z. and R. X. Zai-lin Xu, Submerged arc welding of SA335 P91 steel, *Weld. Technol.*, vol. 4, 2005.

[51] Y. C. Han, Y., XU, D.L. and Chen, R & D of P91 Steel Welding Wire for Automatic Submerged Arc Welding, *Electr. Power Constr.*, vol. 6, 2007.

[52] R. V. Rao and V. D. Kalyankar, Experimental investigation on submerged arc welding of Cr–Mo–V steel, *Int. J. Adv. Manuf. Technol.*, vol. 69, no. 1–4, pp. 93–106, Oct. 2013, doi: 10.1007/s00170-013-5007-9.

[53] P. Mohyla and K. Foldynová, Effect of post-welding heat treatment on mechanical properties of joints of steel P92 formed by submerged arc welding, *Met. Sci. Heat Treat.*, vol. 56, no. 3–4, pp. 206–209, 2014, doi: 10.1007/s11041-014-9732-y.

[54] S. Zhang, T. Melfi, and B. K. Narayanan, Effects of precipitates on mechanical properties of P91 submerged arc welds, *Sci. Technol. Weld. Join.*, vol. 21, no. 2, pp. 147–156, 2016, doi: 10.1179/1362171815Y.0000000076.

[55] J. Roy, R. N. Rai, and S. C. Saha, Evaluation of microstructure and mechanical properties of P91 steel weldment due to addition of boron trioxide into flux during submerged arc welding, *Weld. World*, vol. 62, no. 1, pp. 1–8, 2018, doi: 10.1007/s40194-017-0515-0.

[56] J. Roy, R. Chakraborti, R. N. Rai, and S. C. Saha, Studies on microstructure and mechanical properties of modified 9Cr–1Mo (P91) steel in submerged arc welding with

TiO2-enriched fluxes, *J. Brazilian Soc. Mech. Sci. Eng.*, vol. 41, no. 10, pp. 1–9, 2019, doi: 10.1007/s40430-019-1968-4.

[57] M. Näsström and M. Karlberg, Welding Heat Input Models, in *Encyclopedia of Thermal Stresses*, R. B. Hetnarski, Ed. Dordrecht: Springer Netherlands, 2014, pp. 6567–6572. doi: 10.1007/978-94-007-2739-7_467.

[58] M. M. Mahapatra, G. L. Datta, B. Pradhan, and N. R. Mandal, Three-dimensional finite element analysis to predict the effects of SAW process parameters on temperature distribution and angular distortions in single-pass butt joints with top and bottom reinforcements, *Int. J. Press. Vessel. Pip.*, vol. 83, no. 10, pp. 721–729, 2006, doi: 10.1016/j.ijpvp.2006.07.011.

[59] M. M. Mahapatra, G. L. Datta, B. Pradhan, and N. R. Mandal, Modelling the effects of constraints and single axis welding process parameters on angular distortions in one-sided fillet welds, *Proc. Inst. Mech. Eng. Part B J. Eng. Manuf.*, vol. 221, no. 3, pp. 397–407, 2007, doi: 10.1243/09544054JEM617.

[60] P. Biswas and N. R. Mandal, Thermomechanical finite element analysis and experimental investigation of single-pass single-sided submerged arc welding of C—Mn steel plates, *Proc. Inst. Mech. Eng. Part B J. Eng. Manuf.*, vol. 224, no. 4, pp. 627–639, 2010.

[61] S. W. Wen, P. Hilton, and D. C. J. Farrugia, Finite element modelling of a submerged arc welding process, *J. Mater. Process. Technol.*, vol. 119, no. 1–3, pp. 203–209, 2001, doi: 10.1016/S0924-0136(01)00945-1.

[62] A. Ghosh, S. Chattopadhyaya, R. K. Das, and P. K, Prediction of Submerged Arc Welding Yield Parameters through Graphical Technique, *Procedia Eng.*, vol. 10, pp. 2797–2802, 2011, doi: 10.1016/j.proeng.2011.04.465.

[63] D. V. Kiran and S. joo Na, Numerical Studies on Submerged Arc Welding Process, *J. Weld. Join.*, vol. 32, no. 4, pp. 339–347, 2014, doi: http://dx.doi.org/10.5781/JWJ.2014.32.4.1.

[64] I. F. Z. Fanous, M. Y. A. Younan, and A. S. Wifi, Study of the Effect of Boundary Conditions on Residual Stresses in Welding Using Element Birth and Element Movement Techniques, *J. Press. Vessel Technol. Trans. ASME*, vol. 125, no. 4, pp. 432–

439, 2003, doi: 10.1115/1.1613952.

[65] M. R. Forouzan, S. M. Mirfalah Nasiri, A. Mokhtari, A. Heidari, and S. J. Golestaneh, Residual stress prediction in submerged arc welded spiral pipes, *Mater. Des.*, vol. 33, no. 1, pp. 384–394, 2012, doi: 10.1016/j.matdes.2011.04.016.

[66] M. R. Nezamdost, M. R. N. Esfahani, S. H. Hashemi, and S. A. Mirbozorgi, Investigation of temperature and residual stresses field of submerged arc welding by finite element method and experiments, *Int. J. Adv. Manuf. Technol.*, vol. 87, no. 1–4, pp. 615–624, 2016, doi: 10.1007/s00170-016-8509-4.

[67] A. Ishigami, M. J. Roy, J. N. Walsh, and P. J. Withers, The effect of the weld fusion zone shape on residual stress in submerged arc welding, *Int. J. Adv. Manuf. Technol.*, vol. 90, no. 9–12, pp. 3451–3464, 2017, doi: 10.1007/s00170-016-9542-z.

[68] A. Ghosh and H. Chattopadhyay, Mathematical modeling of moving heat source shape for submerged arc welding process, *Int. J. Adv. Manuf. Technol.*, vol. 69, no. 9–12, pp. 2691–2701, 2013, doi: 10.1007/s00170-013-5154-z.

[69] F. Html, N. Akkas, D. Karayel, S. S. Ozkan, A. Oğur, and B. Topal, Modeling and Analysis of the Weld Bead Geometry in Submerged Arc Welding by Using Adaptive Neurofuzzy Inference System, vol. 2013, no. 2013, pp. 1–7, 2015.

[70] ANSTO, Simulating phase transformations during the welding of ferritic steels, 2012. https://phys.org/news/2012-10-simulating-phase-welding-ferritic- steels.html (accessed Sep. 30, 2020).

[71] H. Paul and M. Ristinmaa, A Constitutive Model for the Formation of Martensite in Austenitic Steels Under Large Strain Plasticity, vol. 23, no. 7, pp. 1213–1239, 2007, doi: 10.1016/j.ijplas.2006.11.002.

[72] K. Magally, V. Romero, C. Arturo, and B. Ávila, Mathematical Modeling of Phase Transformations and Residual Stress in A Thermomechanical Heat Treatment in AISI 1045 Steel By FEM, no. 7, pp. 118–126, 2016.

[73] A. H. Yaghi, T. H. Hyde, A. A. Becker, and W. Sun, Numerical simulation of P91 pipe welding including the effects of solid-state phase transformation on residual stresses, vol. 221, pp. 213–224, 2007, doi: 10.1243/14644207JMDA152.

[74] B. Taljat, B. Radhakrishnan, and T. Zacharia, Numerical analysis of GTA welding process with emphasis on post-solidification phase transformation effects on residual stresses, *Mater. Sci. Eng. A*, vol. 246, no. 1–2, pp. 45–54, 1998, doi: 10.1016/s0921-5093(97)00729-6.

[75] H. Dai, J. A. Francis, and P. J. Withers, Prediction of residual stress distributions for single weld beads deposited on to SA508 steel including phase transformation effects, *Mater. Sci. Technol.*, vol. 26, no. 8, pp. 940–949, 2010, doi: 10.1179/026708309X12459430509454.

[76] J. B. Leblond, G. Mottet, and J. C. Devaux, A theoretical and numerical approach to the plastic behaviour of steels during phase transformations-II. Study of classical plasticity for ideal-plastic phases, *J. Mech. Phys. Solids*, vol. 34, no. 4, pp. 411–432, 1986, doi: 10.1016/0022-5096(86)90010-4.

[77] D. Dean and M. Hidekazu, Prediction of welding residual stress in multi-pass butt-welded modified 9Cr – 1Mo steel pipe considering phase transformation effects, vol. 37, pp. 209–219, 2006, doi: 10.1016/j.commatsci.2005.06.010.

[78] E. B. Farahani and B. S. Aragh, Three-dimensional finite element modelling of welding residual stresses of medium carbon steel pipes with consideration of solid-state austenite-martensite transformation and post-weld heat treatment, *Proc IMechE Part L J Mater. Des. Appl.*, vol. 0, no. 0, pp. 1–13, 2019, doi: 10.1177/1464420719850205.

[79] S. K. Albert, M. Matsui, T. Watanabe, H. Hongo, K. Kubo, and M. Tabuchi, Variation in the type IV cracking behaviour of a high Cr steel weld with post weld heat treatment, *Int. J. Press. Vessel. Pip.*, vol. 80, no. 6, pp. 405–413, 2003, doi: 10.1016/S0308-0161(03)00072-3.

[80] J. Ohlsson, Effects of different heat treatments on hardness of Grade 91 steel, *Thesis*, 2014.

[81] C. Pandey, M. M. Mahapatra, P. Kumar, N. Saini, and A. Srivastava, Microstructure and mechanical property relationship for different heat treatment and hydrogen level in multi-pass welded P91 steel joint, *J. Manuf. Process.*, vol. 28, pp. 220–234, 2017, doi: 10.1016/j.jmapro.2017.06.009.

[82] V. Sudharsanam, V. Senthilkumar, N. Raju, and R. Vetriselvan, Evaluation of post weld

heat treatment quality of modified 9Cr-1Mo (P91) steel weld by magnetic coercive force measurements, *Arch. Civ. Mech. Eng.*, vol. 15, no. 4, pp. 847–853, 2015, doi: 10.1016/j.acme.2015.05.006.

[83] F. H. Steel, G. Taniguchi, and K. Yamashita, Effects of Post Weld Heat Treatment (PWHT) Temperature on Mechanical Properties of Weld Metals for High-Cr, 2006.

[84] M. V Deo, P. Michaleris, M. V Deo, and P. Michaleris, Mitigation of welding induced buckling distortion using transient thermal tensioning, *Sci. Technol. Weld. Join.*, vol. 8, no. 1, pp. 49–54, 2003, doi: 10.1179/136217103225008919.

[85] E. Armentani, R. Esposito, and R. Sepe, The influence of thermal properties and preheating on residual stresses in welding, *Int. J. Comput. Mater. Sci. Surf. Eng.*, vol. 1, no. 2, pp. 146–162, 2007, doi: 10.1504/IJCMSSE.2007.014870.

[86] M. C. Zondi, Factors that affect welding-induced residual stress and distortions in pressure vessel steels and their mitigation techniques: A review, *J. Press. Vessel Technol. Trans. ASME*, vol. 136, no. 4, pp. 1–9, 2014, doi: 10.1115/1.4026564.

[87] M. Perić, I. Garašić, S. Nižetić, and H. Dedić-Jandrek, Numerical Analysis of Longitudinal Residual Stresses and Deflections in a T-joint Welded Structure Using a Local Preheating Technique, *Energies*, vol. 11, no. 12, 2018, doi: 10.3390/en11123487.

[88] W. Zhang, H. Fu, J. Fan, F. Liu, and B. Qi, Influence of multi-beam preheating temperature and stress on the buckling distortion in electron beam welding, *Mater. Des.*, vol. 139, pp. 439–446, 2018, doi: 10.1016/j.matdes.2017.11.016.

[89] Y. C. Lin and K. H. Lee, Effect of preheating on the residual stress in type 304 stainless steel weldment, *J. Mater. Process. Technol.*, vol. 63, no. 1–3, pp. 797–801, 1997, doi: 10.1016/S0924-0136(96)02727-6.

[90] C. Pandey, M. M. Mahapatra, P. Kumar, F. Daniel, and B. Adhithan, Softening mechanism of P91 steel weldments using heat treatments, *Arch. Civ. Mech. Eng.*, vol. 19, no. 2, pp. 297–310, 2019, doi: 10.1016/j.acme.2018.10.005.

[91] G. K. Padhy, V. Ramasubbu, N. Murugesan, C. Remash, and S. K. Albert, Effect of preheat and post-heating on diffusible hydrogen content of welds, *Sci. Technol. Weld. Join.*, vol. 17, no. 5, pp. 408–413, 2012, doi: 10.1179/1362171812Y.0000000023.

[92] A. K. Singh, T. Debnath, V. Dey, and R. N. Rai, A Study on Effect of Preheating and Post Weld Heat Treatment (PWHT) of Grade P91 Steel, vol. 2, no. 8, pp. 57–62, 2015.

[93] Y. P. Yang and P. Dong, Buckling Distortions and Mitigation Techniques for Thin-Section Structures, *J. Mater. Eng. Perform.*, vol. 21, no. 2, pp. 153–160, 2012, doi: 10.1007/s11665-011-9928-x.

[94] J. Li, Q. Guan, Y. W. Shi, and D. L. Guo, Stress and distortion mitigation technique for welding titanium alloy thin sheet, *Sci. Technol. Weld. Join.*, vol. 9, no. 5, pp. 451–458, 2004, doi: 10.1179/136217104225021643.

[95] Q. Guan, D. L. Guo, C. X. Zhang, and J. Li, Low Stress no distortion welding based on thermal tensioning for effects for thin materials, in *International Scientific-Technical and Production Journal*, December., no. December, B. E. Paton, Ed. Kyis: International Association «Welding», 2006, pp. 1–11.

[96] D. Camilleri, T. G. F. Gray, and D. H. Nash, Mitigation of welding distortion and residual stresses via cryogenic CO2 cooling - a numerical investigation, in *17th International Conference on Computer Technology in Welding and Manufacturing*, 2008, pp. 1–11.

[97] T. Bajpei, H. Chelladurai, and M. Z. Ansari, Mitigation of residual stresses and distortions in thin aluminium alloy GMAW plates using different heat sink models, *J. Manuf. Process.*, vol. 22, pp. 199–210, 2016, doi: 10.1016/j.jmapro.2016.03.011.

[98] Y. Guo, D. Wu, G. Ma, and D. Guo, Trailing heat sink effects on residual stress and distortion of pulsed laser welded Hastelloy C-276 thin sheets, *J. Mater. Process. Technol.*, vol. 214, no. 12, pp. 2891–2899, 2014, doi: 10.1016/j.jmatprotec.2014.06.012.

[99] P. Michaleris and X. Sun, Finite element analysis of thermal tensioning techniques mitigating weld buckling distortion, *Weld. J. (Miami, Fla)*, vol. 76, no. 12, pp. 451-s, 1997.

[100] M. Li, S. Ji, D. Yan, and Z. Yang, Controlling welding residual stress and distortion by a hybrid technology of transient thermal tensioning and trailing intensive cooling, *Sci. Technol. Weld. Join.*, vol. 24, no. 6, pp. 527–537, 2019, doi: 10.1080/13621718.2018.1564473.

[101] D. A. Price, S. W. Williams, A. Wescott, P. Staron, and M. Koçak, Distortion control in

welding by mechanical tensioning, *Sci. Technol. Weld. Join.*, vol. 12, no. 7, pp. 620–633, 2007, doi: 10.1179/174329307X213864.

[102] H. E. Coules, P. Colegrove, L. D. Cozzolino, S. W. Wen, S. Ganguly, and T. Pirling, Effect of high pressure rolling on weld-induced residual stresses, *Sci. Technol. Weld. Join.*, vol. 17, no. 5, pp. 394–401, 2012, doi: 10.1179/1362171812Y.0000000021.

[103] D. Xu, X. S. Liu, P. Wang, J. G. Yang, and H. Y. Fang, New technique to control welding buckling distortion and residual stress with non-contact electromagnetic impact, *Sci. Technol. Weld. Join.*, vol. 14, no. 8, pp. 753–759, 2009, doi: 10.1179/136217109X12505932584736.

[104] D. G. Richards, P. B. Prangnell, S. W. Williams, and P. J. Withers, Global mechanical tensioning for the management of residual stresses in welds, *Mater. Sci. Eng. A*, vol. 489, no. 1–2, pp. 351–362, 2008, doi: 10.1016/j.msea.2007.12.042.

[105] R. V. Rao and V. D. Kalyankar, Experimental investigation on submerged arc welding of Cr–Mo–V steel, *Int. J. Adv. Manuf. Technol.*, vol. 69, no. 1–4, pp. 93–106, Oct. 2013, doi: 10.1007/s00170-013-5007-9.

[106] ESAB arc welding consumables for creep resisting steels . creep resisting steels -, Netherlands, 2008.

[107] N. S. Rossini, M. Dassisti, K. Y. Benyounis, and A. G. Olabi, Methods of measuring residual stresses in components, *Mater. Des.*, vol. 35, pp. 572–588, 2012, doi: 10.1016/j.matdes.2011.08.022.

[108] I. Sattari-Far and M. R. Farahani, Effect of the weld groove shape and pass number on residual stresses in butt-welded pipes, *Int. J. Press. Vessel. Pip.*, vol. 86, no. 11, pp. 723–731, 2009, doi: 10.1016/j.ijpvp.2009.07.007.

[109] X. Pu, C. Zhang, S. Li, and D. Deng, Simulating welding residual stress and deformation in a multi-pass butt-welded joint considering balance between computing time and prediction accuracy, *Int. J. Adv. Manuf. Technol.*, vol. 93, no. 5–8, pp. 2215–2226, 2017, doi: 10.1007/s00170-017-0691-5.

[110] A. H. Mahmoudi, S. Hossain, C. E. Truman, D. J. Smith, and M. J. Pavier, A new procedure to measure near yield residual stresses using the deep hole drilling technique, *Exp. Mech.*, vol. 49, no. 4, pp. 595–604, 2009, doi: 10.1007/s11340-008-9164-y.

[111] N. W.Bonner and D. J Smith, Measurement of residual stresses in a thick section steel weld., *Eng. Integr. Assess.*, pp. 259–274, 1994.

[112] M. B. Prime and A. T. DeWald, The Contour Method, in *Practical Residual Stress Measurement Methods*, G. S. Schajer, Ed. Wiley Blackwell, 2013, pp. 109–138. doi: 10.1002/9781118402832.ch5.

[113] Bueckner H.F., Field singularities and related integral representations., in *Methods of analysis and solutions of crack problems.*, 1973, pp. 239–314. doi: https://doi.org/10.1007/978-94-017-2260-5_5.

[114] P. Pagliaro, M. B. Prime, J. S. Robinson, M. Steinzig, and B. Zuccarello, Measuring Inaccessible Residual Stresses Using Multiple Methods and Superposition, *Exp. Mech.*, vol. 51, no. 7, pp. 1123–1134, 2011, doi: 10.1007/s11340-010-9424-5.

[115] M. B. Prime, Cross-sectional mapping of residual stresses by measuring the surface contour after a cut, *J. Eng. Mater. Technol. Trans. ASME*, vol. 123, no. 2, pp. 162–168, 2001, doi: 10.1115/1.1345526.

[116] V. Richter-Trummer, P. M. G. P. Moreira, J. Ribeiro, and P. M. S. T. De Castro, The contour method for residual stress determination applied to an AA6082-T6 friction stir butt weld, *Mater. Sci. Forum*, vol. 681, pp. 177–181, 2011, doi: 10.4028/www.scientific.net/MSF.681.177.

[117] P. Wilson, H. A. Mantooth, and M. Engineering, Levenberg-Marquardt Algorithm, in *Model-Based Engineering for Complex Electronic Systems*, 2013, pp. 347–367. doi: https://doi.org/10.1016/B978-0-12-385085-0.00010-5.

[118] H. P. Gavin, The Levenburg-Marqurdt Algorithm For Nonlinear Least Squares Curve-Fitting Problems, 2020.

[119] Theory of Nonlinear Curve Fitting, *Origin lab*. https://www.originlab.com/doc/Origin-Help/NLFit-Theory

[120] A. Ghosh, Selection of Appropriate Moving Heat Source Shape of Submerged Arc Welding Process, pp. 6–14, 2012.

[121] A. Barman, N. Chattopadhyay, and H. Hloch, A Study of Thermal Behaviour during Submerged Arc Welding, vol. 59, pp. 333–338, 2013, doi: 10.5545/sv-jme.2012.775.

[122] M. R. Nezamdost, M. R. N. Esfahani, S. H. Hashemi, and S. A. Mirbozorgi, Investigation of temperature and residual stresses field of submerged arc welding by finite element method and experiments, *Int. J. Adv. Manuf. Technol.*, vol. 87, no. 1–4, pp. 615–624, 2016, doi: 10.1007/s00170-016-8509-4.

[123] I. Journal, E. N. Management, and T. Tiruchirapp, Modelling and optimisation of submerged arc welding process parameters using particle swarm optimisation technique, no. April, 2016, doi: 10.1504/IJENM.2010.037932.

[124] G. Fu, J. Gu, M. I. Lourenco, M. Duan, and F. Segen, Parameter determination of double-ellipsoidal heat source model and its application in the multi- pass welding process, *Ships Offshore Struct.*, vol. 10, no. 2, pp. 204–217, 2015, doi: 10.1080/17445302.2014.937059.

[125] Y. Rong, T. Lei, J. Xu, Y. Huang, and C. Wang, Residual stress modelling in laser welding marine steel EH36 considering a thermodynamics-based solid phase transformation, *Int. J. Mech. Sci.*, vol. 146–147, no. January, pp. 180–190, 2018, doi: 10.1016/j.ijmecsci.2018.07.046.

[126] S. Cho, J. Kim, S. Cho, and J. Kim, Analysis of residual stress in carbon steel weldment incorporating phase transformations, *Sci. Technol. Weld. Join.*, vol. 7, no. 4, pp. 212–216, 2013, doi: 10.1179/136217102225004257.

[127] D. Dean and M. Hidekazu, Prediction of welding residual stress in multi-pass butt-welded modified 9Cr – 1Mo steel pipe considering phase transformation effects, *Comput. Mater. Sci.*, vol. 37, pp. 209–219, 2006, doi: 10.1016/j.commatsci.2005.06.010.

[128] A. H. Yaghi, D. W. J. Tanner, T. H. Hyde, A. A. Becker, and W. Sun, Finite element thermal analysis of the fusion welding of a P92 steel pipe, *Mech. Sci.*, vol. 3, pp. 33–42, 2012, doi: 10.5194/ms-3-33-2012.

[129] H. K. D. H. Bhadeshia, J. a. Francis, R. B. Rogge, P. J. Withers, and L. Karlsson, Transformation Plasticity in Steel Weld Metals, *Proc. 10th Int. Aachen Weld. Conf.*, no. January 2014, 2007, doi: 10.1053/j.semperi.2014.07.001.

[130] D. Deng, D. Deng, and H. Murakawa, Influence of transformation induced plasticity on simulated results of welding residual stress in low temperature transformation steel,

Comput. Mater. Sci., vol. 78, pp. 55–62, 2013, doi: 10.1016/j.commatsci.2013.05.023.

[131] C. Franz, G. Besserdich, V. Schulze, H. Müller, and D. Löhe, Influence of transformation plasticity on residual stresses and distortions due to the heat treatment of steels with different carbon contents, vol. d, pp. 481–488, 2004, doi: 10.1051/jp4.

[132] F. D. Fischer, G. Reisner, E. Werner, K. Tanaka, G. Cailletaud, and T. Antretter, New view on transformation induced plasticity (TRIP), *Int. J. Plast.*, vol. 16, no. 7, pp. 723–748, 2000, doi: 10.1016/S0749-6419(99)00078-9.

[133] C. T. Karlsson, Finite element analysis of temperatures and stresses in a single pass butt welded pipe- influence of mesh density and material modelling, *Eng. Comput.*, vol. 6, pp. 133–141, 1989.

[134] A. H. Yaghi, T. H. Hyde, A. A. Becker, and W. Sun, Thermo-mechanical modelling of P91 steel weld microstructure and residual stresses in power plant pipework, *1st Int. Conf. Sustain. Power Gener. Supply, SUPERGEN '09*, no. September, 2009, doi: 10.1109/SUPERGEN.2009.5348007.

[135] E. E. U. Haque and P. R. Hampson, Modelling phase change in a 3D thermal transient analysis, *Int. J. Multiphys.*, vol. 8, no. 1, pp. 49–68, 2014, doi: 10.1260/1750-9548.8.1.49.

[136] E. Keehan, Effect of Microstructure on Mechanical Properties of High Strength Steel Weld Metals, Chalmers University of Technology and Goteborg University, Sweden., 2004.

[137] N. Yurioka, Comparison of preheat predictive methods, *Weld. World*, vol. 48, no. 10, pp. 21–27, 2004.

[138] P. Polcik, T. Sailer, W. Blum, S. Straub, J. Buršík, and a. Orlová, On the microstructural development of the tempered martensitic Cr-steel P 91 during long-term creep—a comparison of data, *Mater. Sci. Eng. A*, vol. 260, no. 1–2, pp. 252–259, 1999, doi: 10.1016/S0921-5093(98)00887-9.

[139] M. C. Zondi, Factors That Affect Welding-Induced Residual Stress and Distortions in Pressure Vessel Steels and Their Mitigation Techniques: A Review, *J. Press. Vessel Technol.*, vol. 136, no. 4, p. 040801, 2014, doi: 10.1115/1.4026564.

[140] Y. C. Lin and C. P. Chou, A new technique for reducing the residual stress induced by welding in type 304 stainless steel, *J. Mater. Process. Technol.*, vol. 48, pp. 693–698, 1995, doi: 10.1887/0750306076/b1388v3c1.

[141] Harlan H. Bengtson, Convection Heat Transfer Coefficient Estimation. pp. 1–40, 2010. [Online]. Available: http://www.s3.amazonaws.com/suncam

[142] M. N. Ilman, M. R. Muslih, N. Subeki, and H. Wibowo, Mitigating distortion and residual stress by static thermal tensioning to improve fatigue crack growth performance of MIG AA5083 welds, *JMADE*, vol. 99, pp. 273–283, 2016, doi: 10.1016/j.matdes.2016.03.049.

[143] J. J. Vora and V. J. Badheka, Experimental investigation on microstructure and mechanical properties of activated TIG welded reduced activation ferritic / martensitic steel joints, *J. Manuf. Process.*, vol. 25, pp. 85–93, 2017, doi: 10.1016/j.jmapro.2016.11.007.

[144] X. W. Zhu, H. Cheng, M. H. Shen, and J. P. Pan, Determination of C Parameter of Larson- Miller Equation 15 CrMo Steel., *Adv. Mater. Res.*, vol. 791–793, pp. 374–377, 2013.

[145] M. Tamura, F. Abe, K. Shiba, H. Sakasegawa, and H. Tanigawa, Larson-miller constant of heat-resistant steel, *Metall. Mater. Trans. A Phys. Metall. Mater. Sci.*, vol. 44, no. 6, pp. 2645–2661, 2013, doi: 10.1007/s11661-013-1631-0.

[146] K. Mithun, K. Saraswathamma, and D. K. Verma, Effect of post weld heat treatment soaking time on microstructure and mechanical properties of TIG welded grade 91 steel, *J. Met. Mater. Miner.*, vol. 29, no. 2, pp. 42–50, 2019, doi: 10.14456/jmmm.2019.17.

[147] T. D. Canonsburg, *ANSYS Mechanical APDL Coupled-Field Analysis Guide*, vol. 3304, no. November. 2013.

[148] C. Heinze, A. Pittner, M. Rethmeier, and S. S. Babu, Dependency of martensite start temperature on prior austenite grain size and its influence on welding-induced residual stresses, *Comput. Mater. Sci.*, vol. 69, pp. 251–260, 2013, doi: 10.1016/j.commatsci.2012.11.058.

[149] S. M. C. Van Bohemen and J. Sietsma, Martensite Formation in Partially and Fully Austenitic Plain Carbon Steels, *Metall. Mater. Trans. A*, vol. 40, no. 5, pp. 1059–1068,

2009, doi: 10.1007/s11661-009-9796-2.

[150] A. K. Mondal, P. Biswas, and S. Bag, Experimental and FE analysis of submerged arc weld induced residual stress and angular deformation of single and double sided fillet welded joint, *Int. J. Steel Struct.*, vol. 17, no. 1, pp. 9–18, 2017, doi: 10.1007/s13296-016-0093-9.

[151] S. Suman, P. Biswas, and P. V. S. S. Sridhar, Numerical prediction of welding distortion in submerged arc welded butt and fillet joints., in *International Conference on Design and Manufacturing, IITDM, Chennai*, 2016, no. 1, pp. 1–5.

[152] J. Mackerle, Finite element analysis and simulation of quenching and other heat treatment processes: A bibliography (1976-2001), *Comput. Mater. Sci.*, vol. 27, no. 3, pp. 313–332, 2003, doi: 10.1016/S0927-0256(03)00038-7.

[153] A. M. A. Pazooki, M. J. M. Hermans, and I. M. Richardson, Finite element simulation and experimental investigation of thermal tensioning during welding of DP600 steel, *Sci. Technol. Weld. Join.*, vol. 22, no. 1, pp. 7–21, 2017, doi: 10.1080/13621718.2016.1180861.

[154] M. Asadi and J. A. Goldak, An Integrated Computational Welding Mechanics With Direct-Search Optimization for Mitigation of Distortion in an Aluminum Bar Using Side Heating, *J. Manuf. Sci. Eng.*, vol. 136, no. 1, p. 11007, 2013, doi: 10.1115/1.4025406.

[155] A. V Damale and K. N. Nandurkar, Numerical simulation of side heating for controlling angular distortion in multipass MMAW butt welded plates, *Sadhana*, vol. 40, no. April, pp. 487–502, 2015.

[156] Y. Guo, D. Wu, G. Ma, and D. Guo, Trailing heat sink effects on residual stress and distortion of pulsed laser welded Hastelloy C-276 thin sheets, *J. Mater. Process. Technol.*, vol. 214, no. 12, pp. 2891–2899, 2014, doi: 10.1016/j.jmatprotec.2014.06.012.

[157] M. Asadi and J. A. Goldak, An Integrated Computational Welding Mechanics With Direct-Search Optimization for Mitigation of Distortion in an Aluminum Bar Using Side Heating, *J. Manuf. Sci. Eng.*, vol. 136, no. 1, p. 011007, 2013, doi: 10.1115/1.4025406.

[158] J. Li, Q. Guan, Y. Shi, D. Guo, Y. Du, and Y. Sun, Studies on characteristics of temperature field during GTAW with a trailing heat sink for titanium sheet, vol. 147, pp. 328–335, 2004, doi: 10.1016/j.jmatprotec.2003.12.012.

[159] P. Dong, S. Song, and J. Zhang, Analysis of residual stress relief mechanisms in post-weld heat treatment, *Int. J. Press. Vessel. Pip.*, vol. 122, no. 1, pp. 6–14, 2014, doi: 10.1016/j.ijpvp.2014.06.002.

[160] C. Pandey, M. M. Mahapatra, P. Kumar, F. Daniel, and B. Adhithan, Softening mechanism of P91 steel weldments using heat treatments, *Arch. Civ. Mech. Eng.*, vol. 19, no. 2, pp. 297–310, 2019, doi: 10.1016/j.acme.2018.10.005.

[161] C. Pandey, A. Giri, M. M. Mahapatra, and P. Kumar, Characterization of microstructure of HAZs in as-welded and service condition of P91 pipe weldments, *Met. Mater. Int.*, vol. 23, no. 1, pp. 148–162, 2017, doi: 10.1007/s12540-017-6394-5.

[162] Richard A.M. Napitupulu, Influence of heating rate and temperature on austenite grain size during reheating steel, in *IOP Conference Series: Materials Science and Engineering*, 2017, pp. 1–8. doi: 10.1088/1757-899X/237/1/012038.

[163] K. H. Dhandha and V. J. Badheka, Effect of activating fluxes on weld bead morphology of P91 steel bead-on-plate welds by flux assisted tungsten inert gas welding process, *J. Manuf. Process.*, vol. 17, pp. 48–57, 2015, doi: 10.1016/j.jmapro.2014.10.004.

List of Publications

Publication from thesis works:

International journal (SCI):

1. **S Suman**, A Tiwari, P Biswas, M. M. Mahapatra, FE analysis of thermal induced stresses in submerged arc welded Chromium-Molybdenum steel and its mitigation through heat treatment, **Journal of Materials Engineering and Performances** 29 (12), 8271- 8285, DEC, 2020.
2. **S Suman**, P Biswas, Comparative study on SAW welding induced distortion and residual stresses of CSEF steel considering solid state phase transformation and Preheating, **Journal of Manufacturing Processes** 51, 19-30, JAN, 2020.
3. **S Suman,** P Biswas, A Tiwari, Microstructure Evolution and Mechanical Behaviour of SAW Weldments of CSEF Steel on Preheating and PWHT, **Trans Indian Inst Met** (2020), APRIL, 2020.
4. **S Suman**, P Biswas, Residual Stresses in Single and Double-Sided Submerged Arc Welded Cr- Mo Grade 91 steel – Experimental Investigation and FE Validation, **Welding in the world** (Under review)
5. **S Suman**, P Biswas, Finite Element Analysis of In- Process Thermal Mitigation of Welding Induced Residual Stresses in Thick Plate Welds of 9Cr-1Mo-V Steel Considering Phase Transformation (Communicated)

International journal proceedings (Scopus):

6. **S Suman**, P Biswas, S K Patel, V P Singh, A Kumar, B Kuriachen, Measurement of residual stresses in submerged arc welded P91 steel using surface distortion, **Materials Today: Proceedings,** 21 (3), 1707-1712, JAN 2020.

Book chapters:

7. **S Suman**, P Biswas, Computational Modelling of In-process Mitigation Technique to Control Residual Stress in Thick Plate Welding, **Next Generation Materials and Processing Technologies, Springer (In press),** 2021

8. **S Suman**, P Biswas, Numerical Study of Welding Distortion in SAW Welded Creep Strength Enhanced Ferrite Steel Joint, **Advances in Mechanical Engineering**, **Springer**, FEB 2020.

Publication related to thesis works:

International journal (SCI):

9. **S Suman**, P Sridhar, P Biswas, D Das, Prediction of welding-induced distortions in large weld structure through improved equivalent load method based on average plastic strains, **Welding in the World** 64 (1), 179-200, DEC, 2019.

International journal proceedings (Scopus):

10. **S Suman**, P Biswas, Thermo-mechanical study of single and multi-pass welding of CSEF steel for residual stresses and distortions considering solid state phase transformation **Materials Today: Proceedings**, 28 (2), 789-795, JAN 2020.
11. **S Suman**, P Biswas, S Baranwal, V Mekala, Finite Element Modelling of side heating for mitigation of residual stress and distortion in SAW welded P91 steel weld, **Materials today: proceedings,** 28 (4), 2511- 2521, MAY 2020.

Book chapters:

12. **S Suman**, A Tiwari, P Pankaj, P Biswas, B Kuriachen, A Sinha, Modelling of Welding Sequences for Minimization of Weld-Induced Distortions and Residual Stresses, **Advances in Additive Manufacturing and Joining**, **Springer**, 609-617, DEC 2019.
13. **S Suman**, P Pankaj, A Tiwari, P Biswas, B Kuriachen, A Sinha, Effect of Pre-and Post-welding Processes on the Distortion Pattern in a SAW-Welded Butt Joint of P91 Steel Plate, **Advances in Additive Manufacturing and Joining**, **Springer**, 631-639, DEC 2019.

Appendix

Appendix A

Machine Name	Make and Model	Specifications
UTM	Instron, UK	• Hydraulic power pack pumping capacity 25 ltr/min • Testing Method: Load control and position control (strain and displacement)
Micro hardness tester	Make: Omni Tech	• Indentation force 50,100,300,500,2000 gF • Dwell time:5 to 60 s
Stereomicroscope	Make: Nikon, Model:SMZ25	• Zoom ratio:25: 1 • Magnification range: 0.63−15.75× • Motorized zoom • Zooming observation: BF/DF/FL/Simple polarizing
Optical microscope	Make: Carl Zeiss, Model: Axiotech-100HD, 3D	• Magnification: 50−5000× • Table movement: 3 −axis measuring system, reflecting light measuring step 75 mm ×55 mm ×50 mm • Lens: Binocular photo type • Camera: Axio-Cam and Axio vision 4.8.2 software (in built)
Field emission scanning electron microscope (FESEM)	Make: Zeiss, Model: Sigma	• Specimen chamber: 330 mm inner dia, 270 mm height • Specimen weight: up to 0.5 kg tilted; up to 2 kg not tilted • Movement: X =125 mm, Y=125 mm, Z =50 mm, T = −10° to 360°, R = 360° continues • Specimen stage: 5 axis motorized cartesian

XRD	Panalytical, X-pert	• 3 kW generator and direct optical positioning • Pre-FIX incident and diffracted beam • X ray lens with attenuator, fixed divergence slits 1/32° • High resolution goniometer with optically encoded sample positioning enables a minimum step of 0.0001°
Wire cut EDM	Make: Fostex Model: FDK 7735	• Max. cutting speed- 160- 180 mm/min • Max. cutting angle- 6º, 15º • Positional accuracy- 0.015/300 mm
Die Sinking EDM	Make: Sparkonix	• Max Electrode Wt. 50 kg • Max Job Height 325 mm • Daylight (With Electrode Holder) 385 mm • Shut Height 135 mm
Coordinate measuring machine (CMM)	Make: Carl Zeiss Model: Vista (Bridge type)	• Operating mode- motorised • Software- U soft • Scanning speed- max. 200 mm/ min. • Benchtop- 16″ × 20″ × 14″.

Appendix B

(Contour residual stress measurement technique)

Nonlinear surface fitting:

- Algorithm: Levenberg Marquardt algorithm
- Model: Polynomial 2D
- Polynomial equation:

$$z = z_0 + A_1 \times x + A_2 \times pow(x, 2) + A_3 \times pow(x, 3) + A_4 \times pow(x, 4) + A_5 \times pow(x, 5) + B_1 \times y + B_2 \times pow(y, 2) + B_3 \times pow(y, 3) + B_4 \times pow(y, 4) + B_5 \times pow(y, 5)$$

where

$z_0, A_1, A_2, A_3, A_4, A_5, B_1, B_2, B_3, B_4, B_5$ are constants.